INTRAGRATING SENSING USING CHIRPED OPTICAL FIBRE BRAGG GRATINGS

A thesis submitted

by

Anbhawa Nand

MSc, BSc, PGDip(PH), GCTT, GCEd (USP)

for the degree of

DOCTOR OF PHILOSOPHY

Optical Technology Research Laboratory

School of Electrical Engineering

Faculty of Health, Engineering and Science

Victoria University

Australia

2007

To my wife Sarita and daughter Ashneeta

Declaration

"I, Anbhawa Nand, declare that the PhD thesis entitled,

CHIRPED FIBRE BRAGG INTRAGRATING POSITION AND STRAIN MEASUREMENT SENSOR

is no more than 100,000 words in length, exclusive of tables, figures, appendices, references and footnotes. The thesis contains no material that has been submitted previously, in whole or in part, for the award of any other academic degree or diploma. Except where otherwise indicated, this thesis is my own work".

…….

Anbhawa Nand

dated the 3rd day of April, 2007

Acknowledgements

I am indebted to many individuals who have provided assistance and support during the period of this research. Foremost, I would like to thank my supervisors, Associate Professor Stephen Collins and Professor Greg Baxter for providing the opportunity to undertake this research and their constant guidance, useful comments, encouragement and discussions in all aspects of this research.

I am also grateful to Dr Dan Kitcher for his unconditional support, helpful discussions and assistance in modelling of intragrating sensors during the course of this research. A special thank to Dr Scott Wade for his useful comments and help in grating fabrication. I would also like to thank my fellow post-graduate students, technical and administrative staff of the School of Electrical Engineering for their assistance and friendship.

I also acknowledge the Victoria University Postgraduate Scholarship scheme for providing the scholarship for this research, the Australian Research Council for providing the financial support for the purchase of relevant equipment for this project and the use of Swinburne-Monash-DSTO grating fabrication system, Monash University's thermal camera and Finite Element Method (FEM) software.

Finally, I would like to express my deep appreciation to my wife Sarita and daughter Ashneeta for their unconditional support, patience and encouragement throughout the duration of this thesis.

Abstract

This thesis describes a study of intragrating position (localised heat source) and strain measurement sensor systems. The design, development and performance of intensity (power) reflection spectrum based intragrating sensing systems employing chirped fibre Bragg gratings (CFBGs) are investigated.

Intragrating sensing is the process of obtaining a continuous profile of a measurand over the grating length from either the amplitude or phase, or both the amplitude and phase of its measured reflection response. Techniques for intragrating sensing employing conventional fibre Bragg gratings have been reviewed and analysed in order to design an intragrating sensor which overcomes the problems associated with the existing sensor systems. The inability to determine the position of the disturbance, direction of the strain gradient and the broadening of the spectra together with the reduction in reflectance complicates the grating inverse reconstruction technique to recover the disturbance profile and is also computationally expensive. Thus the selection of CFBGs is desirable because each Bragg wavelength in the broadband reflection spectrum from a CFBG corresponds to particular local position along the grating. Thus a change in the reflection intensity spectrum, due to a disturbance, at a particular wavelength can be quantified to a local position in the grating and hence the spatial distribution of the measurand can be evaluated. The thesis consists of four major sections: fabrication of CFBGs, sensor calibration, intragrating position and strain measurements.

Techniques for the production and controlling the spectral response of CFBGs suitable for intragrating sensing application were investigated using two fabrication techniques; the prism interferometer and the scanning phase mask system. The modelling and experimental results showed that fabrication constraints exist for designing a suitable sensor for intragrating measurements with the prism technique, and thus most of the gratings used for this research were fabricated with the scanning phase mask system.

The analysis of results for strain/temperature characterisation, showed that CFBGs fabricated in hydrogenated standard telecommunications fibre have a temperature coefficient approximately 20% higher than standard FBGs in the 1550 nm region with

identical strain coefficients. Thus a simple technique for strain-independent temperature measurement is proposed and demonstrated using a sensor head with a combination of a standard FBG and a CFBG. This is an additional finding of the research.

The intragrating position measurements within a CFBG sensor were investigated as a function of grating strength. Five linear CFBGs of chirp rate 20 nm/cm, approximate length of 15 mm with varying levels of reflectance (6-53%), fabricated with the scanning phase mask technique were employed for the determination of the centre position of a localised heat source within a CFBG. An iterative approach in conjunction with a fast Fourier transform (FFT) was implemented for solving the inverse problem of obtaining the nonuniform temperature distribution from the measured intensity reflection spectrum. The extracted temperature distribution was characterised by the three parameters of amplitude, width and the centre position. The precision of the inferred centre position of the localised heat source was investigated as a function of grating strength. It was demonstrated that the centre position root mean square (rms) error generally improves with grating strength up to approximately 30% peak reflectance and then decreases with further increase in grating strength for both the high and moderate temperature amplitudes which were investigated. A position rms error below 0.03 mm and a repeatability rms error of 0.005 mm were obtained for the centre position measurements with the CFBG intragrating sensor for grating strengths in the range 20-30%. The position rms error reported is the best to date for CFBG based intragrating sensing systems.

The intragrating strain measurements were investigated using three embedded CFBGs sensors to determine nonuniform strain distribution near a stress concentration within a notched aluminium specimen subjected to an axial tensile force. The strain distribution was determined from the analysis of the intensity reflection spectrum through the use of an integration method which did not require an initial strain distribution hypothesis. The best case performance was obtained with the sensor having a reflectance of around 23%. The shape of the recovered strain distributions were in reasonable agreement with that predicted by the finite element method (FEM) modelling however some discrepancies were noted. These are most likely due to incomplete transfer of surface strain within the specimen through 3-layers (host/adhesive/fibre) to the fibre core. A repeatability rms error of less than 4 $\mu\varepsilon$ in the extracted strain profiles was obtained.

Table of Contents

List of Figures

List of Tables

CHAPTER 1

INTRODUCTION

1.1 Background

Optical fibre sensors (OFS) have received a great deal of research interest in recent years due to their significant sensing capabilities. Compared to conventional electro-magnetic sensors and transducers, OFS exhibit a number of distinct advantages such as (Kersey *et al.,* 1997 and Rao, 2002):

- EMI immunity,
- remote sensing capabilities for long distance application,
- operation in hazardous environments,
- small size and light weight; i.e. suitable for installing or embedding into structures,
- high sensitivity and wide bandwidth, and
- multiplexing capabilities either as multipoint quasi-distributed or fully distributed sensors for application in smart structures.

These sensing capabilities have been incorporated in the development of various optical fibre sensing systems for industrial, engineering and laboratory based applications. In most of these sensing systems, optical fibre sensors act as transducers and convert measurands such as temperature and strain into a corresponding change in the optical radiation. Since light is characterised by amplitude (intensity), phase, frequency and polarisation, any one of these parameters may undergo a change. Thus the effectiveness of the optical fibre sensor depends on its ability to convert the measurands into these parameters reliably and accurately.

Of all the developments in the field of OFS, Fibre Bragg Grating (FBG) sensor technology has generated the most interest during the last decade. The fundamental reasons for the growing interest is that compared with other OFS, FBG sensors have a

number of distinguishing advantages (section 1.3). Significant progress has been made in applications involving strain and temperature measurements where FBGs are either attached or embedded into structures, thus making them ideal for Fibre-Optic Smart Structures (Rao, 1997 and 1999). Recent developments include the use of FBGs as quasi-distributed and intragrating sensors for structural health monitoring (Kersey *et al.,* 1997). These techniques involve obtaining a continuous profile of the measurand (e.g. temperature, strain) over the entire grating length to more effectively map the distribution of these parameters near attachment points, cracks or stress concentrations.

1.2 Fibre Bragg Gratings

Since their discovery nearly 30 years ago (Hill *et al.,* 1978), FBGs have had a significant impact on modern optical fibre telecommunications and optical fibre sensing systems. The reasons are that FBGs can perform many of the primary functions such as reflection, diffraction, dispersion and filtering (spatial and polarization) in a highly efficient and low energy loss manner (Othonos *et al.,* 1999). Other areas of application include fibre lasers, fibre amplifiers, medical, the electrical power industry and structural monitoring.

A Fibre Bragg Grating in its most basic form consists of a periodic modulation of the index of refraction along the fibre core. These gratings are photo-inscribed into a few centimetres of the fibre core, using a variety of techniques, to induce changes in the core index of refraction. The procedure normally used involves illuminating a short length of the fibre with an ultraviolet light interferogram. The modulation of the index of refraction is possible because of the phenomenon of photosensitivity in the fibre core. The magnitude of the index modulation (Δn) depends on the writing beam wavelength, writing beam intensity, net dosage and the composition of the fibre host material.

The grating reflects a spectral peak if broadband light is transmitted along the fibre. When the Bragg condition is satisfied, the contribution of reflected light from each grating plane adds constructively. The constructively added light is back reflected at a certain wavelength (known as the Bragg wavelength, λ_B). The Bragg wavelength is a

function of the grating pitch (period) and the index of refraction along the grating and is given as

$$\lambda_B = 2n\Lambda \qquad 1.1$$

where λ_B is the reflected Bragg wavelength, n is the effective refractive index of the fibre core and Λ is the grating pitch (or period of index modulation).

Since certain physical quantities (particularly strain and temperature) influence both parameters (grating period and index of refraction), they therefore cause a change in the Bragg wavelength of the light that is reflected back. Thus the basic principle of operation commonly used in FBG based sensor systems is to monitor the shift in the reflected Bragg wavelength signal due to changes in the measurand (e.g. temperature, strain).

1.3 Advantages of Fibre Bragg Gratings

FBGs have become key passive devices for application in optical fibre telecommunications and in the rapidly developing field of optical fibre sensors due to a number of advantages over other optical fibre sensors (Rao, 1997 and 1999). These include that FBGs:

- when interrogated are insensitive to fluctuations in the irradiance of the illuminating source,
- can be fabricated without changing the fibre diameter,
- have the potential to be mass-produced at low cost,
- have unique wavelength-division (WDM) and time-division multiplexing (TDM) capabilities,
- have great potential in sensing applications for simultaneous measurements of important physical parameters and in quasi-distributed sensor networks,
- can be used in fibre-optic smart structures where they can be attached or embedded into structures for the provision of real-time sensing information.

Table 1.1 shows a comparison between FBG sensors with other fibre-optic strain sensors for application in smart structures (Rao, 1997).

Parameters	FBG	FP	TM	PM
Linear response	yes	yes	yes	yes
Absolute measurement	yes	yes	yes	yes
Range to resolution	high	high	low	low
Sensor gauge length	short	short	long	long
Mechanical strength	high	low	high	high
Multiplexing	yes	yes	yes	yes
Mass production	yes	yes	yes	yes
Potential cost	low	low	low	low

Table 1.1 Advantages of FBG sensors over other fibre-optic sensors, FP: Fabry-Perot Interferometric Sensors, TM: Two Mode Fibre Optic Sensors and PM: Polarimetric Fibre-Optic Sensors (Source: Rao, 1997).

1.4 Chirped Fibre Bragg Gratings

Significant interest has recently been focused on chirped fibre Bragg gratings (CFBGs) for applications in telecommunications and sensing. Chirped gratings have a nonuniform period along their length and exhibit a broadened spectral response. That is, they reflect a spectral band of wavelengths related to the range of grating periods along the grating length. For gratings with nonuniform periodicity, different sections of the grating contribute to the reflectance at different wavelengths (Kersey *et al.,* 1997 and Othonos *et al.,* 1999). The Bragg wavelength is a function of position along the grating and each section of the grating contributes to the "local" Bragg wavelength given by

$$\lambda_B(z) = 2n(z)\Lambda(z)\,, \qquad 1.2$$

where $n(z)$ is the local average refractive index as a function of position along the grating and $\Lambda(z)$ is the period of index modulation (pitch) along the grating.

Chirp in a grating can be imparted by a number of techniques as listed below (Othonos *et al.,* 1999 and Kashyap, 1999):

- axially varying either the period of the grating (Λ) or the effective index of refraction (n_{eff}) of the core or both,
- applying nonuniform strain along a fibre prior to or after grating fabrication,

- fabricating gratings in a tapered fibre under applied strain,
- fabricating gratings in a fibre bent with respect to the interference fringes, and
- fabricating gratings in a thermally diffused region of the fibre core (Cho *et al.,* 2004).

Chirp in gratings may take many different forms with the period varying symmetrically (either increasing or decreasing around a central pitch in the centre of the grating), linearly, quadratically, randomly or with jumps along the length of the grating. Chirped gratings have applications in dispersion compensation in telecommunications, WDM transmission, optical fibre amplifiers for pulse amplification and amplifier gain flattening, band-blocking and band-pass filters, fibre lasers, pulse shaping in ultra fast-pulsed laser systems and sensing.

Chirped gratings have been reported for a range of sensing applications: temperature-strain discrimination (Rao *et al.,* 2001, Frazao *et al.,* 2005, Cusano *et al.,* 2006), temperature-independent strain sensing (Xu *et al.,* 1995, Kim *et al.,* 2000), temperature-independent curvature measurements (Dong *et al.,* 2001), temperature-independent tilt sensing (Dong *et al.,* 2005), distributed temperature sensing (Won *et al.,* 2004) and extraction of nonuniform temperature profiles (Kersey *et al.,* 1997). They have also been demonstrated as position-dependent pressure sensors in monitoring esophageal pressures (Swart *et al.,* 2005), optical wear sensors (Gilloolly *et al.,* 2004) and for the detection of crack locations in composite materials (Okabe *et al.,* 2004 and Palaniappan *et al.,* 2005, 2006).

As a result of the work reported in this thesis, CFBGs have been demonstrated: for strain-independent temperature measurements (Nand *et al.,* 2006a), as intragrating sensors for the extraction of nonuniform temperature profiles along a grating (Nand *et al.,* 2005a, 2005b, Kitcher *et al.,* 2004, 2005a, 2005b), for the measurement of a temperature gradient (Kitcher *et al.,* 2006a), for the determination of the position of a localised heat source (Nand *et al.,* 2005c, Nand *et al.,* 2006) and for the measurement of a localised strain distribution (Nand *et al.,* 2007). Furthermore, the reflectance spectra of CFBGs have been shown experimentally, and verified theoretically to be directionally dependent due to cladding mode excess loss (Kitcher *et al.,* 2005c, 2006).

1.5 Fibre Bragg Intragrating Sensing

FBG sensors have been multiplexed using an array of FBGs to obtain strain and temperature distributions at discrete locations along a structure to provide quasi-distributed sensing (Tjin *et al.,* 2002). Such sensing systems, however, provide only an average of the measurand along the length of each grating and thus would be unsuitable for applications involving regions of high strain or large temperature gradients. In such applications, a continuous profile of the measurand as a function of position along the grating length with millimetre positional resolution is required to detect cracks or to pinpoint hot spots.

Intragrating sensing refers to applications for which it is desired to obtain a continuous profile of a measurand over the grating length (Kersey *et al.,* 1997). The technique involves detailed analysis of either the amplitude or phase or both amplitude and phase of the measured reflection spectrum to obtain a fully distributed profile of the measurand. The technique uses the fact that different sections of the grating contribute to the reflectance at different wavelengths when the gratings' modulation periodicity is nonuniform along its length. Each section of the grating contributes to the "local" Bragg wavelength given by equation 1.2. Thus a fully distributed profile of the measurand along the grating length may be derived from the Bragg wavelength as a function of position along the grating.

In applications where strain along a FBG sensor is uniform, the strain can be determined from the shift in the reflected Bragg wavelength of the grating. However, in applications where a strain gradient exists, the reflected spectrum will not only be shifted but also distorted because of the induced chirp in the grating (Huang *et al.,* 1995). Thus, the shape of the measured reflection spectrum depends on the strain distribution along the grating. These changes in the reflection spectrum caused by a nonuniform measurand field along the length of the grating, forms the basis of this relatively new technique of intragrating sensing.

When a uniform grating is subjected to a nonuniform strain or temperature distribution, different sections of the grating contribute to different Bragg wavelengths according to the local state of the measurand. This broadens the spectrum and reduces the peak

reflectance. This nonuniformity modifies both the intensity and the phase of the reflected spectrum of the grating. Thus by analysing either the intensity or phase component of the reflected spectrum, or both, the "modified" Bragg wavelength (as a function of the position along the grating) may be determined. Hence by taking the difference between the modified Bragg wavelength ($\lambda_B^1(z)$) and the reference Bragg wavelength ($\lambda_B^0(z)$) as a function of position along the grating length, yields ($\Delta\lambda_B(z)$), from which either the temperature or strain distribution can be obtained from the known sensitivity of the sensor.

However, there is a distinct advantage in using chirped fibre Bragg grating for intragrating sensing. For a chirped grating, each wavelength in the reflected intensity spectrum corresponds to a particular (local) position along the grating. Thus a change or modification in the reflected intensity spectrum due to a physical quantity, such as strain or temperature, can be directly related to a local position along the grating and hence the spatial distribution of strain or temperature gradients can be determined. Such a determination can be extremely complicated when using a conventional uniform FBG. Thus researchers in this field have suggested the use of chirped gratings for intragrating sensing because of its ability to determine nonuniform strain and temperature fields with a superior spatial resolution. Kersey *et al.,* (1997) verified theoretically that spatial resolution is further improved when the Bragg wavelength changes more rapidly with position due to either an initial chirp in the grating or an applied strain gradient or both, provided the gradient is not sufficiently large to cancel the initial chirp.

To determine the Bragg wavelength as a function of position, four techniques have been presented which are discussed in detail in section 2.4. There are:

- Intensity-spectrum based intragrating sensing,
- Phase-spectrum based intragrating sensing,
- Combined intensity and phase spectrum measurements, and,
- Low coherence reflectometry measurement.

1.6 Scope of the Thesis and Research Objectives

Sensors of all types are vital for the measurement of important physical quantities for industrial applications. Compared to conventional electrical sensors, fibre Bragg grating sensors offer improved novel techniques for applications in structural health monitoring for composite materials, civil infrastructure and engineering structures.

Recently, significant interest has centred on designing sensors that seek to obtain a fully distributed profile of the measurand near either an attachment point, lap joints, cracks or stress concentrations for smart structure applications. Though distributed measurements are currently possible with either quasi-distributed sensing using an array of multiplexed FBGs or optical fibre based distributed sensing (Rayleigh, Raman and Brillouin) systems, however both these techniques have certain drawbacks. The former provides only an average of the disturbance along the length of each grating and is constrained by the design of FBG arrays and the available spectral source bandwidth. The latter suffers from poor position resolution of the order of 1 metre. Such resolutions are not sufficient (by 3 orders magnitude) to pinpoint hotspots or detect cracks in a structure.

Thus there is demonstrable need to design FBG sensors with improved capabilities to detect localised temperature or strain near stress concentrations with better spatial resolution. Intragrating sensing offers an option to overcome these problems by providing a continuous profile of a measurand over the grating length to map the strain and/or temperature distribution. Therefore it is proposed, in this project, to design and develop intragrating temperature and strain sensor systems based on chirped fibre Bragg gratings due to their following advantages in sensing applications:

- broad bandwidth spectrum provides a high sensitivity range to monitor localised and extreme values of temperature and strain and the spatial distribution of these along the grating,
- capability of measuring non-monotonic measurand fields,
- can be tailored to simultaneously discriminate between strain and temperature and provide temperature-independent strain (Xu *et al.,* 1995, Kim *et al.,* 2000), or strain-independent temperature sensing, and,
- the performance such as precision and spatial resolution are dependent on chirp rate within the CFBG.

The principal aims of the research project were to design, fabricate and develop optical fibre sensor systems employing CFBGs for the determination of the position of a localised heat source and the measurement of a nonuniform localised strain distribution using the intensity reflection spectrum, $R(\lambda)$, based intragrating sensing technique. Laboratory testing of the sensors was conducted on representative structural specimens, with the view to improve precision and repeatability of position and strain measurements together with the spatial resolution.

The specific objectives of the project were:

- investigation of the fabrication techniques for the production of chirped gratings suitable for intragrating sensing applications,
- modelling of the CFBG spectra using a discrete Fourier transform (FFT) grating reconstruction technique,
- determination of the strain/temperature coefficients of the CFBG sensors and the development of sensors with high strain/temperature sensitivities capable of intragrating sensing,
- investigation of CFBG sensors for possible application in strain-independent temperature measurements,
- design, construction and implementation of intragrating temperature and strain measurement sensing systems for application of localised temperature (heat source) and strain gradient,
- modelling of the effect of localised temperature disturbance on the reflectance spectra of a CFBG and the use of an iterative FFT grating simulation technique, operating on the reference spectrum and hypothetical temperature distributions, for solving the inverse problem of obtaining the temperature distribution from the measured intensity reflection spectrum, $R(\lambda)$, of a CFBG,
- assessment of the CFBG sensor system performance in relation to precision and repeatability of the centre position of a localised heat source on grating strength, $R(\lambda)$,
- modelling of the surface strain distribution along the specimen using the numerical structural finite element method (FEM) based on the linear elasticity theory of solid mechanics, using the FEMAP/NASTRAN software,
- extraction of the nonuniform strain profile along the CFBG sensor from the changes in the measured power reflectance spectra between the perturbed and

unperturbed grating using the integration of difference technique, and,

- in-laboratory testing of the sensor systems developed on representative structural specimens using the intensity reflection spectrum, $R(\lambda)$, based intragrating sensing technique.

CHAPTER 2

BACKGROUND ON DISTRIBUTED AND INTRAGRATING SENSING

2.1 Introduction

This chapter reviews the field of distributed sensing (applications employing optical fibres) and intragrating sensing (applications employing FBGs) as sensing elements. The term distributed sensing describes the technique of obtaining a continuous profile of the measurand spatially distributed along the sensor length. Thus distributed sensing has potential application into areas involving underground power cables and structural health monitoring. Distributed sensor systems offer a number of advantages over conventional sensing systems: measurement of physical parameters continuously over the sensor length (possibly several km for optical fibres) using a single sensing element, remote sensing capabilities and high-speed measurements using a single processor to control data acquisition. Distributed sensing can be broadly classified into two basic categories:

Optical fibre as the intrinsic sensing element: Techniques based on optical time-domain reflectometry also referred to as backscatter. In this the backscattered signal due to one of the several mechanisms such as Rayleigh, Raman or Brillouin scattering is analysed to obtain information on the spatial variation of the measurand along the fibre length.

Fibre Bragg grating based sensing systems: The use of FBGs in quasi-distributed multiplexed systems, fully distributed systems and intragrating sensing. In this, the shift in the Bragg wavelength of the reflected signal due to a measurand is analysed to obtain information on the measurand as a function of position along the grating.

2.2 Distributed Optical Fibre based Sensing

2.2.1 Optical Time Domain Reflectometry (OTDR) technique

Many distributed optical fibre sensing (DOFS) systems employ the principle of Optical Time Domain Reflectometry (OTDR). The OTDR is effectively a one-dimensional optical radar. In this technique a pulse of laser light is periodically launched into one end of the sensing fibre via a directional coupler and the time dependent characteristics of the light that is backscattered to the same fibre end are measured. As the pulse propagates along the fibre, it is scattered by several mechanisms (Rayleigh, Raman and Brillouin scattering) back to the launching end where it is detected by the receiver.

The OTDR operation is based on the measurand-dependent localised loss due to the perturbation of the fibre by the measurand (strain, temperature, pressure etc.) field. This causes a change in the backscattered signal versus time-delay curve (OTDR curve). The change in signal at a particular time-delay corresponds to the spatial position of the perturbation. Thus variation in the back-scattered signal provides information on the measurand as a function of distance along the fibre. Therefore, DOFS systems offer capabilities of making spatially distributed measurement of a measurand field over the fibre length.

In an unperturbed fibre of uniform diameter, the intensity of the backscattered light is an exponential decay function with time (Hartog, 1983). Practically, the intensity of the backscattered light deviates from the exponential form due to variations in fibre compositions, fibre diameter, numerical aperture, longitudinal changes in the Rayleigh scattering coefficient, temperature, strain and other physical parameters. Thus if the speed of the propagation of light in the fibre is known, the backscattered power can be resolved to provide the spatial distribution of optical attenuation along the fibre. Therefore the OTDR can provide measurement of any external physical parameter, which influences the attenuation in the fibre. Figure 2.1 shows a functional diagram of an OTDR (Hartog, 1983).

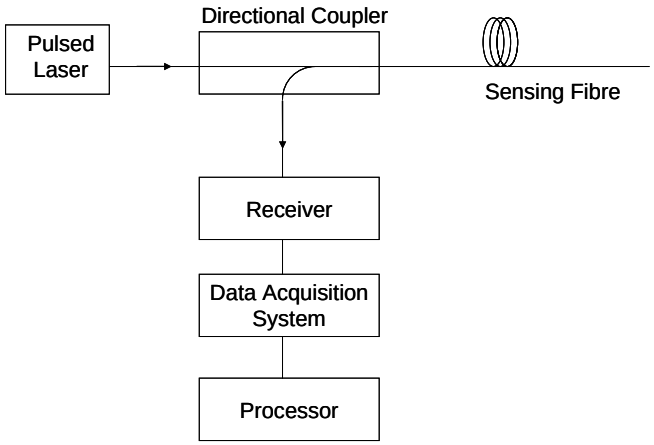

Figure 2.1 Functional diagram of an Optical Time Domain Reflectometer.

The back scattered power, $P(t)$, returning to the launching end after time, t, is expressed as (Hartog, 1983)

$$P(t) = P_0 W \eta(z) \exp(-\int_0^t \alpha(z) v_g dt), \qquad 2.1$$

where P_0 is the power launched into the fibre, W is the pulse width, v_g is the group velocity, $\alpha(z)$ is the local attenuation coefficient and $\eta(z)$ is the backscatter factor (the ratio of the backscatter power to the probe pulse energy). Distance, z, from the launching end is related to the delay time, t, (elapsed time between the launch of the pulse and the received backscattered light) as $z = v_g t/2$.

Distributed optical fibre based sensing systems have been reviewed extensively by (Rogers, 1999). They employ several scattering mechanisms for mapping the measurand as a function of position along the fibre, ranging from the earliest systems, the Rayleigh back scattering (as in an OTDR) to commercialized Raman systems which measure the ratio of anti-Stokes to Stokes intensities, to a recent technique based on the Brillouin interaction between the optical pulse and a continuous counter-propagating wave in a single mode fibre. The ability of distributed optical fibre sensing systems to determine physical parameters as a function of position along the fibre have generated intensive research interest. The next sections summarise these scattering mechanisms, briefly.

2.2.2 Rayleigh scattering

Rayleigh scattering arises from the small spatial variations in the refractive index of the optical fibre due to thermally-induced density changes and composition of the medium. The Rayleigh signal is unshifted from the launch wavelength and has the strongest intensity in the backscattered spectrum. It is, however, only very weakly sensitive to temperature differences along the fibre. In a conventional OTDR, Rayleigh backscatter is used to provide information about signal loss, fibre breaks and inhomogeneties along the fibre length for telecommunications. Rayleigh back-scattering has been demonstrated for distributed sensing applications to measure temperature and strain. Table 2.1 lists some of the applications employing this technique together with sensing range, precision, and spatial resolution achieved to date.

Sensing Mechanism	Physical Quantity Measured	Sensing range	Precision temp./strain	Spatial resolution	Reference
Coherent Rayleigh backscatter	Strain	0.5 m	1 nε/√Hz at 2 kHz	NA	Posey *et al.,* 2000
Rayleigh backscatter/ EDFA	Temperature	100 m	10 - 20 °C	10 m	Ko *et al.,* 1996
Rayleigh backscatter	Temperature	100 m	±5 °C	0.1 m	Boiarski *et al.,* 1995
Rayleigh backscatter/ liquid-core fibre	Temperature	100 m	±1 °C	1 m	Hartog, 1983

Table 2.1 Rayleigh scattering-based distributed sensing (NA: Not applicable).

2.2.3 Raman Scattering

Raman Scattering results from the interaction of the propagating light with the lattice vibration modes of the fibre material. The interaction results in the absorption of an incident photon by the molecule. Thus the molecule is raised to a virtual excited state and emits a photon of a different energy (different wavelength), either greater or smaller than the incident photon. This frequency shift in the scattered photon equals the characteristic vibrational frequencies of the molecules. The Raman spectrum comprises of two components - the Stokes (longer wavelength, lower energy) and the anti-Stokes (shorter wavelength, higher energy). The Stokes line is only weakly sensitive to temperature while the anti-Stokes line is highly sensitive to temperature fluctuations.

Most of the Raman distributed temperature sensing (RDTS) systems monitor the ratio of anti-Stokes to Stokes back scattered signals and is given by the expression (Kimura *et al.,* 2001)

$$\frac{I_A}{I_S} = \frac{(v_0 + v_r)^4}{(v_0 - v_r)^4} \exp\left(\frac{-hcv_r}{kT}\right), \qquad 2.2$$

where I_A is the intensity of the anti-Stokes light, I_S is the intensity of Stokes light, v_0 is the wave number of the input laser, v_r is the wavenumber shift of Raman scattering, h is Planck's constant, c is the speed of light, k is Boltzmann's constant and T is the absolute temperature of the sensing fibre.

Equation 2.2 together with the principle of OTDR can be applied to determine the spatial distribution of the temperature along the fibre. Raman distributed temperature sensors (RDTS) based on spontaneous Raman scattering are available commercially and have been reviewed extensively (Hartog, 1995). Commercial RDTS have evolved in recent years from (spatial resolution of 7.5 m, sensing length of 2 km) to systems capable of (spatial resolution of 1 m, sensing length of 8 km with a temperature resolution of 2 °C). Table 2.2 lists some of the applications employing this technique for distributed sensing together with precision, sensing range and spatial resolution achieved to date.

Sensing Mechanism	Physical Quantity Measured	Sensing range	Precision temp./ strain	Spatial resolution	Reference
Spontaneous Raman back-scatter (commercial RDTS, FTR150)	Temperature	120 m	±2.5 °C	1 m	Kimura *et al.,* 2001
Spontaneous Raman back-scatter (commercial York DTS 80)	Temperature	8 m	±1 °C	1 m	Dubaniewicz *et al.,* 1998
Spontaneous Raman back-scatter (Laser source = 1.65 μm)	Temperature	>10 km	± 4°C	10 m	Kee *et al.,* 1999
Raman back-scatter/Spread spectrum technique	Temperature	1 km	NA	10 m	Everard *et al.,* 1989
Spontaneous Raman back-scatter/OFDR (ROFDR)	Temperature	10 km	2.4 K	NA	Farahani *et al.,* 1999
Spontaneous Raman back-scatter	Temperature	30 km	± 1°C	5 m	Hara *et al.,* 1999

Table 2.2 Raman scattering-based distributed sensing (NA: Not applicable).

2.2.4 Brillouin scattering

Brillouin scattering refers to the scattering of an incident lightwave by the acoustic phonon of a medium. That is, the backscattering of light due to the interaction between the incident photon and an acoustic photon. When this process occurs in an optical fibre, the backscattered light undergoes a frequency shift known as the Brillouin frequency. The Brillouin scattering produces both the frequency down-shifted (Stokes) and frequency up-shifted (antiStokes) photons. The frequency shift is given by

$$\nu_B = \frac{2n\nu_A}{\lambda_L}, \qquad 2.3$$

where ν_B is the Brillouin frequency shift, n is the refractive index of the fibre core, ν_A is the longitudinal acoustic velocity of the fibre glass and λ_L is the free space wavelength of the forward propagating light. The Brillouin frequency shift has been shown to be linearly dependent on both temperature and strain and has been used in numerous sensing systems to obtain distributed temperature and strain measurements. The development of distributed sensing techniques based on Brillouin scattering has been reviewed extensively (Horiguchi *et al.,* 1995). Table 2.3 lists some of the applications employing this technique for distributed sensing together with precision, sensing range and spatial resolution achieved to date.

Sensing Mechanism	Physical Quantity Measured	Sensing range	Precision temp./strain	Spatial resolution	Reference
Brillouin scattering	Strain	NA	±10 με	0.5 m	Bao *et al.,* 2001
Brillouin scattering/FBG	Simultaneous Strain/temp.	NA	±22 με ±1.9 °C	NA	Davis *et al.,* 1997
Brillouin frequency shift	Simultaneous Strain/temp.	3682 m	±60 με ±5 °C	2 m	Lee *et al.,* 2001
Brillouin frequency shift	Strain	500 mm 250 mm	±20 με ±40 με	NA	Brown *et al.,* 1999
Brillouin gain	Temperature	22 km	±1 °C	100 m	Bao *et al.,* 1993
Brillouin scattering	Temperature	51 km	NA	NA	Bao *et al.,* 1995
Spontaneous Brillouin scattering	Temperature	NA	10 K	40 m	Souza, 2006
Spontaneous Brillouin scattering	Temperature	20 km	±3-6 °C	7 m	Lecoeuche *et al.,* 2000

Continued on next page

Continued from previous page					
Noise-initiated Brillouin scattering	Simultaneous Strain/temp.	1200 m	±100 με ±4 °C	40 m	Parker *et al.,* 1998
Spontaneous Brillouin scattering/FBG	Temperature	25 km	±1-7 °C	2 m	Wait *et al.,* 2001
Brillouin scattering/ Signal processing technique	Temperature	NA	±2 °C	5 m	Bernini *et al.,* 2004
Stimulated Brillouin scattering	Dynamic Strain	5 cm	±38 με	8.8 Hz	Hotate *et al.,* 2003
Spontaneous Brillouin backscatter	Simultaneous Strain/temp.	1200 m	±100 με ±4 °C	40 m	Parker *et al.,* 1997
Spontaneous Brillouin backscatter/Brillouin frequency shift	Temperature Simultaneous Strain/temp.	30 km 6.3 km	±1.6 °C ±3 °C ±80 με	2 m 1.3 m	Alahbabi *et al.,* 2004a
Spontaneous Brillouin backscatter	Temperature	100 km	±8 °C	50 m	Alahbabi *et al.,* 2004b
Spontaneous Brillouin backscatter/ Raman amplification	Temperature	100 km	±8 °C	20 m	Alahbabi *et al.,* 2004c
Spontaneous Brillouin backscatter/Brillouin frequency shift/ Raman amplification	Temperature Simultaneous Strain/temp.	100 km 50 km	±1.7 °C ±3.5 °C ±85 με	20 m 5 m	Alahbabi *et al.,* 2006

Table 2.3 Brillouin scattering-based distributed sensing (NA: Not applicable).

2.3 Distributed Fibre Bragg Grating based Sensors

To obtain a distributed profile of nonuniform temperature or strain along a structure, FBG sensors have been multiplexed using wavelength-division-multiplexing (WDM) to enable quasi-distributed measurements (Kersey, 1997, Rao, 1997, 1999, Tian *et al.,* 2001 and Tjin *et al.,* 2002). The WDM technique relies on the fact that many FBGs with different resonant Bragg wavelengths can be fabricated at arbitrary locations onto a single optical fibre, and then interrogated independently to provide a quasi-distributed measurement over large structures. Multiplexing of FBG sensors enable a low cost alternative to conventional strain gauge technology. However, the number of FBG sensors multiplexed at multiple locations is a function of both the source optical bandwidth and grating operational bandwidth. Thus a prior knowledge of the measurement range and the location of the measurand for a given test is essential for the design of an optimal multiplexed FBG sensor system.

A number of multiplexing techniques for FBGs sensors such as wavelength-division multiplexing (WDM), time-division multiplexing (TDM), spatial-division multiplexing (SDM) and combinations of these have been proposed, designed, developed and implemented. However, most of the practical applications have relied on WDM schemes. Thus this section reviews WDM in combination with other schemes, sensor interrogation techniques and the application of these in quasi-distributed sensing.

2.3.1 Wavelength-Division Multiplexing (WDM)

The wavelength encoded nature of output from fibre Bragg grating sensors facilitate wavelength division multiplexing (WDM). As stated earlier, the WDM technique is based on fabrication of many FBGs with different resonance Bragg wavelengths at appropriate locations along a single optical fibre. Each FBG sensor is allotted a different section of the available optical source bandwidth (figure 2.2). In figure 2.2, the array of four FBGs occupy an optical bandwidth of 120 nm. The bandwidth range allotted to each sensor is proportional to the expected strain range at the location of the grating. As the FBGs experience strain, they shift in wavelength within their allotted optical bandwidth range. This enables quasi-distributed strain sensing by associating each spectral bandwidth with a particular spatial location.

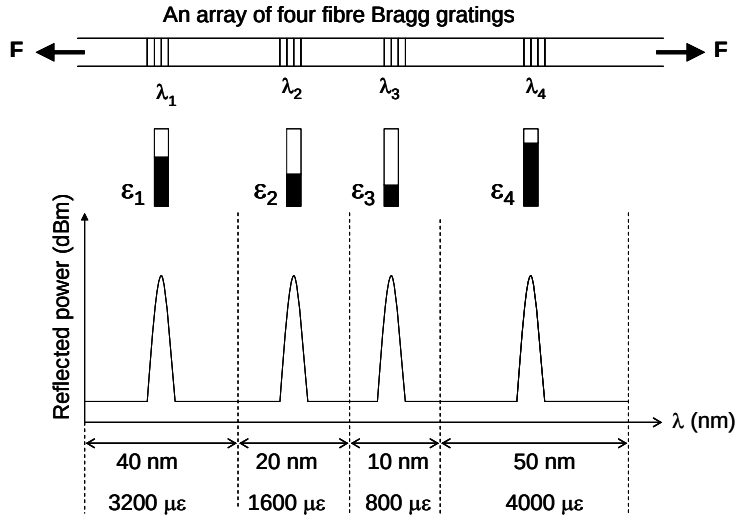

Figure 2.2 Standard WDM technique for multiplexed fibre Bragg grating strain sensors showing allotted optical bandwidth for each sensor in relation to the expected strain range.

In standard WDM techniques, the sensor network is arranged such that the sensors' operational bandwidths do not overlap or else spillover of the optical signals will occur resulting in errors in detection of the Bragg wavelength and thus the measured strain or temperature. Another constraint of WDM is the design of FBG arrays. Development of multi-element-grating arrays imposes additional requirements on grating design technology such as the precision of individual grating Bragg wavelengths, allotted sensor bandwidth, Bragg wavelength shift for a particular application and available spectral source bandwidth. Other factors which need to be addressed for arrays with closely spaced resonance Bragg wavelengths are the downward drift of Bragg wavelength due to either out-diffusion of hydrogen during annealing, or as a result of heat treatment used to embed the arrays into composites or structures. This is normally incorporated into the array design either by increasing the bandwidth allotted to each sensor or by manufacturing the arrays at a slightly higher resonance Bragg wavelength than that targeted (Fells *et al.,* 1997).

WDM techniques can be classified into a number of networks such as series, parallel and branching. WDM allows tens of sensors per fibre, but time division multiplexing (TDM) can multiply this by several times by re-using the source spectrum. In a combined WDM/TDM serial configuration, multiple FBG arrays are fabricated, each at a greater distance along the fibre. Thus reflections from FBGs at successively greater distances along the fibre, return to the detector at successively later times. Therefore by using a hybrid WDM/TDM technique, a large number of arrays of FBGs can be multiplexed and interrogated. Figure 2.3 shows some WDM/TDM schemes. The multiplexing techniques have been reviewed extensively elsewhere (Rao, 1997, Kersey *et al.,* 1997); here only recent improvements in sensor multiplexing techniques are discussed.

Two new WDM schemes; a hybrid star-bus topology and an amplified double-bus configuration have been demonstrated experimentally (Achaerandio *et al.,* 1999). The hybrid star-bus topology uses an erbium-doped fibre ring laser as a simultaneous multiple wavelength operation light source and distribution scheme. The amplified double-bus topology uses a single-wavelength tunable laser as the source. The optical SNR was similar for both topologies with the hybrid-star bus exhibiting approximately

8 dB higher signal power. The other advantage of the hybrid-star bus is its capacity to obtain information simultaneously from the sensors.

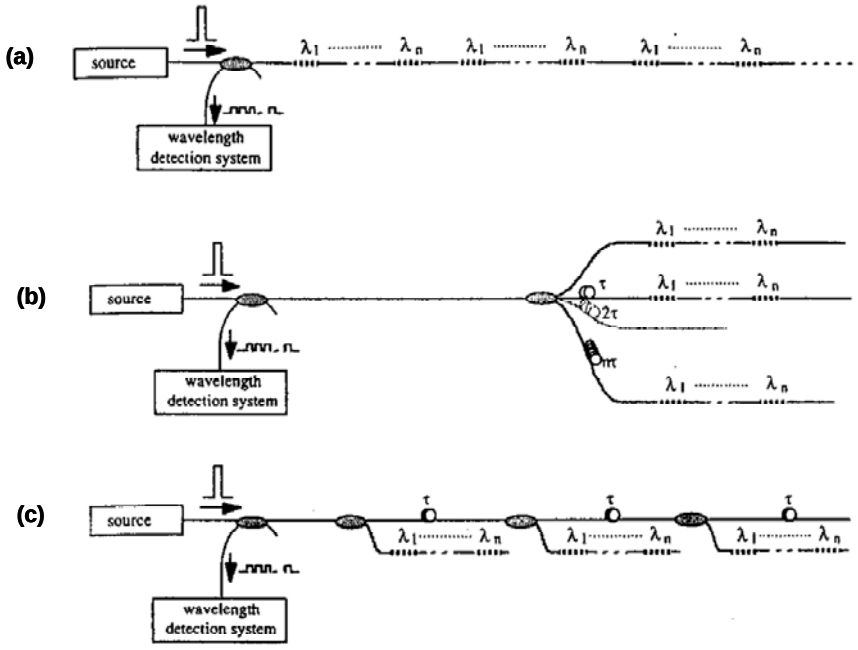

Figure 2.3 WDM/TDM addressing topologies for FBG arrays. (a) Serial system with low reflectivity gratings, (b) parallel network and (c) branching network. (Kersey et al., 1997).

A twin Bragg grating interferometric sensor exhibiting high multiplexing capability utilising a combination of wavelength and frequency division multiplexing employing low reflectivity Bragg gratings was demonstrated (Shlyagin *et al.,* 2002). It has the capability to increase the number of multiplexed sensors by at least 10 times in the 1.5 μm wavelength region. Another technique employing a chirped fibre grating Fabry-Perot (FP) sensor was demonstrated for multiple wavelength addressing (Koo *et al.,* 1998). The sensor consists of two co-located chirped gratings arranged such that their chirp direction was opposite to each other and functioned as an array of co-located FP cavities with different wavelength addressable cavity lengths. A strain sensitivity of 0.001 nm/με, resolution of (3 ± 1) με and sensing range of 1300 με were achieved.

2.3.2 Wavelength-Division Multiplexing (WDM) Interrogation Techniques

The success of FBG based distributed sensing systems rely on the precision of interrogation techniques employed to detect the Bragg wavelength shift due to the

external perturbation. Most demodulators function by converting wavelength shifts into electrical signals. The precise measurement of Bragg wavelength shift induced by the measurand is crucial for improved sensor performance. The most commonly used FBG interrogation (wavelength detection) techniques are based on tunable filters, scanning interferometers, fibre lasers, charge coupled device (CCD) spectrometers, frequency locking circuits and high resolution optical spectrum analysers (OSA). The principles of FBG interrogation techniques have been reviewed extensively elsewhere (Rao, 1997, Kersey *et al.,* 1997); here only recent developments in interrogation systems together with interrogators employing chirped gratings are presented.

An interrogation system consisting of electro-optic instrumentation together with Edge Emitting Light Emitting Diode (ELED) and a scanning narrow band filter has been demonstrated (Davis *et al.,* 1996). The system uses WDM, combined with sequential addressing of separate fibre arrays via a single mode fibre switch. The system has the capability to monitor 5 arrays of 12 FBG sensors. A Bragg grating based fast tunable filter prototype for application in WDM systems has also been reported (Iocco *et al.,* 1999). The operation was based on two piezoelectric actuators compressing an apodised FBG, thus tuning to the shift in the central Bragg wavelength of the sensing grating. A linear relationship between the wavelength shift and the piezoelectric actuator displacement over the 45 nm range was obtained.

A wavelength interrogation technique based on an optical power detection scheme for multipoint strain sensing has been proposed to calibrate the measurand directly (Chiang *et al.,* 2002). The scheme did not require the multiplexed FBG sensors to be spectrally separated, as is the case with other conventional interrogating systems, and could also work with slightly overlapping spectra. Strain measurements of high linearity (±0.4 %) and good sensitivity (2 με) were demonstrated. A simulated annealing (SA) technique to improve the performance of FBG sensors in a WDM network calculated the resonance Bragg wavelength of a FBG strain sensor network as opposed to the conventional peak detection (CPD) technique (Shi *et al.,* 2004). Strain detection error of approximately 2.5 με was obtained for overlapping spectra.

Interrogation techniques for FBG sensors have recently employed chirped gratings to transform wavelength induced changes due to measurands into power fluctuations for demodulation purposes. A low-cost single sensor interrogation technique for strain and temperature sensing based on the deliberate mismatching of the reflected spectra of two identical broadband chirped gratings (sensing and reference) was demonstrated (Fallon *et al.,* 1997). When the sensing grating experiences strain, its spectra will be linearly shifted resulting in the reflected light falling outside the reflection bandwidth of the reference grating and being transmitted to the photodetector. A similar principle of overlapping the spectra of two identical chirped gratings was employed for extreme strain measurements (Fallon *et al.,* 1997). The maximum sensing range was determined by the bandwidths of the gratings and the system was capable of simultaneous interrogation of all multiplexed sensors.

A novel FBG strain sensor demodulator using the UV induced birefringence of a CFBG based on the wavelength-dependent travel-length of the light reflected from a chirped grating was proposed (Kim *et al.,* 2001). This resulted in different polarisation states for different wavelengths of light reflected from the chirped grating. A similar sensor interrogation technique based on the wavelength dependence of the phase group-delay response of light reflected from a chirped grating was proposed and implemented (Chtcherbakov *et al.,* 2004). A tensile strain range of 10,000 με was demonstrated experimentally.

Another FBG sensor interrogation scheme utilizing the multiple bandpass filter characteristics of a linearly chirped grating based Sagnac loop was demonstrated (Zhao *et al.,* 2002, 2003). The scheme showed good linearity between the applied strain and the reflected output power, with static and dynamic strain resolutions of ±4.2 με and 0.406 με/√Hz, respectively.

2.3.3 Quasi-distributed sensing using WDM techniques

Due to their multiplexing capabilities, FBG sensors offer the potential for applications in the field of quasi-distributed sensing in smart structures. Multiplexed FBG sensor arrays can be attached to, or embedded into, structures for multipoint monitoring of

physical parameters such as strain, stress, temperature, cracks and vibrations at arbitrary locations. Figure 2.4 shows the basic structure of a quasi-distributed FBG sensor array, where each FBG has a different resonance wavelength (Tjin *et al.,* 2002). Many applications of FBG sensors in quasi-distributed sensing schemes have been reported. This section briefly reviews the applications of FBGs and chirped gratings in quasi-distributed sensing.

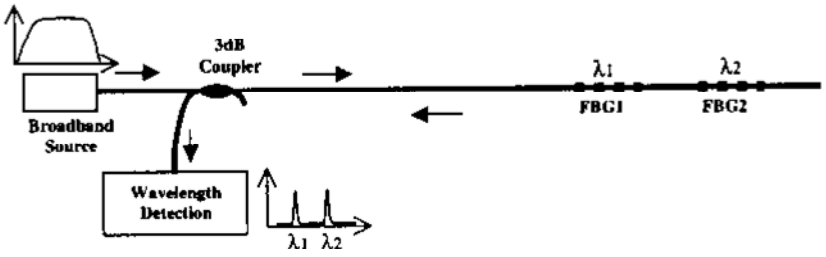

Figure 2.4 Basic FBG-based quasi-distributed sensing system (Tjin et al., 2002).

The use of FBGs in structural health monitoring to provide real-time data of civil structures subjected to environmental stress is useful for preventive maintenance in structures. Multiplexed FBG based strain sensors embedded into carbon composite materials (CCMs) were mounted onto concrete structures to determine the strain changes at different locations within the structure during cyclic tests (Tjin *et al.,* 2002). The FBG sensors were shown to have good linearity and repeatability, with a resolution of 1 με and an accuracy of 5 με after temperature compensation. Temperature resolution of 0.04 °C with an accuracy of 0.2 °C was obtained from a FBG sensor array mounted alongside the strain sensors.

Distributed strain sensing with multi-element FBG arrays embedded in fibre-resin composite panels by the continuous resin transfer moulding^{TM} (CRTM)^{TM} process have been reported (Friebele *et al.,* 1994). The composite panel was subjected to three-point bending test under various weights and the strain distribution was estimated from the shifts in λ_B of the FBG arrays. The measured strain compared well with that calculated from beam theory and that determined from nonlinear finite element analysis. A strain error of 17 με was obtained.

Another example of quasi-distributed strain sensing used extremely short length FBGs with well-defined spectra (Wu *et al.,* 2002). The use of short length gratings with spatial width as small as few hundred micrometre overcame the problem of distortion of FBG spectra due to localised nonuniform strain. This sensor system has applications in aerospace. An improved quasi-distributed strain sensing utilising apodised FBG arrays reduced crosstalk between sensing arrays (Chisholm *et al.,* 1998). However apodisation resulted in increased grating bandwidth, thus reducing the resolution of the system. The trade-offs between apodisation, grating bandwidth, source bandwidth and spatial resolution in the design of grating arrays for application in quasi-distributed sensing was investigated.

An important feature of any highly distributed FBG based sensing system is the much larger number of measurements possible at multiple locations along a single optical fibre with reduced installation cost compared to conventional strain gauge technology. This high density of measurements is useful to test engineers for the visualisation of strain contours along the structure. One such strain sensing system, employing FBGs at thousands of locations along a composite wing structure, used four 8 m long optical fibres with 800 FBG arrays per fibre, interrogated by an optical frequency domain reflectometer (OFDR) (Childers *et al.,* 2001). The large number of FBG sensors generated two dimensional mapping of the strain fields. In another application, four sets of an array of five FBGs were embedded into an aerospace carbon fibre composite material to determine strain distribution during three point bending tests (Dockney *et al.,* 1997). Each grating in the array was 2 mm long with a nominal Bragg wavelength separation of 4 nm. The spatial separation of arrays was (50.0 ± 0.1) mm.

Recently a quasi-distributed strain sensor employing chirped Moiré fibre Bragg gratings (CMFBG) has been demonstrated (Gillooly *et al.,* 2005). CMFBG is a superposition of two CFBGs of different periods. A dual scan phase mask fabrication technique was used to inscribe the grating. Initially a chirped grating was written in the fibre followed by a second identical inscription over the same position under strain application. This creates a beat effect in the refractive index profile along the grating. At each node within a particular beat effect, a passband is created, which corresponds to a unique position along the grating. The strain at a discrete point along the grating was measured

by monitoring the wavelength shift of the passbands. An average spatial resolution of 164 μm over the grating length and a strain sensitivity of (0.8±0.01) pm/με was obtained. Such a sensing system has application in mapping strain distributions around a miniature deformation or crack in a surface.

A number of applications of quasi-distributed temperature sensing have also been reported. Smith *et al.* (2002) and Patterson *et al.* (2001) reported developing a quasi-distributed temperature sensor consisting an array of FBGs, illuminated by a superluminescent diode (SLD) and interrogated by a fibre Fabry-Perot (FFP) tunable filter. The sensing array consisted of seven gratings, each 1 mm long. The sensor has been tested for hyperthermic in-vivo treatment of tumours in rabbit livers.

In summary, quasi-distributed sensing utilises FBG sensor arrays positioned at strategic locations along a structure to map strain/temperature distribution along the structure. The technique, however, provides only an average of the measurand along the length of each grating by tracking the peak reflection Bragg wavelength of each grating sensor. Thus it is unsuitable for applications where a continuous profile of the measurand, as a function of position along the grating length, with millimetre position resolution is required (e.g. to pinpoint hot spots or detect cracks). The technique works well for large structures where spatial resolution is not a priority but is not appropriate when high spatial resolution is required.

2.4 Theory and Application of Intragrating Sensing

Intragrating sensing refers to any technique that enables a continuous profile of a measurand to be obtained over the length of the grating. In applications where strain or temperature along a fibre Bragg grating is uniform, the strain or temperature can be determined from the shift in the reflected Bragg wavelength of the grating. This wavelength shift has been used extensively as an indicator of applied strain or temperature in all conventional Bragg-grating sensing applications (Rao, 1997, 1999, Davis *et al.,* 1996, Tjin *et al.,* 2002). However, in applications where strain or temperature gradients exist, the reflected spectrum will not only be shifted but also distorted due to nonuniform changes in the period (pitch length) and refractive index

over the grating length. Thus the shape of the measured reflected spectrum is a function of strain and/or temperature distribution along the grating. The information about the strain or temperature distribution along the length of the grating is encoded in the "modified" Bragg wavelength as a function of position, z, given as

$$\lambda'_B(z) = 2n'(z)\Lambda'(z), \qquad 2.4$$

where $n'(z)$ is the local average 'dc' refractive index as a function of position along the grating and $\Lambda'(z)$ is the local period of index modulation as a function of position along the grating.

Hence, when a uniform grating is subjected to a non-uniform strain or temperature distribution, different sections of the grating contribute to the reflectance at different wavelengths. That is, each sub-section of the grating contributes to the "local" Bragg wavelength according to the local state of the measurand given by equation 2.4. This broadens the spectrum and reduces the peak reflectance of the uniform FBG. Both the intensity and phase spectrum of the grating are affected by this nonuniformity in the measurand. Thus intragrating sensing involves detailed analysis of the reflected power or the phase spectrum to obtain a continuous profile of the measurand over the grating length. To determine the local Bragg wavelength as a function of position, four techniques have been presented: the intensity-spectrum based intragrating sensing, phase-spectrum based intragrating sensing, combined intensity and phase measurements and low coherence reflectometry measurement (Kersey *et al.,* 1997).

Improved capabilities to detect localised temperature and strain and distribution of these along the length of the grating with better spatial resolution are of great interest. Thus intragrating sensing has application in structural health monitoring to identify such features as: strain transfer points, the location of cracks, debonding and health of repaired patches. In these applications, a continuous profile of the measurand as a function of position along the sensor length with sub-millimetre spatial resolution is essential.

In the following sections the fundamentals of the four intragrating sensing techniques, together with FBG reconstruction techniques employed for solving the inverse problem

of retrieving the strain or temperature profiles from the intensity, phase or both intensity and phase of the measured reflection spectrum, are reviewed.

2.4.1 Intensity-Spectrum Based (Reflected Power Spectrum) Intragrating Sensing

Intensity-spectrum based intragrating sensing is the simplest technique for retrieving the strain $\varepsilon(z)$ or temperature $T(z)$ profile along a grating from its measured intensity reflection spectrum, $R(\lambda)$. In this, the local Bragg wavelength, $\lambda_B(z)$, along the grating at position z, is calculated from the reflection spectrum, $R(\lambda)$. Consider the case of a uniform grating subjected to a non-uniform strain field. The applied strain modifies the grating pitch and also the local refractive index. The main effect of the spatial variation of the grating pitch $\Lambda(z)$ and the local refractive index $n(z)$ is that each reflected wavelength in the spectrum corresponds to a particular position of the grating tuned to that wavelength. The local Bragg wavelength, $\lambda_B(z)$, can be obtained by equating the solution of the following integral on the left-hand side (λ generated) to the integral on the right-hand side (z generated), (LeBlanc *et al.,* 1996),

$$\int_{\lambda[z=-L/2]}^{\lambda(z)} -\ln[1-R(\lambda')]d\lambda' = \pm\frac{\pi^2}{2}\int_{-L/2}^{+L/2}\frac{\Delta n^2(z')}{n(z')}dz', \qquad 2.5$$

where $\Delta n(z)$ is the depth of refractive index modulation within the grating due to variations in the writing beam, $n(z)$ is the local refractive index along the fibre core due to the combined effect of variation in the writing beam and the refractive index changes due to an applied strain and L is the grating length.

From equation 2.5, it can be seen that this method requires a detailed knowledge of grating characteristics [specifically $\Delta n(z)$, the depth of refractive index modulation along the grating]. Thus by calculating $\lambda_B(z)$ from equation 2.5, the local strain as a function of position along the grating, z, can be calculated from equation 2.6 (LeBlanc *et al.,* 1996)

$$\lambda_B(z) = 2n(z)\Lambda(z) = 2n_0\Lambda_0[1+\varepsilon^{opt}(z)]. \qquad 2.6$$

In equation 2.6, n_0 is the average refractive index over the grating length, Λ_0 is the average modulation spatial period and $\{\varepsilon^{opt}(z) = \varepsilon_z(z) + [\delta n^{\text{perm}}(z) + \delta n^{\varepsilon}(z)]/n_0\}$ is the "optical strain" which is a function of applied axial strain field, $\varepsilon_z(z)$, deviations from n_0 due to non-uniformities in the writing beam, $\delta n^{\text{perm}}(z)$, and the refractive index changes within the fibre core due to the applied strain, $\delta n^{\varepsilon}(z)$. Thus to determine the spatial distribution of applied strain, the refractive index along the fibre core must first be known precisely and the experiment must be performed at constant temperature to preclude temperature induced refractive index changes.

A limitation of this approach is that only profiles in which $\lambda_B(z)$ is a monotonic function of position along grating length can be interpreted. That is, only monotonically increasing or decreasing strain profiles $\varepsilon(z)$ along the grating can deduced when a uniform grating is used for measurement and the sign of the strain gradient is indeterminate.

The intensity-spectrum based (ISB) approach has been used extensively to determine strain and temperature distributions. Huang *et al.* (1995) demonstrated that the reflection spectrum of a FBG can be used to evaluate strain gradients present over the grating mounted onto a cantilever beam. The simulated spectra, $R(\lambda)$, of several strain distributions calculated using the transfer matrix method (*TMM*) approximation (section 3.6.2) were fitted iteratively to the experimentally measured spectra to calculate the strain profile. A strain gradient resolution of 10 με/mm was estimated from the measurement resolution, grating length and the average grating Bragg wavelength.

LeBlanc *et al.* (1996) demonstrated the intensity reflection technique to map the axial strain profile, $\varepsilon_Z(z)$, near a circular hole in an aluminium plate from its experimentally measured reflection spectrum $R(\lambda)$. Strain resolution of 80 $\mu\varepsilon$ and spatial resolution of 0.8 mm were obtained. This technique was, however, restricted to monotonically varying strain fields of large gradients.

A detailed review of the limitations and errors associated with the intensity-spectrum based demodulation approach has been presented (Huang *et al.,* 1998). Huang *et al.* (1998) and LeBlanc *et al.* (1996) showed that the technique results in large errors for

low strain gradients; such errors are more pronounced near grating ends. This is because the contribution to a particular wavelength $\lambda_B(z_i)$ is not from a single point, z_i, of the grating but from a range of z centred around it. The length of this region, known as the effective length (L_{eff}), was shown to be inversely proportional to the square root of the local strain gradient as:

$$L_{eff} = \sqrt{\frac{\Lambda_0}{\left|\frac{d}{dz}\varepsilon^{opt}(z)\right|_{z=z_i}}} \quad . \tag{2.7}$$

Thus the local strain ($\varepsilon(z_i)$) determined by this method was essentially the average strain over the effective length. The large errors at grating ends resulted from part of the L_{eff} being outside the grating planes, which was treated as having an infinite grating period and thus infinite strain. Equation 2.7 suggests the higher the strain gradient, the shorter the L_{eff}, the better the spatial resolution. Thus, to improve the accuracy and resolution of the measurements, the use of chirped gratings was suggested by the authors.

Peters *et al.* (2000) presented an experimental verification of the response of embedded FBGs to a non-homogeneous strain field using the ISB technique. The experimental spectral responses of known strain fields were simulated using the *TMM* to determine the arbitrary strain distribution. Peters *et al.* (2001) applied embedded FBGs to measure strain near a stress concentration within a solid structure from its measured transmission spectra. The measured transmission spectra were simulated using the *TMM* model of the FBG to determine the local non-uniform strain distributions. The shapes of transmission spectra were shown to vary with the distance of the FBG from the stress concentration.

In an alternative approach, the response of FBG sensors embedded into a host (composite) material under a non-uniform strain distribution was investigated using the strain-transfer mechanism (Ling *et al.,* 2005). Firstly the strain distribution of the host material subjected to a load was numerically calculated using the finite element method (FEM). Then the in-fibre strain distribution of the embedded FBG sensor was obtained using the strain-transfer mechanism. Finally the in-fibre strain distribution was used to simulate the measured reflection spectra using the *TMM*. A good agreement between the experimental and simulated spectra was obtained.

An adaptive simulated annealing (ASA) optimisation algorithm in combination with the T-matrix method has been demonstrated for reconstructing the reflection spectrum of a FBG (Shi *et al.,* 2003). The technique is based on the application of optimisation methods to recover the FBG parameters. Strain precision of few microstrain and a spatial resolution of 0.2 mm were obtained. Another application of the ASA algorithm in combination with *TMM* for recovering the strain profile from the measured $R(\lambda)$ of a grating mounted along a cantilever beam has been reported (Li *et al.,* 2005). Strain precision of few microstrain and a spatial resolution of 0.184 mm were obtained.

An approach based on a simulated annealing evolutionary (SAE) algorithm and transfer matrix model has been demonstrated to demodulate the strain profile along a FBG distributed strain sensor (Yun *et al.,* 2005). The method combines ASA and evolutionary programming to reconstruct the strain profile from the intensity reflected spectrum alone. Numerical simulations showed good agreement between the applied and reconstructed strain profiles and a spatial resolution of 0.5 mm was reported.

Recently, genetic algorithm (GA) approaches have been demonstrated for solving the inverse problem of FBG strain sensors from the intensity reflection spectrum (Casagrande *et al.,* 2002). The theoretical spectral responses of known strain distributions calculated by solving Riccati-type differential equations were fitted to the measured spectra through polynomial coefficient optimization. However, the approach was capable of synthesising only a few of the FBG parameters, applicable only to monotonic fields and required a suitable form of the strain distribution hypothesis for the fitting process. Thus the technique is not very suitable for embedded sensors in structures where the strain fields are expected to vary continuously.

An improved GA for the inversion of FBG spectral data from the measured $R(\lambda)$, to determine the strain distribution along the grating has been presented (Gill *et al.,* 2004). The method encodes the axial strain distribution along a FBG into a local period distribution for each grating segment for the calculation of $R(\lambda)$ by the *TMM*. Though the technique is capable of reconstructing non-linear and discontinuous strain distributions in regions of significant gradients, it is computationally expensive and requires better optimisation of GA parameters than the previous described technique.

The use of GA to perform the inverse extraction of multiple FBG parameters from two thermally modulated FBG reflection intensity spectra has also been demonstrated (Cheng *et al.,* 2005, Huang *et al.,* 2006). The approach was used to simulate the experimental $R(\lambda)$ of both uniform and chirped FBGs using the *TMM*. The technique was capable of extracting multiple grating parameters such as period, position, length, refractive index modulation, chirp direction and phase response to fully characterise a CFBG. Thus the requirement to measure the complex reflection spectra and the ambiguity with chirp direction were eliminated. However, a large computation time to generate acceptable results and the requirement of a well controlled temperature distribution are the major limitations of the technique.

A novel technique for the reconstruction of the local grating period of a FBG structure from its corresponding complex reflection response using the time-frequency (TF) signal analysis in combination with the Wigner-Ville distribution and spectrogram has been presented (Azana *et al.,* 2000). Using numerical simulation, the technique was tested with several grating structures to recover arbitrary strain distributions along a FBG. The method does not impose any restrictions on the applied strain field and showed good agreement between exact and reconstructed strain functions. The limitations are that it can only recover information about the grating period and length. An alternative experimental demonstration of the TF signal analysis technique for application in distributed sensing was proposed (Azana *at el*., 2001). The approach was capable of accurately evaluating constant strain distributions, strain discontinuities and profiles of large strain gradients.

In another application, a linear temperature gradient was applied to a FBG sensor (Larkin *et al.,* 2004). The resulting variations in the measured $R(\lambda)$ were examined to extract spectral parameters which characterise the spectral distortions due to the temperature gradient. These parameters were then used in a LabView based look-up table approach to solve the inverse problem of temperature distribution along the sensor.

As mentioned earlier, the main limitation of intensity-spectrum based approach is that only profiles in which $\lambda_B(z)$ is monotonic with a known sign of strain gradient can be

measured. The spatial resolution of the measurement is position dependent (Kersey *et al.,* 1997)

$$\delta z(z) = \frac{1}{2}\sqrt{\frac{2n_0\Lambda_0^2}{\left|d\lambda_B(z)/dz\right|}}\ , \qquad 2.8$$

where the minimum distinguishable feature size, $\delta z(z)$, is the spatial resolution along the grating direction, z, $\lambda_B(z)$ is the local Bragg wavelength along the grating at point z, n_0 is the average refractive index over the grating length and Λ_0 is the average modulation spatial period. Equation 2.8 suggests that the spatial resolution will be improved when the Bragg wavelength changes more rapidly with position due to either an initial chirp in the grating or an applied strain/temperature gradient or both if the gradient is not large enough to cancel the initial chirp (Kersey *et al.,* 1997, LeBlanc *et al.,* 1996 and Huang *et al.,* 1998). Furthermore, to overcome the monotonic field limitation of this technique the use of CFBGs were suggested. CFBGs would increase the spatial resolution of the measurements and enable non-monotonic fields to be measured The following paragraphs report on intra-grating sensing schemes based on chirped, chirped sampled and chirped Moiré fibre Bragg gratings.

A fully distributed temperature sensor using a linearly CFBG has been demonstrated (Won *et al.,* 2004). The measured reflected spectrum resulting from an applied temperature was fitted with a numerical model of the grating response of a known temperature profile calculated using the *TMM*. Using least squares fitting of the calculated spectrum to the measured spectrum, temperature change, position and width of the localised heating were determined to within 2.2 K, 149 μm and 306 μm of the applied values, respectively. CFBG sensors have also been applied for the detection of crack locations in a carbon fibre reinforced plastic laminates (Okabe *et al.,* 2004). The measured $R(\lambda)$ was simulated by the *TMM* using assumed distributions of period $\Lambda(z)$ and average refractive index $n(z)$ due to an applied axial strain. The crack locations were identified directly from the position of dips in the spectrum around a particular wavelength, which corresponds to a unique position on the CFBG.

The use of changes in the reflected intensity spectra of CFBGs to detect transverse matrix cracks in transparent glass fibre reinforced plastic (GFRP) crossply laminates

have been investigated (Palaniappan *et al.,* 2005, 2006). The development and position of a crack were identified from approximately sinusoidal variation in the intensity of reflected spectrum. The measured reflected spectra were simulated using a stress transfer model and commercial (OptiGrating) software to predict the strain distribution in the vicinity of the crack.

Chirped sampled fibre gratings (CSFG) have also been demonstrated for distributed sensing of pressure over a few centimetres (Mohanty *et al.,* 2005). CSFG consists of a series of uniform FBGs (subgratings) of nearly equal reflectance fabricated with a chirped phase mask. The number of subgratings is determined by the length and the chirp rate of the phase mask The CSFG resembles a multiplexed uniform FBG sensor with each sub-grating behaving as a sensing point. The sensor operates by monitoring the central wavelength shift of each subgrating. When a transverse load or pressure is applied to the grating, the central wavelength of the affected/shifted sub-grating gives the location of the load, and the magnitude of the load can be calculated from the wavelength shift.

The use of chirped Moiré fibre Bragg gratings (CMFBG) as distributed temperature (Gillooly *et al.,* 2004) and load (Gillooly *et al.,* 2004) sensors have been demonstrated. The technique uses shifts in the pass bands of the CMFBG due to an applied temperature or load to obtain a distributed measurement over the length of the grating. The wavelength of each pass band corresponds to a specific location along the grating, and thus the conversion from wavelength to position, z, can be obtained using the relation, $z = \frac{\lambda_0 - \lambda_z}{n_{eff} C}$, where λ_0 is the start wavelength of the grating, λ_z is the wavelength at a position along the grating, n_{eff} is the effective refractive index and C is the chirp rate of the grating. A thermal resolution of 0.2 °C and a spatial resolution of 164 μm were obtained for the distributed temperature sensor. The distributed load sensor was shown to have an average spatial resolution of 164 μm and a load precision of 0.15 N/mm or 50 με.

2.4.2 Phase-Spectrum Based Intragrating Sensing

The strain, $\varepsilon(z)$, or temperature, $T(z)$, distribution along a FBG can also be extracted from its measured phase spectrum, $\psi(\lambda)$. Like the intensity reflection spectrum, the information about strain/temperature distribution is also encoded in the phase spectrum of a grating. The phase-spectrum based (PSB) technique is based on the correlation between the wavelength-dependent penetration depth of light in a non-uniform (chirped) grating and the phase delay of the reflected wave (Huang *et al.,* 1996). That is, a FBG subjected to a strain gradient, will experience chirp and therefore a change in optical pitch-length along the grating will be a function of strain distribution. Thus each resonant wavelength is reflected from a certain depth (the penetration depth) within the grating where its corresponding pitches are located. Therefore using the linear dependence of phase delay on penetration depth and linear dependence of resonant wavelength on applied strain, the measured phase spectrum can be used to evaluate the strain distribution as a function of position along the grating.

The principle of the PSB method is based on the same concept of dispersion in a chirped grating. After an optical wave travels a distance, L, through a medium of refractive index, n, its phase change is given as

$$\psi = 2n\pi L/\lambda \,. \tag{2.9}$$

Its phase slope with respect to wavelength (which is proportional to group delay) can be obtained by differentiating equation 2.9

$$\frac{d\psi}{d\lambda} = -\frac{2n\pi}{\lambda_c^2} L \,, \tag{2.10}$$

where λ_c is the central wavelength of the spectrum.

For a CFBG with average refractive index, n_0, along the grating, the group delay ($d\psi/d\lambda$) parameter is wavelength-dependent because the wave travelling distance (the penetration depth) is wavelength-dependent. Also for the grating, the travelling distance

is double the penetration depth, z_P (i.e. $L = 2z_P$). Thus the penetration depth or grating position can be expressed in terms of wavelength as

$$z_P(\lambda) = -\left(\frac{\lambda_c^2}{4n_0\pi}\right)\frac{d\psi}{d\lambda}. \qquad 2.11$$

Note that $z_P(\lambda)$ is just the inverse of $\lambda_B(z)$; thus from a knowledge of the Bragg wavelength as a function of position, the strain distribution along the grating can be obtained since the local Bragg wavelength is strain dependent.

The advantages of the PSB approach are that the sign of the strain gradient can be determined and the index modulation, $\Delta n(z)$, along the grating does not need to be known with a high degree of accuracy as is the case with the intensity based approach. The limitations are that it is only applicable to monotonically varying strain fields of certain gradients and has low accuracy when the strain gradient is low especially near grating ends. Another drawback is that to obtain phase spectrum measurements, an interferometric detection scheme similar to a Michelson interferometer is required. This necessitates the use of a high speed tunable laser source, which makes the measurement system complex and costly. Considering that both ISB and PSB approaches have similar limitations, the ISB technique is preferred due to its practicality for many applications, and the simplicity of the measurement system and demodulation process.

Huang *et al.* (1995, 1996) demonstrated the PSB approach for strain sensing based on the measurement of the phase spectrum, $\psi(\lambda)$, of the reflected light from a FBG. That is, from a measured phase spectrum, ψ versus λ, the group delay spectrum, $d\psi/d\lambda$ versus λ can be obtained by differentiation. Then using the linear dependence of the group delay on penetration depth, z_P, the penetration depth can be expressed in terms of the resonant wavelength. Finally, since the resonant wavelength is strain dependent, the strain distribution as a function of position along the grating can be obtained.

A detailed review of the limitations and errors associated with the PSB demodulation approach has been presented (Huang *et al.,* 1998). Huang *et al.* (1995, 1996, 1998) verified, experimentally and analytically, that the accuracy of PBS method decreases

near grating ends for low strain gradients and suggested that it could be improved by pre-chirping the grating. Pre-chirping reduces the effective length along the sensor from which a particular wavelength is reflected and thus the discrepancies between the extracted and theoretical strain fields are minimised.

An application of the PSB method in monitoring esophageal pressure was demonstrated (Swart *et al.,* 2005). The time-dependent group delay response of a 100 mm long CFBG sensor was used to determine the pressure, $P(z)$, as a continuous function of position along the esophagus. To calculate $P(z)$, a linear relationship between the wavelength location of the maximum phase perturbation and the position along the sensor where the perturbation occurred was assumed. A position uncertainty of ±1.5 mm was reported.

2.4.3 Combined Intensity and Phase Measurements

Although the intensity based and phase based intragrating sensing techniques can be used independently to evaluate the strain distribution along a FBG sensor, the detailed spatial distribution of the strain field remains indeterminant. The information on the spatial distributions of the pitch length, average refractive index and index modulation depth is contained in its complex spectrum described by both amplitude and phase (Huang *et al.,* 1996). Therefore, in principle, to completely characterize a FBG and to map the strain field distribution, both intensity, $R(\lambda)$, and phase, $\Psi(\lambda)$, spectra are required.

This technique is based on the well-known Fourier relations between the complex grating reflection coefficient, $r(\lambda)$, and the complex grating coupling coefficient, $\kappa(z)$. In the limit of the low grating reflectance approximation, the complex grating reflection coefficient, $r(\lambda) = \sqrt{R(\lambda)}e^{-i\psi(\lambda)}$ is the Fourier transform of the complex grating coupling coefficient, $\kappa(z) = \kappa(z)e^{i\phi(z)}$. In these equations, $\sqrt{R(\lambda)}$ and $\psi(\lambda)$ are respectively the amplitude and phase of the complex grating reflection coefficient, $r(\lambda)$. $\kappa(z)$ is the spatial coupling distribution and $\phi(z)$ is the phase of the spatial coupling distribution along the grating. Thus it can be seen that $r(\lambda)$ and $\kappa(z)$ are Fourier transform pairs and it follows that,

$$\text{if} \quad r(\lambda) = \text{FFT}[\kappa(z)]$$
$$\text{then} \quad \kappa(z) = \text{iFFT}\,[r(\lambda)].$$

Thus the coupling coefficient, $\kappa(z)$, can be expressed as the inverse Fourier transform of the complex grating reflection coefficient, $r(\lambda)$, according to the relation (Duck *et al.,* 2000)

$$\kappa(z)e^{i\phi(z)} = \frac{-2n}{\lambda_0^2}\int_0^{\infty} r(\lambda)e^{(-4\pi ni\frac{\lambda-\lambda_0}{\lambda_0^2}z)}d\lambda\,, \tag{2.12}$$

where λ_0 is the nominal centre wavelength of the grating and the spatial phase of coupling distribution, $\phi(z)$, is related to the strain distribution by the relation (Huang *et al.,* 1998)

$$\varepsilon(z) = -\frac{d\phi(z)}{dz}\cdot\frac{\Lambda_0}{2\pi a}\,, \tag{2.13}$$

where Λ_0 is the initial grating pitch distribution and the grating gauge factor, a, can be expressed as (Huang *et al.,* 1998)

$$a = 1 - n_{eff}^2[p_{12} - v(p_{11}+p_{12})]/2\,, \tag{2.14}$$

where p_{11} and p_{12} are the strain-optic coefficients for the fibre, v is the Poisson's ratio and n_{eff} is the effective refractive index of the unperturbed grating.

Thus, both, the strain distribution, $\varepsilon(z)$, and the coupling coefficient, $\kappa(z)$, can be recovered by an inverse Fourier transform of the measured intensity, $R(\lambda)$, and the phase, $\psi(\lambda)$, spectrum of the grating. This demodulation technique eliminates all limitations imposed on the strain field by other approaches and is capable of resolving any arbitrary unknown strain profile and the theoretical spatial resolution is not restricted by the effective length of the sensor. The only limitation is that the maximum grating reflectance, max[$R(\lambda)$], has to be less than 30% to obtain $\varepsilon(z)$ with reasonable precision (Huang *et al.,* 1998). The requirement of a Michelson interferometer in the optical arrangement to measure phase information, necessitates the use of a fast tuning laser source with high wavelength resolution for fringe discrimination.

An example of the FFT approach based on the combined intensity, $R(\lambda)$, and the phase, $\psi(\lambda)$, spectra for the measurement of the arbitrary strain profile along a non-uniform cross section cantilever beam has been demonstrated (Ohn *et al.,* 1997). A spatial resolution of 2.58 mm was achieved and a theoretical strain precision of approximately 25 $\mu\varepsilon$ was predicted.

A detailed theoretical and experimental review of the FFT demodulation approach based on the combined $R(\lambda)$ and $\psi(\lambda)$ spectra to retrieve arbitrary strain profiles together with its limitations has been presented (Huang *et al.,* 1998). The validity of the approach to recover non-uniform strain profiles was verified by embedding a FBG sensor in a specially designed cantilever beam with two slots cut into it. Good agreement between theoretical (beam bending theory) and FFT evaluated strain profiles at slot locations were obtained with a spatial resolution of about 1 mm. Limitations of the technique include the fact that the maximum grating reflectance has to be less than 30% and a fast tuning laser source is required for the phase measurements.

Another example of the FT approach to recover strain distributions was proposed (Duck *et al.,* 2000). In this technique, the interferometric arm was eliminated from the experimental arrangement and the group delay was measured by the modulation phase shift method and converted to phase using the relationship between delay and phase. Strain resolution of ±24 με and a spatial resolution of 1.65 mm were obtained.

The work contained in this thesis also describes an iterative approach, in conjunction with the FFT technique, for solving the inverse problem of obtaining the temperature distribution from the measured amplitude reflection spectrum of a CFBG sensor (Nand *et al.,* 2006). In these measurements (sections 5.5 and 5.6), the expensive phase spectrum response was not required. Instead an iterative FFT approach was used to adjust the parameters of a temperature hypothesis, $T(z)$, in order to fit the measured spectrum of CFBG that had been modified by a localised heat source. RMS deviations to within 0.03 mm of applied values of the position of the localised heat source were obtained. The reconstruction of grating spectra by this iterative FFT technique is described in detail in section 5.5.

2.4.4 Low Coherence Reflectometry

Low coherence reflectometry (LCR) is another technique that has been demonstrated to obtain distributed strain measurement along a grating. This interrogation technique consists of a single mode fibre Michelson interferometer illuminated by a broadband ELED source (Volanthen *et al.,* 1996). The sensing grating is located in one arm of the interferometer while the other arm contains a narrowband reference grating. The reference grating is strained to provide a wavelength tunable reflection. The grating is interrogated by sequentially measuring the wavelength of sub-sections. The position in the grating to be interrogated is selected by balancing the optical path lengths of the interferometer while the local Bragg wavelength is determined by the tunable filter. Thus from the local Bragg wavelength, $\lambda_B(z)$, strain field data may be derived. However, in this technique, strain information can also be determined directly from the strain applied to the reference grating.

Volanthen *et al.* (1996) presented the first measurement of an arbitrary strain profile within a FBG using the LCR technique. Strain distributions, $\varepsilon(z)$, for non-monotonic fields were estimated with strain accuracy of 50 με. Unlike earlier distributed grating sensor systems, this method was not restricted to monotonically varying strain fields of large gradients.

Volanthen *et al.* (1997) presented two new experimental configurations (closed-loop and open-loop) to test the performance of the LCR technique with the view to improving previously published results. Both configurations were similar to (Volanthen *et al.,* 1996), except that the reference arm contained a broadband mirror and variable fibre delay. The location in the grating to be interrogated was selected by balancing its path length with that of the mirror and the local Bragg wavelength was determined by a tunable optical filter. The essential sensing parameters were measured as follow: the position from the variable delay, the local Bragg wavelength using the tunable filter and the reflectance from the amplitude of the interference fringes.

The theoretical spatial resolution of LCR was defined as the range of distances in the grating that the amplitude of the interference fringes, from a selected point, are greater than half their maximum value (Volanthen *et al.,* 1997). The spatial resolution (l_{res}) was

shown to be dependent upon the filter bandwidth ($\Delta\lambda_f$), refractive index (n) of the fibre and the interrogation wavelength (λ) according to

$$l_{res} = \frac{\lambda^2}{n\Delta\lambda_f}\ln(2)\sqrt{\frac{2\ln(2)}{\pi}}. \qquad 2.15$$

Arbitrary strain and temperature profiles along the grating have been determined experimentally with a spatial resolution of 300 μm and a strain precision of 5.4 με/√Hz using these configurations.

A new experimental method for determining non-uniform strain fields based on a combination of the LCR and a layer peeling technique was demonstrated (Giaccari *et al.,* 2005). The gratings' complex impulse response was measured by LCR and the local FBG parameters were reconstructed by the layer peeling technique. Axial strain distribution was determined with an absolute error of 30 με.

2.5 Nonuniform Strain Sensing using Embedded FBGs

The section provides a brief review of the current state of the field of non-uniform strain sensing using embedded FBGs. Fibre Bragg gratings have been employed extensively as strain sensors in applications involving structural health monitoring because of their high sensitivity, small size, light weight and ease of embedment into the structures. However in some applications such as regions of strong strain gradients near stress concentrations, a continuous profile of the strain distribution as a function of position along the grating with better spatial resolution is required to map non-uniform strain distributions.

In non-uniform strain sensing using uniform FBGs, the assumption that the reflection spectrum remains a single distinct peak is no longer valid; indeed the peak broadens and the reflectance decreases due to nonuniform changes in both the grating pitch and the average refractive index. That is, the measured reflection spectrum no longer undergoes a simple global wavelength shift but changes form as well. Thus the Bragg wavelength shift is not a linear function of applied strain and can no longer be used simply as an

indicator of the applied strain since the shape of the spectral response changes. The shape of the reflection spectrum is a function of strain distribution along the grating and can be recovered using the intragrating sensing techniques described in section 2.4. The following five paragraphs report on nonuniform strain sensing using embedded uniform FBGs.

Huang *et al.* (1995, 1996, 1998) presented a series of papers relating to non-uniform strain sensing using embedded uniform FBGs based on the grating reconstruction techniques described in section 2.4. Strain gradients and strain profile along a FBG surface mounted onto a cantilever beam were experimentally determined with a strain gradient resolution of 10 με/mm (Huang *et al.,* 1995) and a spatial resolution of about 1 mm (Huang *et al.,* 1998). The use of an ASA algorithm to determine the distributed strain profile along a cantilever beam from its measured amplitude reflection spectrum was reported (Li *et al.,* 2005). Strain error of a few microstrain and a spatial resolution of 0.184 mm were obtained. Ohn *et al.,* (1997) used the FFT technique to determine an arbitrary strain profile along a non-uniform cross section cantilever beam. A spatial resolution of 2.58 mm and a theoretical strain error of approximately 25 με were obtained.

LeBlanc *et al.* (1996) and Huang *et al.,* (1998) demonstrated the use of the intensity reflection spectrum intragrating sensing technique to calculate the axial strain profile $\varepsilon_Z(z)$ near a circular hole in an aluminium plate. Strain resolution of 80 $\mu\varepsilon$ and a spatial resolution of 0.8 mm were obtained (LeBlanc *et al.,* 1996). Duck *et al.* (2000) employed the FFT technique to recover the strain distribution 1 mm from a circular hole in an aluminium beam. A strain resolution of ±24 με and a spatial resolution of 1.65 mm were obtained.

Peters *et al.* (2000) presented an experimental verification of the response of the embedded FBGs to a non-homogeneous strain field using the ISB technique described in section 2.4.1. Peters *et al.* (2001) applied embedded FBGs to measure nonuniform strain distribution near a stress concentration within a solid structure. In both applications, the experimental spectral responses were simulated using the *TMM* to determine the arbitrary applied strain distributions.

Casagrande *et al.* (2002) demonstrated a GA approach for the reconstruction of FBG parameters from its measured $R(\lambda)$ in a non-uniform strain sensing application. The strain gradient acting on a uniaxial aluminium test specimen was evaluated by fitting the calculated spectra to the measured spectra.

The in-fibre strain distribution of a FBG sensor embedded into a host (composite) material, subjected to a three-point bending test (non-uniform strain field), was evaluated using the strain-transfer mechanism (Ling *et al.,* 2005). The simulated spectra, using the *TMM* employing the in-fibre strain distribution, were in good agreement with the measured spectra.

Though uniform FBGs show sensitivity to non-uniform strain fields and are capable of quantitatively evaluating the strain fields, identifying the location of strain gradients is extremely difficult and computationally expensive using the grating inverse reconstruction techniques discussed in section 2.4. To overcome the problem, CFBGs have recently been demonstrated for the detection of crack locations in composite materials (Okabe *et al.,* 2004 and Palaniappan *et al.,* 2005, 2006). The use of a CFBG is desirable because the broadband reflection spectrum from a CFBG can be expressed as a function of position along the grating. Okabe *et al.* (2004) applied CFBGs for the identification of crack locations in a carbon fibre reinforced plastic (CFRP) subjected to tensile load. The crack locations were identified directly from the position of dips in the spectrum around a particular wavelength which corresponds to a unique position on the chirped grating. Palaniappan *et al.* (2005, 2006) analysed the changes in the reflection intensity spectra of CFBGs to detect transverse matrix cracks in glass fibre reinforced plastics (GFRP). The development and position of cracks were identified from an approximately sinusoidal variation in the intensity of reflected spectrum. The experimental and simulated reflection spectra were in reasonable agreement.

2.6 Chapter Summary

Optical fibre scattering-based distributed sensing systems are capable of sensing physical parameters over greater distances with sensing range in of the order of tens of kilometres; however for such systems the spatial resolution is limited around one metre.

These are suitable for long-range applications where millimetre spatial resolution is not a concern. Fibre Bragg grating-based distributed sensing systems on the other hand have good spatial resolution as low as millimetres with sensing range limited around a metre, and are suitable for localised applications where a continuous profile of the measurand as a function of position along the grating length with millimetre position resolution is required (e.g. to pinpoint hot spots or detect cracks and de-bonding in structures).

Table 2.4 compares the performance of the various distributed sensing techniques listed in this chapter with emphasis on major advantages, disadvantages and the best combination of sensor outcome parameters in relation to strain/temperature precision ($\Delta\varepsilon$ or ΔT), strain/temperature resolution ($\delta\varepsilon$ or δT), spatial resolution (δz) and sensing range (z) that has been reported to date.

Sensing Technique	Advantages	Disadvantages	Best sensor outcome	Reference
Rayleigh scattering	Strongest backscattered signal. Simple detection systems.	Weakly sensitive to temperature variations. Requires special fibre.	z = 100 m δz = 0.1 m ΔT = ±5 °C	Boiarski *et al.,*1995
Raman scattering	Commercialised systems available.	Weak signal requires lot of data averaging. Low SNR. Sophiscated opto-electronic detection systems.	z = 30 km δz = 5 m ΔT = ±1 °C	Hara *et al.,* 1999
Brillouin scattering	Systems capable of simultaneous temperature/strain distributed measurements. Long sensing range.	Spatial resolution limited around 1 m. Complex and expensive system configuration.	z = 30 km δz = 2 m ΔT = ±1.6°C	Alahbabi *et al.,* 2004a
Quasi-distributed FBG sensing	Multipoint monitoring of physical parameters. Better spatial resolution compared to scattering based distributed sensing.	Provides only an average of the measurand along a FBG sensor. Constrained by the design of sensing FBG arrays and available spectral source bandwidth.	ΔT = ±0.2°C δT = 0.04 °C $\Delta\varepsilon$ = ±5 με $\delta\varepsilon$ =1 με	Tjin *et al.,* 2002

Continued on next page

Continued from previous page				
Intensity-based Intragrating sensing, $R(\lambda)$.	Simple and practical measurement systems. Simple demodulation process. Requires only intensity spectrum, $R(\lambda)$, to evaluate intragrating Measurement.	Limited to monotonic field profiles. Poor accuracy at grating ends for low strain gradients.	$\delta\varepsilon$ =80 με δz = 0.8 mm δz = 0.184mm ΔT = ±2.2 K Δz = ±149 μm ΔT = ±0.2 °C $\Delta\varepsilon$ = ±50 με δz = 164 μm Δz = ±0.03 mm	LeBlanc *et al.,* 1996 Shi *et al.,* 2003 Won *et al.,* 2004 Gillooly *et al.,* 2004a, 2004b Nand *et al.,* 2006
Phase-based Intragrating sensing, $\psi(\lambda)$	Requires only phase spectrum $\psi(\lambda)$ to evaluate intragrating measurement. Can resolve sign of strain gradient for monotonic field profiles. Index modulation $\Delta n(z)$, along the grating does not need to be known with a high degree of accuracy.	Complex and expensive measurement systems. Requires a fast tuning laser source. Limited to monotonic field profiles.	Δz = ±1.5 mm	Swart *et al.,* 2005
Combined $R(\lambda)$ and $\psi(\lambda)$ based intragrating sensing	Not limited to monotonic field profiles. Complete demodulation of any arbitrary unknown strain profile. Good spatial resolution around 1 mm.	Expensive measurement system. Fast tuning laser source with high wavelength resolution required. Computationally expensive as both $R(\lambda)$ and $\Psi(\lambda)$ need to be processed. Limited to gratings with low reflectance; max$[R(\lambda)]$ < 30%.	δz = 1 mm $\delta\varepsilon$ = ±24 με δz = 1.65 mm	Huang *et al.,* 1998 Duck *et al.,* 2000
Low Coherence Reflectometry	Not restricted to monotonically varying strain fields of large gradients. Strain information can be determined directly from the strain applied to the reference grating.	Complex and expensive measurement systems. Interrogation technique similar to a Michelson interferometer is required.	Δε = ±5.4 με/√Hz δz = 300 μm	Volanthen *et al.,* 1997

Table 2.4 Summary of the performance of the various distributed sensing techniques.

CHAPTER 3

FABRICATION AND MODELLING OF CHIRPED FIBRE BRAGG GRATING SPECTRA

3.1 Introduction

This chapter reviews the fabrication techniques for the production of fibre Bragg gratings with an emphasis on chirped fibre Bragg gratings (CFBGs). A large number of experimental techniques have been proposed and reported to date for the production of CFBGs and controlling the grating spectral reflection response, bandwidth, chirp rate, strength and apodisation. Chirp in a grating can be imparted by a number of techniques as summarised by Kashyap (1999) and Othonos & Kalli (1999). Chirp in gratings may take many different forms with the period varying symmetrically (either increasing or decreasing around a central pitch in the centre of the grating), linearly, quadratically, randomly or with jumps along the length of the grating.

The chapter also provides a brief review of photosensitivity in optical fibres, and fibre Bragg grating fabrication techniques, whilst concentrating mostly on the principal techniques reported to date for the production of chirped fibre Bragg gratings. It then discusses in detail the two techniques employed in this research for the fabrication of chirped gratings. The chapter concludes with a discussion of the simulation techniques commonly employed to model FBG spectra, while focussing on the FFT grating reconstruction technique extensively used in this research to model CFBG spectra.

3.2 Photosensitivity in Optical Fibres

The phenomenon of photosensitivity observed within silica glasses, co-doped with various materials has led to the production of a wide range of fibre Bragg grating-based optical devices. Photosensitivity was first observed in germania-doped silica fibre by (Hill *et al.,* 1978) and has since been studied extensively (Poumellec *et al.,* 1996). Photosensitivity refers to a property of the glass that leads to a permanent change in the refractive index of the core of the optical fibre when exposed to an intense UV optical interference pattern. Such a periodic perturbation of the refractive index along the length of the fibre is referred to as a fibre Bragg grating. The existence of high photosensitivity within a fibre core is crucial to the fabrication of high quality Bragg gratings. To date germanium co-doped silica fibres remain the most photosensitive fibres for grating fabrication and it has been shown experimentally that germanium-boron co-doping produces a large index modulation in the order of 10^{-3} through hydrogenation. Photosensitivity has also been shown to be a function of photochemical and thermo-chemical reactions occurring in the core of the fibre.

The reliability and long-term stability of grating-based devices are important parameters for consideration in communications and sensing applications. Grating reliability is a function of a number of parameters, such as the nature and concentration of dopants incorporated into the core, type of photosensitivity, UV irradiation power density and photosensitisation processes used. To this effect it is relevant to discuss the mechanisms responsible for different types of fibre photosensitivity and its enhancement by hydrogenation and other photosensitisation techniques.

3.2.1 Photosensitivity Models

Even though the microscopic mechanisms responsible for different types of photosensitivity have not been completely understood, several models of photo-induced refractive index change have been proposed and experimentally verified to date, and these have been reviewed extensively elsewhere (Douay *et al.,* 1997, Kashyap, 1999).

The photosensitivity model most extensively studied, the colour centre model is based on the breaking of the germanium-oxygen vacancy defect bonds in germanium-doped

silica on absorption of UV radiation around the 244 nm wavelength band. On absorption of a photon, the GeO defect bond breaks forming a colour centre characterised by the presence of a Si^{+} hole and a released electron that is free to move within the glass matrix and can be retrapped at the original site or at some other defect site. The newly trapped electron causes a reconfiguration of the shape of the molecule which changes the absorption properties of doped silica in the UV region of the spectrum, resulting an increase in the refractive index given by the Kramers-Kronig relationship (Douay *et al.,* 1997). Atkins *et al.* (1993) reported that no significant change in photosensitivity was observed (both in terms of grating growth rate or final reflectivity) after a write/erase/write cycle, thus supporting the colour centre model. The colour centre model of photosensitivity has also been reported to account for photosensitivity in rare-earth-doped fluorozirconate (ZBLAN) glasses (Williams *et al.,* 1997). They reported that the mechanism of photosensitivity in Ce, Tb, Tm and Pr doped ZBLAN glasses involves colour centre(s) creation through a stepwise absorption of two photons. Though the model is generally accepted, it provides only an estimate of refractive index changes in hydrogenated germanosilicate fibres and accounts for only a small part of index changes observed in non-hydrogenated fibres.

The densification model of photo-induced refractive index change (Poumellec *et al.,* 1996) is based on structural modification of the glass in the fibre core into a more compact configuration. The structural changes in the glass matrix due to UV absorption results in changes in glass volume which accounts for the permanent change in refractive index according to the Lorentz-Lorenz relationship (Douay *et al.,* 1997). Another mechanism resulting in densification of germanosilicate fibres has been proposed (Bernardin *et al.,* 1990). The model is based on the collapse of a higher order ring structure into one comprising only of two or three rings due to the effect of UV irradiation. The densification model accounts for at least 40% of photosensitivity observed in non-hydrogenated germanosilicate and aluminosilicate fibres.

The stress-relaxation model is based on the assumption that breaking of chemical bonds on exposure to UV radiation results in the relief of compressive internal stress which was frozen within the core of the fibre during the fibre drawing process. Thus the change in refractive index is characterised by the photoelastic process of stress relief during fabrication.

To date, the observed changes in refractive index have not been fully characterised by the application of any single model. The colour centre model accounts for a large part of refractive index changes in hydrogenated germanosilicate fibres while the densification model is able to explain at least 40% of photosensitivity in nonhydrogenated germanosilicate and aluminosilicate fibres. Thus it is highly likely that more than one mechanism is responsible for induced index modulation during grating fabrication. Since new experimental results are continually emerging, it is likely that photoinduced index changes should be much better understood in the near future.

3.2.2 Photosensitisation Techniques

Enhanced photosensitivity in optical fibres is desirable mainly for the ease of grating fabrication. Thus a number of photosensitisation techniques such as increasing the levels of germanium-oxygen-deficiency centre (GODC defects) in germanosilicate preforms, hydrogen loading, flame brushing, codoping with boron (B), tin (Sn) and rare-earths and pre- and post- thermal treatments have been devised to enhance photosensitivity.

One of the widely used techniques for increasing photosensitivity in germanosilicate fibres is the hydrogen loading technique (Lemaire *et al.,* 1993, Atkins *et al.,* 1993). The technique relies on low temperature, high pressure hydrogen loading in a chamber to allow hydrogen molecules to diffuse into the fibre core prior to UV exposure. On exposure to UV irradiance, the hydrogen molecules react in the glass with Ge-O-Si sites to produce OH groups and bleachable GODC. The increased concentration of Ge oxygen deficient centres, through photolytic and thermal reactions between hydrogen and germanium atoms, enhances fibre photosensitivity resulting in a large permanent refractive index change in the fibre core. However, the mechanisms involved in hydrogen–induced photosensitisation are more complex than simple thermal formation of GODCs and detailed models of the photosensitisation process have been presented (Canning, 2000 and Kashyap, 1999).

Though hydrogen loaded fibres lock-in enhanced photosensitivity when exposed to UV irradiation, it has been shown that the index modulation of gratings inscribed in hydrogenated fibres decay much faster than non-hydrogenated fibres. The decay is

linked to hydrogen molecules out-diffusing after grating fabrication which makes it less stable in elevated temperature sensing applications due to a shift in the resonance Bragg wavelength. Techniques have been devised recently to improve the thermal stability of gratings written in hydrogen loaded fibres. Guan *et al.* (2000) and Aslund *et al.* (2000) have shown that the thermal stability of hydrogenated optical fibres can be significantly enhanced by pre-irradiating the fibres with a UV beam (UV presensitisation) before grating fabrication. Such gratings maintained more than 60% of their initial index modulation after 10 hours at 605 °C.

Other schemes for increasing the photosensitivity include increasing the concentration of germanium in germanosilicate fibre or codoping of the fibre preforms with codopants such as boron, tin and rare earths. Increasing the fibre photosensitivity using codoping techniques has been reviewed extensively elsewhere (Dong *et al.,* 1995, Dong *et al.,* 1995, Brambilla *et al.,* 2000, 2001, Dragomir *et al.,* 2003, Blows *et al.,* 2002, Willams *et al.,* 1997 and Oh *et al.,* 2002).

3.3 Fibre Bragg Grating Fabrication Techniques

To date a number of fabrication schemes based both on holographic and non-holographic techniques have been proposed to suit the type of grating application desired. This section provides an overview of the current external fabrication techniques for FBGs. In this, gratings are side written into the core of a photosensitive fibre by exposure to a UV light source and generally have greater reflectance due to the large index modulation. Techniques which fall under this category include inteferometric (holographic), point-by-point and phase mask.

3.3.1 Interferometric (Holographic) Fabrication Technique

Meltz *et al.* (1989) were the first to demonstrate this technique for inscribing Bragg gratings into the core of photosensitive fibres. The technique employs the splitting of the writing UV laser beam, directly or indirectly, into two separate beams and subsequently recombining them at the fibre where an interference pattern is produced. The interferogram is written transversely onto the fibre and, because of the

photosensitivity of the fibre in the UV domain, induces a permanent refractive index modulation along the core of the fibre. Interferometric techniques can be further divided into two distinct experimental arrangements of amplitude or wavelength-splitting interferometry.

Amplitude-splitting is the reduction of a beam by splitting the UV radiation directly into two beams of equal intensity by a beam splitter. The beams are recombined to produce an interference pattern along the fibre axis. The Bragg grating period (Λ) is related to the writing UV beam wavelength (λ_{uv}) and the half beam intersecting angle (ϕ) by the equation

$$\Lambda = \frac{\lambda_{uv}}{2\sin\phi}. \qquad 3.1$$

The advantages of the technique are that the Bragg wavelength is tunable by controlling the angle (ϕ) or the laser wavelength and has the flexibility of adding optical components into the apparatus to modify the interference fringes (e.g. use of cylindrical lenses to produce chirped gratings). The limitation is that mechanical vibrations during long exposure affect the coherence of the UV beam and the accuracy of the FBG writing.

3.3.1.1 Prism Interferometers

In this set-up, a single source and a prism form the basis for interference of the UV writing beam. The UV beam is spatially bisected by the prism edge, and half the beam is spatially reversed by total internal reflection from the prism face. The interference between the direct and the reflected beams at the output face of the prism inscribes the grating in the fibre core. The advantages are wavelength tunability and requirement of just one optical component. Disadvantages are that the interference results in the folding of the beam onto itself, and thus the requirement of a UV source with good spatial coherence.

3.3.1.2 Lloyd Interferometer

In this set-up a dielectric mirror is used instead of a prism, which introduces a phase change to the portion of the writing beam that is incident on the high-reflectivity mirror. The centre of the beam is centred at the interface between the mirror edge and the fibre. The interference fringe is formed by the overlap of the direct and deviated portions of the UV beam. A focussing cylindrical lens is used to focus the fringe pattern along the core of the fibre. The advantages are the requirement of only one optical component, Bragg wavelength tunability and lower susceptibity to reduction in interference contrast due to mechanical vibrations.

3.3.2 Phase-Mask Technique

The phase-mask is a transmission diffraction grating that creates a spatial modulation onto the fibre when illuminated by UV light. The phase-mask is made from a flat slab of silica glass with a one-dimensional periodic corrugation etched into fused silica surface. The phase-mask is transparent to a UV beam. The profile of the periodic corrugations is designed to suppress the zeroth-order diffracted beam to less than 3% of the total transmitted power. Most of the transmitted power (~40%) is contained in each of the +1 and −1 diffracted orders (Hill *et al.,* 1993, 1997). The two ±1 diffracted order beams interfere to produce a periodic pattern that photo-imprints a refractive index modulation in the core of the photosensitive fibre placed in contact with corrugations of the phase mask, as shown in figure 3.1. The period of the grating is ($\Lambda_{pm}/2$), where Λ_{pm} is the phase mask period.

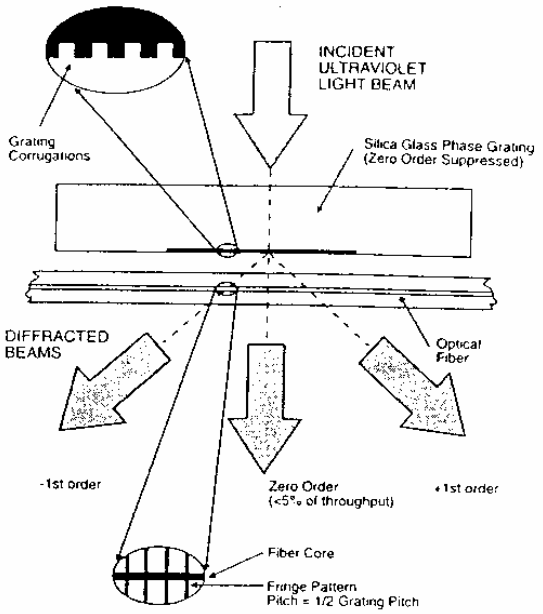

Figure 3.1 Schematic of a phase mask technique for photoimprinting a fibre Bragg grating into the core of a photosensitive fibre (Hill et al., 1993).

Hill *et al.* (1993) were one of the first to use the phase-mask technique. Using a KrF excimer 249 nm laser with 12 ns pulse duration as the writing beam and a phase-mask periodicity of 1060 nm, a 0.95 mm long FBG with a peak reflectance of 16% was fabricated. Others who reported the use of a phase mask with modified experimental arrangements for grating fabrication prior to the commercialisation of the technique include Anderson *et al.* (1993) who fabricated a 94% reflectivity grating at 1508.5 nm resonance wavelength, Prohaska *et al.* (1993) who fabricated gratings with tunable Bragg wavelengths by introducing a curvature in the incident wavefront using a lens, and Dockney *et al.* (1996) who demonstrated a phase mask based interferometer using a tunable laser source to fabricate an array of Bragg gratings with highly controlled centre wavelengths.

The complexity of the FBG fabrication system, the requirement of mechanical stability of the writing apparatus and the requirement for coherence of the UV laser beam are reduced by the phase-mask technique. This permits the use of cheaper UV excimer lasers and offers the potential of mass production at low cost.

3.3.3 Point-by-Point Technique

In the point-by-point technique, a change in the refractive index is induced locally across a short length (~μm) along the core of the fibre, one step at a time, by illumination with a UV source. In a typical experimental arrangement a single pulse of UV light from an excimer laser is passed through a mask containing a slit. The slit is imaged onto the core of the fibre at a finite point, corresponding to one grating plane, by a focussing lens for a fixed exposure time. This modifies the local refractive index of the core in the region of the irradiated section. The fibre is then translated parallel to the fibre axis through a distance Λ (corresponding to the grating pitch) and the process is repeated to form the grating structure.

Malo *et al.* (1993) used the technique to fabricate Bragg reflectors using a KrF excimer laser to illuminate a 15 μm slit. A focussing lens of 15 mm focal length was used to image the slit onto the core of the fibre at a finite point. Gratings with high reflectance of 70%, periodicity of 1.59 μm and length 360 μm were fabricated. The advantages are the flexibility of control over the grating parameters and the possibility of fabrication of chirped and longer length FBGs.

Recent advancements in the technique include full automation of the writing process, where either the fibre is translated relative to the UV fringe pattern or the UV beam is scanned along the fibre core. Asseh *et al.* (1997) demonstrated a fully automated technique to fabricate 20 cm long Bragg gratings with complex reflectivity profiles using a translation stage. Miller *et al.* (2002) reported the UV beam scanning technique to fabricate low reflectivity flat top chirped and apodised gratings with sidebands suppressed to -30 dB. The UV beam from a frequency-doubled argon laser was scanned along the fibre core by a 45° mirror mounted on a motorised translation stage. Thus the exposure and hence the apodisation profile could be controlled by the scan rate.

3.4 Chirped Fibre Bragg Grating Fabrication Techniques

Numerous applications of CFBGs in telecommunications and sensing have led to the design of a variety of fabrication techniques for controlling the spectral response of such gratings. Chirped gratings can be divided broadly into two categories being amplitude and periodicity (pitch) chirping. In amplitude chirping, the amplitude of the refractive index modulation along the length of the grating is varied while the period of the grating is kept constant. On the other hand, in periodicity chirping, the period of the refractive index modulation along the length of the grating is varied while the amplitude of the index modulation is kept constant. However, certain characteristic properties of periodicity chirping such as the potential to create a broader bandwidth and its relative ease of fabrication, offer advantages in specific applications and thus have been used extensively. Periodicity chirping can be introduced by: using a chirped phase mask, subjecting the fibre to a strain gradient during fabrication, writing gratings on prestrained fibres, straining the fibre after grating fabrication, writing gratings in fibre tapers, or interfering wavefronts of dissimilar curvatures in a holographic arrangement. A schematic diagram of a chirped grating employing periodicity chirping is illustrated in figure 3.2.

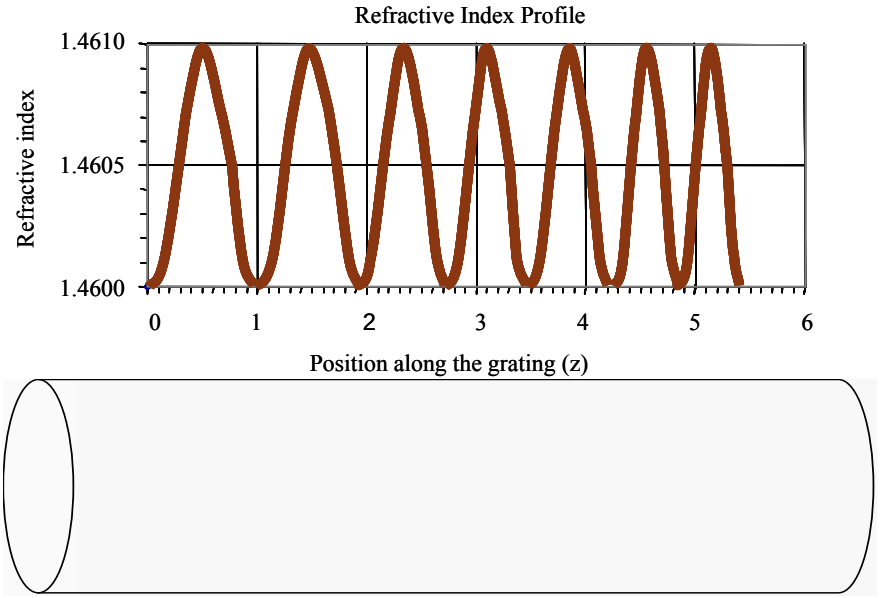

Figure 3.2 Schematic diagram of a CFBG employing periodicity chirping

CFBGs can be fabricated using all of the techniques described in section 3.3 for the fabrication of conventional FBGs. However, the external writing techniques (i.e.

interferometric or phase mask) are more commonly used for their fabrication. These techniques offer good control over grating parameters and thus the grating spectral response can be tailored for specific applications in sensing and telecommunication.

3.4.1 Interferometric (Holographic) Technique

A two-beam interferometer involving dissimilar curvatures in the interfering wavefronts is one of the more flexible and controllable techniques for the fabrication of chirped gratings. This involves placing two cylindrical lenses in the two arms of the interferometer. This generates wavefronts of dissimilar curvature in the interference pattern on to the fibre core. A schematic representation of the holographic two-beam interferometer arrangement is shown in figure 3.3.

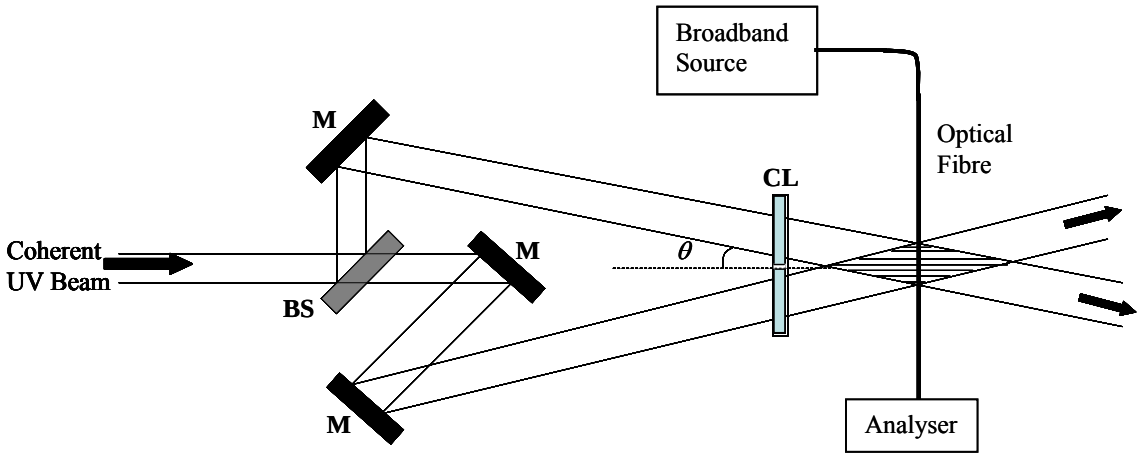

Figure 3.3 Schematic diagram of holographic two-beam interferometer arrangement. (CL: Cylindrical Lens; BS: Beam Splitter; M: Mirror)

Byron *et al.* (1993) reported the use of the technique to fabricate chirped gratings in a tapered photosensitive fibre. The introduction of tapers alters the waveguide properties of the fibre resulting in a change in the effective refractive index along the length of the taper. The variation of the effective refractive index introduces a chirp in the grating if fabricated along the tapered section of the fibre. The reflection profile of the chirped gratings was centred around 1.5312 μm with a reflectance of 20% and a reflection bandwidth of 2.9 nm. This technique is well suited to applications where highly controlled but relatively small chirps are desired.

In a similar uniform-period exposure arrangement, Sugden *et al.* (1994) introduced chirp by bending the fibre with respect to the interference fringes. The curved photosensitive fibre was placed in a two-beam interference field with a uniform fringe spacing Λ. Thus the period $\Lambda(z)$ of the resultant chirped grating varied according to the equation $\Lambda/\cos\phi(z)$, where $\phi(z)$ is the angle between the fibre and the normal to the exposing fringe pattern at position z along the grating. This technique is well suited for the production of chirped gratings with desired reflectance and bandwidth combinations. Farries *et al.* (1994) reported the production of broadband (44 nm) chirped gratings using wavefronts of dissimilar curvature in a holographic two-beam interferometer arrangement. Two cylindrical lenses were used for the formation of curved wavefronts and a third was used to focus the interfering beams onto the fibre core. By adjusting the relative positions of the cylindrical lenses, the bandwidth could be controlled resulting in a reflectance of over 90%.

Garchev *et al.* (1998) presented a novel method for the production of broad-bandwidth wavelength-tunable CFBGs using the combination of a lens and prism interferometer arrangement. The grating chirp rate, bandwidth and centre wavelength were easily controlled by simple adjustments of the experimental arrangement. Gratings with approximately quadratic profile with a peak reflectance wavelength of about 1441 nm, bandwidth of 1.8 nm and peak reflectance of approximately 80% were produced. Gratings with approximately linear chirping profile are also possible with the technique.

Wang *et al.* (2001) described a modified Talbot interferometer technique for producing chirped gratings. It incorporates a phase mask and a cylindrical lens into the two-beam interferometric technique. The cylindrical lens is used to introduce a curvature on the ± 1 diffracted orders of the UV beam from the phase mask. The two diffracted beams were re-combined at the fibre by a pair of mirrors to fabricate CFBGs with wavelengths in the range 550-1350 nm. The Bragg wavelength and the bandwidth could be controlled by translating either the fibre and/or the phase mask. Miller *et al.* (2002) also reported the use of a modified Talbot interferometer technique together with post-exposure rescan to fabricate an array of CFBGs for strain sensor applications. The Bragg wavelength, chirp, exposure and the apodisation profiles were controlled easily using computerised scanning of the beams along the fibre.

Lien *et al.* (2003) demonstrated fabrication of gratings with controllable chirp profile on polymer material polydimethylsiloxane (PDMS) coated with photoresist S1805 (Shipley) layer. The chirp profile can be tuned by selecting a specific geometric profile of the material and controlling the stretching force applied during fabrication.

3.4.2 Chirped Phase Mask Technique

The chirped phase mask is a highly precise and controlled technique for fabricating CFBGs. The mask is divided into subsections, each having its own period that is progressively changing in a functional form (e.g. linear or quadratic) depending on the type of chirp required. A novel technique of using a "stepped-chirp" phase mask for the fabrication of both linear and quadratic wavelength-chirped gratings was reported (Kashyap *et al.,* 1994). Gratings with lengths of 8 mm, bandwidths between 3 and 15 nm and reflectances ranging from 75-95% were demonstrated. The technique relies on the fabrication of step-chirped phase masks using electron-beam lithography. The chirp in the phase mask is built in short (δl) sections with each section differing in period from the previous one. Thus the resulting phase mask having N-sections of different period can be used to replicate chirped gratings. Apodised stepped CFBGs with a length of 100 mm and a bandwidth of 0.75 nm were also demonstrated (Kashyap *et al.,* 1996).

Zheng *et al.* (2006) also demonstrated the inscription of piece-wise stepped-chirped FBGs. The gratings were written with a uniform phase mask in a pre-stretched fibre by varying its length during exposure. Byron *et al.* (1995) demonstrated the stretch-write technique to fabricate stepped chirped gratings by scanning a UV beam along a uniform-period phase mask. The technique involved straining the fibre section under UV exposure and then either relieving or increasing the strain after writing. A chirped grating with a bandwidth of 10 nm and a length of 30 mm was demonstrated.

Other techniques employing a chirped phase mask include the use of a spherical lens (in combination with a phase mask) and the fibre tilted with respect to the phase mask during exposure (Painchaud *et al.,* 1995). The reflection bandwidth was shown to be a function of tilt angle, period of the phase mask, length of the grating, focal length of the spherical lens and the distance between the lens and the phase mask. Chirped gratings

with a bandwidth of 6 nm and peak reflectance of 96% were fabricated. A scanning Talbot interferometer setup employing a chirped phase mask as beam splitter was reported for fabrication of apodised CFBGs (Floreani *et al.,* 2003). Gratings with a Bragg wavelength in the range 900-1570 nm, length 2.5-10 mm and bandwidth of 5 nm were fabricated. A similar arrangement was used for tuning the Bragg wavelength (over 250 nm) of CFBGs (Kashyap, 1998). Liu *et al.* (2003) reported fabrication of CFBGs by applying an axial force to a uniform FBG adhered to a plastic plate. The chirp rate for both linearly and nonlinearly CFBGs could be controlled and a bandwidth of 0.5 nm was obtained.

The use of fibre tapers to fabricate CFBGs has attracted a lot of interest. Fibre tapers alter the waveguide properties of the fibre. The decreasing core size decreases the effective refractive index along the length of the taper, thus introducing a chirp in the grating in the region of the taper. Putnam *et al.* (1995) reported fabricating CFBGs in a tapered fibre subjected to a tensile load during fabrication. The resultant strain gradient along the taper produced a nonuniform shift in the Bragg period, resulting in chirped gratings. Tapers were fabricated with a computer controlled HF acid etching process. Two methods of chirping using tapers were investigated. In case I, the fibre was first tapered and the gratings were then written while the fibre was subjected to a tensile load. In case II, the gratings were first written into an untapered fibre, and the fibre was then tapered by the etching process and strain was applied. The second method resulted in greater chirp per unit applied strain. The technique is suited for the production of both linear and nonlinear chirped gratings. Dong *et al.* (1995) demonstrated the fabrication of gratings with larger chirp rate using stronger tapers. A strain gradient along the taper was used to produce chirp either during or after fabrication. Linearly chirped gratings with bandwidths up to 4.8 nm were fabricated.

Other applications of fibre tapers for the production of CFBGs include (Dong *et al.,* 1995, Zhu *et al.,* 2001, and Frazao *et al.,* 2005). The method proposed by Dong *et al.* (1995) relied on etching a taper over the fibre containing a uniform FBG. The variation of local effective modal index along the taper profile introduced a chirp in the grating. The technique is based on the same principle of variation in effective modal index along the taper profile (Frazao *et al.,* 2005). Zhu *et al.* (2001) reported chirping uniform FBG

by bonding the grating to the surface of a tapered plate that was strained by loading. A bandwidth of 2 nm and a grating length of 5 cm were obtained.

In an alternative technique, chirp was introduced by the thermal diffusion of the dopants (germanium and boron) from the core region into the cladding region (Cho *et al.,* 2004, Okude *et al.,* 1996). The technique is based on the change in the effective refractive index of the guided mode due to a decrease in core index by the changing core diameter.

3.5 Chirped Grating Fabrication Techniques Investigated in this Project

This section reports on the grating chirping techniques investigated in this project. The prism interferometer technique at OTRL, Victoria University and the scanning phase mask fabrication system at Swinburne University were used to fabricate chirped gratings for this project. The two techniques are described in detail, focussing mainly on the grating parameters, advantages, limitations and the suitability of the gratings for intragrating sensing applications.

3.5.1 The Prism Interferometer Technique (Victoria University)

The method of manufacturing chirped Bragg gratings using a prism interferometer chirping technique developed by (Garchev *et al.,* 1998) was modelled and investigated in detail for the production of gratings suitable for sensing applications.

The technique combines the prism interferometer technique used for the production of uniform period grating and the interference of dissimilar wavefronts to produce non-uniform period gratings. It uses a simple combination of a prism and a cylindrical lens. The cylindrical lens focuses the beam to produce a divergent beam in the plane containing the optical fibre, before being directed into a 45° quartz prism. The beam is split into two emerging beams (the refracted beam at the incident face and the reflected beam from the side) with dissimilar wavefronts within the prism as shown in figure 3.4 The refracted and the reflected beams interfere at the exit face of the prism to produce an interference pattern with nonuniform fringe spacing along the prism surface. A second cylindrical lens is used to focus the interfering beams perpendicular to the fibre

axis. The chirp rate, bandwidth and the wavelength of the gratings are a function of the UV beam diameter, focal length of the cylindrical lens, the effective distance of the focal point from the prism surface, the angle of incidence and prism geometry and are easily controlled by the variation of these parameters. Thus the technique is capable of producing broad bandwidth wavelength-tunable chirped fibre Bragg gratings.

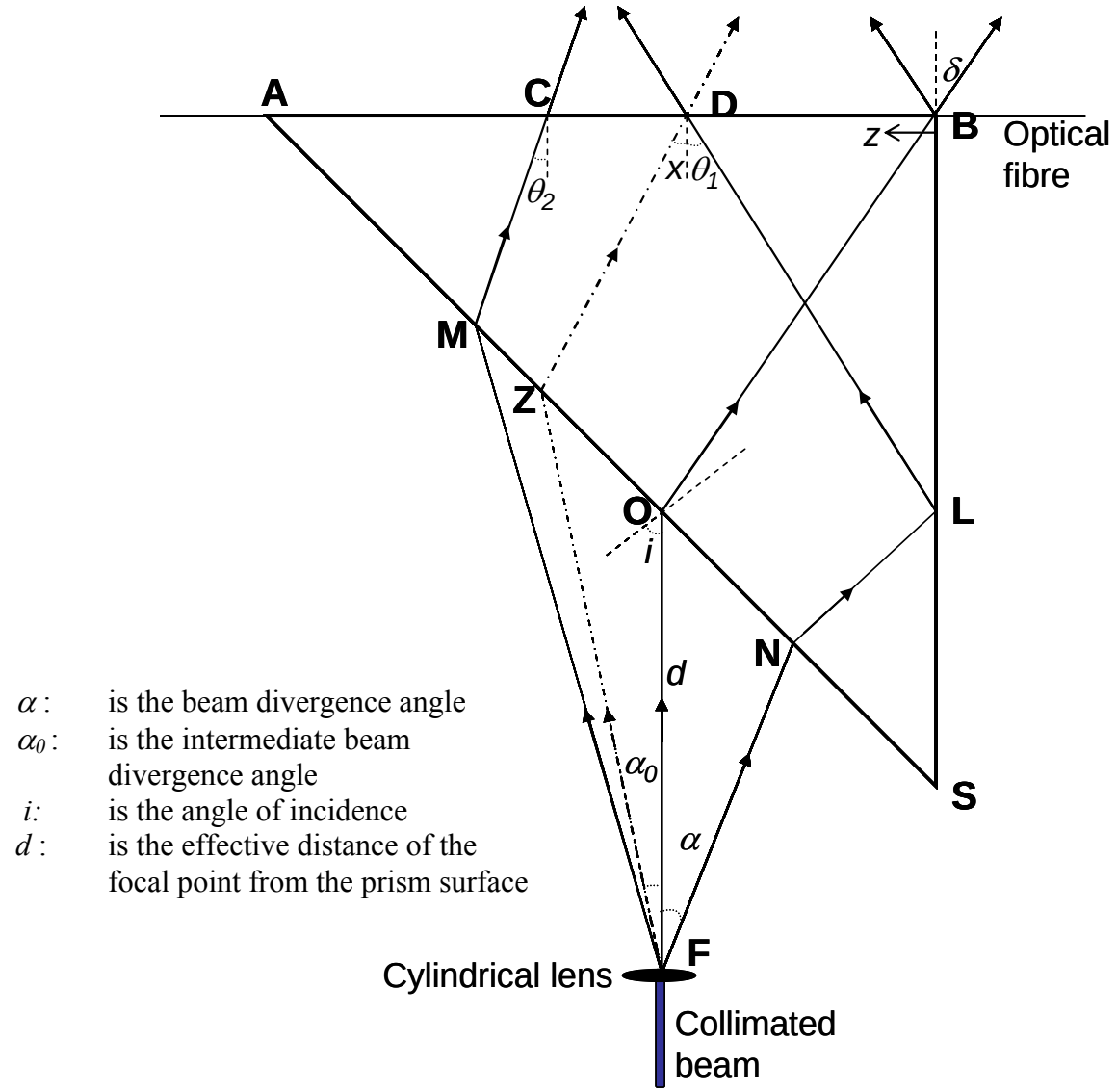

Figure 3.4 Schematic of the prism interferometer showing the propagation of divergent beams through the prism. The line BD defines the interference region with non uniform fringe spacing along the prism surface (Garchev et al., 1998)

3.5.1.1 The Prism Interferometer Chirping Technique

Periodicity chirping by the prism interferometer relies on the interference between wavefronts of dissimilar curvature through holographic exposure. The two divergent beams generated by the prism (Fig. 3.4), overlap at the exit face (*AB*) of the prism to produce an interference pattern with non-uniform fringe spacing. The local periodicity, $\Lambda(z)$, of the chirped gratings based on two-beam interference equation has the form (Garchev *et al.,* 1998)

$$\Lambda(z) = \Lambda(\theta_1, x) = \frac{\lambda_{UV}}{n[\sin(\theta_1) + \sin(x)]}, \qquad 3.2$$

where both variables θ_1 and x (marked on figure3.4) are functions of angle of incidence, i, beam divergence angle, α, effective distance, d, and grating position, z. Thus, each section of the grating contributes to the "local" Bragg wavelength. The chirping profile function has an approximate quadratic form (Garchev *et al.,* 1998)

$$\Lambda(z) = \Lambda_{\max} - bz^2, \qquad 3.3$$

where Λ_{max} is the fringe spacing at the prism vertex and b is the chirping profile coefficient. Thus by varying the parameters i, α and d the grating characteristics such as wavelength, chirping profile coefficient and grating length can be controlled.

3.5.1.2 Modelling Prism Interferometer Technique for Intragrating Sensing Application

Fabrication of gratings with the prism interferometer has been modelled for the design of improved sensors for intragrating temperature and strain measurements. To optimize temperature, strain and position resolution during localised measurements, the following investigations were conducted.

Modelling 1

The dependence of Bragg wavelengths around 1550 nm region on the angles of incidence for the case of zero beam divergence angle ($\alpha = \alpha_0 = 0$) was modelled. This region was investigated because, according to Garchev *et al.* (1998), this technique

allows fabrication of gratings with much larger bandwidths compared with other regions for a given grating length. The modelling was performed using equations 3.2 and 3.3. Figure 3.5 shows the expected Bragg wavelengths around 1550 nm for angles of incidence around 63° for ($\alpha = \alpha_0 = 0$). This seems to be the maximum angle of incidence for which gratings can be practically written as verified by a He-Ne laser experiment. At angles of incidence greater than 63°, clipping of the UV beam at the corner, *S,* of the prism limits the length of the gratings to unacceptably small values for sensing applications.

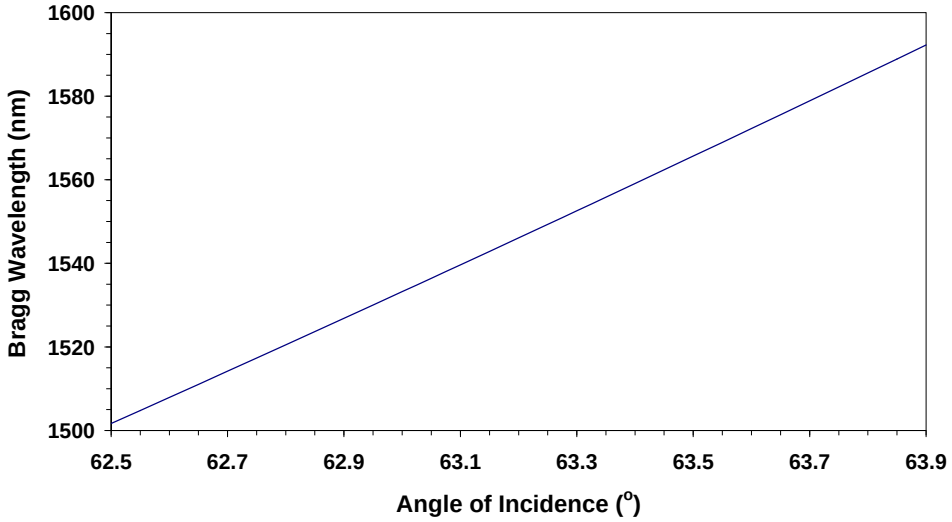

Figure 3.5 Expected Bragg wavelengths around 1550 nm at angles of incidence around 63 °for the case of ($\alpha = \alpha_0 = 0$), for the prism interferometer.

Modelling 2

The Bragg wavelengths achievable at the maximum angle of incidence i = 63° for the case of a divergent beam ($\alpha = \alpha_0 \neq 0$) in the range 0 - 20° was modelled. Figure 3.6 shows the expected Bragg wavelengths for beam divergence angles in the range 0 - 20° at i = 63°. The graph shows strong dependency of Bragg wavelengths on the combination of parameters α and α_0. The Bragg wavelength decreases gradually for values of ($0 \leq \alpha = \alpha_0 < 6°$) and rapidly for ($\alpha = \alpha_0 \geq 6°$). Hence Bragg wavelengths possible in the 1550 nm region are strongly dependent on α and α_0 and wavelengths are limited to less than 1532 nm.

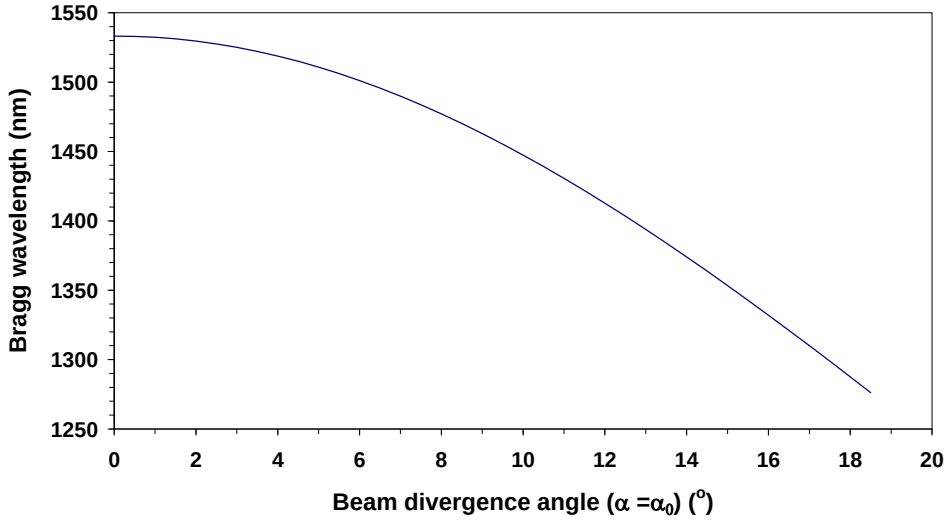

Figure 3.6 Expected Bragg wavelengths at i = 63 ° for the case of ($\alpha = \alpha_0 \neq 0$) in the range 0 - 20 ° for the prism interferometer.

Modelling 3

The expected spatial resolution, $\delta_z(z)$, for intragrating measurements were calculated using equation 2.8. Figure 3.7 shows the expected resolution for intragrating sensing at $i = 63°$ for three different combinations of beam divergence angles α and α_0 ($\alpha_0 = 0.8\alpha$, $\alpha_0 = 0.9\alpha$ and $\alpha_0 = \alpha$) at the end of the grating with minimum chirp rate. The figure shows that the resolution is strongly dependent on the combination of parameters α and α_0 in the range (0 - 6°) and is poorest for the case of $\alpha = \alpha_0$. For $\alpha \geq 6°$, the effect of α and α_0 is minimal and the resolution seems to be limited to around 50 μm. Thus for best spatial resolution, the combination of α and α_0 in the range $\alpha \geq 6°$ should be selected. This however would compromise the achievable Bragg wavelengths to less than 1500 nm, as shown in figure 3.6.

Modelling results show that the characteristics of a grating fabricated using this technique is dependent on a number of factors such as the beam divergence angle (α), angle of incidence (i), effective distance of the focal point from the prism surface (d) and the writing beam profile. Thus to optimise sensor spatial resolution, the above parameters need to be carefully controlled.

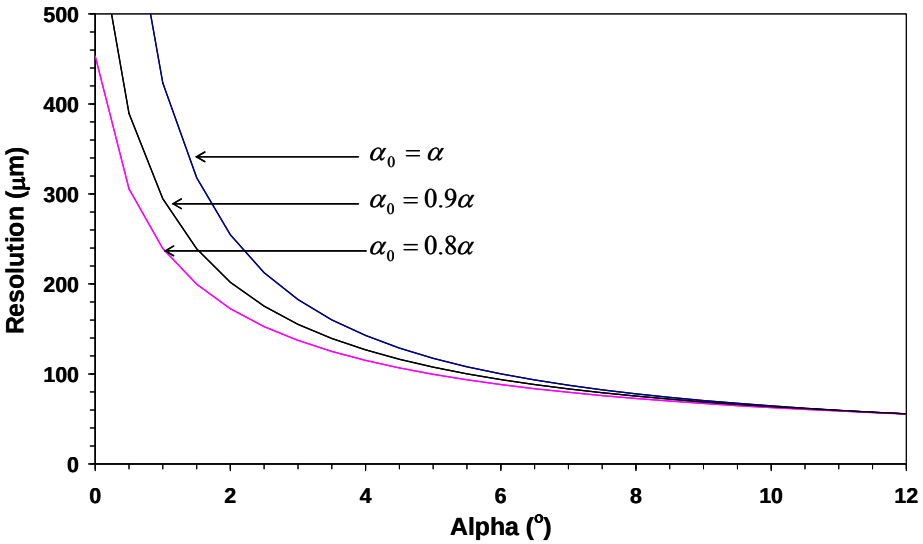

Figure 3.7 Expected spatial resolution in intragrating sensing for gratings fabricated at $i = 63°$ using different combinations of α and α_0, for the prism interferometer.

Figure 3.8 shows an example of the measured and FFT simulated transmitted spectra of a chirped grating fabricated with the system. The details of the FFT algorithm used for the simulation is described in section 3.6.3. The system parameters used were $i = 62.3°$, $\alpha_0 = \alpha = 3.4°$ and $d = 20$ mm. The grating parameters were FWHM bandwidth ≈ 5 nm, reflectance ≈ 35% and index modulation ($\Delta n \approx 2\times10^{-4}$). The transmission response is not a linear function of Bragg wavelengths. The variable transmission response could be due to the decrease in RI modulation amplitude near the edges of the writing UV beam because of the geometry of the exposure provided by the prism chirping technique.

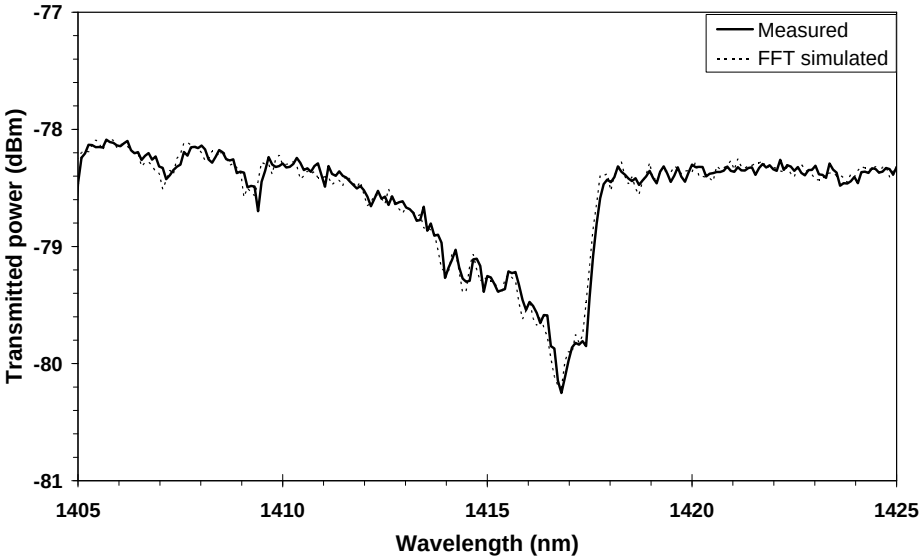

Figure 3.8 Measured and FFT simulated spectra of a chirped grating fabricated with the prism interferometer.

Table 3.1 shows target parameters for a grating suitable for intragrating measurements fabricated by this technique. These have been estimated based on the possible limit of resolution for a thermal model (≥ 125 μm), measurement system of using 500 point distributed measurements along the grating length and OSA resolution of 0.05 nm. The length of chirped gratings possible with this technique was verified experimentally to be less than 5 mm. This will limit the spatial resolution desirable both for a thermal and strain model in intragrating sensing. Apart from invariably small lengths which limit the spatial resolution, certain other constraints such as an approximate quadratic chirping profile limits the achievable FWHM bandwidth resulting in non-linearly chirped gratings. These non-linear chirped gratings are not suitable for designing a suitable sensor for intragrating measurements with the prism technique.

Parameters	**Minimum**	**Maximum**
Length (mm)	60	100
Bragg Wavelength (nm)	1530	1610
Chirp Rate ($\frac{d\lambda_B}{dz}$) (nm/mm)	0.5	1

Table 3.1: Target parameters of a CFBG suitable for intragrating sensing for the technique.

3.5.2 The Phase-mask based Scanning FBG Fabrication Technique (Swinburne University)

The majority of CFBGs used for this investigation were fabricated using this facility. The FBG writing system shown in figure 3.9 is a fully automated computer controlled system which was initially developed by JDS-Uniphase (Australia) for commercial fabrication of gratings for telecommunication applications. The system consists of a Coherent Sabre frequency doubled (CW) argon-ion laser operating at approximately 244 mW mounted on a granite block to reduce mechanical vibrations during grating fabrication.

Beam location and stability were monitored by computer controlled beam steering mirrors and a beam height adjusting telescope. A computer controlled Aerotech high precision translation stage was used to redirect and focus the laser beam onto a small section of the optical fibre as shown. The focussing was achieved by a steering mirror and a cylindrical lens mounted on the translation stage. The precise position of the fibre

in the interference field pattern behind the chirped phase mask was also computer controlled.

The system allows the grating parameters such as apodisation profile, length, bandwidth and reflectance to be user defined and controlled. The grating reflectance (exposure) was controlled by varying the scan rate of the laser beam along the phase mask using the high performance linear translation stage. A piezo phase mask shaker (dither) was used to flatten the average exposure, and apply controlled apodisation by gradually increasing the dither towards the grating ends. This suppressed side lobes at the ends of the grating spectrum. A linearly chirped phase mask and variable scan rates were used to fabricate gratings with a range of peak reflectances.

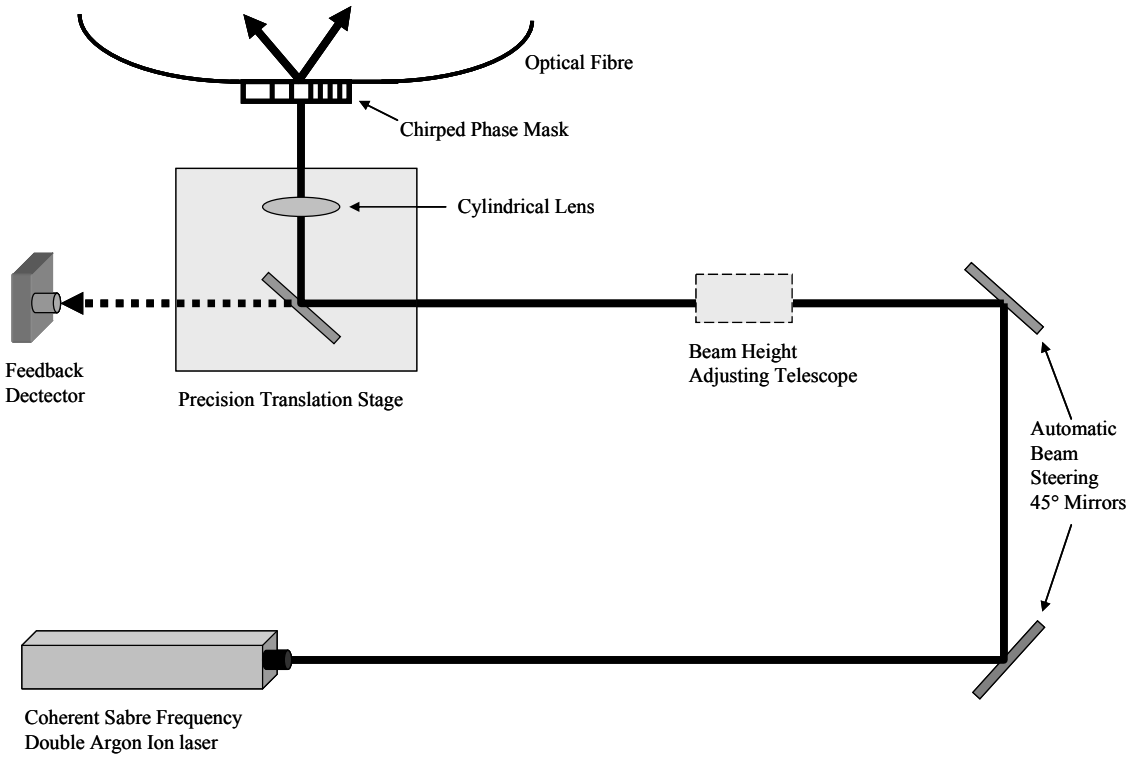

Figure 3.9 Schematic diagram showing the optical arrangement of the scanning FBG fabrication facility at Swinburne University.

3.6 Fibre Bragg Grating Simulation Techniques

Many techniques for simulating the spectral response of both uniform and non-uniform FBGs from known grating parameters (period, refractive index and index modulation) have been reported in literature. The most commonly used are the direct numerical integration of the coupled mode equations, the transfer matrix (T-matrix) approximation of the coupled mode theory and the fast Fourier transform technique.

Though the coupled mode theory is a good tool for modelling accurately the spectral response of FBGs, the direct numerical integration of coupled mode equations is computationally intensive and thus not very practical for analysing large amounts of experimental data. The transfer matrix approximation, on the other hand, is a fast and accurate technique and has been widely used to model uniform, chirped and apodised Bragg gratings. In this approach the grating is divided into M smaller subgratings, each with uniform coupling properties. Each section is defined by its transfer matrix and the coupled mode equations are used to calculate the spectral response of the short section (δl_1) of the grating. The spectral response of the first subgrating is used as the input field for the second subgrating (δl_2) and the process is repeated until the entire complex profile grating is modelled. Thus the overall grating structure is characterised by a global matrix obtained as the product of the individual matrices of each subgrating. The Fourier transform approach has a high computation speed and, in the limit of weak grating reflectance, is in good agreement with the transfer matrix method.

This section first provides a summary of the two basic analysis methods for two-mode coupling in Bragg gratings: the direct numerical integration of the coupled mode equations and the conventional transfer matrix model (TMM) approximation. The fundamental mathematical equations of the coupled mode theory and the TMM approximation are presented. The section concludes with a description of the Lab view based Fourier transform technique (FFT) developed for this project.

3.6.1 Coupled-Mode Theory for two Mode Coupling in Bragg Gratings

A FBG is defined as a periodical perturbation to the effective refractive index, n_{eff}, of the optical fibre core as described by Erdogan (1997)

$$\delta n_{eff}(z) = \overline{\delta n}_{eff}(z)\left\{1 + \nu \cos\left[\frac{2\pi}{\Lambda_0} z + \phi(z)\right]\right\}, \tag{3.4}$$

where ν is the fringe visibility, Λ_0 is the nominal period, $\phi(z)$ is the grating chirp and $\overline{\delta n}_{eff}$ is the "dc" index change averaged spatially over a grating period. The perturbation δn_{eff} is assumed to be small. The dominant interaction in a Bragg reflection grating in a single-moded fibre is the coupling between the forward-propagating and counter-propagating guided modes of the fibre initiated by the refractive index perturbations in the fibre core. Thus from coupled mode theory, the following first order differential equations describing mode propagation through the grating in the z direction are obtained (Erdogan, 1997, Ling *et al.,* 2005)

$$\frac{d\Re(z)}{dz} = i\hat{\sigma}\,\Re(z) + i\kappa\, S(z), \tag{3.5}$$

$$\frac{dS(z)}{dz} = -i\hat{\sigma}\, S(z) - i\kappa\,\Re(z), \tag{3.6}$$

where $\Re(z)$ and $S(z)$ are the amplitudes of the forward and backward propagating modes, respectively. $\hat{\sigma}$ is the general "*dc*" self-coupling coefficient as a function of the propagating wavelength, λ, defined as

$$\hat{\sigma} = 2\pi n_{eff}\left(\frac{1}{\lambda} + \frac{1}{\lambda_D}\right) + \frac{2\pi}{\lambda}\overline{\delta n}_{eff} - \frac{1}{2}\phi'(z) \tag{3.7}$$

where $\phi'(z) = d\phi/dz$ and $\phi'(z) = 0$ for a uniform grating, and $\lambda_D = 2n_{eff}\Lambda_0$ is the design wavelength, and κ is the "*ac*" coupling coefficient defined as

$$\kappa = \frac{\pi}{\lambda}\nu\overline{\delta n}_{eff}. \tag{3.8}$$

The amplitudes $\Re(z)$ and $S(z)$ are defined as

$$\Re(z) = A(z)\exp(i\delta z - \phi/2), \tag{3.9}$$

$$S(z) = B(z)\exp(-i\delta z + \phi/2). \tag{3.10}$$

The length of a uniform grating is assumed to be L, and thus the limit of the grating is defined as $-L/2 \le z \le L/2$, while the boundary conditions of the grating are $\Re(-L/2) = 1$ at $z = -L/2$ and $S(L/2) = 0$ at $z = L/2$. This is based on the assumption that the forward going wave is incident from $z = -\infty$ [i.e. $\Re(-L/2) = 1$] and no reflected wave exists for $z \ge L/2$, since there is no perturbation beyond the end of the grating [i.e. $S(L/2) = 0$]. Thus we have one boundary condition at $z = -L/2$ and one at $z = L/2$. It can be shown that the solution to equation 3.11, yields same reflectance for the real boundary conditions ($\Re(-L/2) = 1$, $S(L/2) = 0$) as for the "dummy case" with boundary conditions set as ($\Re(L/2) = 1$, $S(L/2) = 0$) (Erdogan, 1997). Hence the "dummy case" can be used to numerically integrate backwards starting from $z = L/2$ to $z = -L/2$ to calculate $\Re(-L/2)$ and $S(-L/2)$.

Equations 3.5 and 3.6 can be solved numerically, using various techniques, to obtain exact solutions. In one such technique (Prabhugoud *et al.,* 2004), the equations were transformed into a Ricatti differential equation by substituting $\rho(z) = S(z)/\Re(z)$ and a fourth order Runge-Kutta numerical integration with an adaptive step size was then used to solve by integrating backwards from $z = L/2$ to $z = -L/2$.

The reflectance, $R(\lambda)$, of the Bragg grating is calculated as a function of wavelength as

$$R(\lambda) = \left|\frac{S(-L/2)}{\Re(-L/2)}\right|^2. \tag{3.11}$$

Since the direct numerical integration of equations 3.5 and 3.6 are computationally intensive and not practical for analysing large amounts of experimental data, the piecewise-uniform approach (transfer matrix method) is often preferred to model both uniform and chirped gratings.

3.6.2 Transfer Matrix Approximation Method (TMM)

The T-matrix approximation is used widely to model FBGs with non-constant properties. In this approach, the grating is assumed to be divided into *M* small sections, each with uniform coupling properties. That is, for each of the sub-gratings of length (Δz), the "*dc*" self-coupling coefficient, $\hat{\sigma}$, and the "*ac*" coupling coefficient, κ, are assumed constant. Each sub-grating is defined by its transfer matrix and the coupled mode equations are used to calculate the output fields of the sub-grating. The output of the first subgrating is used as the input field for the second subgrating. Thus defining $\Re_i$ and S_i to be the field amplitudes after traversing the *i*th grating section, the propagation through this uniform section can be described by a 2×2 matrix, F_i,

$$\begin{bmatrix} \Re_i \\ S_i \end{bmatrix} = F_i \begin{bmatrix} \Re_{i-1} \\ S_{i-1} \end{bmatrix}, \tag{3.12}$$

where F_i is the matrix of the *i*th subgrating and described as

$$F_i = \begin{bmatrix} \cosh(\gamma_B \Delta z) - i\dfrac{\hat{\sigma}}{\gamma_B}\sinh(\gamma_B \Delta z) & -i\dfrac{\kappa}{\gamma_B}\sinh(\gamma_B \Delta z) \\ i\dfrac{\kappa}{\gamma_B}\sinh(\gamma_B \Delta z) & \cosh(\gamma_B \Delta z) + i\dfrac{\hat{\sigma}}{\gamma_B}\sinh(\gamma_B \Delta z) \end{bmatrix}, \tag{3.13}$$

in which Δz is the length of the *i*th subgrating and (γ_B) is defined as $\gamma_B \equiv \sqrt{\kappa^2 - \hat{\sigma}^2}$.
Thus the T-matrix formulation, *F*, for the entire grating can be written as

$$\begin{bmatrix} \Re(-L/2) \\ S(-L/2 \end{bmatrix} = [F] \begin{bmatrix} \Re(L/2 \\ S(L/2) \end{bmatrix}, \tag{3.14}$$

where *F* is the total response matrix of the grating and can be written as the product of the response matrices of the *M* individual subgratings as

$$[F] = [F_M] \bullet [F_{M-1}] \cdots\cdots\cdots\cdots \bullet [F_1]. \tag{3.15}$$

Therefore the reflectance of the entire grating as a function of wavelength can be computed using equation 3.12. The main advantages of the T-matrix method is that it is capable of simulating both weak and strong FBGs and is computationally efficient compared to the direct numerical integration of the coupled mode equations. One limitation of the T-matrix approximation is that number of subgratings (M) cannot be arbitrarily large since several grating periods are required for complete coupling. In other words, the minimum subgrating (section) length must be greater than a few periods long (Erdogan, 1997). That is $\Delta z >> \Lambda$, which requires M to be

$$M << \frac{2n_{eff}L}{\lambda_D}, \tag{3.16}$$

where λ_D is the design wavelength. Furthermore, the number of sections required for the T-matrix approximation is also dependent on the precision required and typically $M \cong 100$ is sufficient to model chirped gratings. However, to model L = 15 mm, $d\lambda/dz$ = 20 nm/cm chirped gratings investigated in this project, M = 2001 was used.

The T-matrix method is currently the most commonly used numerical model to calculate the spectral response of FBGs. A complete theoretical analysis of the technique is presented elsewhere (Yamada *et al.,* 1987, Erdogan, 1997, Ling *et al.,* 2005) together with modified versions (Prabhugoud *et al.,* 2004, Miller *et al.,* 2006).

3.6.3 FFT Grating Design Algorithm Operation

The FFT model was implemented initially in LabView by Dr Daniel Kitcher, a Research fellow with OTRL at VU. Figure 3.10 shows a simplified version of the Virtual Instrument (vi) block diagram for the FFT grating design model implemented for this project. Shown on the figure are the sub·vi's ("define FBG" and "setup FBG") called by the FFT.vi for implementing the grating simulation process. The inputs of the sub·vi define FBG are the number of grating segments, the number of grating planes per segment, FBG parameters such as *ac* and *dc* index modulation, start Bragg wavelength, grating length, chirp rate and exposure function profiles. The output of the sub·vi is the

grating definition consisting of *ac* and *dc* index modulations, grating pitch and phase as a function of position, *z*, along the grating. The inputs of the sub·vi setup FBG are the number of segments and grating definition consisting of a cluster of five elements listed above. The outputs of the sub·vi are local Bragg frequencies (F_B) and amplitude and phase of the local coupling coefficient, $\kappa.dz$. These are fed into the FFT·vi for generating a spectrum of the grating from the known grating parameters.

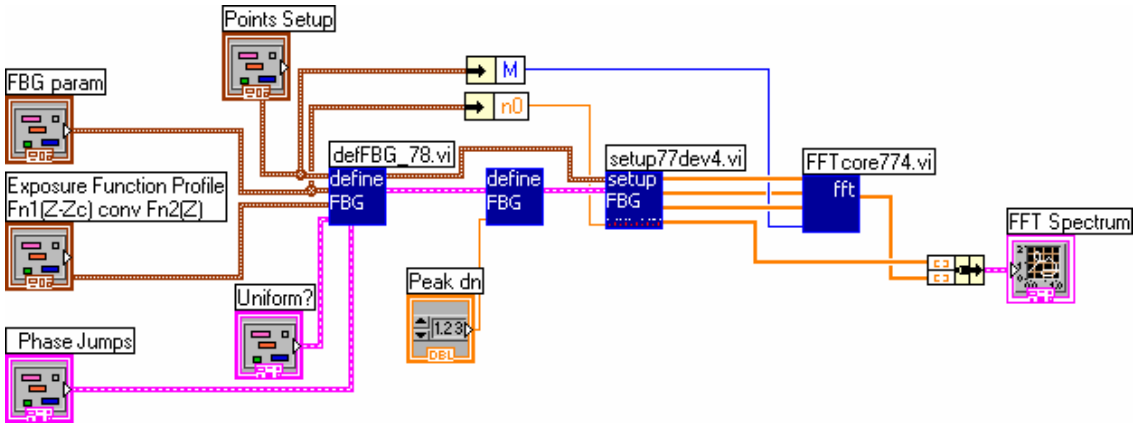

Figure 3.10 Block diagram for the FFT grating design model in Labview.

The detailed block diagram of the FFT core·vi is shown in figure 3.11. The operation of the FFT grating simulation algorithm is described below.

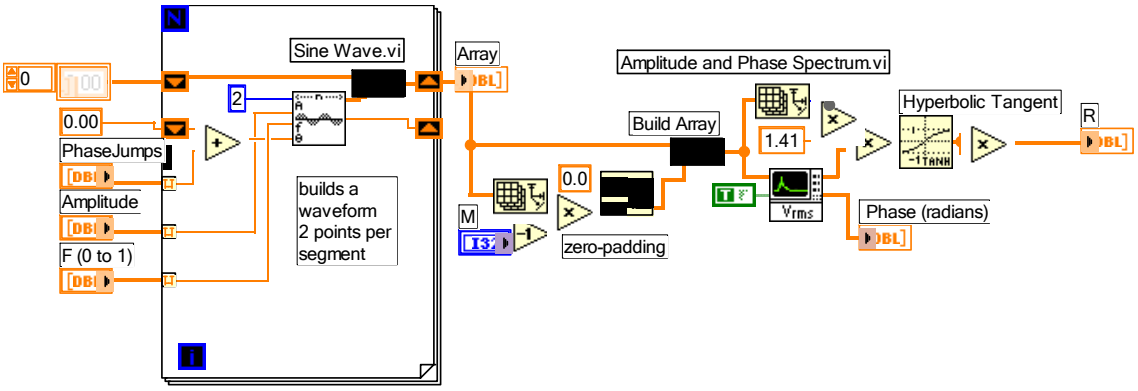

Figure 3.11 Block diagram for the FFT core·vi algorithm in Labview.

The amplitudes of the dc refractive index (A_n) versus position (z) along the grating and local Bragg periods (Λ_B) were used to generate a list of local Bragg frequencies (F_B). The local Bragg frequencies are used to build a set of 2001 segments each containing a number of grating planes. Each segment was defined by the local average refractive index, average local period, amplitude and the phase. The contribution to reflectance of

each section is proportional to the local ac coupling coefficient $\kappa.dz$. The local ac coupling constant was calculated and integrated over the segment length to generate a set of reflectance contributions at regularly timed intervals. A sine waveform was synthesized at each grating segment based on the amplitude ($A_n = \kappa_n.dz$) and phase (Φ_n) of the local average refractive index. The dc refractive index modifies the phase of the sinusoid in which these samples are generated, resulting in disturbances to the output spectrum representative of the effect of local heating or local strain within the CFBG.

A discrete FFT of the sine waveform was taken to generate the magnitude of the reflective contributions at each frequency. The discrete FFT algorithm is implemented by executing the fast radix-2 FFT routines. Consider the sequence of N complex numbers $x_0, x_1,\cdots\cdots, x_{N-1}$. These are transformed into the sequence of N complex numbers $X_0, X_1\cdots\cdots, X_{N-1}$ by the radix-2 FFT according to the equation

$$X_k = \sum_{n=0}^{N-1} x_n e^{-\frac{2\pi i}{N}nk} \quad \text{where } k = 0,\cdots\cdots, N-1. \tag{3.17}$$

The radix-2 FFT algorithm divides the sequence size into two interleaved halves with each recursive stage. It first computes the FFT of the even-indexed numbers $e_m = x_{2m}(x_0, x_2, \ldots\ldots x_{N-2})$ and of the odd-indexed numbers $o_m = x_{2m+1}(x_1, x_3, \ldots\ldots x_{N-1})$ and then combines the two results to produce the Fourier transform of the whole sequence. Thus the technique can then be performed recursively to reduce the calculation time. The computing time for the radix-2 FFT is proportional to $N\log_2(N)$. The only requirement is that the number of points in the sequence be a power of 2. This is not problematic as the number of sample points can be freely chosen by the user.

In this application, the complex sequence consists of the coupling coefficient, $\kappa.dz$, defined by the respective amplitude and phase of the local average refractive index of each segment. The output of the FFT is the complex amplitude reflection coefficient, $r(\lambda)$. The transformation $R(\lambda) = \tanh^2|r(\lambda)|$ was applied to the FFT output $r(\lambda)$ to convert from magnitude to power reflectance. This corrected the amplitude to agree

with coupled mode theory for uniformly exposed gratings. Figure 3.12 shows the peak reflectance of the FFT model output compared with that predicted by the function $R = \tanh^2(\kappa L)$.

Thus a Fourier transform (FFT) of the contributions to reflectance at each of the N sections of the grating planes is the core of this grating design model. The FFT method assumes that light propagates the entire length of the grating and is reflected from all grating planes, which is true for weak gratings with less than 50% reflectance investigated in this project. It also has high computation speed as required for grating simulation and on-line processing of distributed measurements. Thus due to its millisecond calculation time and the use of gratings with low reflectance for measurements in this project, the FFT model was implemented for simulating the spectral response of the gratings.

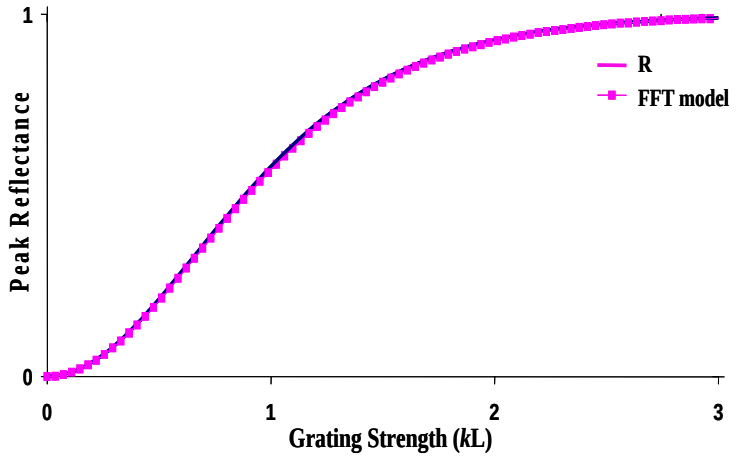

Figure 3.12 Comparison of the peak reflectance of the FFT model output with that predicted by the function $R = \tanh^2(\kappa L)$

3.6.4 Modelling CFBG spectra using the FFT algorithm

Figure 3.13 shows the calculated spectral response of a linearly chirped grating modelled using the LabView based FFT algorithm. The chirping function was represented by the equation $\lambda(z) = 1525 + 20z$, where λ is in nm and z is in cm. The spectral reflection response shown in the figure is typical of linearly chirped gratings with uniform ac index modulation profile written in any wavelength region. A grating length of 15 mm, chirp rate of 20 nm/cm, starting Bragg wavelength of 1525 nm and

uniform *ac* index modulation amplitude of 0.0003 were used in the calculation of the spectra. The relatively flat spectral response for most of the bandwidth of the grating can be explained by the constant chirp rate resulting in an equal number of grating planes contributing to the local resonance Bragg wavelength. The presence of ripples along the grating length is due to the combined effect of multiple reflections within the grating structure and varying levels of back-coupling in different grating regions. The increased reflectance (ringing) observed at the ends of the grating's spectral response is as expected. This is due to the Fourier transform of the grating's exposure shape function having an abrupt start and end.

The spectral response of linearly chirped gratings could be smoothed out if an apodised exposure profile is used to control the *ac* index modulation at the ends of the grating. The technique relies on maintaining an unchanging average refractive index throughout the grating length while gradually increasing and decreasing the index modulation amplitude on penetration into and exiting from the grating, respectively. Thus for the study of intragrating measurements, a convolution of a Gaussian and a cosine tapered window function was used as the exposure function to model the CFBGs' spectral response. Figure 3.14 shows the spectrum of a linear chirped fibre Bragg grating modelled with the above exposure function.

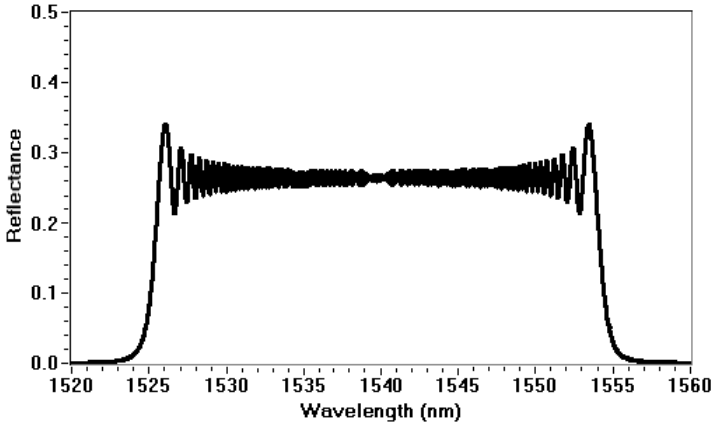

Figure 3.13 FFT calculated spectral response of a linearly CFBG with uniform index modulation exposure profile along the grating length (L = 15 mm, chirp rate = 20 nm/cm and Δn =0.0003).

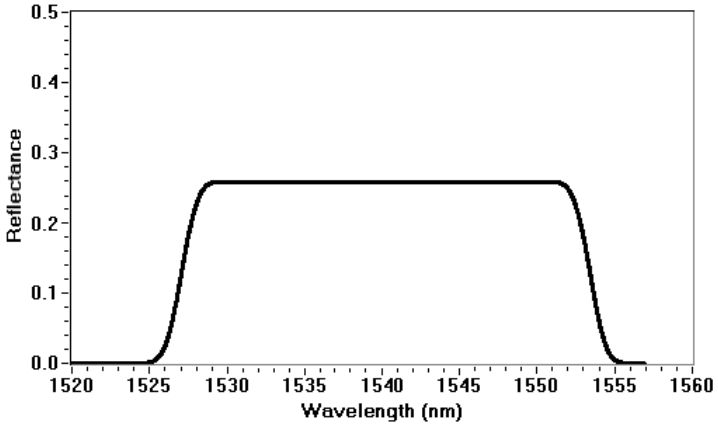

Figure 3.14 FFT calculated spectral response of a linearly CFBG with convolution of Gaussian and cosine tapered window function used as the exposure function (L = 15 mm, chirp rate = 20 nm/cm and Δn =0.0003).

Figure 3.15 shows the measured and FFT simulated spectra for chirped gratings *A-E* (described in chapter 5) fabricated using the scanning FBG fabrication system. The simulated spectra for the five gratings were obtained by employing a non-uniform grating definition profiles obtained from the measured reference spectrum. That is, the FFT model operated on an estimate of the amplitude of the refractive index modulation of the grating obtained by applying an inverse transformation to the measured reference spectrum. These non-uniform grating definition parameters extracted from the reference spectrum were fed into the FFT algorithm for generating a simulated spectrum. These gratings, having a range of reflectances, were used for the determination of the centre position of a localised heat source.

3.7 Chapter Summary

Fabrication and modelling of CFBGs using the two techniques have shown that certain constraints exist in designing a suitable sensor for intragrating sensing using the prism interferometer technique. The length of the grating possible with the technique is invariably small, which will limit the spatial resolution desirable for intragrating measurements. Furthermore, the chirping profile of gratings have an approximate quadratic form, which limits the achievable FWHM bandwidth, resulting in non-linearly chirped gratings. These gratings have been found to be not very suitable for the application desired in this project.

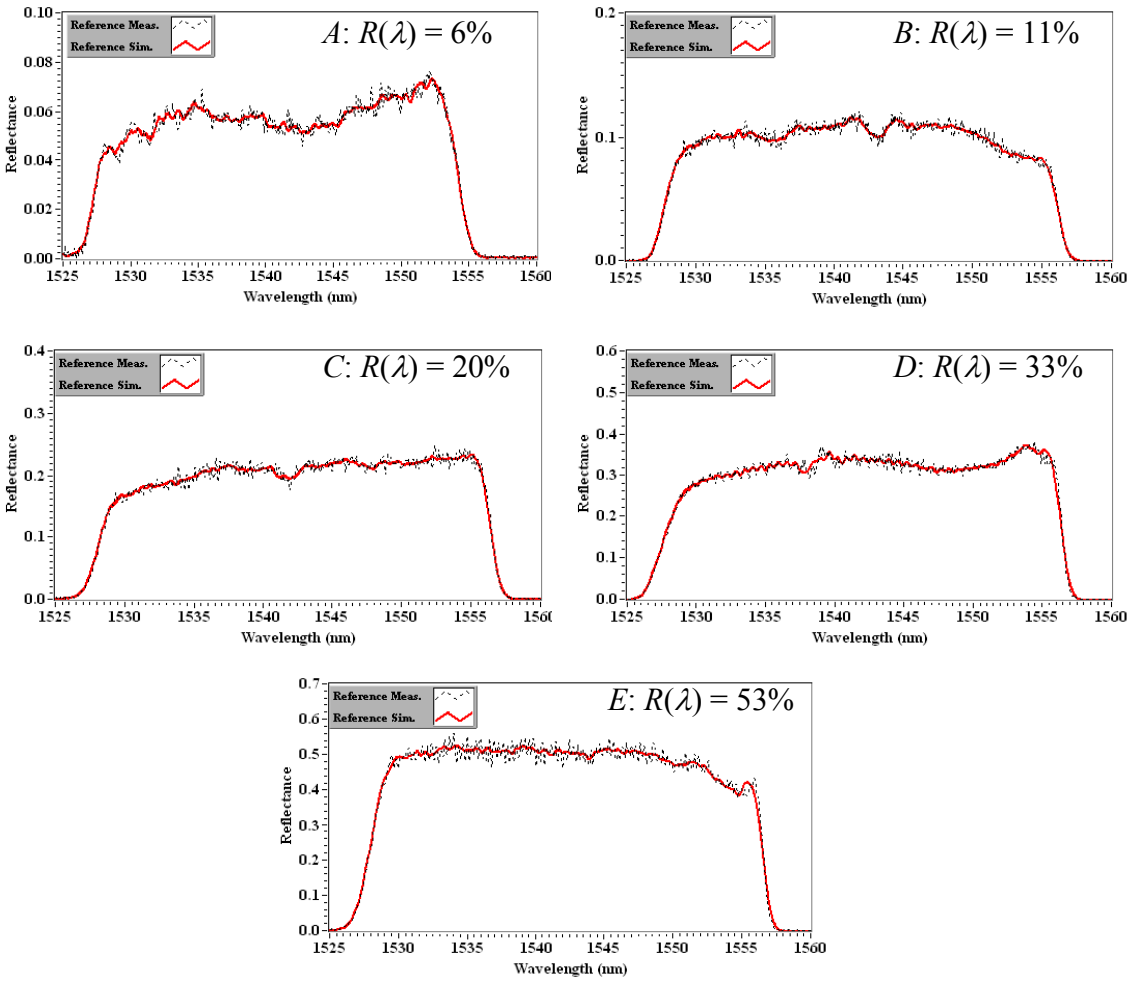

Figure 3.15 Measured and FFT simulated spectra for gratings fabricated with the scanning FBG fabrication system

Thus gratings fabricated with a linear chirped phase mask using the scanning FBG fabrication system were modelled using the FFT grating simulation technique and used for the measurement of localised position of a heat source and nonuniform strain distribution. The spectral reflection responses of the chirped gratings, required for these applications, were easily controlled by the scanning fabrication system.

CHAPTER 4

TEMPERATURE AND STRAIN CHARACTERISATION OF CHIRPED FIBRE BRAGG GRATINGS

4.1 Introduction

Fibre Bragg gratings (FBGs) make promising candidates as sensors because of their significant sensing advantages, the most important of which is that the information on a measurand is encoded in the Bragg wavelength. Thus problems associated with source power fluctuations, bending losses, backscattering/reflection losses are eliminated. However, before the deployment of any sensor systems based on FBG, a detailed in-laboratory characterisation of the sensor in order to assess their performance in relation to precision and repeatability of measurements is essential. When FBGs are employed as mechanical sensors to monitor structural strain, the shift in Bragg wavelength is a function of strain (or damage state of the structure to which the FBG is attached or embedded). Thus for proper interpretation of measurement results, strain and temperature sensitivities of the Bragg gratings used are essential.

This chapter describes the calibration techniques employed to evaluate the temperature and strain response of the CFBG sensors fabricated for this work. A comparison of the temperature and strain sensitivities obtained is made with those of standard FBGs fabricated using both the prism and phase mask techniques. The chapter concludes by proposing a simple technique for strain–independent temperature measurement using a sensor head with a combination of a standard FBG and a CFBG.

4.2 Theoretical Background on Temperature and Strain Characteristics of a Fibre Bragg Grating

The Bragg wavelength (λ_B) of an optical fibre grating is a function of the grating period and the effective refractive index of the fibre core represented by equation 1.1. Thus any change in refractive index or the grating period due to physical parameters (particularly strain and temperature) will change the Bragg wavelength of the light that is reflected back.

The strain induced shift of the fibre Bragg grating results from two effects, the physical elongation of the optical fibre corresponding to a change in grating pitch and the change in the effective refractive index due to photo elastic effects (Murukesshan *et al.,* 2001, Kersey *et al.,* 1997). Thus the Bragg wavelength shift due to strain response can be expressed as

$$\Delta\lambda_B = (1 - p_e)\lambda_B \varepsilon , \tag{4.1}$$

where ε is the applied strain and p_e is the photoelastic coefficient of the fibre given by

$$p_e = (n_{eff}^2 / 2)[p_{12} - v(p_{11} + p_{12})], \tag{4.2}$$

where p_{ij} are the strain-optic coefficients and v is Poisson's ratio.

The temperature response of the Bragg wavelength is due to two factors, the change in the effective refractive index of the glass due to the thermo-optic effect and the thermal expansion of the glass resulting in a change in the grating pitch. Thus the Bragg wavelength shift due to temperature can be expressed as

$$\Delta\lambda_B = (\alpha + \xi)\lambda_B \Delta T , \tag{4.3}$$

where α is the thermal expansion coefficient and ξ is the thermo-optic coefficient of the silica fibre. Both parameters α and ξ are functions of temperature and have been observed to be non-linear at high temperatures (Pal *et al.*, 2004). For silica fibres, the

thermo-optic effect is the dominant factor accounting for approximately 95% of the observed shift in the Bragg wavelength. Thus equation 4.3 can be rewritten by substituting for α and ξ as

$$\Delta\lambda_B = \left[\left(\frac{\partial\Lambda}{\partial T}\Big/\Lambda\right)+\left(\frac{\partial n_{eff}}{\partial T}\Big/n_{eff}\right)\right]\lambda_B\Delta T\,. \tag{4.4}$$

Therefore if a FBG sensor is subjected simultaneously to both strain and temperature changes, the combined Bragg wavelength shift can be expressed as

$$\Delta\lambda_B = \left[(1-p_e)\varepsilon+(\alpha+\xi)\Delta T\right]\lambda_B\,. \tag{4.5}$$

Thus the Bragg wavelength shift can be rewritten using the above defined variables as

$$\Delta\lambda_B = \left(\left\{1-\left(\frac{n_{eff}^2}{2}\right)\left[p_{12}-\nu(p_{11}+p_{12})\right]\right\}\varepsilon+\left[\left(\frac{\partial\Lambda}{\partial T}\Big/\Lambda\right)+\left(\frac{\partial n_{eff}}{\partial T}\Big/n_{eff}\right)\right]\Delta T\right)\lambda_B\,. \tag{4.6}$$

Table 4.1 shows some typical values of strain ($\frac{\partial\lambda_B}{\partial\varepsilon}$) and temperature ($\frac{\partial\lambda_B}{\partial T}$) sensitivities of a FBG at different operating wavelengths for silica fibres at room temperature (Rao, 1997).

Wavelength (nm)	**Strain Sensitivity (pm/με)**	**Temperature Sensitivity (pm/°C)**
830	0.64	6.8
1300	1.0	10
1550	1.2	13

Table 4.1 Typical values of strain (pm/με: picometres per microstrain) and temperature (pm/℃: picometres per degrees Celsius) sensitivities of FBG sensors at different operating wavelength for silica fibres (Rao, 1997).

4.3 Temperature Calibration of Chirped Fibre Bragg Gratings

The reflectance spectra of the fibre Bragg gratings were measured with an Er^{3+}dual-band broadband (EBS-7210) light source via a 3 dB 1550 nm ETEK 70070902 coupler. The reflected spectra from the grating were measured through the other input port using an optical spectrum analyser (OSA) with a resolution of 0.1 nm and saved on a computer via the GPIB interface port similar to figure 4.2.

4.3.1 Annealing of the gratings

The thermal stability of FBGs at elevated temperatures are of significant importance in sensing applications. Gratings fabricated in hydrogenated fibres have been shown to have a rapid initial decay in index modulation within the first hour. These gratings are thus less stable compared to gratings fabricated in non-hydrogenated fibres, pre-UV irradiated fibres (Guan *et al.,* 2000), and UV-presensitized hydrogen-outdiffused fibres (Aslund *et al.,* 2000).

Regardless of the form of pre-treatment of a fibre to enhance its photosensitivity prior to grating fabrication, thermal decay normally occurs over time. The mechanisms for thermal decay of gratings fabricated in hydrogen-loaded germanosilicate fibres are well documented (Kannan *et al.,* 1997) and modelled to predict the lifetime of the gratings (Erdogan *et al.,* 1994). One such mechanism states that formation of gratings involves the excitation of the glass to a metastable state. That is, the electrons excited by UV light during the fabrication process are trapped to a broad energy distribution of trap states (Kannan *et al.,* 1997, Erdogan *et al.,* 1994). Associated with these states is a distribution of activation energy barriers which need to be overcome for the index modulation to decay. Thus, when a defect site is able to overcome its activation energy barrier with thermal help, the contribution of the site to the UV-induced refractive index modulation (Δn) is lost and the grating decays. The thermal detrapping is a function of trap activation energy depth. Sites with low activation energies decay faster than sites with high activation energies. A number of models have been developed to predict the thermal decay of gratings over the lifetime. These include the mathematical power-law

and the experimental accelerated aging curve approach (Erdogan *et al.,* 1994) and a log-time model (Baker *et al.,* 1997).

Thus to remove these thermally reversible processes responsible for decay in refractive index modulation, the gratings were annealed to out-diffuse excess hydrogen and to ensure improved stability and repeatability of measurements during sensing. Gratings were annealed for 150 s at 330 °C by placing them against a slot in an aluminium plate. Annealing resulted in a decrease in the power reflectance of the grating by approximately 10% and a blue-shift in the Bragg reflection wavelength of the chirped gratings. Annealing stabilises the thermal stability of the gratings by removing the contribution to index modulation of defect centres that are not stable. Thus the final index modulation after annealing is more stable and will not decay further on application of elevated temperatures and with time by more than 0.1% (Aslund *et al.,* 2000). Therefore the reflectance and transmission spectra of the grating will be more stable and the Bragg wavelength shifts during sensing applications will be true indicative of the physical quantity being measured.

4.3.2 Normalisation of reflectance spectra

The reflection spectrum data, $R(\lambda)$, were normalised to 14.6 dB above an average measured reflection spectrum of an FC/PC connector, through the coupler. The FC/PC connector located in place of the grating provided a spectrally flat Fresnel reflection of -14.6 dB from the glass-air surface. The glass-air reflectivity for a SMF-28 fibre can be calculated using equation 4.7.

$$R = \frac{\left(n_{eff} - 1\right)^2}{\left(n_{eff} + 1\right)^2} \cong \frac{\left(1.445 - 1\right)^2}{\left(1.445 + 1\right)^2} \cong 0.0331 \cong -14.6\,\text{dB} \qquad 4.7$$

Thus a curve 14.6 dB above the measured $R(\lambda)$ of an FC/PC connector is that expected of a 100% reflector. This curve, shown in figure 4.1, was used to normalize the measured reflected spectra data, $R(\lambda)$, from the gratings. The power level of this curve was found to be close to the reflected power level from the 3 dB coupler.

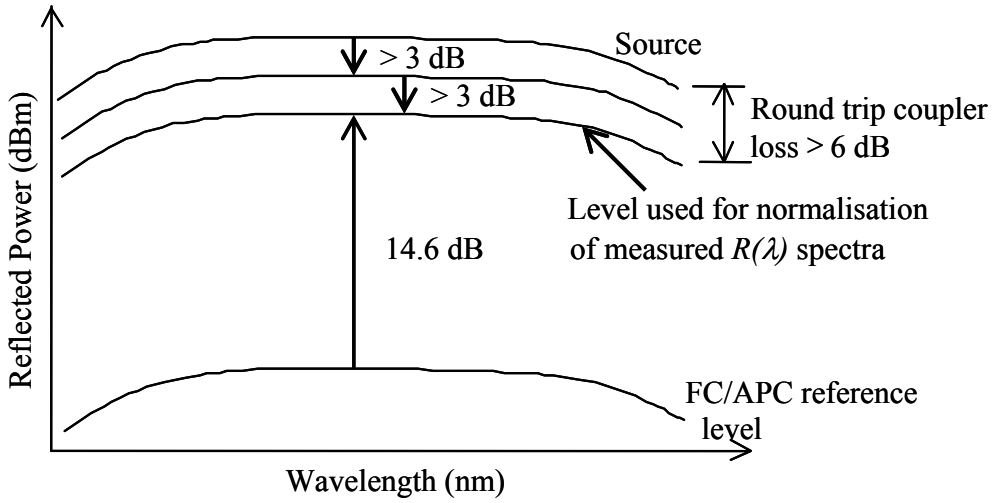

Figure 4.1 Normalisation of the reflectance spectra of the gratings.

4.3.3 Temperature calibration technique

After fabrication and annealing of the gratings, the temperature sensitivities of the gratings at elevated temperatures were obtained. The thermal charaterisation of the Bragg wavelength of the chirped gratings were performed by placing the sample gratings in the central temperature-stabilised region of a calibrated carbolite tube oven. The variation in the temperature output of the oven was approximately 2 °C at 150 °C within the 20 cm length of the central region. The temperature of the oven during the calibration process was verified by a K-type thermocouple located alongside the CFBG.

The temperature dependence of the Bragg wavelength was measured using the experimental arrangement shown in figure 4.2. The parameters of the nine gratings (F-N) selected, fabricated in hydrogen loaded standard telecommunications Corning SMF-28 fibre, are listed in table 4.2 presented at the end of section 4.3. The CFBGs, (L-N) are representative samples of gratings used for the position and strain measurements reported in chapters 5 and 6 respectively. The temperature and strain sensitivities of gratings (A-E) and (O-Q) are listed in tables 5.1 and 6.1 respectively.

The gratings were monitored in reflection as shown in figure 4.2. The unused port was properly terminated to suppress reflections that could introduce interference signals.

Reflection spectra from the gratings were measured using an optical spectrum analyser (OSA) with a resolution of 0.1 nm and saved on a computer via the GPIB interface. Ten measurements were taken at each temperature, both for increasing and decreasing temperature cycles. Each repeat measurement was obtained by averaging 50 OSA measurements. The Bragg wavelength shifts at each temperature were observed to be quite consistent over the repeated measurements with a wavelength uncertainty of ±0.01 nm at the OSA resolution used. A settling time of approximately 15 min was allowed at each temperature to achieve a thermal equilibrium between the gratings and the oven before measurements. The reflection spectrum data, $R(\lambda)$, were normalized as described in section 4.3.2, and the average Bragg wavelength shift calculated at each temperature.

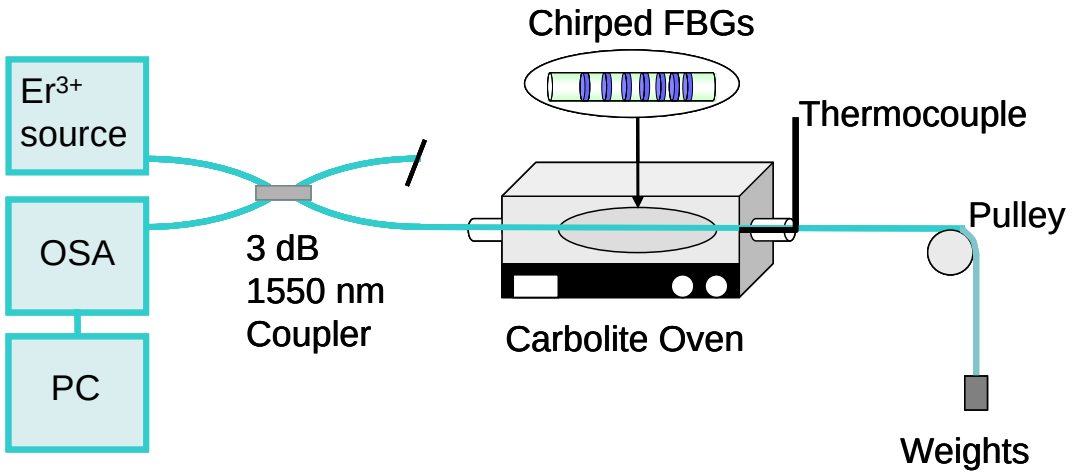

Figure 4.2 Schematic diagram of the experimental arrangement for temperature and strain calibration of sensors.

4.3.4 CFBG spectra analysis

The simplest means of analysing the Bragg wavelength shift due to a measurand is referred to as the 'minima' method that, depending on the sensor design, analyses the transmitted or reflected FBG spectrum by determining the minimum or maximum intensity, respectively (Trpkovski *et al.,* 2005). This method, however, is susceptible to resolution limitations and signal noise. Furthermore it involves extracting a single intensity with its corresponding wavelength, which is unsuitable for the linearly chirped gratings with broadband spectra, investigated in this work.

Thus for this work, the Bragg wavelength shift was determined using the half-maximum (HM) method. This technique initially normalizes the FBG spectrum before identifying the maximum reflected intensity. The half maximum (HM) intensity (50% of the nomalised reflected intensity) is used as a threshold and compared with values from the array of normalised reflected intensities. The two HM intensities are obtained from either side of the array of normalised reflected intensities. These two HM intensity values are then used as an index to interpolate for their corresponding wavelengths from an array of wavelength values and the central Bragg wavelength is calculated as

$$\lambda_B = \frac{\lambda_L + \lambda_R}{2}, \tag{4.8}$$

where λ_L and λ_R are the wavelengths corresponding to the HM intensities at the left and right hand side of the CFBG spectra. This method is more accurate as it uses two measurements of wavelengths to calculate the Bragg wavelength shift.

4.3.5 Temperature calibration of standard FBGs (Prism technique)

In this section, the temperature responses of standard fibre Bragg gratings fabricated with the prism technique are presented. In figure 4.3, the centre Bragg wavelength is plotted as a function of temperature for grating F. The dotted line on the graph represents a linear fit to the experimental data whereas the solid line represents the best higher order polynomial fit. The temperature response of the Bragg wavelength using a linear fit to data can be expressed as

$$\lambda_B(T) = 0.00985T + 1553.80 \tag{4.9}$$

where λ_B is the corresponding Bragg wavelength (nm) at temperature, T (°C). From the derivative ($\frac{\partial \lambda_B}{\partial T}$) of equation 4.9, the thermal sensitivity of the grating is 9.85 pm/°C.

The temperature response of the Bragg wavelength using the best polynomial (2nd order) regression is

$$\lambda_B(T) = 6.0 \times 10^{-6} T^2 + 0.00795T + 1553.89, \tag{4.10}$$

where λ_B is the corresponding Bragg wavelength (nm) at temperature, T (°C). The second order polynomial (figure 4.3) provides a good fit to experimental data over the whole measurement range. The coefficients of determination (r^2), used to evaluate the quality of regression, was 0.999958 which was better than the linear fit value of 0.997746. From the derivative of equation 4.10, the temperature sensitivity of the grating is observed to be a function of temperature and varies from 8.21 pm/°C at room temperature of 22 °C to 11.55 pm/°C at 300 °C.

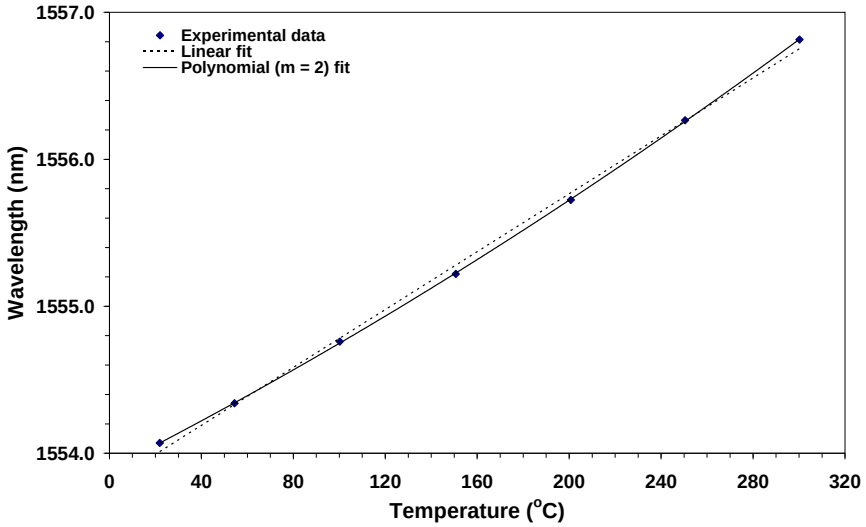

Figure 4.3 Central Bragg wavelength vs. temperature for grating F showing linear and best fitted polynomial regression to the experimental data.

Figure 4.4 is a plot of residual wavelengths for both the linear and polynomial fits over the temperature range investigated. It can be observed that the deviation of linear regression from data is dependent on measurement range and varies in a parabolic fashion over the measurement range. The rms error in the measurement with linear fit is 0.045 nm, which would lead to a significant error in temperature of 4.6 °C using thermal sensitivity obtained by using the linear fit. It can also be observed from figure 4.4, that the deviations from the measured experimental data over the entire experimental range are much smaller for the polynomial fit. The rms error is less than 0.006 nm for the polynomial fit. This would result in an rms temperature error of less than 0.8 °C for temperatures in the range 0 to 300 °C which would be acceptable for this work involving position measurement of a localised heat source. Results for other prism gratings are summarised in table 4.2.

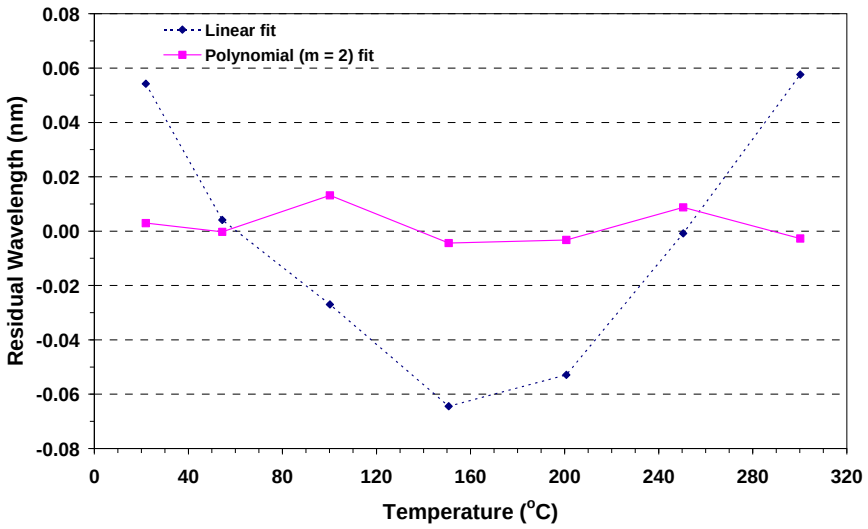

Figure 4.4 Comparison of the residual wavelengths for linear and the best polynomial fit with temperature for grating F.

4.3.6 Temperature calibration of standard FBGs (Phase mask technique)

This section reports the results of temperature calibrations of standard FBGs fabricated with the phase mask technique. In figure 4.5, the centre Bragg wavelength is plotted as a function of temperature for grating I. The dotted line on the graph represents a linear fit to experimental data whereas the solid line represents the best higher order polynomial fit. The temperature response of the Bragg wavelength using linear and best polynomial regression is given by equations (4.11) and (4.12), respectively, as

$$\lambda_B(T) = 0.00987T + 1541.37\,, \tag{4.11}$$

$$\lambda_B(T) = 6.0\times10^{-6}T^2 + 0.00795T + 1541.47\,, \tag{4.12}$$

where λ_B is the corresponding Bragg wavelength (nm) at temperature, T (°C). The (r^2) values were 0.997666 and 0.999928 for linear and polynomial fit respectively. The thermal sensitivity using a linear fit is 9.87 pm/°C and for the polynomial fit it is a function of temperature and varies from 8.21 pm/°C at room temperature of 22 °C to 11.55 pm/°C at 300 °C. These are consistent with those obtained for standard gratings with the prism technique.

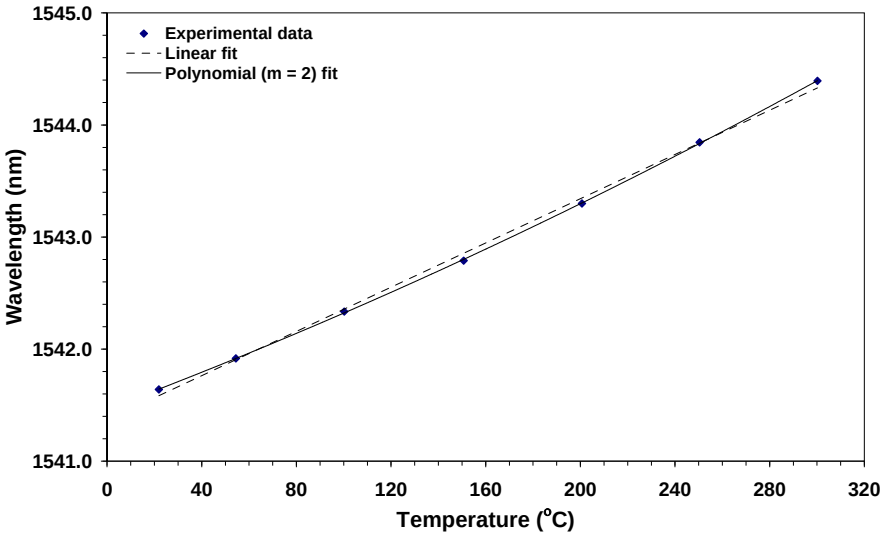

Figure 4.5 Central Bragg wavelength vs. temperature for grating I showing linear and best fitted polynomial regression to the experimental data.

Figure 4.6 is a plot of residual wavelengths for the linear and the polynomial fit to experimental data. The deviations are much smaller for the polynomial fit. The rms error in the measurement with a linear fit is 0.045 nm, which would lead to a significant error in temperature of 4.6 °C. The rms error in measurement with polynomial fit is less than 0.008 nm, which would result in an rms temperature error of less than 1.0 °C for temperatures in the range 0 to 300 °C. Results for other phase mask gratings are presented in table 4.2.

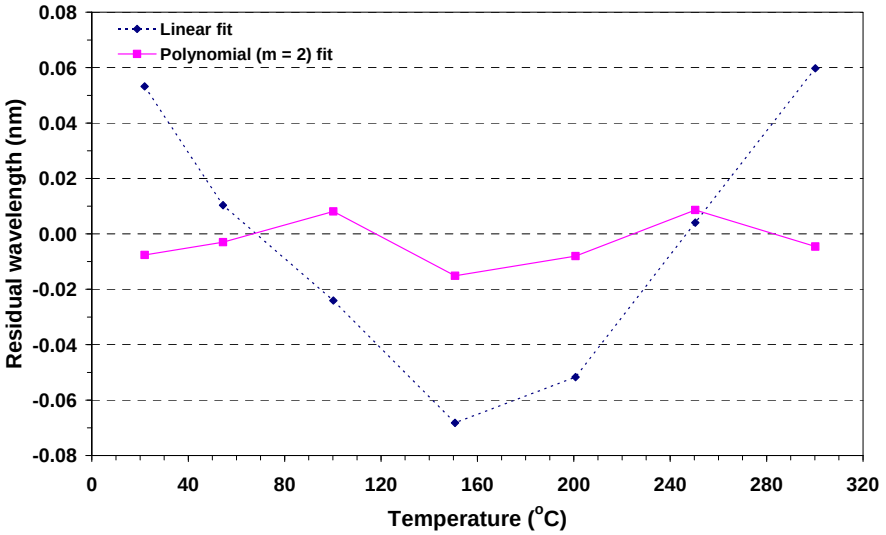

Figure 4.6 Comparison of the residual wavelengths for linear and the best polynomial fit with temperature for grating I.

4.3.7 Temperature calibration of CFBGs (Phase mask technique)

This section reports on the results of the temperature calibration of CFBGs fabricated with a linear chirped phase mask (centre pitch, Λ = 1.0665 μm, chirp rate = 20 nm/cm) using the scanning FBG fabrication system. Figure 4.7 shows the reflection spectra of grating *L* during temperature calibration.

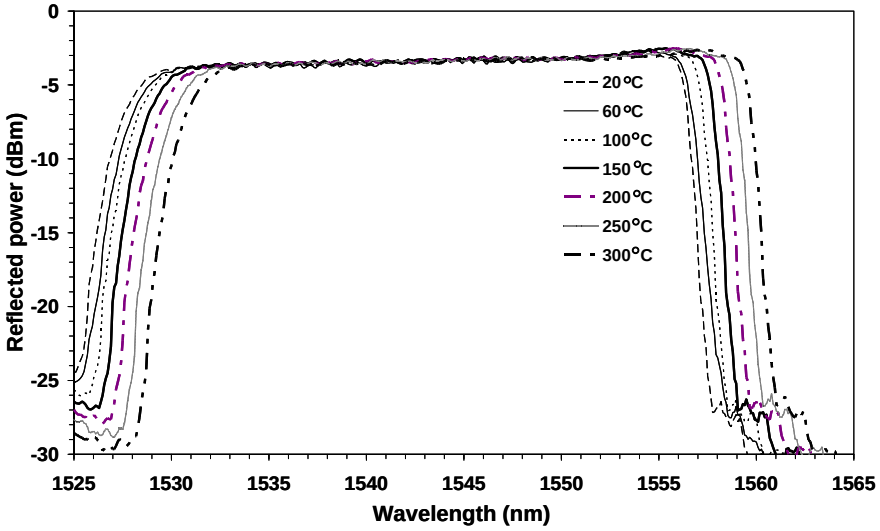

Figure 4.7 Temperature calibration spectra for chirped grating L.

In figure 4.8, the central Bragg wavelength is plotted as a function of temperature for grating *L*. The dotted line on the graph represents a linear fit to the data whereas the solid line represents the best higher order polynomial fit. The temperature response of the Bragg wavelength using linear and best polynomial regression can be expressed by equations 4.13 and 4.14, respectively, as

$$\lambda_B(T) = 0.01152T + 1541.27, \tag{4.13}$$

$$\lambda_B(T) = 8.5\times10^{-6}T^2 + 0.00882T + 1541.41, \tag{4.14}$$

where λ_B is the corresponding Bragg wavelength (nm) at temperature, T (°C). The (r^2) values were 0.996587 and 0.999926 for linear and polynomial fit, respectively. The thermal sensitivity using the linear fit was 11.52 pm/°C and for the polynomial fit, it is a function of temperature, and varies from 9.19 pm/°C at room temperature of 22 °C to 13.92 pm/°C at 300 °C. These values of the temperature coefficient are higher than those for standard FBGs, fabricated both with the prism and phase mask techniques.

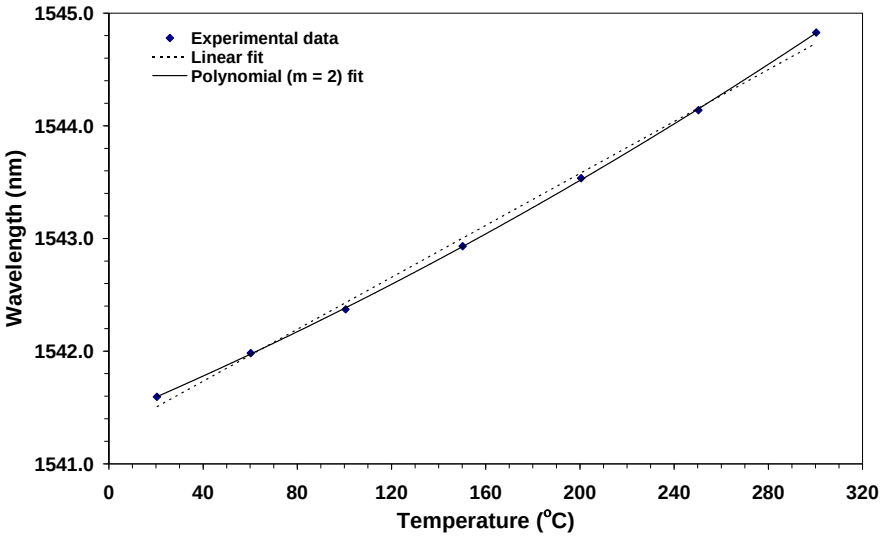

Figure 4.8 Central Bragg wavelength vs. temperature for chirped grating L showing linear and best fitted polynomial regression to the experimental data.

Figure 4.9 is a plot of residual wavelengths for the linear and polynomial fits to experimental data, showing much smaller deviations for the polynomial fit. The rms error with linear fit is 0.064 nm, which would lead to a temperature error of 5.6 °C. The rms error with polynomial fit is less than 0.010 nm, which would result in an rms temperature error of less than 1.1 °C for temperatures in the range 0° to 300 °C. A third order polynomial fit to data was also considered to ascertain if the rms error in the measurement could be further improved. This, however, did not improve the rms error. The results of other CFBGs are presented in table 4.2.

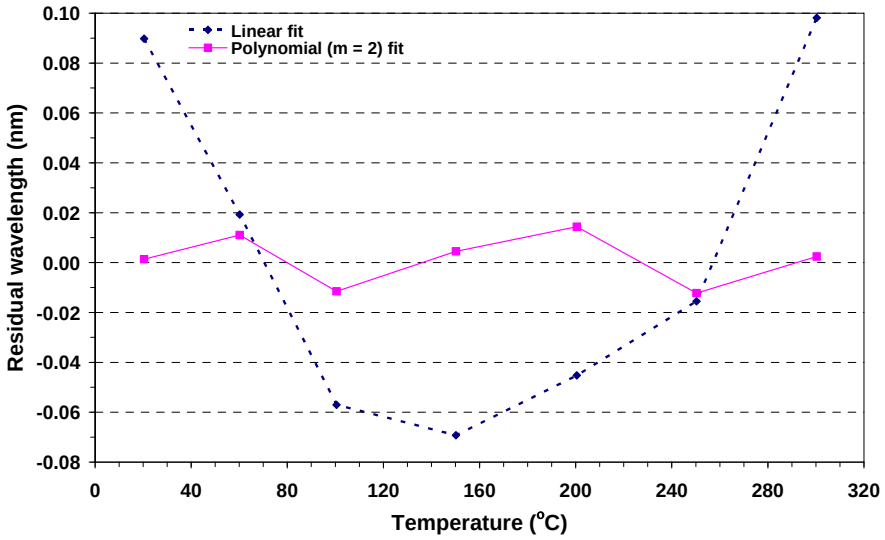

Figure 4.9 Comparison of the residual wavelengths for linear and the best polynomial fit with temperature for grating L.

	Prism			Phase mask					
	Standard FBGs			Standard FBGs			Chirped gratings		
	F	G	H	I	J	K	L	M	N
Central Bragg wavelength, λ_B, (nm)	1553.79	1551.81	1566.37	1541.37	1538.42	1542.84	1541.27	1541.27	1541.96
Reflectance (%)	80.5	78.5	82.5	84.5	85.6	84.8	33.2	40.5	30.8
FWHM bandwidth (± 0.1) nm	2.1	2.2	2.2	0.8	1.0	0.9	28.2	19.5	28.4
Temperature measurement range (°C)	22 -300	22-300	22-300	22-300	22-300	22-300	22-300	22-300	22-300
Best polynomial fit for regression	2^{nd} order	2^{nd} order	2^{nd} order	2^{nd} order	2^{nd} order	2^{nd} order	2^{nd} order	2^{nd} order	2^{nd} order
Temperature sensitivity linear fit (pm/°C)	9.85	9.89	9.92	9.87	9.82	9.84	11.52	11.59	11.68
Temperature sensitivity best polynomial fit at 22 °C (pm/°C)	8.21	8.22	8.19	8.21	8.18	8.19	9.19	9.47	9.29
Temperature sensitivity best polynomial fit at 300 °C (pm/°C)	11.55	11.50	11.58	11.55	11.57	11.47	13.92	13.70	13.96
RMS error in measurement with linear fit (nm)	0.045	0.048	0.052	0.045	0.051	0.046	0.064	0.055	0.059
RMS error in measurement with polynomial fit (nm)	0.006	0.007	0.006	0.009	0.008	0.010	0.010	0.011	0.011
RMS error in temperature with linear fit (°C)	4.6	4.9	5.2	4.6	5.2	4.7	5.6	4.8	5.1
RMS error in temperature with polynomial fit (°C)	0.7	0.9	0.7	1.1	1.0	1.2	1.1	1.2	1.2
Thermo-optic coefficient, ξ ($\times 10^{-6}$/°C) at 22 °C	4.894	4.907	4.839	4.936	4.927	4.918	5.573	5.754	5.635
Thermo-optic coefficient, ξ ($\times 10^{-6}$/°C) at 300 °C	7.043	7.021	7.003	7.103	7.131	7.044	8.642	8.499	8.663

Table 4.2 Summary of temperature sensitivities for standard FBGs fabricated with the prism and the phase mask techniques and CFBGs fabricated with the phase mask.

4.3.8 Summary of temperature sensitivities of the gratings

Table 4.2 shows that CFBGs show significantly (~20%) higher temperature sensitivities compared with standard FBGs fabricated both, with the prism and phase mask techniques, for both linear and polynomial fit (m = 2). Chirped gratings show an average temperature sensitivity of 11.55 pm/°C for the linear fit and approximately 9.25 pm/°C at room temperature and 13.90 pm/°C at 300 °C for the polynomial fit.

The temperature dependent thermal sensitivities of all gratings are illustrated in figure 4.10. It can be observed from figure 4.10, that thermal sensitivities of both standard and chirped Bragg gratings show linear dependence with temperature with chirped gratings

having significantly higher gradients. The curves for the individual standard FBGs are difficult to be distinguished from each other. The chirped gratings on the other hand show slight variation in thermal sensitivities with temperature. These variations are not significant within the limit of uncertainty, and could be attributed to grating parameters such as length, bandwidth, central resonance Bragg wavelength and reflectance. Thus, the higher thermal sensitivities of chirped gratings can be exploited in strain-independent temperature measurements, using a combination of a standard and a chirped grating written in the same fibre.

The temperature sensitivities obtained were used in Labview algorithms of FFT grating simulation models and disturbance function fitting algorithms for the determination of the centre position of a localised heat source for subsequent intragrating temperature measurements.

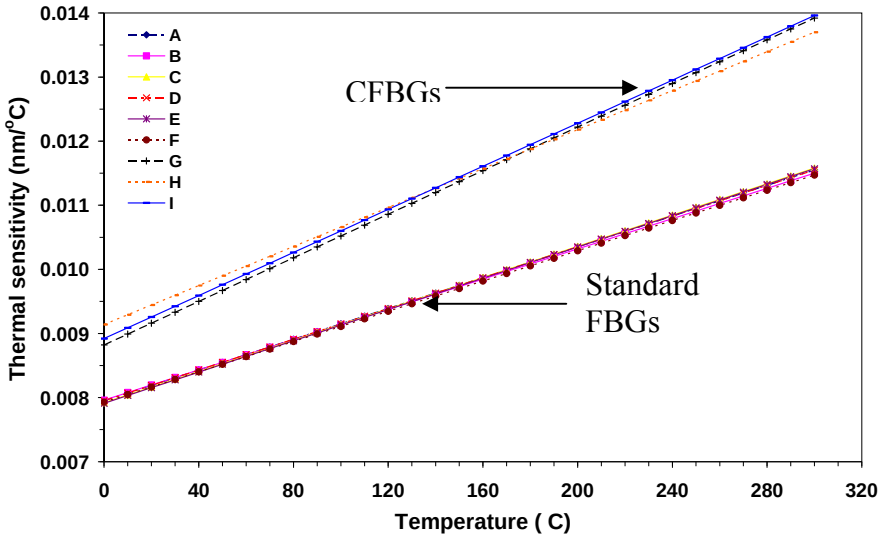

Figure 4.10 Dependence of thermal sensitivities of the gratings studied with temperature.

4.4 Strain Calibration of Chirped Fibre Bragg Gratings

4.4.1 Strain calibration technique

The strain characterization of CFBGs was performed using the experimental arrangement shown in figure 4.2. The dependence of the Bragg wavelength on strain ($\partial\lambda_B/\partial\varepsilon$) was measured using the standard technique of applying axial stress to the fibre by hanging weights (mg) to a fibre and monitoring the Bragg wavelength shift. The strain (ε) was calculated from the presumed values of the cross-sectional area (A) and Young's modulus (Y) of the fibre as

$$\varepsilon = \frac{mg}{AY}. \qquad 4.15$$

The method of weights can only be used for fibres of known dimensions and composition, as optical fibre stress can only be calculated for these. The fibre cross-sectional area (πr^2) is generally presumed to be equal to 1.23×10^{-8} m^2, despite manufacturing tolerance for optical fibre radius of up to 1%, or 1 μm. The value of Young's modulus for the optical fibre requires knowledge of its composition, and mismatched internal residual stresses caused, for example, by expansion during photorefractive modification will alter the effect on the FBG of externally applied stress. The method of applying weights to a fibre is a more repeatable technique when compared to that of stretching a known length (l_0) of fibre and measuring the change in length (Δl) and calculating the strain as the ratio of ($\Delta l/l_0$).

Strain was applied to the fibres using weights of 0, 32, 57, 82, 107, 132, 157, 182 and 207 g. Strain application was taken through increasing and decreasing cycles to check the repeatability of the measurements. Ten measurements were taken at each load application, both for increasing and decreasing cycles, at an OSA average of 5 and software average of 10. The measurements were repeated at four different oven temperatures of 20, 50, 80 and 100 °C to assess the influence of temperature on strain calibration. The gratings were monitored in reflection using an OSA resolution of 0.1 nm as shown in figure 4.2 and the average Bragg wavelength shift at each load application was calculated. The Bragg wavelength shifts at each load application was

observed to be quite consistent over the repeated measurements with a wavelength uncertainty of ±0.01 nm at the OSA resolution used.

4.4.2 Strain calibration of standard FBGs (Prism technique)

In this section, the strain responses of standard fibre Bragg gratings fabricated with the prism technique are presented. In figure 4.11, the centre Bragg wavelength is plotted as a function of applied strain at four different temperatures for grating *F*. The figure shows that the Bragg wavelength is a linear function of applied strain; thus linear fits to experimental data at all temperatures were employed. The effect of temperature on the strain response of the Bragg wavelength (strain sensitivity) results in an offset in the y-intercept. The strain response of the Bragg wavelength can be expressed using linear regression at each temperature as

$$\lambda_B(\varepsilon) = 0.001179\varepsilon + 1554.07 \text{ at } T = 22\ ^\circ\text{C} \quad 4.16$$

$$\lambda_B(\varepsilon) = 0.001178\varepsilon + 1554.31 \text{ at } T = 50\ ^\circ\text{C} \quad 4.17$$

$$\lambda_B(\varepsilon) = 0.001165\varepsilon + 1554.56 \text{ at } T = 80\ ^\circ\text{C} \quad 4.18$$

$$\lambda_B(\varepsilon) = 0.001178\varepsilon + 1554.76 \text{ at } T = 100\ ^\circ\text{C} \quad 4.19$$

where λ_B is in nm and ε is in με. From derivatives of equations 4.16-4.19, the strain sensitivity of grating, *F*, was calculated to be approximately (1.18 ± 0.01) pm/με at all temperatures.

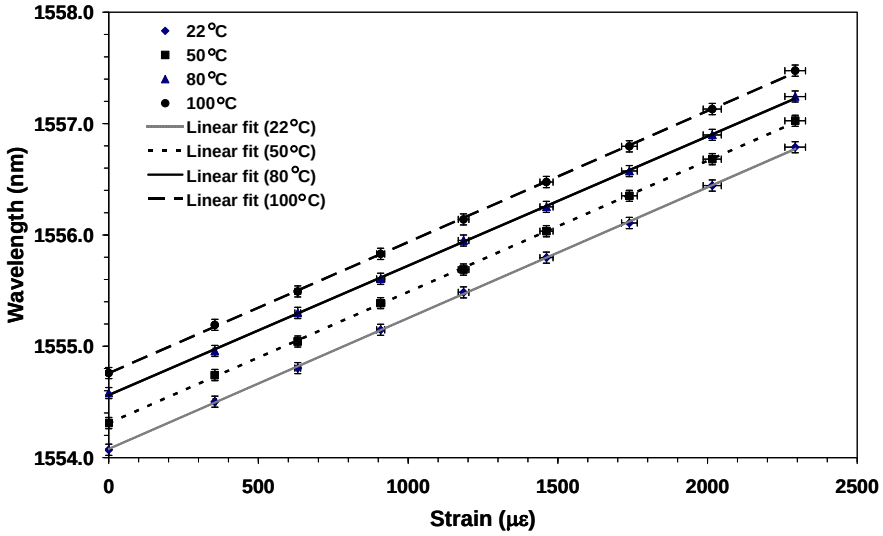

Figure 4.11 Central Bragg wavelength vs. applied strain for grating F showing the linear fit regression to the data at 4 temperatures.

In figure 4.12, residual wavelengths for the linear fit to experimental data are plotted for the four temperatures. It can be observed that the deviation from data varies between ± 0.02 nm over the whole strain measurement range. The rms error in Bragg wavelength measurements with linear fit is approximately 0.01 nm for strain calibration at all temperatures (table 4.3). This would result in rms strain errors of less than 10 με (table 4.3) over the measurement range which is equivalent to an applied force error of ±9 mN, which would be acceptable for most applications. The strain sensitivities of other prism gratings are presented in table 4.3.

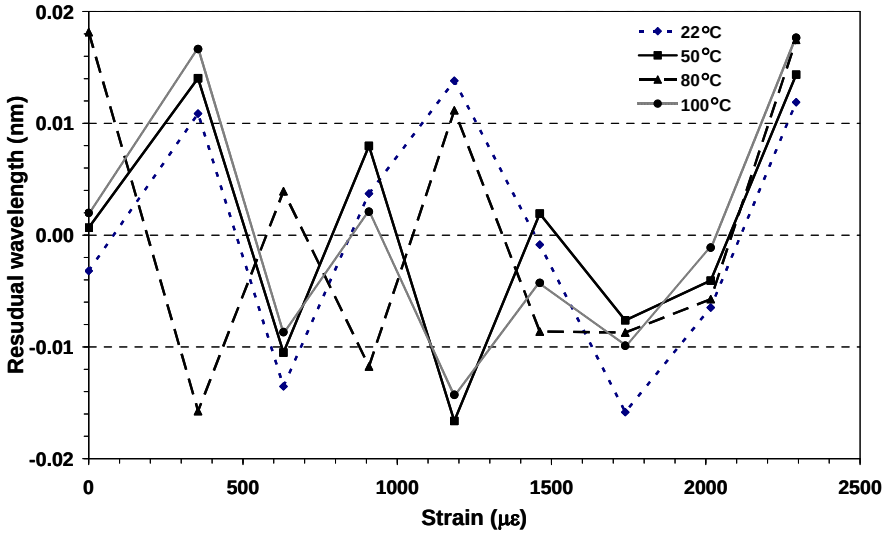

Figure 4.12 Comparison of the residual wavelengths for linear fit with applied strain at 4 temperatures for grating F.

Parameters	**Prism Gratings**											
	F				**G**				**H**			
	22 °C	50 °C	80 °C	100 °C	22 °C	50 °C	80 °C	100 °C	22 °C	50 °C	80 °C	100 °C
Strain sensitivity linear fit (pm/με)	1.179	1.178	1.165	1.178	1.175	1.169	1.177	1.175	1.174	1.179	1.168	1.172
RMS error in measurement with linear fit (nm)	0.0103	0.0102	0.0111	0.0105	0.0104	0.0102	0.0109	0.0098	0.0095	0.0102	0.0108	0.0102
RMS error in strain with linear fit (με)	8.7	8.7	9.5	8.9	8.8	8.7	9.3	8.3	8.1	8.7	9.3	8.7

Table 4.3 Summary of strain sensitivities for standard FBGs fabricated with the prism technique

4.4.3 Strain calibration of standard FBGs (Phase mask technique)

This section reports on the strain calibration of standard fibre Bragg gratings fabricated with the phase mask technique. In figure 4.13, the centre Bragg wavelength is plotted as a function of applied strain at four different temperatures for grating *I*. Linear fits to experimental data at all temperatures were considered. The strain response of the Bragg wavelength can be expressed using linear regression as

$$\lambda_B(\varepsilon) = 0.001177\varepsilon + 1541.64 \quad \text{at } T = 22\ ^\circ\text{C} \tag{4.20}$$

$$\lambda_B(\varepsilon) = 0.001179\varepsilon + 1541.91 \quad \text{at } T = 50\ ^\circ\text{C} \tag{4.21}$$

$$\lambda_B(\varepsilon) = 0.001166\varepsilon + 1542.17 \quad \text{at } T = 80\ ^\circ\text{C} \tag{4.22}$$

$$\lambda_B(\varepsilon) = 0.001177\varepsilon + 1542.33 \quad \text{at } T = 100\ ^\circ\text{C} \tag{4.23}$$

where λ_B is in nm and ε is in με. From derivatives of equations 4.20-4.23, the strain sensitivity of phase mask grating, *I*, was calculated to be approximately (1.18 ± 0.01) pm/με, at all temperatures. The calculated strain sensitivity is consistent with that of gratings fabricated with the prism technique.

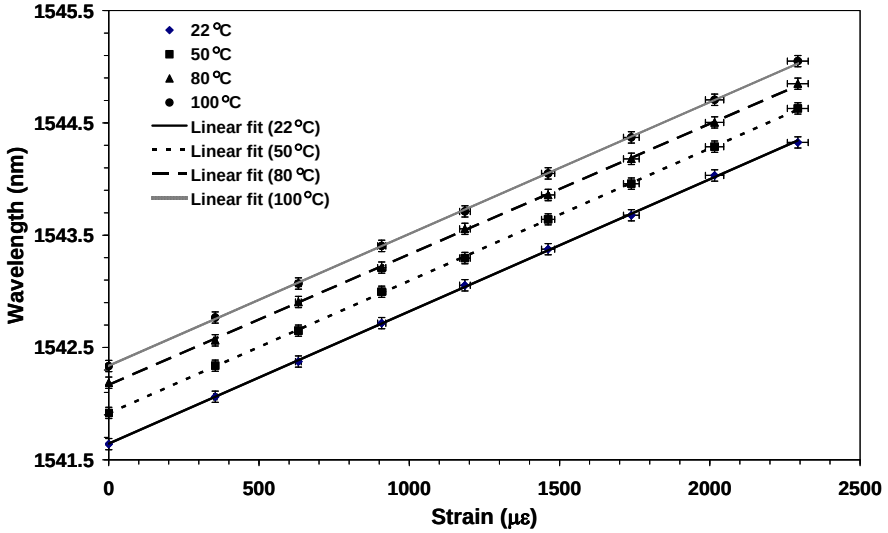

Figure 4.13 Central Bragg wavelength vs. applied strain for grating I showing linear fit regression to the experimental data at 4 temperatures

In figure 4.14, residual wavelengths from linear fit to experimental data are plotted for all four temperatures. It can be observed that the deviation from data varies between ±0.02 nm over the entire strain measurement range. The rms error in Bragg wavelength

measurements with linear fit is approximately 0.01 nm for strain calibrations at all temperatures (table 4.4). This would result in rms strain error of less than 10 με (table 4.4) over the measurement range which is equivalent to an applied force error of ±9 mN. The strain sensitivities of other phase mask gratings are listed in table 4.4.

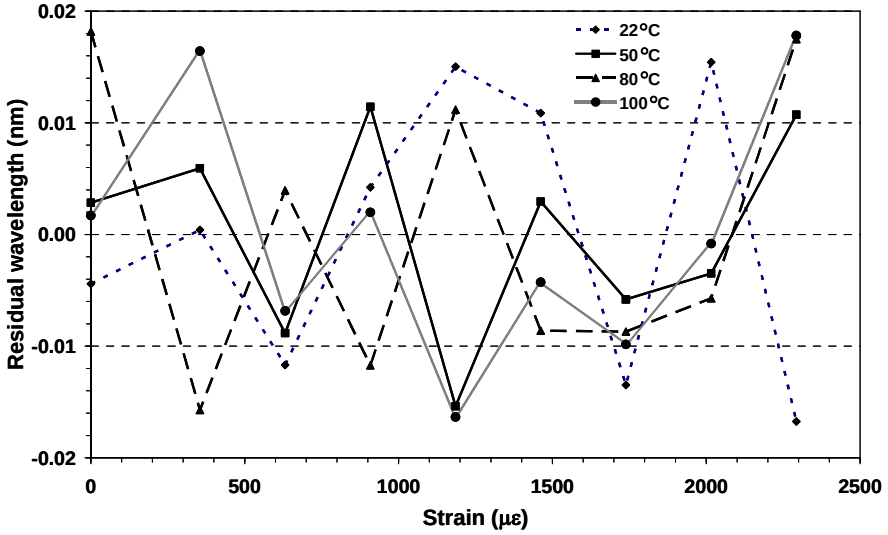

Figure 4.14 Comparison of the residual wavelengths for linear fit with applied strain at 4 temperatures for grating I.

Parameters	**Phase Mask Gratings**											
	I				**J**				**K**			
	22 °C	50 °C	80 °C	100 °C	22 °C	50 °C	80 °C	100 °C	22 °C	50 °C	80 °C	100 °C
Strain sensitivity linear fit (pm/με)	1.177	1.179	1.166	1.177	1.178	1.168	1.179	1.175	1.175	1.179	1.167	1.172
RMS error in measurement with linear fit (nm)	0.0116	0.0086	0.0116	0.0107	0.0108	0.0114	0.0109	0.0089	0.0099	0.0108	0.0112	0.0101
RMS error in strain with linear fit (με)	9.9	7.3	9.9	9.1	9.2	9.8	9.3	7.6	8.4	9.2	9.6	8.6

Table 4.4 Summary of strain sensitivities for standard FBGs fabricated with the phase mask technique.

4.4.4 Strain calibration of CFBGs (Phase mask technique)

This section reports on the results of the strain response of CFBGs fabricated with a linear chirped phase mask (centre pitch, Λ = 1.0665 μm, chirp rate = 20 nm/cm) using the scanning FBG fabrication system. Figure 4.15 shows the strain calibration reflection spectra for the chirped grating, *M*, at a temperature of 100 °C.

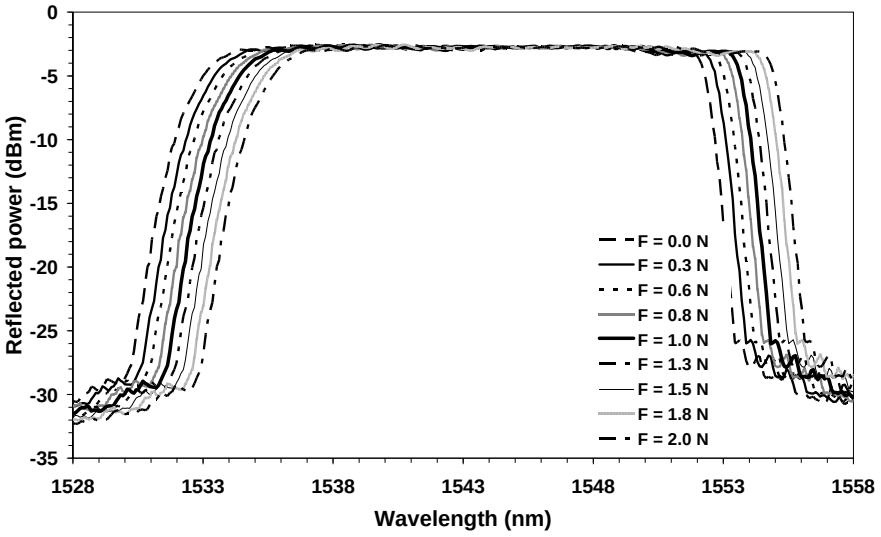

Figure 4.15 Strain calibration spectra for chirped grating M at 100℃.

In figure 4.16, the central Bragg wavelength is plotted as a function of applied strain at four temperatures. Linear fits to experimental data at all temperatures using linear regression resulted in

$$\lambda_B(\varepsilon) = 0.001179\varepsilon + 1541.38 \quad \text{at } T = 22\ ^\circ\text{C} \tag{4.24}$$

$$\lambda_B(\varepsilon) = 0.001177\varepsilon + 1541.64 \quad \text{at } T = 50\ ^\circ\text{C} \tag{4.25}$$

$$\lambda_B(\varepsilon) = 0.001167\varepsilon + 1542.01 \quad \text{at } T = 80\ ^\circ\text{C} \tag{4.26}$$

$$\lambda_B(\varepsilon) = 0.001179\varepsilon + 1542.15 \quad \text{at } T = 100\ ^\circ\text{C}, \tag{4.27}$$

where λ_B is in nm and ε is in με. From the derivatives of equations 4.24-4.27, the strain sensitivity of chirped grating, *M*, was calculated to be approximately (1.18 ± 0.01) pm/με at all temperatures. This is consistent with the strain sensitivities obtained for the standard FBGs fabricated with both the prism and the phase mask techniques.

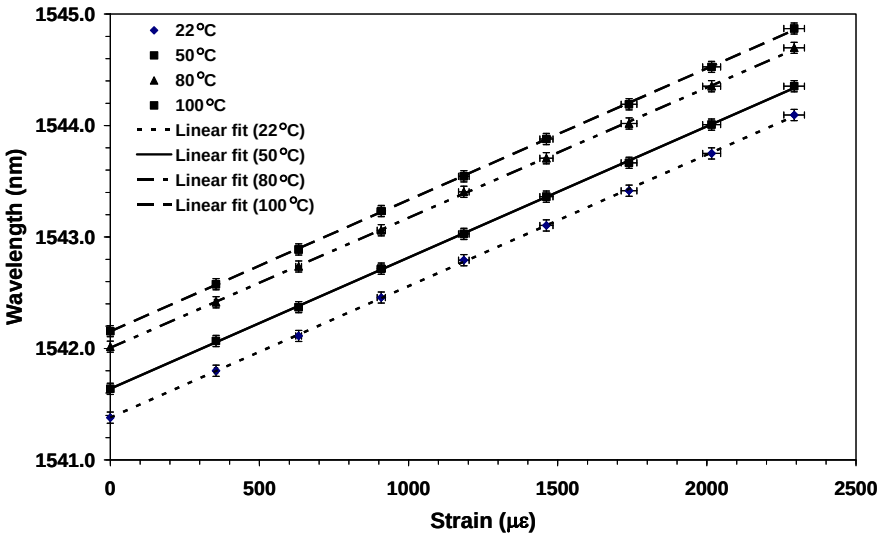

Figure 4.16 Central Bragg wavelength vs. applied strain for grating M showing the linear regression fits to the data at 4 temperatures.

In figure 4.17, residual wavelengths from linear fit to experimental data are plotted for all four temperatures. It can be observed that the deviation from data varies between ±0.02 nm over the entire strain measurement range. The rms error in Bragg wavelength measurements with the linear fit is about 0.01 nm for strain calibrations at all temperatures (table 4.5). This would result in rms strain error of less than 10 με (table 4.5) over the strain measurement range which is equivalent to an applied force error of ±9 mN. The strain sensitivities of other CFBGs are presented in table 4.5.

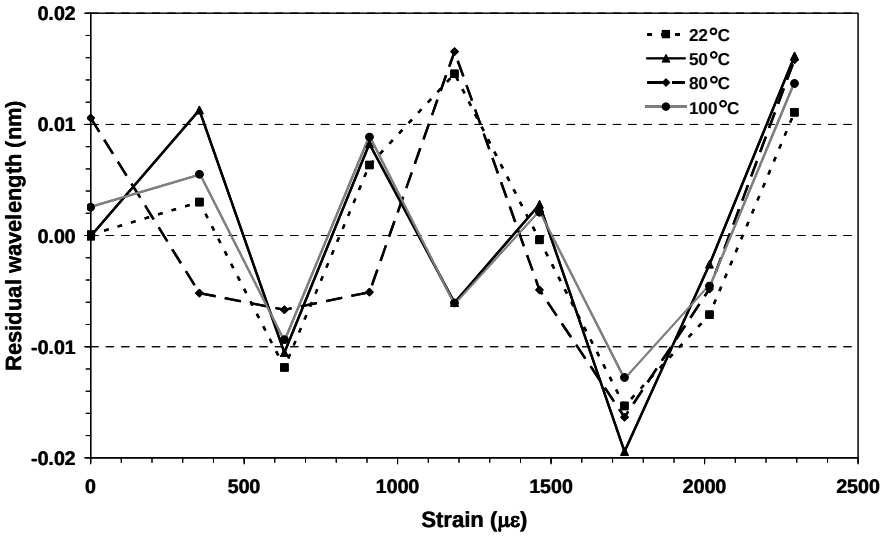

Figure 4.17 Comparison of the residual wavelengths for linear fit with applied strain at 4 temperatures for chirped grating M.

Parameters	Chirped Phase Mask Gratings											
	L				M				N			
	22 °C	50 °C	80 °C	100 °C	22 °C	50 °C	80 °C	100 °C	22 °C	50 °C	80 °C	100 °C
Strain sensitivity linear fit (pm/με)	1.179	1.181	1.168	1.175	1.179	1.177	1.167	1.179	1.180	1.182	1.162	1.176
RMS error in measurement with linear fit (nm)	0.0114	0.0093	0.0108	0.0110	0.0095	0.0105	0.0107	0.0083	0.0109	0.0104	0.0104	0.0106
RMS error in strain with linear fit (με)	9.7	7.9	9.3	9.4	8.1	8.9	9.2	7.0	9.2	8.8	8.9	9.0

Table 4.5 Summary of strain sensitivities for CFBGs fabricated with the phase mask technique

4.5 Strain-Independent Temperature Measurement

The analyses of this chapter showed that CFBGs fabricated in hydrogenated plain telecommunications fibre have a temperature coefficient that is approximately 20% higher than standard FBGs in the 1550 nm region with similar strain coefficients. Thus the higher thermal coefficient of the chirped gratings over the wider temperature range (0-300 °C) can be exploited in strain-independent temperature measurements using a combination of a standard and a chirped grating written in the same fibre.

4.5.1 Introduction and background

Considerable research has been devoted to FBG sensors for measuring strain and temperature, particularly for smart structure applications. However the inherent response of FBG sensors to both strain and temperature has complicated independent measurement procedures for these two measurands. Several methods have been proposed and investigated to overcome the problem of cross sensitivity and are well documented (Trpkovski *et al.,* 2005).

Recently, schemes based on dual-grating sensors utilizing the dependence of both temperature and strain sensitivities on grating type have been reported (Shu *et al.,* 2002, Pal *et al.,* 2004 and Shu *et al.,* 2004). All these investigations have exploited the different temperature and similar strain sensitivities of well known grating types (type I, type IIA, type IA) to design sensors either for simultaneous measurement of strain and

temperature or strain-independent temperature measurements. The problem of cross-sensitivity has also been addressed by a number of investigations employing CFBGs. CFBGs have been reported for temperature-strain discrimination (Rao *et al.,* 2001, Frazao *et al.,* 2005, Cusano *et al.,* 2006) and temperature-independent strain sensing (Xu *et al.,* 1995, Kim *et al.,* 2000).

4.5.2 Theory

Most schemes for strain-temperature discrimination have assumed a linear approximation of the thermal and strain response of FBGs and used the matrix inversion analysis technique to determine the temperature and strain coefficients as described below (Xu *et al.,* 1994, Frazao *et al.,* 2005). The shift in Bragg wavelength of the grating ($\Delta\lambda_B$), due to a combined effect of strain and temperature can be expressed as

$$\Delta\lambda_B(\varepsilon, T) = K_\varepsilon \Delta\varepsilon + K_T \Delta T \tag{4.28}$$

where K_ε and K_T are the strain and temperature coefficients of the FBG. Therefore the shifts in the Bragg wavelengths of the two sensors, a standard FBG and a CFBG used for the measurements, can be expressed by a sensitivity matrix as

$$\begin{bmatrix} \Delta\lambda_1 \\ \Delta\lambda_2 \end{bmatrix} = \begin{bmatrix} K_{T1} & K_{\varepsilon 1} \\ K_{T2} & K_{\varepsilon 2} \end{bmatrix} \begin{bmatrix} \Delta T \\ \Delta\varepsilon \end{bmatrix}, \tag{4.29}$$

for the discrimination of temperature and strain. In equation 4.29 K_{T1}, $K_{\varepsilon 1}$ and K_{T2}, $K_{\varepsilon 2}$ are the temperature and strain coefficients of a standard and a CFBG respectively. The elements of the **K** matrix can be determined experimentally by separately measuring the changes in the Bragg wavelengths with temperature and strain for the two gratings. Thus by knowing **K**, the changes in temperature and strain can be determined by solving the following matrix equation, provided the matrix is well conditioned.

$$\begin{bmatrix} \Delta T \\ \Delta \varepsilon \end{bmatrix} = \frac{1}{K_{T1}K_{\varepsilon 2} - K_{T2}K_{\varepsilon 1}} \begin{bmatrix} K_{\varepsilon 2} & -K_{\varepsilon 1} \\ -K_{T2} & K_{T1} \end{bmatrix} \begin{bmatrix} \Delta\lambda_1 \\ \Delta\lambda_2 \end{bmatrix} \quad 4.30$$

Equation 4.30 can be further simplified for this application since $K_{\varepsilon 1}$ is approximately equal to $K_{\varepsilon 2}$ for the two gratings as experimentally verified. This would significantly reduce the signal processing required for decoupling the strain and temperature from the measurements of the sensors. The matrix inversion technique, however, may not be appropriate when wider temperature range is considered as reported in this work.

Thus the analysis technique proposed by Pal *et al.* (2004), which takes into account both the nonlinear thermal and linear strain response of the gratings, has been used to decouple the strain and temperature. In this approach, since the strain coefficients of the two gratings are assumed to be approximately the same, the strain independent temperature can be measured directly from the difference in temperature coefficients of the two gratings as

$$\lambda_{B1}(T) - \lambda_{B2}(T) = \sum_{j=0}^{m} K_{1jT} \cdot (T)^j - \sum_{j=0}^{m} K_{2jT} \cdot (T)^j \,, \quad 4.31$$

where λ_{B1} and λ_{B2} are the corresponding Bragg wavelengths of the two gratings, T is the applied temperature, K_{1jT} and K_{2jT} are the temperature coefficients of the two sensors considering the best order (m) nonlinear polynomial fit to the thermal response of the gratings.

4.5.3 Analysis

In this section the strain-independent temperature measurement is demonstrated using the results of two sensors presented above. For this purpose, the standard FBG, *I*, and CFBG, *L*, were selected. Figure 4.18 shows the variation of the central Bragg wavelength for two gratings as a function of temperature under zero axial strain plotted on the same graph. Shown on the graph are both the linear and the best higher order polynomial fit to the experimental data. The best polynomial (2^{nd} order) regression for the two gratings can be expressed as

$$\lambda_{BT1}(T) = 6.0\times10^{-6}T^2 + 0.00795T + 1541.47\,, \qquad 4.32a$$

$$\lambda_{BT2}(T) = 8.5\times10^{-6}T^2 + 0.00882T + 1541.41\,, \qquad 4.32b$$

where λ_{BT1} and λ_{BT2} are the corresponding Bragg wavelengths (nm) for the standard and CFBGs respectively at temperature, T (°C).

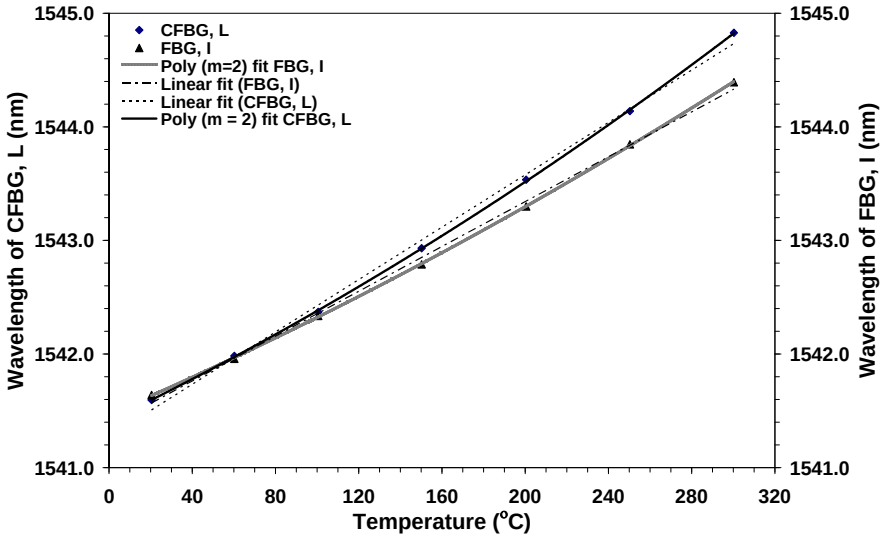

Figure 4.18 Central Bragg wavelength vs. applied temperature for the two gratings under zero axial strain. Solid lines represent the best fitted polynomial regression whereas the dotted lines represent the linear fit to the data.

Figure 4.19 shows the strain response of the above two gratings at two (22 and 100 °C) temperatures.

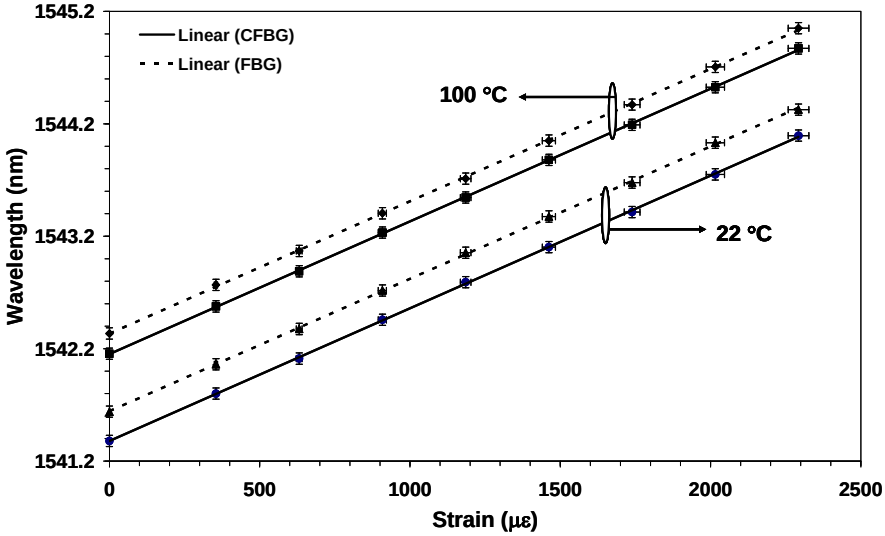

Figure 4.19 Central Bragg wavelength vs. applied strain for the two gratings at two temperatures. Solid lines represent linear fit regression to the data for the CFBG whereas the dotted lines represent that of the FBG.

Using linear regression, the variation of Bragg wavelength with applied strain for the two gratings at room temperature (22 °C) can be expressed as

$$\lambda_{B\varepsilon 1}(\varepsilon) = 0.001177\varepsilon + 1541.64 \text{ ,} \quad 4.33a$$

$$\lambda_{B\varepsilon 2}(\varepsilon) = 0.001179\varepsilon + 1541.38 \text{ ,} \quad 4.33b$$

where $\lambda_{B\varepsilon 1}$ and $\lambda_{B\varepsilon 2}$ are the corresponding Bragg wavelengths for the standard and the CFBG respectively at an applied strain, ε (με).

From above, where the strain coefficients of the two gratings have been experimentally verified to be exactly the same within limits of uncertainty (1.18 pm/με) over the measured temperature range, the strain-independent temperature can be obtained using the analysis technique (Pal *et al.,* 2004). This can be evaluated by subtracting (4.32a) from (4.32b). The resulting calibration equation can be expressed as

$$\Delta\lambda_B(T) = 2.5\times10^{-6}T^2 + 0.00087T - 0.06 \quad 4.34$$

From the derivative of equation 4.34, the temperature-dependent sensitivity for the measurement varies from 0.98 pm/°C to 2.37 pm/°C at 22 °C and 300 °C, respectively. The rms error in strain-independent temperature measurement was calculated to be 2.2 °C and 1.5 °C at 22 °C and 300 °C respectively.

This approach can also be used to for simultaneous measurement of strain and temperature. This could be achieved by first solving for temperature from equation 4.34 using the difference in Bragg wavelength shift due to temperature for the two sensors. Applied strain can then be evaluated from either set of equations (4.32a) and (4.33a) or (4.32b) and (4.33b) by eliminating the temperature effect from the total shift in Bragg wavelength for either one of the sensors. Alternatively, both strain and temperature can be obtained by substituting the strain and temperature coefficients determined experimentally into the conventional matrix equation 4.30.

4.6 Chapter Summary

The analysis of results showed that CFBGs have approximately 20% higher temperature coefficient than standard FBGs in the 1550 nm region, with similar strain coefficients, when a wider temperature range is considered. Second order polynomial regression was considered to fit experimental data for the thermal response of the Bragg wavelength and linear fits were used for strain responses of the Bragg wavelength for all gratings. Chirped gratings showed an average temperature sensitivity of 9.25 pm/°C at room temperature and 13.90 pm/°C at 300 °C. Standard FBGs showed an average temperature sensitivity of 8.20 pm/°C at room temperature and 11.50 pm/°C at 300 °C for both fabrication techniques. All gratings showed similar strain sensitivities around an average of 1.18 pm/με. This is as expected, since strain is an elastic property of the fibre resulting in uniform change in the grating pitch. The slight variation in strain sensitivities between FBGs, results from different resonance wavelengths of the gratings rather than from intrinsic material characteristics.

Based on the analysis, a simple technique for strain-independent temperature measurement is proposed using a sensor head with a combination of a standard and a CFBG. Strain-independent temperature measurement has been demonstrated over the temperature and strain range of 22 – 300 °C and 0 - 2500 με respectively. Temperature dependent sensitivity of 0.98 pm/°C and 2.37 pm/°C for strain-independent temperature measurement with rms errors of 2.2 °C and 1.5 °C at 22 °C and 300 °C, respectively has been obtained. Though the large bandwidth of the CFBG may constrain the multiplexing capabilities of the system, the signal processing and system calibration are nevertheless simple.

The underlying mechanisms responsible for the higher thermal sensitivity of the CFBGs need further investigation. This could be due to the formation of type IIA grating, however, this needs to be further verified under controlled experiments for gratings fabricated in other types of fibres.

CHAPTER 5

POSITION MEASUREMENT OF A LOCALISED HEAT SOURCE USING INTENSITY REFLECTION SPECTRUM BASED INTRAGRATING SENSING

5.1 Chapter Overview

This chapter begins by describing the design of a localised heat application (hot wire) apparatus together with experimental techniques employed for intragrating position measurements. The principle of operation of the sensor is then formulated and relevant equations developed. The effect of localised temperature on the local Bragg wavelength and reflectance spectra of chirped gratings is then modelled. It then describes the modelling of the temperature distribution, $T(z)$, using a range of disturbance functions together with the iterative approach employed in conjunction with the Fast Fourier Transform (FFT) grating reconstruction technique for solving the inverse problem of recovering the temperature distribution, due to localized heating, from the measured reflected power spectrum.

The fitting processes employed to fit the FFT simulated spectrum to the measured spectrum, using a three-parameter automatic disturbance function fitting algorithm operating on position, width and amplitude of temperature change to extract temperature distribution, $T(z)$, along the CFBG sensor, are then discussed in detail. The relative accuracy of the centre position of a localised temperature change within a CFBG is then investigated as a function of grating strength. The chapter concludes by assessing the dependence of the system performance on grating strength to optimise the precision and repeatability of the centre position measurements.

5.2 Introduction

Techniques for intragrating sensing based on conventional FBGs have had varying degree of success (LeBlanc *et al.,* 1996, Huang *et al.,* 1995, 1995, 1996, Volanthen *et al.,* 1996, 1997 and Ohn *et al.,* 1997). One way to overcome problems associated with conventional FBGs is to use chirped fibre Bragg gratings (CFBGs). For a chirped grating, each wavelength in the reflected intensity spectrum corresponds to a particular (local) position along the grating. Thus a change or modification in the reflected intensity spectrum due to a measurand can be directly related to a local position along the grating and hence the spatial distribution of the measurand can be determined. CFBGs with a broadband spectrum also provide a high sensitivity range to monitor extreme values of strain and the spatial distribution of these along the grating.

For example they have been used to extract nonuniform temperature profiles along a grating (Kersey *et al.,* 1997, Won *et al.,* 2004, Nand *et al.,* 2005b). They have also been demonstrated as position-dependent pressure sensors in monitoring esophageal pressures (Swart *et al.,* 2005) and as intra-grating sensors for determining the position of a localised heat source (Nand *et al.,* 2005c, 2006) as well as the measurement of temperature gradient (Kitcher *et al.,* 2006). The chirp rate and reflectance within the CFBG will affect its performance such as precision and spatial resolution. A low chirp rate of 0.77 nm/cm and reflectance of approximately 70% resulted in the disturbance producing internal Fabry-Perot cavities (Won *et al.,* 2004). Chirped gratings enable non-monotonic field profiles and peak localised strain and temperature to be measured and also increase the spatial resolution of the measurement as given by equation 2.8. The resolution will be improved when the Bragg wavelength is changing more rapidly with position (Bragg wavelength gradient) due to either an initial chirp in the grating or an applied strain/temperature gradient or both if the gradient is not large enough to cancel the initial chirp (Kersey *et al.,* 1997).

Improved capabilities to detect localised temperature (hotspots) and strain gradients (near attachment points, cracks or stress concentrations) and the distribution of these along the length of the grating with better spatial resolution are of great interest for structural health monitoring. Identification of conditions within a structure prior to the occurrence of structural failure prolongs its life and reduces the cost of repair.

This chapter reports on the precision of position determination, extracted from the reflected power spectrum when a nonuniform temperature distribution is applied to CFBGs of much greater chirp rate and lower reflectances than other comparable measurements (Won *et al.,* 2004, Swart *et al.,* 2005). A localised temperature disturbance (heat source) was applied sequentially to every 0.05 mm position along the grating length, z. The measured reflected intensity spectrum, $R(\lambda)$, of the CFBG was simulated by the FFT grating design model operating on the reference spectrum and hypothesis temperature distributions, $T(z)$. The spectrum generated from the FFT model was fitted to the measured spectrum employing the three-parameter fitting of the centre position, width and amplitude of the temperature change to extract the temperature distribution, $T(z)$, along the grating length, z. The precision of the inferred centre position of the localised heat source as a function of varying levels of grating reflectance was investigated.

5.3. Experimental Techniques

5.3.1 Grating fabrication

CFBGs used for this investigation were fabricated in hydrogen-loaded standard Corning SMF-28 telecommunications fibre with a linear chirped phase mask using the Swinburne scanning FBG fabrication system described in chapter 3. The phase mask had a centre pitch Λ = 1.0665 μm and chirp rate ($d\lambda/dz$) = 20 nm/cm. The fibres were hydrogen loaded at approximately 100 atm at 50 °C for 9 days. Stripped sections of fibres were exposed with a CW beam from a 244 nm frequency doubled argon-ion laser operating at approximately 240 mW. A dither function was used to flatten the average refractive index along the grating length and to apply controlled apodisation to remove ripples at the ends of the grating spectrum. The phase mask was linearly chirped at 20 nm/cm to vary the local Bragg wavelength along the length of the grating. Variable scan rates were used to control the exposure and hence fabricate gratings with a range of peak reflectance values. Grating strengths targeted were in the range 10 to 50% after annealing at 150 s at 330 °C. Table 5.1 shows the scan rates used, measured peak reflectance, approximate reflection bandwidths together with temperature and strain sensitivities of the gratings. A total of five linearly chirped gratings of approximate

length 15 mm were fabricated to examine the dependence of intra-grating sensor accuracy on grating strength. The reflection spectrum, $R(\lambda)$, data were normalised to 14.6 dB above an average measured reflection spectrum of an FC/PC connector, through a 3 dB, 1550 nm ETEK 70070902 coupler, as described in section 4.3.2. The reflected 'reference' spectra of the gratings having approximate peak reflectance between of 6 and 53%, used for the position measurements of the localised heat source, are plotted in figure 5.1.

Sample	**Scan rate, (mm/s)**	**Peak reflectance (± 2%)**	**FWHM reflection bandwidth (± 0.5 nm)**	$\frac{\partial \lambda_B}{\partial T}$ **at 300 °C (pm/°C)**	$\frac{\partial \lambda_B}{\partial \varepsilon}$ **(pm/με)**
A	3.2	6	26.9	13.90	1.17
B	2.2	11	28.1	13.88	1.18
C	1.7	20	28.3	13.92	1.18
D	1.3	33	28.4	13.95	1.17
E	0.9	53	28.4	13.96	1.18

Table 5.1 Grating fabrication details including the scan rates, resultant reflection properties and temperature and strain sensitivities.

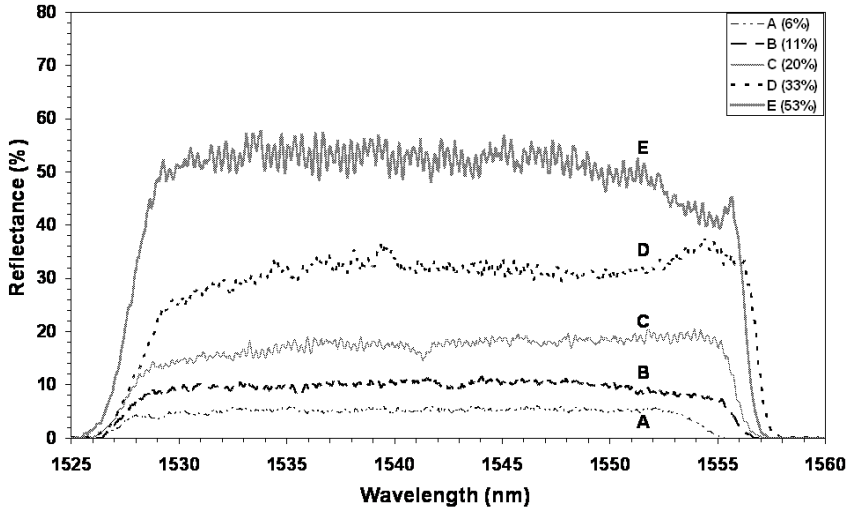

Figure 5.1 Reflection spectra of the gratings used for the position measurements.

5.3.2 Experimental arrangement

Figure 5.2 shows the "hot wire" experimental apparatus, in which localized heating was applied to the grating through contact with a thin electrically heated nichrome wire. The wire, 0.10 mm in diameter, was connected between two insulating ceramic beads mounted on a teflon block. The block was attached to a micrometer, to allow the

disturbance position on an optical rail to be controlled. The fibre inscribed with the CFBG sensor was attached between two fibre chucks mounted at the opposite ends of the optical rail. The grating was monitored in reflection using an Er^{3+}dual-band broadband (EBS-7210) light source via a 3 dB 1550 nm coupler. The reference and disturbed spectra were measured using an OSA with a resolution of 0.1 nm and saved on a computer. The hot wire heat source was applied along the length of the grating in 0.05 mm increments at a constant heater power of 1.60 W under forced convection by a CPU fan mounted 3 mm above the top of the nichrome wire. The heat source was applied to more than 300 positions along the length of the grating. A cooling time of approximately 2 minutes was allowed for the temperature distribution to settle before measurement at the next location. The forced convection ensured that constant temperature was maintained on the sensor and reduced the width of the localised heat application resulting in more stabilised OSA traces and a sharper disturbance profile along the grating. The measurements were repeated at a different heater power of 0.40 W to examine the performance of the sensor at different peak localised temperature. The peak localised temperature of the fibre at each heater power was measured with an IR camera to compare with that inferred by the chirped fibre Bragg intragrating sensor.

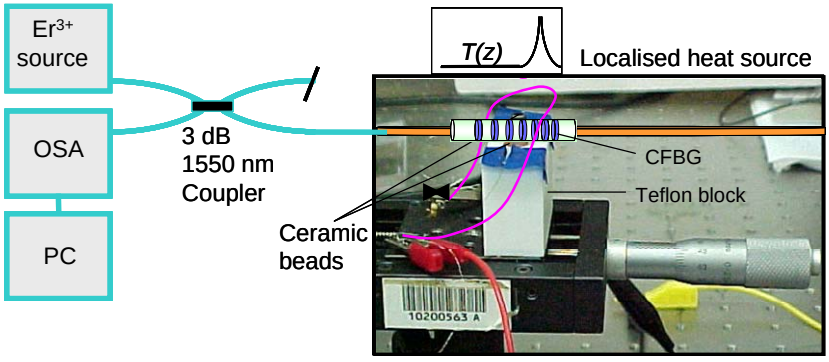

Figure 5.2 Schematic diagram of the experimental set-up including the localized temperature disturbance measurement (hot wire) apparatus.

5.3.3 Temperature measurements using the IR camera

An attempt was made to determine the peak localised temperature of the fibre, at the point of contact with the heater element, using a thermal infrared (IR) camera with an imaging frequency of 50 Hz. A temperature calibration curve as a function of current

for both the heater element and the fibre was obtained. This was implemented by taking a series of images of the fibre and the heater elements at various values of currents. Ten images were taken at each value of current, both for increasing and decreasing current cycles, and the images recorded. Figure 5.3 shows an example of the image taken for the optical fibre at a current of 0.25 A. The temperature of the fibre and the heater element were determined from the recorded images by taking a line scan across the fibre and the heater element. The temperature calibration curves of both the optical fibre and the heater element are shown in figure 5.4.

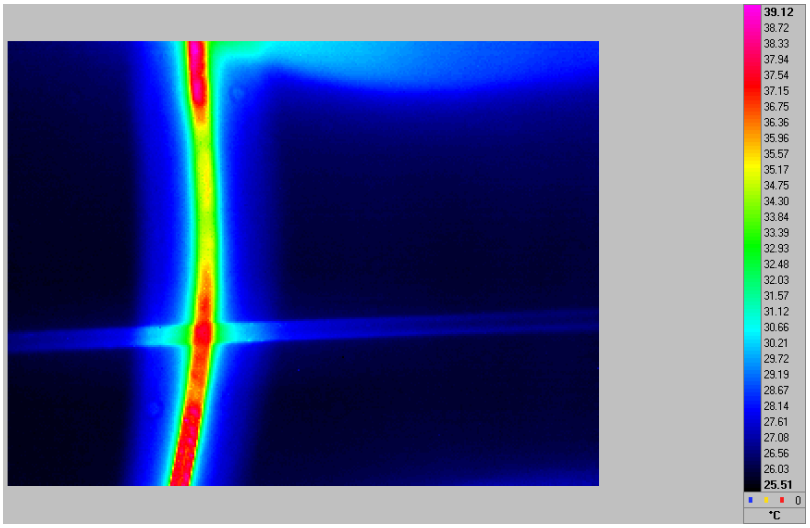

Figure 5.3 An example of the image taken for the optical fibre at a current of 0.25 A.

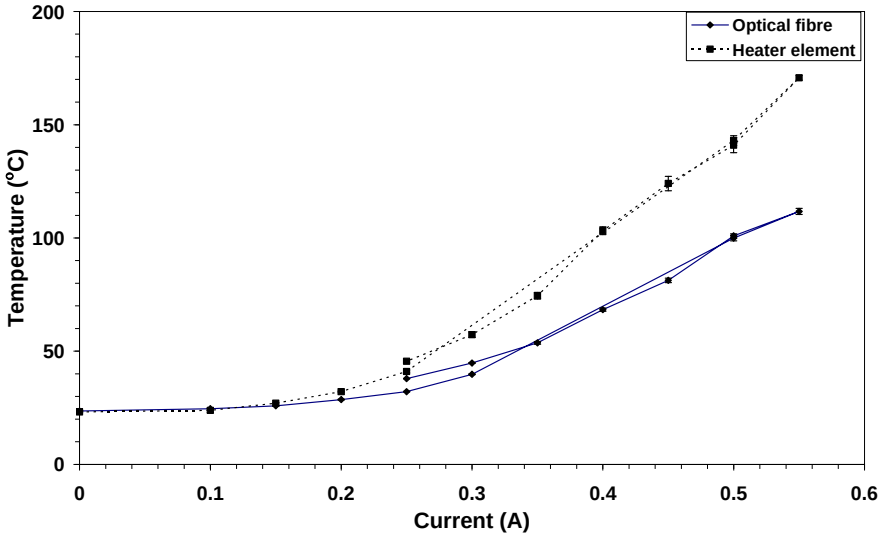

Figure 5.4 Temperature calibration curves from IR camera as a function of current for the optical fibre and the heater element (nichrome wire).

In the current experimental setup, it was difficult to measure the temperature of the optical fibre under forced convection. For temperature measurements, the CPU fan mounted on top of the heater element had to be removed to allow the IR camera to be focussed onto the heater element and the fibre. Thus the temperature calibration curves presented above are for natural convection, which were not the conditions under which the intragrating position measurements were performed. Another limitation for recording the images (temperature) of the optical fibre, at the point of contact with the heater element, was the obstruction by the heater element sitting on top of the fibre. Thus the temperature recorded by the IR camera was the surface temperature of the fibre in the near neighbourhood of the point of contact.

Furthermore, the surface temperature would also be slightly different from the core temperature of the fibre where the CFBG sensor is located even if temperature variation along the radius of the fibre (~ 62.5 μm) is assumed to be constant. Therefore the temperature inferred by the CFBG sensor can not be directly compared with that predicted by the IR camera and thus the actual temperature measurements cannot be absolutely verified in this research. Other methods explored to determine the temperature of the fibre were from the electrical resistance of the nichrome wire, and that predicted by a heat transfer model developed for the hot wire experimental apparatus. However, both these methods provided only an estimate of the fibre temperature; thus results regarding the determination of peak localised temperature by the intragrating CFBG sensor have not been presented in this research.

5.4. Principle of Sensor Operation

5.4.1 Effect of localised temperature on local Bragg wavelength and reflectance of chirped gratings

Consider the case of a chirped fibre Bragg grating with a linearly varying period of refractive index modulation along the length of the grating. For the "periodicity" chirped gratings used in these measurements, the chirping profile can be represented by the function:

$$\Lambda(z) = \Lambda_0 + cz, \tag{5.1}$$

where Λ_0 is the minimum grating pitch and $c = d\Lambda/dz$ is the rate of variation of grating pitch with length. Thus the Bragg reflection wavelength, $\lambda_B(z)$, can be described as a function of position along the grating by

$$\lambda_B(z) = 2n_0(z)\Lambda(z) = 2n_0(z)(\Lambda_0 + cz) = 2n_0(z)\Lambda_0 + 2n_0(z)cz = \lambda_0 + \gamma z, \tag{5.2}$$

where $n_0(z)$ is the average refractive index along the length of the undisturbed chirped fiber Bragg grating, λ_0 is the minimum Bragg wavelength of the grating and $\gamma = 2n_0(z)c$ is the chirp rate of the grating. Therefore the local Bragg wavelength along the grating is given as:

$$\lambda_B(z) = \lambda_0 + \gamma z. \tag{5.3}$$

In this application, temperature gradients exist along the grating length. Therefore the reflected spectrum will not only be shifted but also distorted due to chirping of the grating pitch and nonuniform changes in the refractive index over the grating length. The effect of a localised temperature change (ΔT) on the local Bragg wavelength $\lambda_B(z)$ and reflectance of the grating is due to two factors, the change in *dc* refractive index of the glass and the thermal expansion of the glass resulting in a change in the pitch of the grating. Thus the shift in the local Bragg wavelength in the region of the grating subjected to the localised temperature disturbance is given by

$$\Delta\lambda_B(z) = \left[\left(\frac{\partial\Lambda}{\partial T}\Big/\Lambda\right) + \left(\frac{\partial n_0}{\partial T}\Big/n_0\right)\right]\lambda_B(z)\Delta T. \tag{5.4}$$

Neglecting the change in the grating period, since the width of the applied temperature disturbance was small and no significant increase in the effective bandwidth of the spectrum was observed, and also that expansion of glass accounts for less than 5% of the change in Bragg wavelength, we have

$$\frac{\Delta\lambda_B(z)}{\lambda_B(z)} = \left(\frac{\partial n_0}{\partial T}\Big/n_0\right)\Delta T. \tag{5.5}$$

The term on the right-hand side of equation 5.5 is the contribution to the local average *dc* refractive index by the *dc* offset refractive index change [$\Delta n_{dc}(z)$] due to the thermo-optic effect at the location of the temperature disturbance. The modified local Bragg wavelength due to the localised heat source is given as:

$$\lambda_B^{'}(z) = \lambda_B(z) + \Delta\lambda_B(z) = 2\left[n_0(z) + \Delta n_{dc}(z)\right]\Lambda(z). \qquad 5.6$$

The change to *dc* refractive index (Δn_{dc}) due to the localised temperature disturbance modifies the local chirp rate and local Bragg wavelength of the region around this position. The change in chirp rate modifies the grating strength, $A(z)$ and the Bragg wavelength at this z position according to the equations $\frac{A(z)}{d\lambda/dz}$ and (5.6), respectively. The Bragg wavelength of this region shifts proportionally to the magnitude of temperature change, reducing the number of grating planes contributing to this wavelength $\lambda_{B,ref}(z)$ and increasing the contribution at another. This generates a characteristic dip and hump in the reflectance spectrum around the hotspot. The region where the reflectance $R(\lambda)$ is reduced corresponds to the position, z, of the applied temperature disturbance and the increase in reflectance at $R(\lambda)$ corresponds to the magnitude of the temperature change calculated from the wavelength shift.

5.4.2 Modelling the temperature disturbance using the FFT grating simulation technique

In this section, modelling of localised temperature disturbance using the FFT grating simulation technique (section 3.6.3) is examined. The effect of a localised temperature disturbance on the CFBG reflectance spectra was modelled using a range of hypothesis temperature disturbance functions, $T(z)$, of known shape to fit the measured spectra. The hypothesis $T(z)$ consists of index modulation versus position (z). The index modulation ($\Delta n_{dc}(z)$) at the location of the hotspot due to a particular hypothesis, $T(z)$, was fed into the FFT grating design model to generate a reflectance spectrum representative of the hypothesis, $T(z)$. The fitting process is described in the next section. The hypotheses temperature disturbance functions, $T(z)$, investigated in this work were rectangular (flat top or uniform index modulation), a cosine tapered window, raised cosine, Gaussian,

symmetric triangular, triangular squared, bi-exponential, Lorentzian, step and the convolution of a bi-exponential and raised cosine function.

Figure 5.5 shows the FFT modelled localised temperature disturbance at three positions along a 15 mm long, 30% linearly chirped grating showing the modified (disturbed) reflectance spectra. The parameters used in the calculation were exposure ($\Delta n_{ac} = 3.0 \times 10^{-4}$ or $R(\lambda) = 30\%$), peak change in dc refractive index of ($= 2.5 \times 10^{-4}$) at the location of the hot spot, L = 15 mm, chirp rate $d\lambda/dz$ = 20 nm/cm and λ_0 = 1525 nm. The temperature gradient imposes a modification to the chirp rate of the grating around the hotspot. Thus the number of grating planes contributing to reflectance, $R(\lambda)$, at wavelengths inside the gradient region are significantly altered. A region of substantially higher and lower reflectance, $R(\lambda)$, corresponding to greater and smaller chirp rates are clearly visible in the FFT modelled output spectra. The region where the reflectance, $R(\lambda)$, is reduced corresponds to the position, z, of the applied hotspot. The hypothesis temperature function, $T(z)$, employed in generating the FFT simulated spectra of figure 5.5 was the convolution of a bi-exponential and a raised cosine function.

As can be observed from figure 5.5, the transition from reduced to increased reflectance is shifted by the peak temperature induced wavelength shift; thus the two regions of the spectrum are of unequal bandwidth. However the small changes to the bandwidth at the disturbed region of the spectrum due to the Bragg resonance is ignored by the current FFT model as this would add complexity to the model. Another parameter verified from modelling results to have variable effect on the reflectance spectra is the width of the temperature disturbance. For the same temperature amplitude, a smaller disturbance width results in a greater change in the dc refractive index at the location of the hotspot. For a small disturbance width, heat is being concentrated as a point source at a particular position compared to a greater width where the heat source becomes more like a spread function over a larger sensor length resulting in a decrease in dc refractive index change which corresponds to a decrease in the peak localised temperature. Thus, to obtain sensible values of temperature amplitude from the CFBG sensor, the width of the temperature disturbance needs to be constant. Hence the measurements reported in this work were performed at constant heater powers under forced convection.

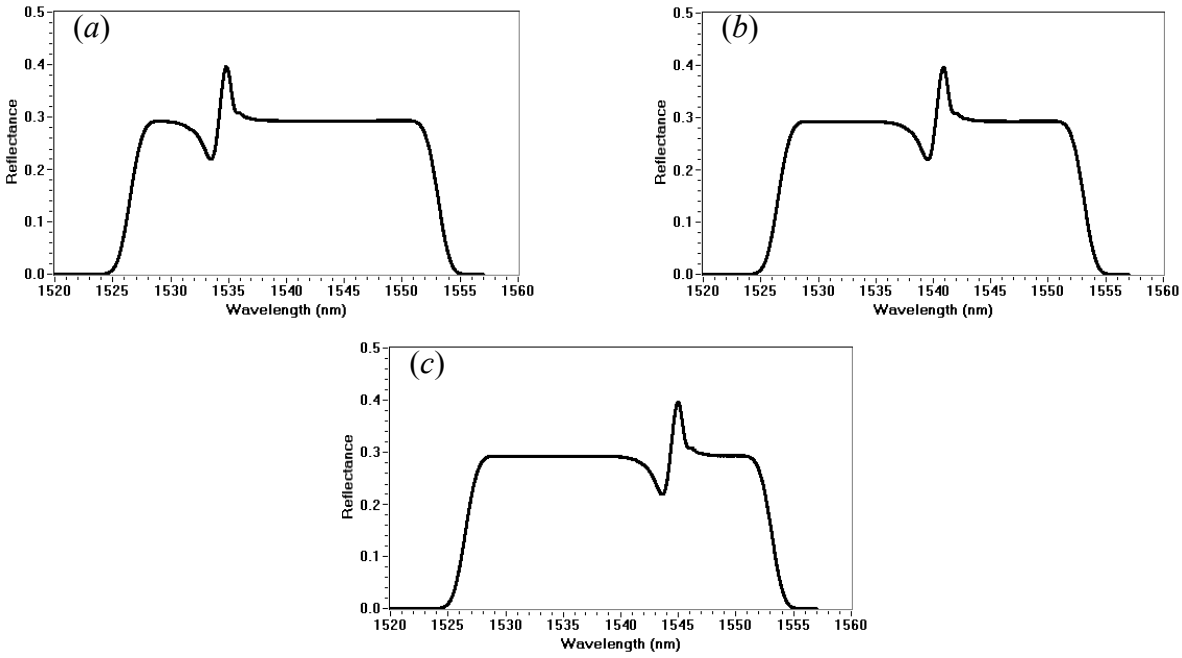

Figure 5.5 FFT modelled localised temperature disturbance at (a) z = –3.00 mm, (b) z = 0.00 mm and (c) z = 2.00 mm along a 30% linearly chirped (20 nm/cm) grating.

Figure 5.6 shows the effect of large temperature gradients on the FFT modelled reflectance spectra of a linearly chirped grating at two different reflectances. All parameters are the same, as those used to generate figure 5.5, except that figure 5.6 (a) is a 30% and figure 5.6 (b) is a 60% grating. Both gratings are subjected to a temperature gradient at the centre (z = 0 mm) resulting in peak dc refractive index change of 7.5×10^{-4} at the location of the hotspot, which is a factor of 3 greater than that of figure 5.5. The effect of a large change in dc refractive index due to a large temperature disturbance results in the reflectance of the grating approaching 100% as seen in figure 5.6 (b) for a 60% grating. This limits the simulation of measured spectra of the grating using the FFT grating design model as the FFT approximation is only valid within limits of low reflectance for $R(\lambda) << 1$. Thus selection of gratings with low initial strength, $R(\lambda)$, is crucial to the precision of the position determination using the FFT technique.

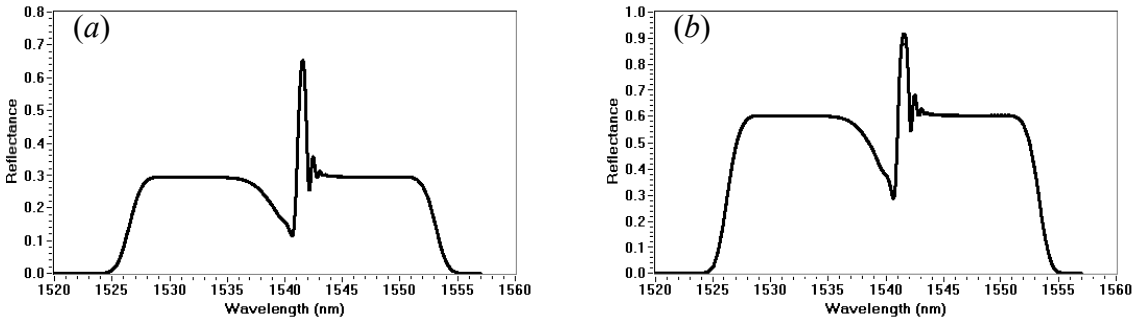

Figure 5.6 FFT modelled localised temperature disturbance, for (a) R(λ) = 30% and (b) R(λ) = 60%, linearly chirped gratings of chirp rate (20 nm/cm), at z = 0.00 mm.

5.5. Data Analysis Techniques

5.5.1 Determination of the temperature profiles - Iterative hypothesis-testing method

Since in these measurements the phase response data were not obtained, an iterative approach was used, in conjunction with FFT, for solving the inverse problem of obtaining the temperature distribution from the measured amplitude reflection spectrum. The iterative approach is used to modify the local Bragg wavelengths around the hot spot by adjusting the parameters of the temperature hypotheses, $T(z)$, so that the difference between the FFT reconstructed $[R_{ref} - R_{data}]$ and measured $[R_{ref} - R_{data}]$ spectra was within acceptable limits. The basic steps involved in the reconstruction of the grating spectra via the iterative approach employing the FFT technique, are described below.

The process of estimating the temperature distribution along the chirped FBG was implemented by automatically adjusting the three parameters of amplitude, width and position of a hypothesis temperature distribution, $T(z)$, of known shape, as described below. Parameters were adjusted until the difference $Q(\lambda)$ between the measured spectra $[R_{ref} - R_{data}]$ yielded an acceptably close fit to the difference $Q'(\lambda)$ between the FFT generated models of the simulated spectra $[R_{ref} - R_{data}]$. The method of providing and adjusting a hypothesis temperature profile to a Bragg grating model is illustrated in the flowchart of figure 5.7 (Nand *et al.,* 2006). The iterative process automatically makes

changes to the amplitude, width, and centre position that are proportional to the error observed in those parameters. The error is calculated automatically from the changes in $Q(\lambda)$, with and without the perturbation, due to the temperature profile, from the simulated and measured spectra.

The FFT model operated on an estimate of the amplitude of the refractive index modulation $dn_{ac}(z)$ of the grating obtained by applying the transformation $dn_{ac}(z) = A_0 \tanh^{-1}\sqrt{R(z)}$ to the amplitude of the measured reference spectrum. Perfectly linear chirp was assumed when extracting the CFBG profile and model parameters.

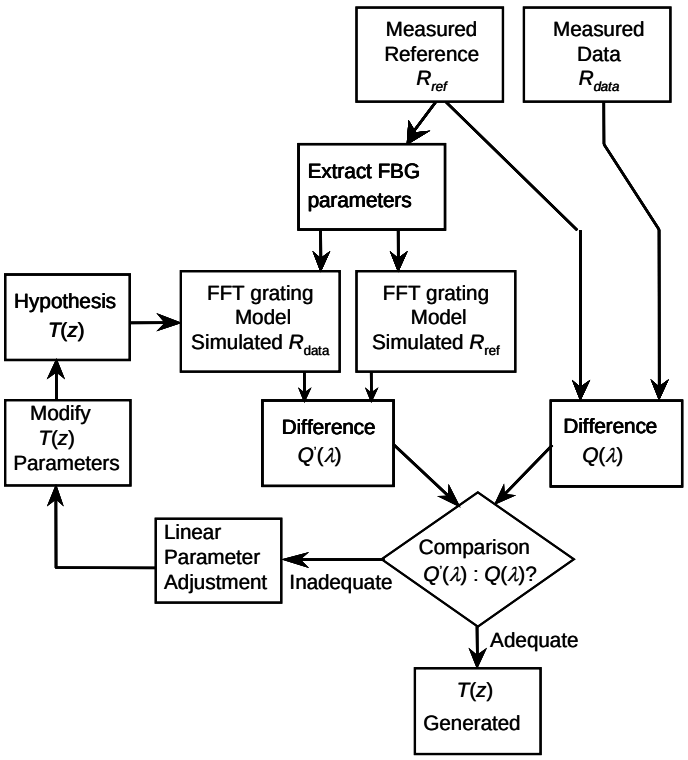

Figure 5.7 Flowchart of iterative disturbance function fitting algorithm.

A candidate function type was user-selected before starting the process, and converted to a hypothesis temperature profile $T(z)$. A range of candidate 'disturbance functions' of refractive index change versus position (z) were examined using the model. The refractive index change due to the disturbance functions was added to the *dc* component of the refractive index of the unperturbed grating at the location of the hotspot. It was demonstrated that elementary functions such as Gaussian, Lorentzian, rectangular and

symmetric triangular squared functions provided an approximate fit to the shape of changes observed in the reflectance spectra (Kitcher *et al.,* 2004). Figure 5.8 shows an example of the fit provided by these temperature hypotheses, $T(z)$ after six iterations. The region around the disturbance has been magnified to show how closely the measured spectra have been simulated by the use of these hypotheses, $T(z)$. The bi-exponential hypothesis provided the best approximation to the measured disturbances, fitting the edges of the disturbance in the spectra closely. However, it failed to adequately fit the neighbourhood of the contact point.

In this work, the hypothesis function employed was the convolution of a bi-exponential and a raised cosine function. The FFT model operated on hypothesis, $T(z)$ and the extracted FBG parameters to simulate the first Born approximation of the FBG. The location, amplitude and width of changes between the modelled spectra were compared to those of the measured spectra, and the three parameters of the hypothesis adjusted automatically by the iterative hypothesis testing algorithm.

The fast computation speed of the FFT based model enabled trials of a large number of hypotheses for fitting the 3-parameters of the hypothesis temperature distribution, $T(z)$, at each location of the disturbance along the grating. Each fitting required typically 10 ms to simulate, and 50 ms to compare and fit the model to the measured spectra. The final fitted values of the centre position and peak temperature at each location of the disturbance were collated, compared with measured values and charted to determine the precision and repeatability of the position of the localised heat source.

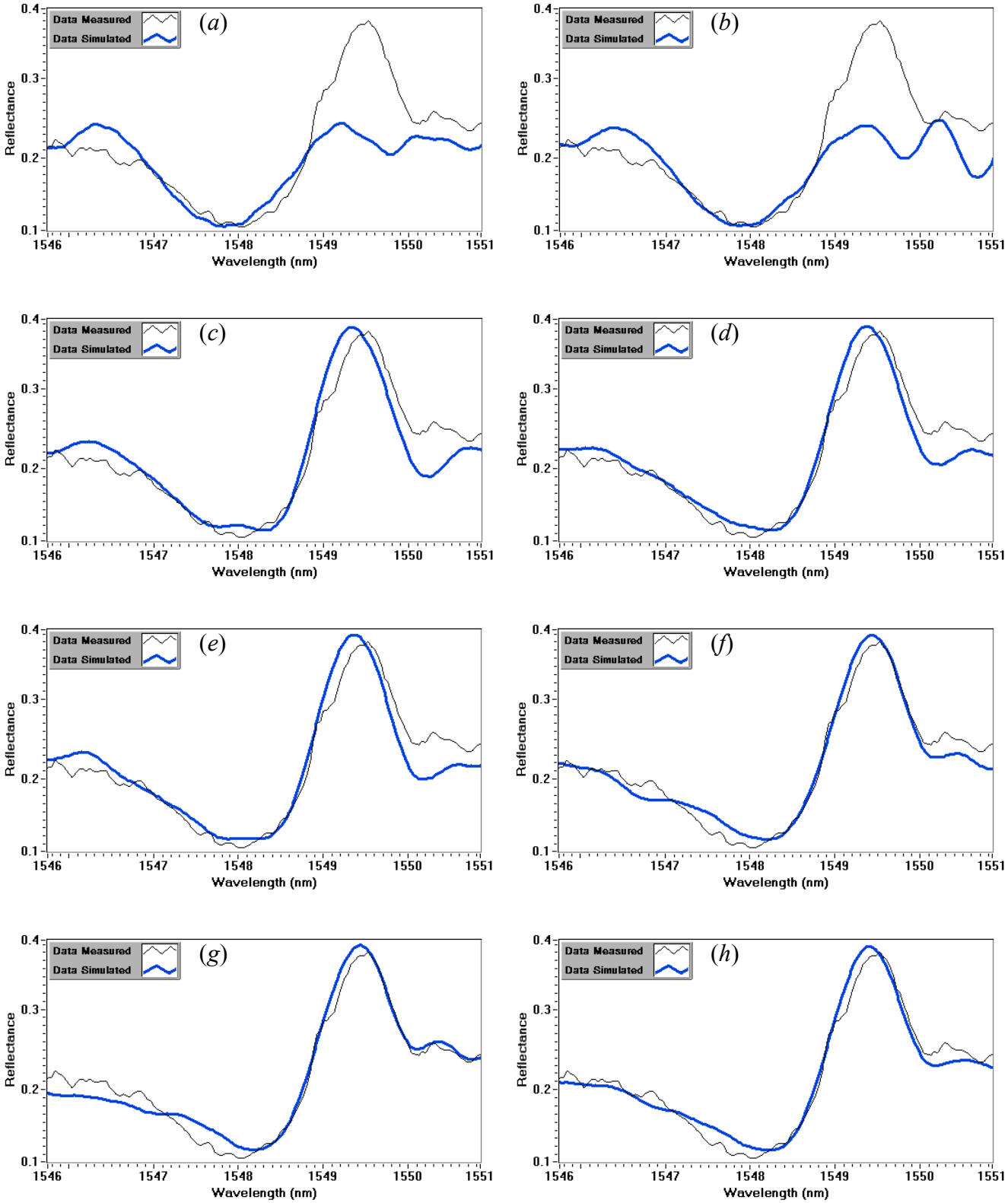

Figure 5.8 Examples of the fit provided by the temperature hypotheses; (a) Rectangular top hat, (b) Cosine tapered window, (c) Raised cosine, (d) Gaussian, (e) Triangular, (f) Triangular squared, (g) Biexponential and (h) Lorentzian.

5.5.2 Grating Reconstruction Inversion Problem – Justification of the FFT Grating Simulation Technique

The spectral response of both uniform and non-uniform Bragg gratings can be calculated through numerical solutions of the coupled mode equations, or using the transfer matrix approximation of the coupled mode theory (Erdogan, 1997) from known grating parameters (period, refractive index and index modulation). Intragrating sensing on the other hand is an inverse reconstruction problem, which involves retrieving these grating parameters which are dependent on the applied strain or temperature profile. Several calculation techniques based on amplitude alone or both amplitude and phase of the measured reflection spectrum have been proposed to reconstruct the grating parameters of a fibre Bragg grating subjected to a non-uniform strain or temperature distribution (section 2.4).

In this work, the FFT technique (Nand *et al.,* 2005b, 2005c, 2006) was used for reconstructing the spatial variation of the refractive index and the local period along the CFBG from its measured reflected power spectrum to recover the temperature distribution due to localised heating. The technique was selected since for distributed measurements, a large change in reflectance $R(\lambda)$ in comparison to noise is preferred to extract the signals. Figure 5.9 is a plot of peak reflectance (R) as a function of grating strength (κL) using the equation $R = \tanh^2(\kappa L)$. The derivative of the curve ($dR/d\kappa L$) with grating strength is also shown. It can be seen that gratings with 30-40% reflectance (shaded lines) have the largest change in $R(\lambda)$ in comparison to noise; i.e. the change in reflectance with the change in grating strength ($dR/d\kappa L$) is a maximum. It has been shown that the FFT method is valid for any arbitrary strain profile, $\varepsilon(z)$, as long as the reflectance $R(\lambda) << 1$ and that $\varepsilon(z)$ can be obtained with reasonable accuracy over the entire grating length (Huang *et al.,* 1998). Furthermore the FFT method does not impose any conditions on the strain or temperature fields to be measured and is capable of predicting the grating spectrum with reasonable precision when subject to any strain or temperature distribution.

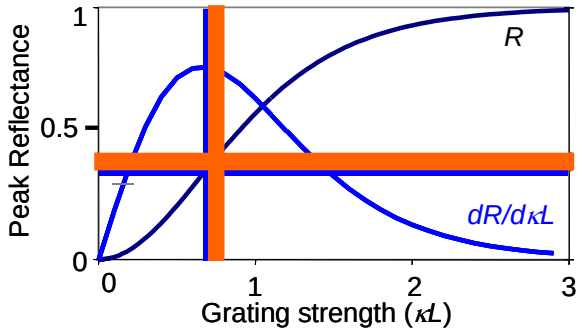

Figure 5.9 Theoretical reflectance versus grating strength [$R = \tanh^2(\kappa L)$] showing the maximum change in reflectance with change in grating strength (shaded lines).

Figure 5.10 illustrates a comparison of the fast Fourier transform Bragg grating model (FFT) against the conventional transfer matrix method (*TMM*) for the case of a local disturbance. The reflectances predicted by the two models are compared for an apodised grating with refractive index modulation amplitude of 0.0004, subjected to a 'hotspot' with a peak refractive index change of 0.0002, corresponding to a temperature change of 23 °C. The *TMM* model calculates a slightly higher reflectance than the FFT, due to repeated resonant reflection within each section of the grating. However for the relatively weak gratings investigated in this work, the difference was small, as shown in figure 5.10. Thus in the limit of weak grating reflections, the FFT technique is in good agreement with the *TMM* technique.

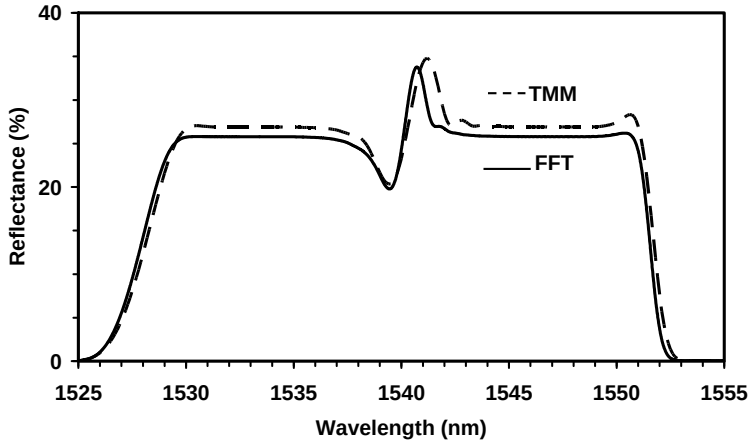

Figure 5.10 Comparison of the FFT model to the conventional TMM model.

Broadening of the temperature induced peak occurs in practice and in the TMM model due to power loss along the resonant sections of the grating. Whilst this broadening effect is absent in the FFT model, it can be seen from figure 5.10 that the main

parameters describing the temperature induced disturbance such as its amplitude, location, and peak to peak width are approximated reasonably well by the FFT. The position of the disturbance (hot-spot), which has been the subject of investigation in this research, coincides sufficiently closely for the two models.

The FFT method also has high computation speed as might be required for on-line processing of distributed measurements. The processing time for TMM model was approximately 15 s, whereas the FFT model was greater than 1000 times faster. Thus due to its high computation speed, the FFT model was implemented for simulating the spectral response of the gratings and to permit near real-time measurements. The use of low reflectance gratings for measurements in this project further justified the selection of the FFT method.

5.6. Results

5.6.1 Extraction of temperature profile using the FFT Technique

Examples of measured and fitted spectra and fitted temperature distributions for two gratings (*C* and *D*) are plotted in figures 5.11 and 5.12 respectively. The results were obtained using the FFT iterative approach described above for solving the inverse problem. The top graphs of each figure show the measured (disturbed) and FFT simulated spectra, $R(\lambda)$, at two positions along the grating. The bottom graphs show the fitted temperature distribution, $T(z)$, to the localized heat source (disturbance) at the two positions. The expected reduction in reflectance at short wavelengths and corresponding increase in reflectance at longer wavelengths are clearly visible. Extracted temperature profiles show that the sensors are able to detect peak localized temperature change and temperature distribution along the grating.

The system automatically generated a detailed fit to the reference and disturbed spectra. A hypothesis temperature profile, shown below the spectra, was obtained automatically by making changes to the amplitude, width, and centre position that were proportional to the error observed in those parameters. The error was calculated automatically from

the changes, $Q(\lambda)$, with and without the perturbation due to the temperature profile, from simulated and measured spectra.

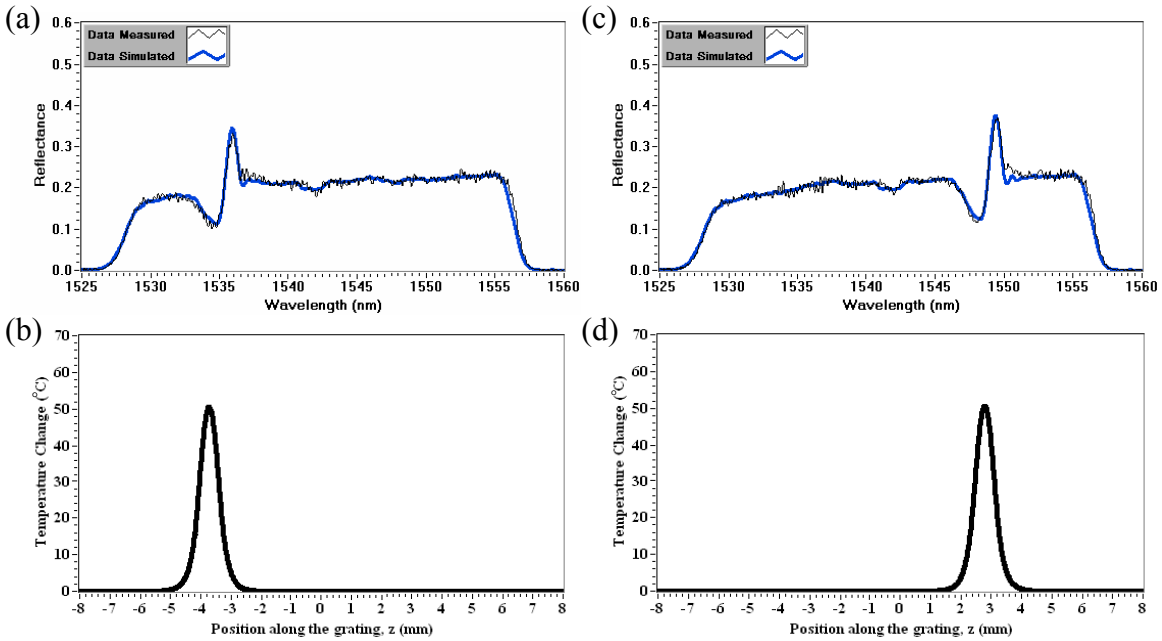

Figure 5.11 Examples of results for grating C. (a) Measured and simulated spectra $R(\lambda)$ and (b) fitted temperature distribution, $T(z)$, for a disturbance at $z = -3.80$ mm and (c) measured and simulated spectra $R(\lambda)$ and (d) fitted temperature distribution, $T(z)$, for a disturbance at $z = 2.90$ mm.

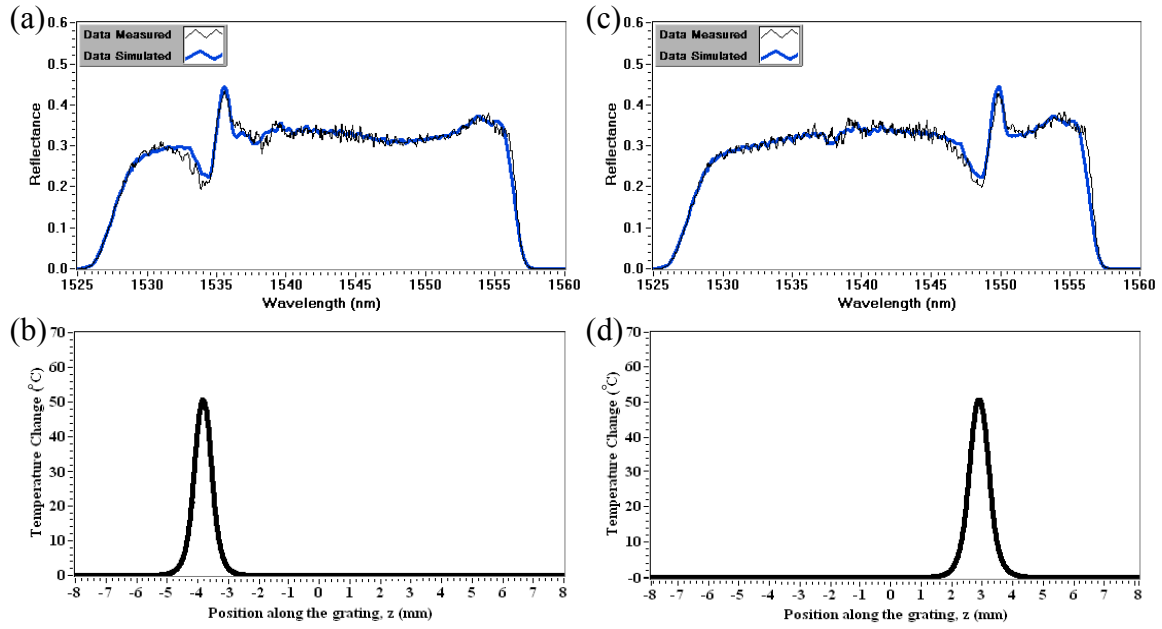

Figure 5.12 Examples of results for grating D. (a) Measured and simulated spectra $R(\lambda)$ and (b) fitted temperature distribution, $T(z)$, for a disturbance at $z = -3.80$ mm, (c) measured and simulated spectra $R(\lambda)$ and (d) fitted temperature distribution, $T(z)$, for a disturbance at $z = 2.90$ mm.

5.6.2 Position Measurements

One of the three parameters, the centre position of the heated wire, was varied during the measurements. The width, shape and amplitude of the temperature profile were, to the best of our knowledge, constant as experiments were performed at constant heater powers under forced convection. However, the peak temperatures inferred by the sensor showed a slight variation of ±0.2 °C along the grating. This could be due to variable thermal contact between the wire and the fibre at different positions. The position $z = 0$ was defined to coincide with the centre of gravity (the weighted centre of the reflectance of the reflected spectrum) of the reference spectrum of the grating. The actual micrometer positions, z (mm), were re-zeroed to agree with the centre of gravity of the reference spectrum and compared to the fitted values of z_{fit} (mm).

The micrometer controlled position of the heated wire was varied, and spectra recorded. The algorithm operated on the measured data and reference spectra, starting with an initial hypothesis of dc refractive index change of 1×10^{-4} resulting in a temperature disturbance of 150 °C at $z = 0$. Given the chirp rate of the grating, changes to the amplitude and centre position were matched by the linear parameter adjustment algorithm and an updated hypothesis of $T(z)$ with improved centre position and amplitude was generated. The algorithm converged to within 2% of parameter values toward final parameter values in two iterations, each requiring less than 10 ms. The algorithm was allowed to run for six iterations, by which time it had reached a steady final hypothesis $T(z)$.

The fitted values of the centre position determined by the fitting process were examined for the whole data set of each grating. Results for all gratings investigated are shown in Figures 5.13-5.17. These results are for the favourable case with a lower heater power of 0.4 W. The leftmost charts, (a), in figures 5.13–5.17 show agreement between the fitted values of disturbance centre position z vs. the actual position of the heater wire determined from the micrometer readings. These charts show no catastrophic errors or failures in the fitting process. The centre charts, (b), show the deviation from linearity of charts (a), through a scatter plot of $(z_{fit} - z)$ vs. z. An ideal sensor would show a straight horizontal line to indicate zero error. We observed for all gratings that a systematic error indicated by ripple in the charts (b) contributed significantly more to errors than any

random spread amongst the repeated measurements. A histogram of all of the points of (b) is shown in (c), illustrating the spread of ($z_{\text{fit}} - z$). The spreads are mostly confined to within an error range of ±0.05 mm over the entire length of the grating except at the ends of the grating where the lack of grating planes within the effective length affects the contribution of the local Bragg wavelength to the reflected power spectrum.

The systematic error in figure 5.15(b) is small and is dominated by fine ripple structure for grating *C*, resulting in a near Gaussian-like histogram in figure 5.15(c). In contrast, there is a substantial drift for all other gratings, as shown in figures 5.13-5.14(b) and 5.16-5.17(b), resulting in broader triangular-like histograms in figures 5.13-5.14(c) and 5.16-5.17(c).

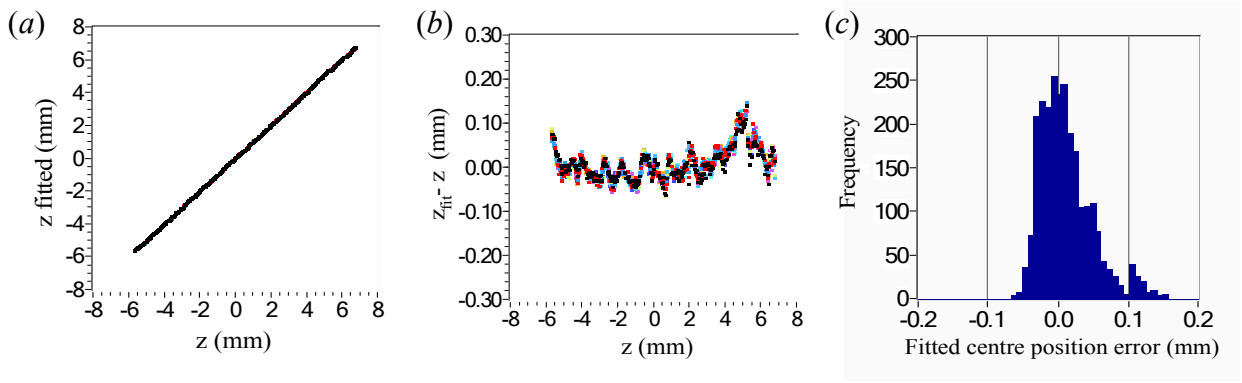

Figure 5.13 Performance of grating A; (a) fitted z versus measured z values, (b) deviations in ($z_{fit} - z$) along the grating and (c) histogram of fitted centre position error.

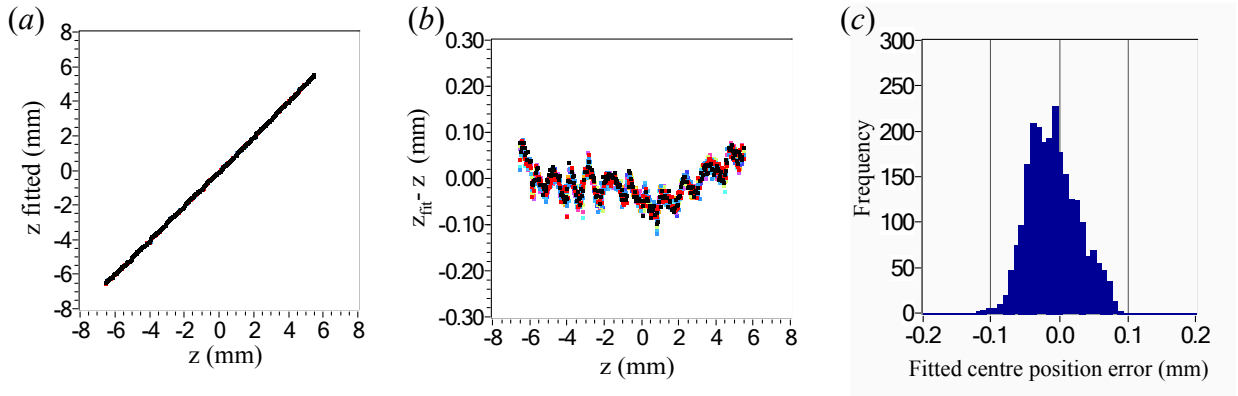

Figure 5.14 Performance of grating B; (a) fitted z versus measured z values, (b) deviations in ($z_{fit} - z$) along the grating and (c) histogram of fitted centre position error.

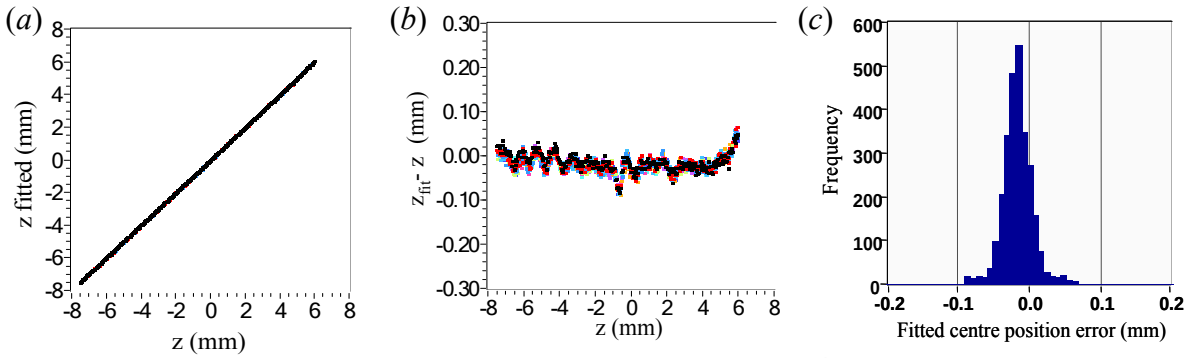

Figure 5.15 Performance of grating C; (a) fitted z versus measured z values, (b) deviations in ($z_{fit} - z$) along the grating and (c) histogram of fitted centre position error.

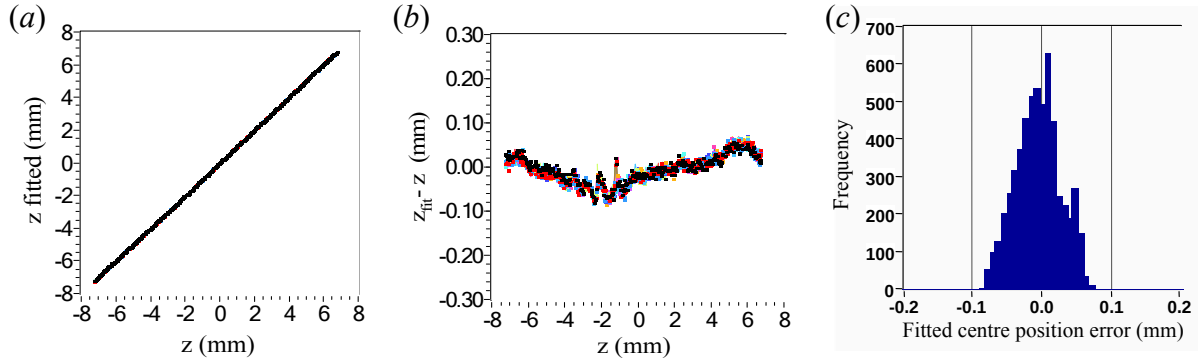

Figure 5.16 Performance of grating D; (a) fitted z versus measured z values, (b) deviations in ($z_{fit} - z$) along the grating and (c) histogram of fitted centre position error.

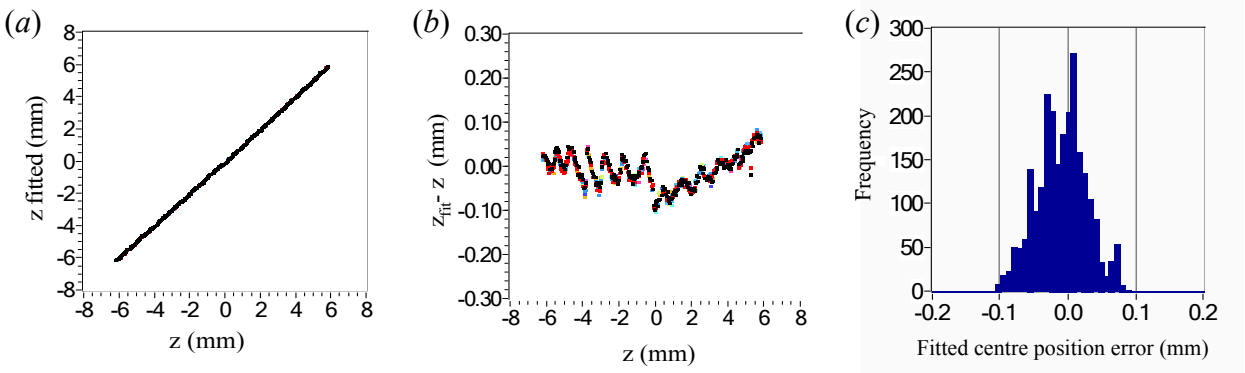

Figure 5.17 Performance of grating E; (a) fitted z versus measured z values, (b) deviations in ($z_{fit} - z$) along the grating and (c) histogram of fitted centre position error.

5.6.3 Repeatability of Position Measurements

The spread of data after the subtraction of the average systematic error indicates the repeatability of measurements. The systematic error in position, due to the ripple structure of the gratings, was found to be the dominant component in centre position

rms error for all gratings. Repeatability of the position measurement was calculated as the rms variation of the fitted centre z within ten repeated measurements. The repeatability errors $z_{fit} - \bar{z}_{fit}$ were collated and the rms repeatability of the whole data set were obtained. The repeatability histograms for all gratings, after the removal of systematic errors, at the lower heater power are shown in figure 5.18. On average the rms repeatability for these gratings was less than 0.007 mm when tested over all positions at both heater powers. The best case performance was obtained for grating *E*, which had the largest signal to noise ratio, at both heater powers as might be expected.

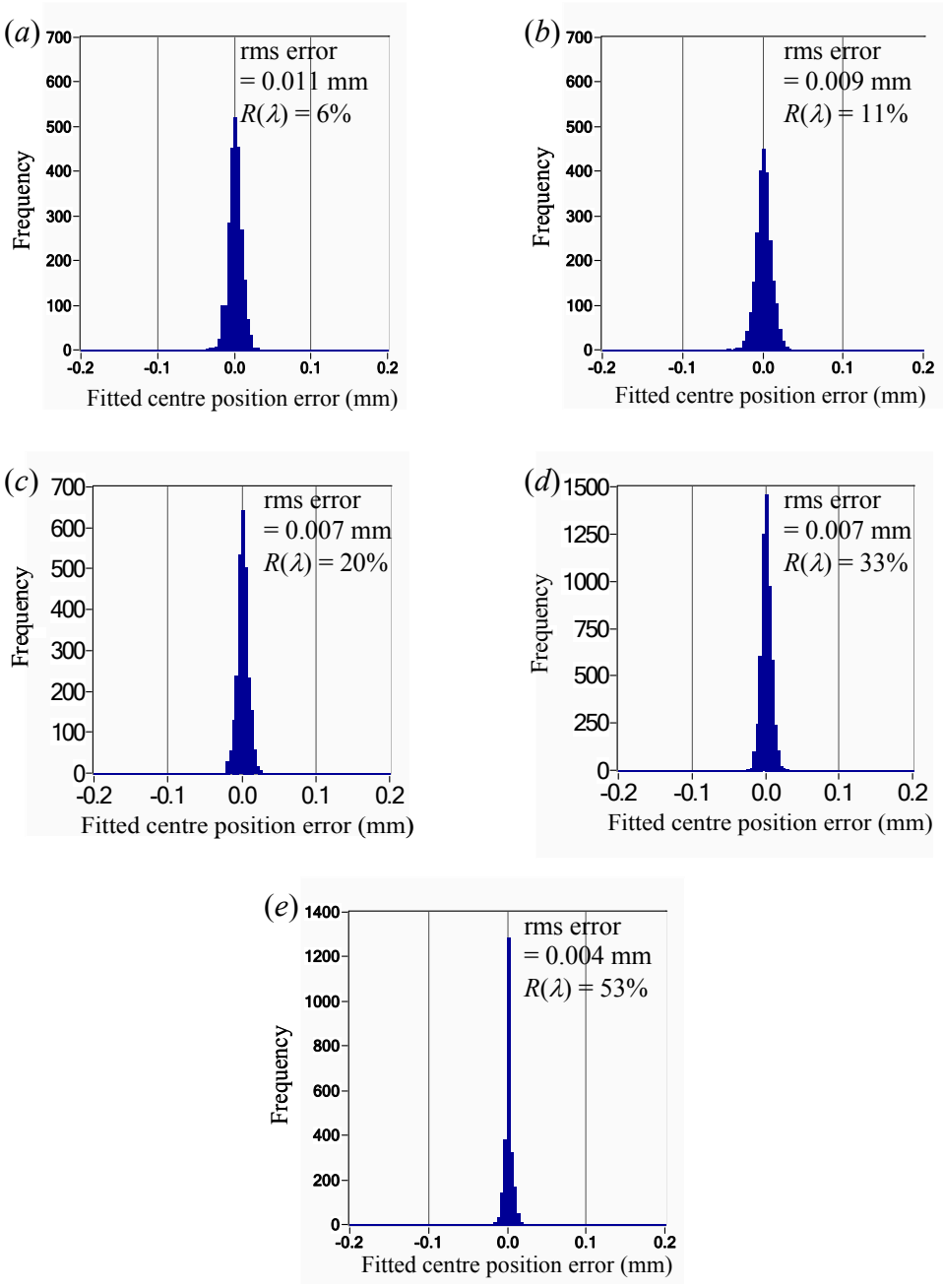

Figure 5.18 Histograms showing fitted centre position errors after the removal of systematic errors for gratings (a) A, (b) B, (c) C, (d) D and (e) E.

5.7. Performance of Sensors

This section investigates the performance of CFBGs as intragrating sensors for the determination of the centre position of a localised heat source. The performance of the measurement system in relation to centre position accuracy and repeatability of position measurements are investigated as a function of grating strength.

5.7.1 Summary of Sensor Performance

Tables 5.2 and 5.3 summarize the performance of the sensor system for the two heater powers employed. The signal to noise ratio was determined from calculation of the rms variation of raw data points amongst repeated measurements, in comparison to the peak signal level in the reference spectrum. This was somewhat worse than the instrument noise floor, typically by 5 dB. The position rms error is the standard deviation obtained from all 3300 points (i.e. 330 z positions × 10 repeat measurements at each z) of ($z_{\text{fit}} - z$) as shown in figures 5.13-5.17(b) and 5.13-5.17(c). The repeatability rms error in ($z_{fit} - \bar{z}_{fit}$) was averaged over all 330 z positions, and indicates the random component of measurement errors due to system noise.

Sample number	**Peak reflectance (± 2%)**	**Signal/noise (± 1 dB)**	**Position rms error (mm)**	**Repeatability rms error (mm)**
A	6	30.7	0.053	0.011
B	11	32.1	0.038	0.009
C	20	32.5	0.026	0.007
D	33	26.6	0.032	0.007
E	53	34.2	0.039	0.004

Table 5.2 RMS errors in centre position and repeatability of measurements at lower peak localized temperature for all gratings investigated (heater power = 0.40 W).

Sample number	Peak reflectance (± 2%)	Signal/noise (± 1 dB)	Position rms error (mm)	Repeatability rms error (mm)
A	6	29.8	0.043	0.009
B	11	31.9	0.033	0.007
C	20	31.3	0.029	0.006
D	33	29.8	0.043	0.010
E	53	34.1	0.043	0.005

Table 5.3 RMS errors in centre position and repeatability of measurements at higher peak localized temperature for all gratings investigated (heater power = 1.60 W).

5.7.2 Position Measurement Performance Testing

Results summarised in Tables 5.2 and 5.3, suggest that the centre position rms error generally improves with grating strength up to approximately 30% peak reflectance, and then decreases with further increase in grating strength for both the high and moderate temperature amplitudes which were investigated. The rms error improves from 0.053 mm for a $R(\lambda) = 5\%$ grating to 0.026 mm for a $R(\lambda) = 20\%$ grating with the moderate temperature amplitude, and from 0.043 mm for a $R(\lambda) = 5\%$ grating to 0.029 mm for a $R(\lambda) = 20\%$ grating with large temperature amplitude. The histograms [figures 5.13-5.17(c)] best show the difference between the performances of the sensors. The rms error was found to be a minimum for peak reflectance close to 20%.

The trend seems to be consistent with theory if the grating strengths indicated are corrected for excess loss. Assuming excess loss to be constant and a function of grating strength, it could be verified that the actual grating strengths are about 10% higher than that measured. Thus grating *C* (20%), which shows best performance at both heater powers, could be about 30% grating. It can also be predicted from theory (figure 5.9) that gratings with 30-40% reflectance have the largest $dR/d\kappa L$. A large change in reflectivity $R(\lambda)$ in comparison to noise is preferred for distributed measurements to extract temperature profiles.

The increase in centre position rms error for gratings around 50% (~60% if corrected for excess loss) can be attributed to modification of the effective refractive index by a dc refractive index change due to a temperature disturbance resulting in the reflectance of the grating approaching 100%. The high reflectance limits the simulation of the

measured spectra of the grating using the FFT grating design model and as a consequence the extraction of temperature profiles. The precision of the position measurements obtained appear to be limited by the performance of the FFT grating reconstruction method which is valid within the limit of low reflectance. As the reflectance of the grating increases, the FFT approximation is less reliable, and thus a decrease in both the precision and repeatability of the position measurements occurs when $R(\lambda)$ deviates from the requirement that $R(\lambda) << 1$.

For gratings with low reflectance, the low signal to noise ratio of the measured spectra could be a contributing factor in the centre position rms errors. A low signal to noise ratio increases the time required to record each spectra and decreases the repeatability of measurements which increases the systematic error in the position measurements. The systematic errors in figures 5.13-5.14 and 5.17(b) are large in comparison with 5.15-5.16(b), and dominated by big ripple structures. This had a direct effect on the position determination using the 3-parameter fitting, where position, width and temperature are interdependent, thus decreasing both the precision and repeatability of position measurement.

5.7.3 Repeatability of Position Measurement Performance Testing

Table 5.2 shows a clear trend of improving repeatability vs. increasing grating strength. Increasing reflectance from 6 to 53% resulted in an improvement of rms repeatability from 0.011 mm to 0.004 mm. This can be understood as a straightforward effect of the improving signal/noise ratio with stronger gratings, which return a stronger signal. It is noted that improvement is marginally slower than √R, which can be used to approximate the trend of repeatability vs. peak reflectance for these small signal cases.

Table 5.3 shows a general trend of improving repeatability vs. increasing grating strength, with the exception of grating *D*, which suffered worse noise as indicated in the third column. Increasing reflectance from 6 to 53% resulted in an improvement of rms repeatability from 0.009 mm to 0.005 mm. The trend is considerably slower than √R, indicating that causes other than instrument noise have become more significant in the large signal measurement cases.

5.8. Discussion

The trend of improving rms error with grating strength up to 20% reflectance, followed by a worsening of rms error for stronger gratings is consistent with theory when excess losses are considered. Gratings stronger than 20% showed considerable excess loss, which varied somewhat along the grating. A higher excess loss imposed a lower limit to the level to which the disturbed spectrum could peak, thus disrupting the estimate of temperature. This and other systematic errors were observed as ripples in the charts of $(z_{\text{fit}} - z)$ vs. z.

Underestimates of the temperature amplitude due to excess loss required the model to assume that the physical location of the disturbance was closer to the wavelength location of the peak, so causing a secondary error in position estimation. The secondary error can be estimated from the chirp rate of 20 nm/cm and the temperature coefficient $d\lambda/dT$. For a temperature error of 10 °C, the secondary position error is 0.05 mm.

Furthermore, the amplitude and width of the disturbance are interrelated, such that a narrower disturbance of larger amplitude presents a disturbance in the spectrum of the correct area. Therefore more secondary position errors could be caused by error in fitting the width of the temperature profile. All of the secondary errors are proportional to the peak temperature, and indeed worse performance is observed in table 5.3 for a high temperature than in table 5.2 for moderate temperature amplitude.

Thus the rms errors in position measurements can be attributed to uncertainty in the modelled grating parameters defining the refractive index modulation depth due to nonuniformity in the grating writing, chirp rate, and temperature sensitivity coefficient $d\lambda/dT$. These are inter-related and influence the grating definition functions used by the model. Furthermore, the three parameters of position, width, and temperature are inter-related, such that a slight variation in temperature contributes to errors in the position determination. Other factors limiting the precision of position measurement include repeated periodic errors and ripple features in the spectrum which are functions of each grating and mechanical vibration of the experimental apparatus.

It is also noted that the FFT model is acceptable for gratings of less than 50% reflectance, but invalid due to classic Bragg resonance effects in stronger gratings. It has been shown (Huang *et al.,* 1998) that the FFT method is valid for any arbitrary strain profile as long as the reflectance $R << 1$.

5.9. Chapter Conclusion

In this chapter, the FFT technique for fitting the position, peak temperature, and width of a candidate shape function for the temperature distribution within a CFBG has been demonstrated. The intragrating sensor is based on the analysis of reflected power spectra arising from a CFBG. The technique uses an iterative approach in conjunction with FFT for solving the inverse problem of obtaining the temperature distribution from the measured amplitude (intensity) reflection spectrum.

The precision and repeatability of the inferred centre position of a localised temperature change within a CFBG has been investigated as a function of grating strength. The measured spectrum of the CFBG due to a localised temperature change (heat source) was simulated using the FFT grating design model. The model operated on the reference spectrum and hypothesis temperature distributions, $T(z)$, to generate a spectrum of a CFBG subjected to a hypothesis temperature disturbance. The simulated spectrum was fitted to the measured spectrum using a three-parameter automated disturbance function fitting algorithm operating on position, width and amplitude of temperature change.

The precision of the centre position of a localised temperature disturbance along a CFBG intragrating sensor has been improved, compared to (Won *et al.,* 2004), to obtain an rms error below 0.03 mm for grating strengths in the range 20-30%. The ability to determine position in intragrating temperature sensing is dependent on grating strength and on the technique employed in reconstructing the grating parameters from its measured reflectance spectrum. Grating strength must be selected carefully to avoid the modified peak reflectance approaching 100% especially when large gradients are involved (Won *et al.,* 2004). The results reported here employed linearly chirped gratings with a fast chirp rate of 20 nm/cm and low reflectance's in the range (5-50) %.

The applied temperature gradients were comparable to the initial chirp of the gratings, but did not exceed the limit of 120 °C/mm, above which the chirp is inverted. The rms error in position (< 0.03 mm) and repeatability (< 0.005 mm) of the centre position measurements obtained are an improvement on those reported previously for distributed temperature measurements employing chirped gratings [Won *et al.,* 2004 (149 μm), Gillooly *et al.,* 2004 (169 μm)].

In these experimental trials, CFBGs with a chirp rate of 20 nm/cm and low reflectances were used. This resulted in spectra which are simple to interpret in comparison to previous work employing a much lower chirp rate (Won *et al.,* 2004). Furthermore, the spectra were an order of magnitude broader than low chirp rate gratings, reducing the resolution requirements of equipment to interrogate the sensor. This technique may suit applications in monitoring the temperature distribution of target and nearby tissues during hyperthermic shock treatment of cancerous tissue and is of the correct dimension and temperature scale to examine temperature profiles in electronic and power conversion devices.

CHAPTER 6

LOCALISED STRAIN MEASUREMENTS USING THE INTENSITY REFLECTION SPECTRUM BASED INTRAGRATING SENSING

6.1 Chapter Overview

The chapter begins by providing a brief introduction to the field of non-uniform strain sensing using embedded FBGs together with the chapter objectives. It then describes the design of uniaxial host specimens for the application of non-uniform localised strain along a CFBG sensor together with the experimental techniques employed for intragrating strain measurements. The principle of the sensor operation is then formulated and relevant equations developed. The effect of localised strain on the local Bragg wavelength and reflectance spectra of CFBGs are then modelled using the equations developed. Following this is a description of the extraction of non-uniform strain profiles along the CFBG sensor using the integration of changes to the power level in the reflection intensity spectrum. The inverse problem of recovering the nonuniform strain distribution along the CFBG sensor is obtained as the cumulative sum of the normalized changes in the power reflectance spectra between the perturbed and unperturbed grating.

The performance of the CFBG sensor is then compared with the strain distribution predicted by linear elastic structural finite element method (FEM) modelling using FEMAP/NASTRAN commercial software.

6.2 Introduction

Embedded uniform FBG sensors have been employed extensively as strain sensors in applications involving structural health monitoring to measure nonuniform strain fields (section 2.5). Though uniform FBGs show sensitivity to non-uniform strain fields and are capable of quantitatively evaluating the strain fields, identifying the location and direction of strain gradients is extremely difficult and computationally expensive. To overcome these problems, CFBGs have recently been demonstrated for the detection of crack locations in composite materials (Okabe *et al.,* 2004, Palaniappan *et al.,* 2005, 2006).

A number of investigations using CFBG sensors for damage detection (cracks) in representative composite structures under the application of a load have also been reported (Okabe *et al.,* 2004, Palaniappan *et al.,* 2005, 2006). The crack locations in a carbon fibre reinforced plastic (CFRP) were identified directly from the changes in the reflected intensity spectra of the CFBGs. The development and position of cracks were identified from the position of dips in the spectrum around a particular wavelength corresponding to a unique position on the chirped grating.

This chapter investigates the ability of embedded CFBG sensors to measure nonuniform localised strain distribution near a stress concentration within a notched aluminium specimen subjected to an axial tensile force, from the shape of the measured intensity reflection spectra (Nand *et al.,* 2007). Due to the shape of the specimen, axial strain gradients exist in the region around the notch (parabolic), where the area of the specimen is reduced by machining. A CFBG sensor is embedded in this region, in order to detect the nonuniform strain distribution. As a result, the shape of the spectral response of the CFBG sensor should change around the location of the strain gradient.

The shape of the strain profile along the CFBG sensor is obtained as the cumulative sum of the normalized changes in the power reflectance spectra between the perturbed (measured data, R_m) and unperturbed (reference, R_{ref}) grating. Unlike other intragrating sensing techniques employing CFBG, this method recovers an intragrating strain profile without trial and error and does not require a hypothesis strain distribution to be postulated. Such an approach would be suitable for sensors located in structures where

the form of the strain field is expected to change continuously or become discontinuous, such as in damage detection systems.

6.3. Experimental Techniques

6.3.1 Grating fabrication

CFBGs used for this investigation were fabricated in hydrogen-loaded standard Corning SMF-28 telecommunications fibre with a linear chirped phase mask using the Swinburne scanning FBG fabrication system described in chapter 3. The phase mask had a centre pitch of Λ = 1.0665 μm and chirp rate of $(d\lambda/dz)$ = 20 nm/cm. A piezo phase mask shaker was used to flatten the average refractive index at the ends of the apodised sensors which have lengths of 15 mm. The sensors were annealed at 330 °C for 150 s to prevent subsequent shifts in the spectra due to out-diffusion of H_2. The sensors were calibrated for temperature and strain as described in sections 4.3.3 and 4.4.1, respectively, before being embedded into the specimen. Table 6.1 shows the scan rates used during fabrication, measured average reflectance, approximate reflection bandwidths together with temperature and strain sensitivities of the gratings. The reflected 'reference' spectra of the three gratings used for the measurement of the localised strain gradients are plotted in figure 6.1. $R(\lambda)$, data were normalised to 14.6 dB above an average measured reflection spectrum of an FC/PC connector, through a 3 dB, 1550 nm coupler, as described in section 4.3.2.

Sample	**Scan rate (mm/s)**	**Average reflectance (± 2%)**	**FWHM reflection bandwidth (± 0.5 nm)**	$\frac{\partial\lambda_B}{\partial T}$ **at 300 °C (pm/°C)**	$\frac{\partial\lambda_B}{\partial\varepsilon}$ **(pm/με)**
O	1.3	14	28.4	13.88	1.18
P	1.0	40	28.6	13.94	1.18
Q	1.2	23	28.5	13.92	1.18

Table 6.1 Grating fabrication details including the scan rates, reflection properties and the temperature and strain sensitivities.

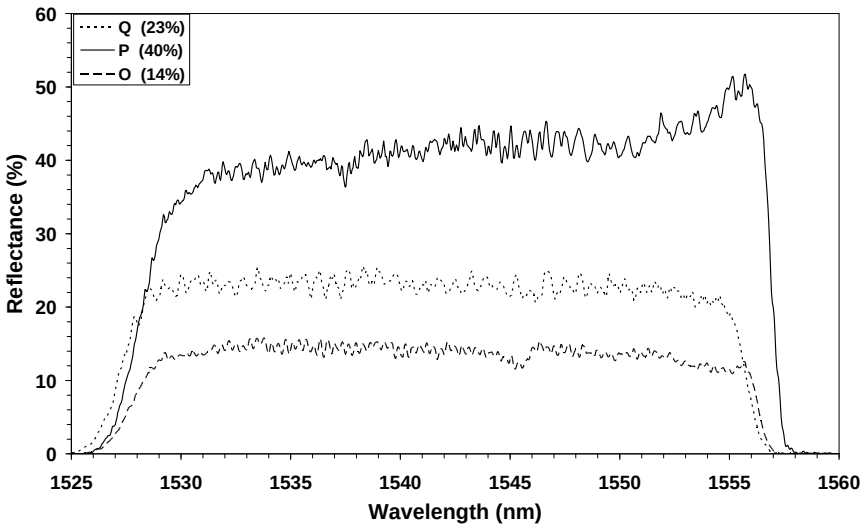

Figure 6.1 Reflection spectra of the embedded CFBGs chirped gratings used for the localised strain measurements.

6.3.2 Experimental system arrangement

To test the response of the CFBG sensors to a non-uniform strain field, near a stress concentration, an aluminium specimen of rectangular cross-section having dimensions of approximately (350 mm × 12 mm × 6 mm) was designed and fabricated. Two approximately rectangular (with a parabolic tip) notches of dimensions (width 1 mm, depth 3 mm) were machined into the specimen to generate a strain gradient along the axial direction of the specimen as shown in figure 6.2. The notch shape was selected to resemble closely a crack in a structure. Five of these specimen were fabricated. Using the shape of the notch and the linear elasticity theory of solid mechanics, the surface strain distribution along the specimen was calculated using finite element modelling as described in section 6.5.2.

A shallow slot of 0.5 mm in diameter machined on the surface (along the centre of the axial direction) of the specimen was used to embed a CFBG sensor. The sensor was embedded in the region of expected high strain gradient at the geometric centre of the notch using Loctite Fixmaster (97483) steel liquid epoxy. The Loctite fixmaster is a two part (resin and hardener) self levelling pourable epoxy that is heavily reinforced with steel powder. Once hardened it forms a strong bond with the host material and can be machined, drilled or filed with similar properties to steel. This epoxy was selected

because of its excellent mechanical properties and strong of attachment to both the fibre and aluminium once in the cured state. The epoxy was allowed to cure for 4 days at room temperature, with a small tension applied to the fibre to keep the fibre straight, prior to testing. This was to minimise the epoxy induced transverse stress on the fibre and the formation of strong bonds between the glass fibre (CFBG sensor), epoxy and the specimen. The epoxy has an approximate tensile strength of 41.4 N/mm^2 and a compressive strength of 93.1 N/mm^2 in the cured state.

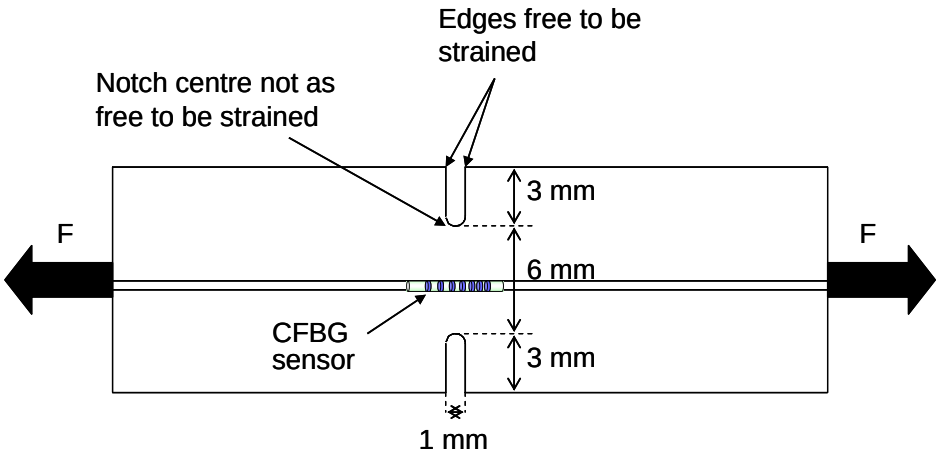

Figure 6.2 Schematic diagram of the aluminium specimen used to generate a strain gradient along the CFBG sensor.

Figure 6.3 shows a schematic of the experimental system used to apply an axial tensile load to the specimen together with the optical arrangement, which is similar to that used for the measurement of the position of a localised heat source described in chapter 5. The CFBG sensor was monitored in reflection using an Er^{3+}dual-band broadband light source via a 3 dB 1550 nm coupler. The reference and disturbed spectra were measured using an OSA with a resolution of 0.1 nm and saved on a computer. The specimen was subjected to a range of controlled static tensile loads using a materials testing machine ("LLoyD Instruments", version 3.1). The load was displacement controlled by means of a supporting frame attached to the actuator shaft of the machine, allowing the applied load and the displacement to be measured electronically. Axial tensile forces ranging from 0.5 kN to 8.0 kN in steps of 0.5 kN were applied to the specimen and the corresponding reflection spectra from the CFBG sensor were monitored and recorded using the optical setup. Each spectrum was obtained by averaging 50 OSA measurements at the specified load. Application of load in the axial direction assumed that transverse stress on the specimen was zero and only the strain in the axial direction

was transferred to the CFBG sensor. A strain calibration curve for the aluminium specimen, obtained from the force-displacement measurements during loading, is plotted in figure 6.4.

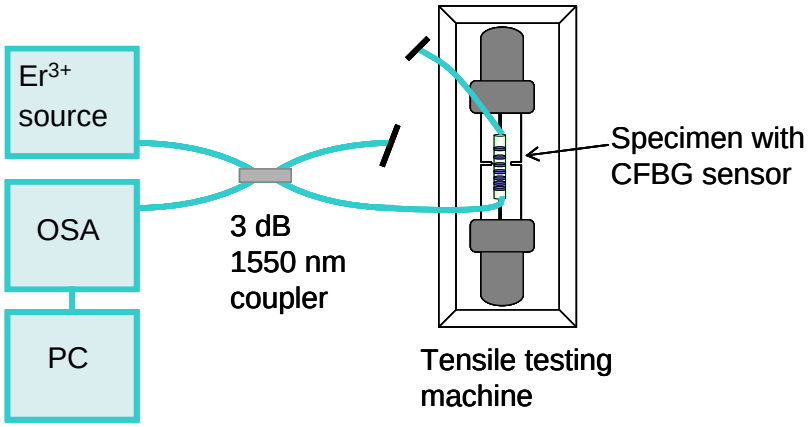

Figure 6.3 Schematic diagram of the experimental system for applying tensile load to the specimen.

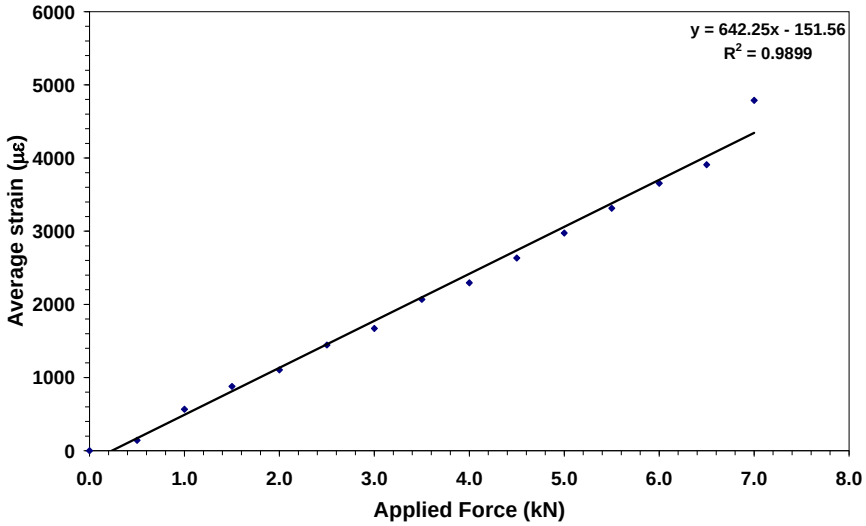

Figure 6.4 Average strain along the aluminium test specimen, obtained from the force-displacement measurement of the tensile testing machine, during loading using the arrangement of Fig 6.3.

6.4. Principle of Sensor Operation

6.4.1 Effect of localised (non-uniform) strain on local Bragg wavelength and reflectance of CFBGs

Consider the case of a CFBG with a linearly varying period of refractive index modulation along the length of the grating. Defining z as the coordinate in the axial direction of the CFBG, the local effective refractive index, $n_{eff}(z)$, can be expressed by the function

$$n_{eff}(z) = n_{eff} + \overline{\delta n}_{eff}(z)\left\{1 + v\cos\left[\frac{2\pi}{\Lambda_0}z + \phi(z)\right]\right\}, \qquad 6.1$$

where n_{eff} is the mode effective refractive index of the optical fibre core, $\overline{\delta n}_{eff}$ is the mean effective index change averaged over a grating period due to illumination by UV inscribing laser light, v is the fringe visibility, Λ_0 is the minimum grating period at zero strain and $\phi(z)$ describes the grating chirp. The chirp profile for this linearly CFBG can be represented as

$$\Lambda(z) = \Lambda_0 + cz, \qquad 6.2$$

where Λ_0 is the minimum grating pitch and $c = d\Lambda/dz$ is the rate of variation of grating pitch with position along the fibre.

Consider the case of a CFBG embedded into a specimen of non-uniform cross-sectional area (notched centre) which is subjected to a constant axial tensile force in the z direction. Due to strain gradients around the notches, the CFBG sensor is subjected to a non-uniform strain field, $\varepsilon_z(z)$ in the axial z direction. The strain gradient induces non-uniform changes in both the local period, $\Lambda(z)$, and local average refractive index, $n(z)$ in the region of the notch. The modification in grating pitch is a function of the physical elongation of the optical fibre due to the applied strain, and the change in mean refractive index is a function of the strain-optic coefficient. Therefore the reflected Bragg wavelengths and the shape of the reflected spectrum, $R(\lambda)$, are a function of strain distribution along the grating. Thus the reflected spectrum is not only shifted but

also undergoes a shape change. The shift in the local Bragg wavelength in the region of the grating subjected to the localised strain gradient can be expressed as

$$\Delta\lambda_B(z) = \left[\left(\frac{\partial\Lambda}{\partial\varepsilon}\Big/\Lambda\right) + \left(\frac{\partial n_{eff}}{\partial\varepsilon}\Big/ n_{eff}\right)\right]\lambda_B(z)\Delta\varepsilon\,. \tag{6.3}$$

Thus the local period, $\Lambda(z)$, and the local average refractive index, $n(z)$ at the location of the strain gradient can be expressed respectively using equations 6.4 and 6.5

$$\Lambda(z) = (\Lambda_0 + cz)\left[1 + \varepsilon_z(z)\right], \tag{6.4}$$

$$n(z) = n_{eff}(z) - \frac{n_{eff}^3(z)}{2}\left[p_{12} - \nu(p_{11} + p_{12})\right]\varepsilon_z(z)\,, \tag{6.5}$$

where $\varepsilon_z(z)$ is the applied axial strain field and p_{11} and p_{12} are strain-optic coefficients and ν is the Poisson's ratio of the fibre. Thus the modified local Bragg wavelength due to the localised strain gradient can be expressed as:

$$\lambda_B^{'}(z) = \lambda_B(z) + \Delta\lambda_B(z) = 2\left\{n_{eff}(z) + \delta n_{eff(\varepsilon)}(z)\right\}\left\{\Lambda(z) + \delta\Lambda_\varepsilon(z)\right\}. \tag{6.6}$$

The strain gradient modifies both the local period, $\Lambda(z)$, and the local average refractive index, $n(z)$ and thus the local chirp rate, the local Bragg wavelength and the grating strength in the region around this position. The Bragg wavelength of this region shifts in proportion to the magnitude of the strain change, reducing the number of grating planes contributing to this wavelength $\lambda_{B,ref}(z)$ and increasing the contribution at higher wavelengths. That is, the loss of a particular pitch length due to local strain results in a fall in power (reflectance) in the reflection spectrum at a particular wavelength and a corresponding increase in the power (reflectance) at other wavelengths. This generates a characteristic dip and hump in the reflectance spectrum around the strain gradient due to a nonlinear chirp. Hence the notch location can be identified from the shape of the reflectance spectrum. The region where the reflectance $R(\lambda)$ is reduced corresponds to the position, z, of the strain gradient and the magnitude of the strain can be calculated from the wavelength shift using the strain sensitivity of the CFBG sensor.

6.5. Data Analysis Techniques

6.5.1 Determination of the non-uniform strain profiles using the ISB intragrating sensing employing the integration method

The non-uniform strain distribution along the CFBG sensor was obtained by an integration technique. The unperturbed (reference, R_{ref}) and the perturbed (measured data, R_m) intensity reflection data were first transformed from units of reflectance, R, to linear units of grating length-coupling strength product, $\overline{Y}$, using equation 6.7. The area under the measured spectrum subjected to a localised strain was normalised to the area of the reference spectrum, taken under conditions of zero load according to equation 6.8 (Kitcher *et al.,* 2006). This normalisation ensured that the area under the reference and the measured spectra remained equal. Before processing, the reflectance values were clipped to lie within the limit (0.0001, 0.999), this being necessary to ensure that the integration algorithm operated only on the non-zero regions of the grating and to remove noise at the ends of the spectra.

$$\overline{Y}(\lambda) = \tanh^{-1}(\sqrt{R(\lambda)} \tag{6.7}$$

$$Y(\lambda) = \overline{Y}(\lambda)\frac{\int \overline{Y}_{ref}(\lambda')d\lambda'}{\int \overline{Y}(\lambda')d\lambda'} \tag{6.8}$$

The start edge wavelength shift, S, between the rising edges of the reference and the strained spectra was found by using a low pass filter for smoothing followed by thresholding. The difference between the spectra; the perturbed (Y_i) and the reference (Y_{ref}) was normalised to the reference spectrum and integrated according to equation 6.9 (Kitcher *et al.,* 2006)

$$Q(\lambda) = S - 2.2\int_{\lambda_1}^{\lambda} \frac{Y_i(\lambda' - S) - Y_{ref}(\lambda')}{Y_{ref}(\lambda')} d\lambda' . \tag{6.9}$$

In equation 6.9, λ_1 is the start wavelength at the rising edge of the spectra. An integration constant of the rising edge alignment shift, S, was added to the results to align the disturbed and the reference spectra. The rising and falling edges of the

perturbed and reference spectra were aligned with an accuracy better than 0.04 nm to prevent integrating the small power difference between the mismatched rising and falling edges of the spectra. The integration was performed twice, first in the forward direction and then on data in the reverse direction to obtain an initial estimate of $Q(\lambda)$. $Q(\lambda)$ is the profile of local wavelength shift. This nonlinear chirp function was used to resample the grating definition at particular wavelength points in the perturbed data spectrum. The process of bidirectional integration was repeated using the nonlinear chirp to obtain a final estimate of the local Bragg wavelength shift, $\Delta\lambda(z)$. The local Bragg wavelength shift as a function of position along the grating was converted to local strain, $\varepsilon(z)$, using the strain sensitivity ($\partial\lambda/\partial\varepsilon$) and the chirp rate of the sensor.

6.5.2 FEM modelling of strain distribution along the aluminium test specimen

The surface strain distribution along the specimen was calculated using the numerical structural finite element method (FEM) based on the linear elasticity theory of solid mechanics, using the commercial FEMAP/NASTRAN software. A 2-D FEM analysis was performed to simulate the strain distribution, since the specimen was subjected to an axial tensile force only. Only one quarter of the specimen was modelled because of the symmetry along the two directions. The mesh consisted of 6407 grid points (nodes) and 5976 rectangular elements. The mesh density around the notch centre was increased to improve the strain resolution for the strong nonuniform strain field expected around this region. The appropriate elastic constants for the test specimen were implemented in the FEM model for the calculation of strain distribution. Figure 6.5 shows the surface strain distribution along the specimen calculated using the FEM. The model shows that the strain peaks at approximately 2.2 mm on either side of the notch centre. The ratio of the strain at the notch centre to peak strains at either side of notch centre is approximately 0.8. This reduction in strain at the notch centre is explained in terms of bending in section 6.6.3.

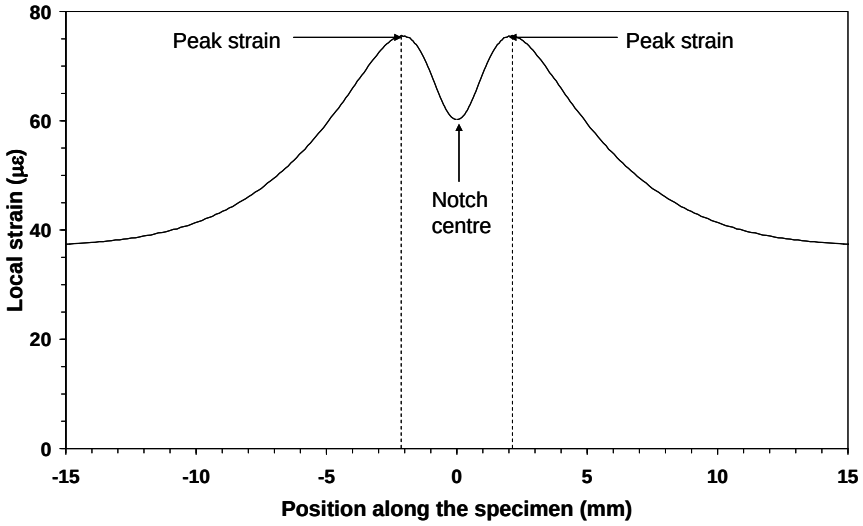

Figure 6.5 The FEM simulated strain distribution along the specimen for an applied force of 0.1 kN.

6.6. Results

6.6.1 Extraction of strain profiles – CFBG sensor O

The reflection spectra of the CFBGs were measured in order to investigate the response of the sensor to a strain gradient in the region around the notch. Figure 6.6 shows the reflected spectra from the grating for the indicated tensile loads. It was observed that during load application, a crack developed (at a low applied strain) in the epoxy within the region of the grating corresponding to a wavelength of approximately 1532 nm. The dimensions of the crack were much smaller than that of the notch. As a result the sensor was able to detect the strain field around the crack which had a strain gradient much greater than the shape induced strain gradient. As expected, the Bragg wavelength around the region of the crack growth shifted to longer wavelengths and the shape of the spectral response of the CFBG sensor changed.

Due to nonuniform changes in the local period, $\Lambda(z)$, and the local average refractive index, $n(z)$, around the crack location, a reduction in power reflectance at this wavelength is visible in the spectra with a corresponding increase in power at higher wavelength. This is because loss of certain pitch lengths due to local strain causes a fall

in the intensity of the reflection spectrum and a corresponding increase in the intensity at higher wavelengths. Thus the Bragg wavelength shifts to higher wavelengths. On application of a load of higher magnitude, the loss in power reflectance around the crack increased with further increase in power at higher wavelengths suggesting the propagation of the crack. That is, both the dip and the peak in the reflection spectrum increased. Away from the crack location, the CFBG sensor experienced an almost uniform strain field; thus the shape of the reflection response is mostly undisturbed.

The whole spectrum also shifts uniformly to higher wavelengths because of the uniform strain due to physical elongation of the fibre. Therefore the position of the development of a crack in the epoxy can be identified from the shape of the intensity reflection spectrum from a CFBG sensor. The region where the reflectance $R(\lambda)$ is reduced corresponds to the position, z, of the crack. The analysis is presented later in this section.

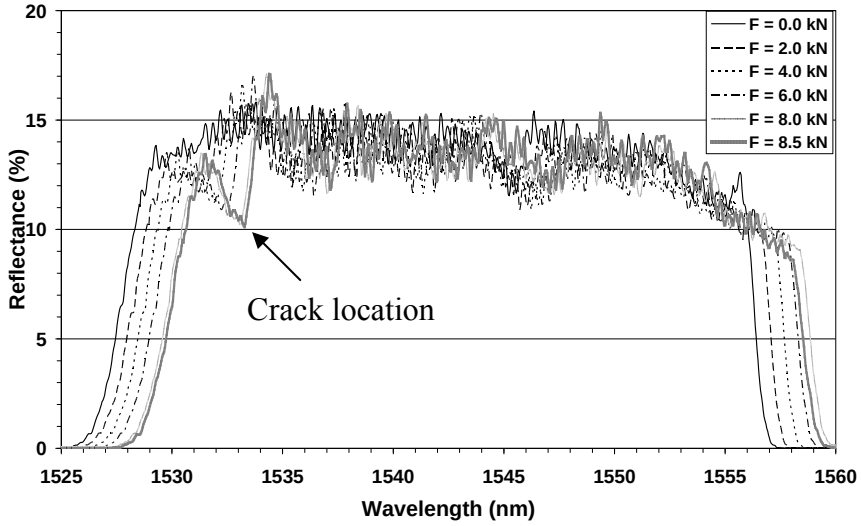

Figure 6.6 Reflection spectra from the CFBG sensor O subjected to various tensile loads during the development of a crack in the epoxy.

Figure 6.7 shows the local Bragg wavelength shift as a function of position along the grating. The sensor shows a nonuniform shift in reflected Bragg wavelength around the crack location ($z \cong -5.5$ mm) compared to other positions along the grating which show almost uniform shift. In the near vicinity of the crack, the change in pitch length is nonuniform due to a strain gradient resulting in nonlinear chirp and thus the change in the shape of the reflected spectrum. At other locations the CFBG sensor undergoes a

uniform change in pitch length due to uniform strain (fibre elongation), thus uniformly shifting the reflected Bragg wavelength to higher values for all locations. The slight nonuniformity in Bragg wavelength shift could be due to factors such as: a wavelength detection error (section 6.7.1) of the sensor, strain transfer mechanism from the surface to the fibre core, epoxy induced stress on the fibre and the bond formation between the epoxy and the CFBG sensor (section 6.8).

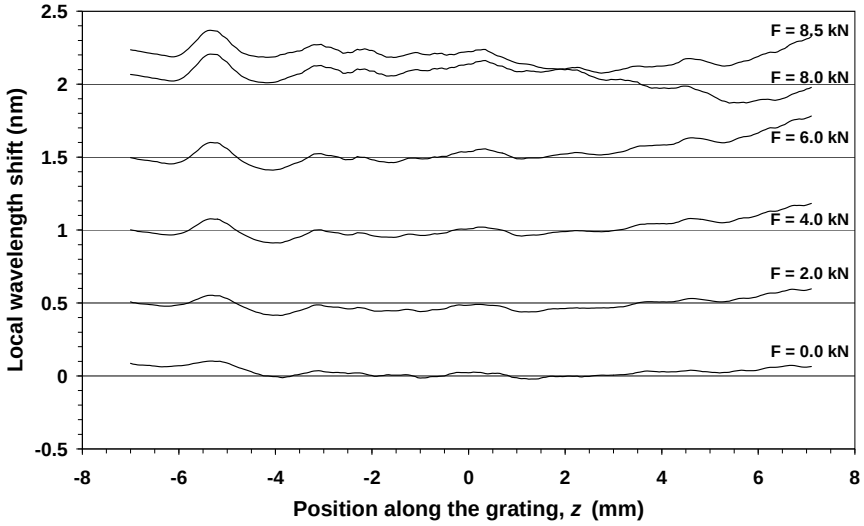

Figure 6.7 The local Bragg wavelength shift as a function of position along the CFBG sensor O during load application.

Figure 6.8 shows the recovered strain profile as a function of position along the grating, obtained using the integration of difference technique (section 6.5.1) for various loads. Thus the sensor is able to recover the shape of the nonuniform localised strain field around the crack location in the epoxy with a strain error of approximately 170 με (section 6.7.1). The extracted strain profiles show a clear trend of increase in strain gradient around the crack with increasing load and almost uniform strain away from the crack location.

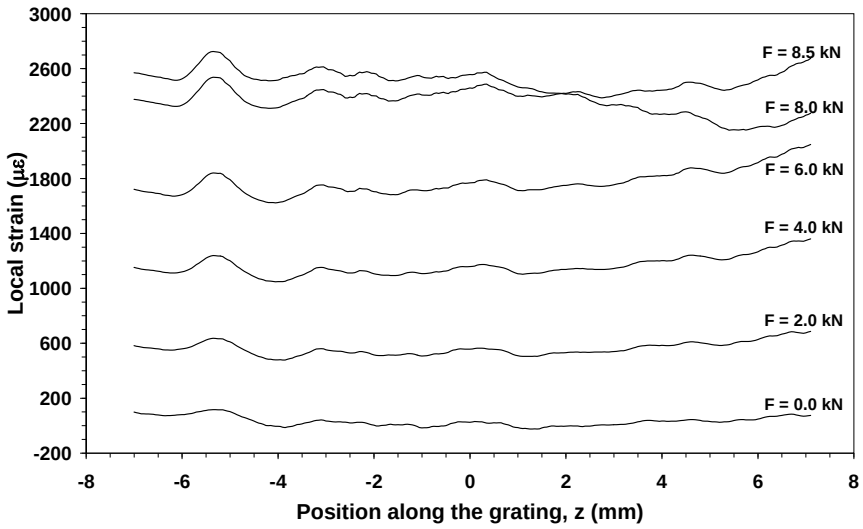

Figure 6.8 The strain profile as a function of position along the CFBG sensor O recovered using the integration method.

6.6.2 Extraction of strain profiles – CFBG sensor P

Figure 6.9 shows the reflected spectra from grating *P* subjected to various tensile loads. Each spectrum at a specified load was obtained by averaging 50 OSA measurements. As expected, the spectral response of the CFBG sensor changed due to induced strain gradients. The reduction in the power reflectance spectra at the notch location with a corresponding increase in power reflectance at either side of the notch centre are clearly visible.

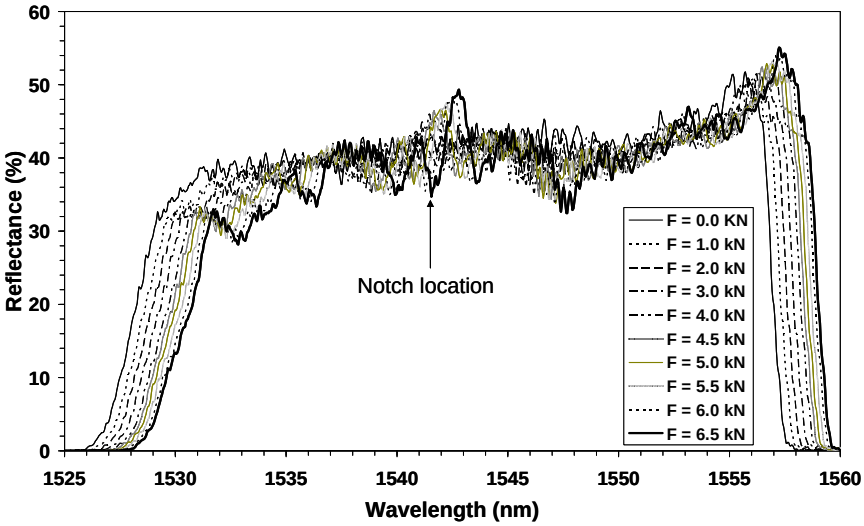

Figure 6.9 Reflection spectra from the CFBG sensor P subjected to various tensile loads.

Figure 6.10 shows the recovered strain profile as a function of position along the grating, obtained using the integration of difference technique (section 6.5.1) for various loads. The average local strain data for 50 repeat measurements at each applied force is presented. The strain profiles obtained for each repeat measurement at a particular applied force were highly repeatable (section 6.7.2). Thus the sensor is able to recover the shape of the nonuniform localised strain field around the notch. The shape of the extracted strain profiles are similar to that predicted by FE simulation; however the peaks on the either side of the notch centre are approximately 4 mm from the centre as compared to about 2.2 mm for the FEM model. This could be due to slight debonding between the fibre jacket and the epoxy resulting in fibre elongation. Thus the maximum peak strains would be experienced further apart from the notch centre with an increase in the applied force. A strain error of approximately 170 με has been estimated (6.7.1).

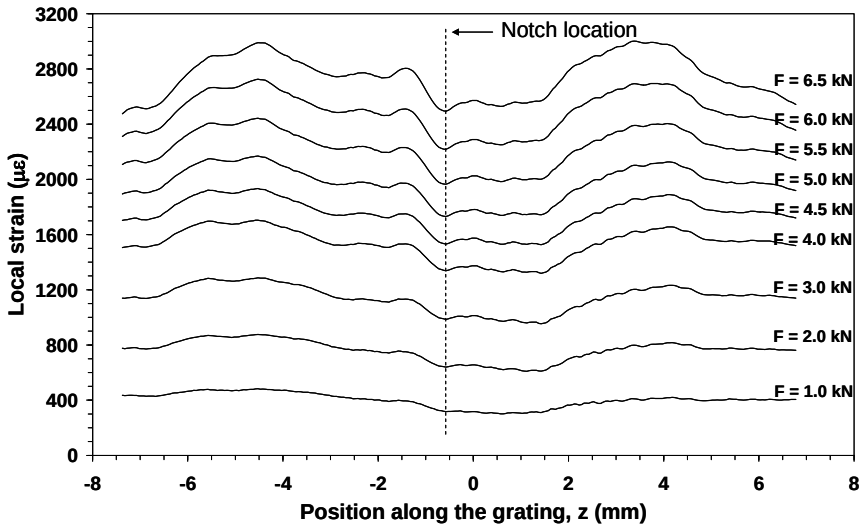

Figure 6.10 The strain profile as a function of position along the CFBG sensor P, obtained using the integration method.

6.6.3 Extraction of strain profiles – CFBG sensor Q

Figure 6.11 shows the reflected spectra from grating *Q* subjected to various tensile loads. The spectral response, $R(\lambda)$, of the CFBG sensor shows a characteristic dip and hump around the shape induced strain gradients. As expected, the local Bragg wavelengths around the notch shift to longer wavelengths and the grating chirp becomes nonlinear. The occurrence of two dips and humps suggest that there are two regions of peak strain on either side of the notch centre, which is in agreement with FEM

modelling. The modified peak reflectance, $R(\lambda)$, is approaching 80%, which justifies the use of gratings with low reflectance for intragrating measurements when large gradients are involved (Nand *et al.,* 2006).

Figure 6.12 shows the local Bragg wavelength shift as a function of position along the grating. The sensor shows nonuniform shift in the reflected Bragg wavelengths due to nonuniform changes in the pitch length resulting in nonlinear chirps and thus the change in the shape of the reflected spectrum around the notch centre. The nonlinear chirp is observed to increase with the magnitude of the applied force.

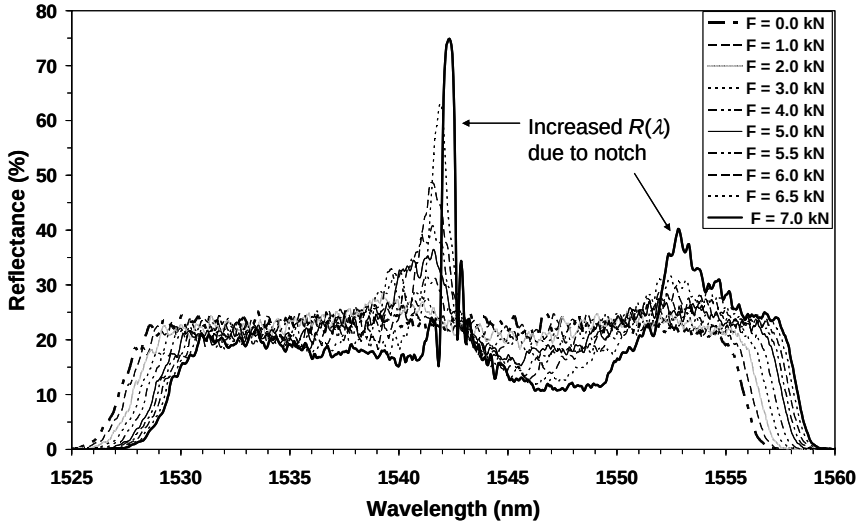

Figure 6.11 Reflection spectra from the CFBG sensor Q subjected to various tensile forces.

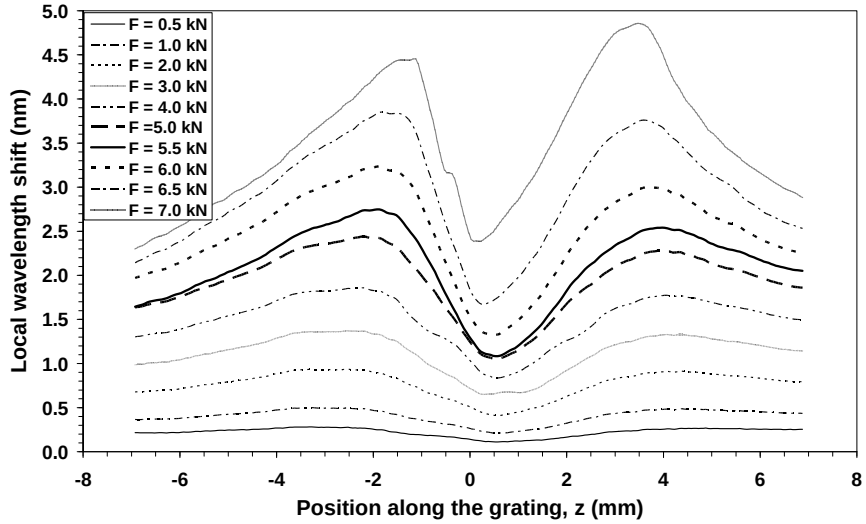

Figure 6.12 The local Bragg wavelength shift as a function of position along the CFBG sensor Q during load application.

Figure 6.13 shows the strain profiles (average of 50 repeat measurements) as a function of position along the grating at various applied forces, extracted from the CFBG spectra using the integration of difference technique (Nand *et al.,* 2007). A number of features are evident in the extracted strain profiles:

- the presence of two symmetric regions of high strain approximately 6 mm apart,
- the slight inward shift of approximately 0.5 mm in the position of the strain peaks at higher loads,
- the nonlinear increase in both the peak strains and the strain at the notch centre for applied forces greater than 4 kN,
- The ratio of strain at the notch centre (S_c) to the peak strains (S_P) are approximately 0.5 for forces < 4 kN, and slightly less than 0.5 for forces > 4 kN,
- The strain profiles are highly repeatable (section 6.7.2).

The extracted strain profiles are limited by the following uncertainties: strain error of approximately 170 με in the extracted $\varepsilon(z)$ due primarily to variations in the applied load (section 6.7.1), uncertainty in the sampling resolution of the measured data, the Bragg wavelength detection error, the Bragg wavelength alignment and shift error in the integration of difference (IOD) algorithm and the generation of the z axis from the grating chirp rate. Thus the inward shift in the position of the strain peaks is insignificant within the limits of position uncertainty. The observed trend could also be due to some systematic error either in the measurement system or the processing of $\varepsilon(z)$ by the IOD algorithm or both. The reduction in the ratio, (S_c/S_P), could be explained as the contribution to the strain field due to the bending of the specimen at higher forces.

Importantly, though, the shape of the recovered strain profiles and the positions of the regions of peak strains on either side of the notch centre, are in reasonable agreement with that predicted by FEM modelling, as shown in figure 6.5. The observed strain distribution can be explained in terms of bending around the edges of the notch centre, as the specimen is strained under a tensile force. The notch centre is not as free as the outer edges (figure 6.2) to be strained due to stronger bonding with the neighbouring molecules. The outer edges which are free to be strained, exhibit rotational behaviour about the notch centre. The strain due to this torque propagates towards the central axis where the CFBG sensor is located. This adds to the strain field around these regions resulting in peaks on either side of the notch centre.

Figure 6.14 shows an example of the reference and disturbed spectral response together with the extracted strain distribution at an applied force of 5.5 kN for sensor *Q*. The peaks of the strain distribution coincide closely with the valleys (dips) in the reflectance spectrum as expected.

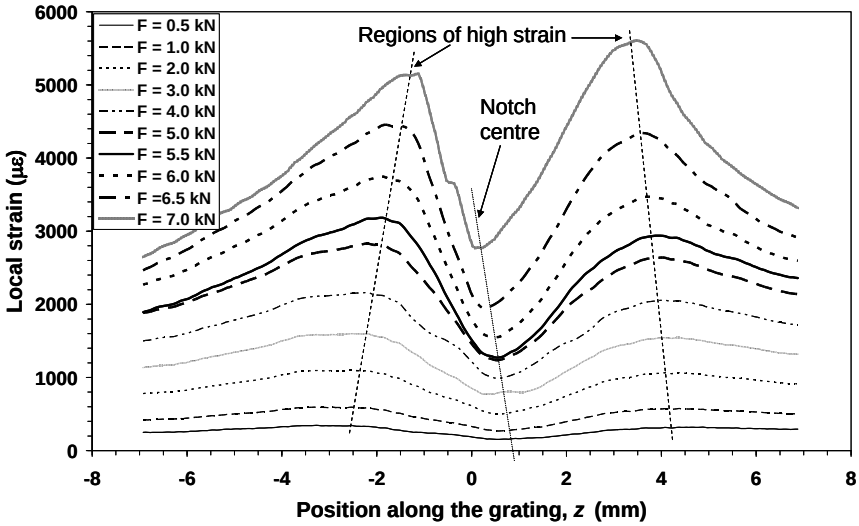

Figure 6.13 The strain profile as a function of position along the CFBG sensor Q obtained using the integration method.

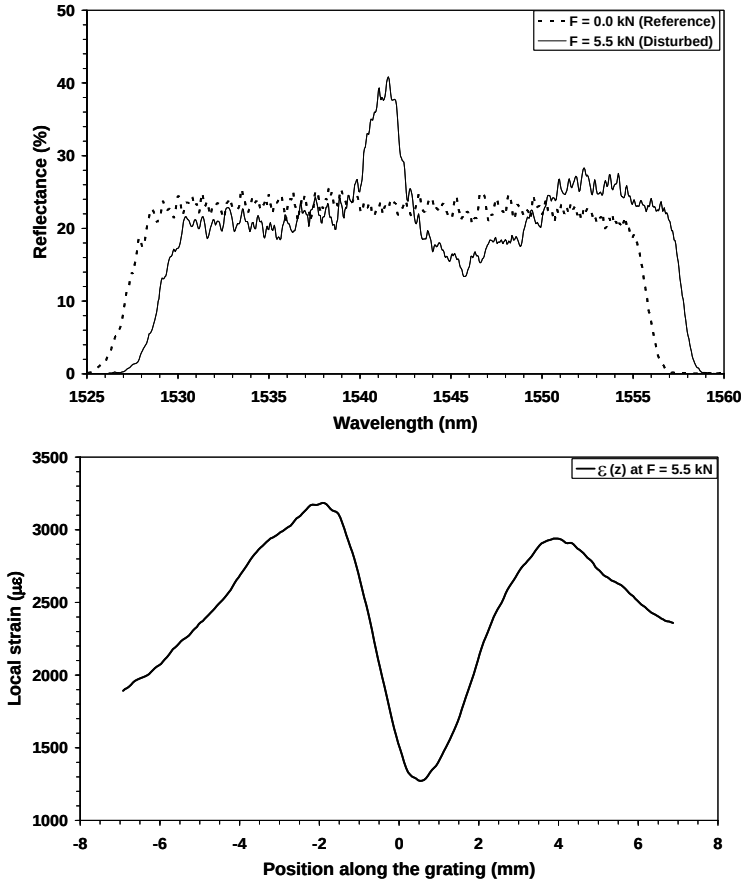

Figure 6.14 An example of the reference and disturbed spectral response together with the extracted strain distribution, ε(z), at F = 5.5 kN for sensor Q.

Figure 6.15 shows the extracted and FEM simulated strain profiles around the notch at an applied force of 1.0 kN for the sensor *Q*. There is good correlation between the shapes of these curves. However, closer inspection shows that the experimental strain evaluated by the sensor is approximately 100 με lower than that predicted by FEM calculations with the deviation being higher at the notch centre. This discrepancy is most likely due incomplete transfer of surface strain within the specimen through the 3-layers (host/adhesive/fibre) to the fibre core where the sensor is located. The deviations between the modelled and measured strain around the notch centre further verifies that sharply varying strain fields are weakly transferred to the sensor (Duck *et al.,* 1999, 2000, Ling *et al.,* 2005).

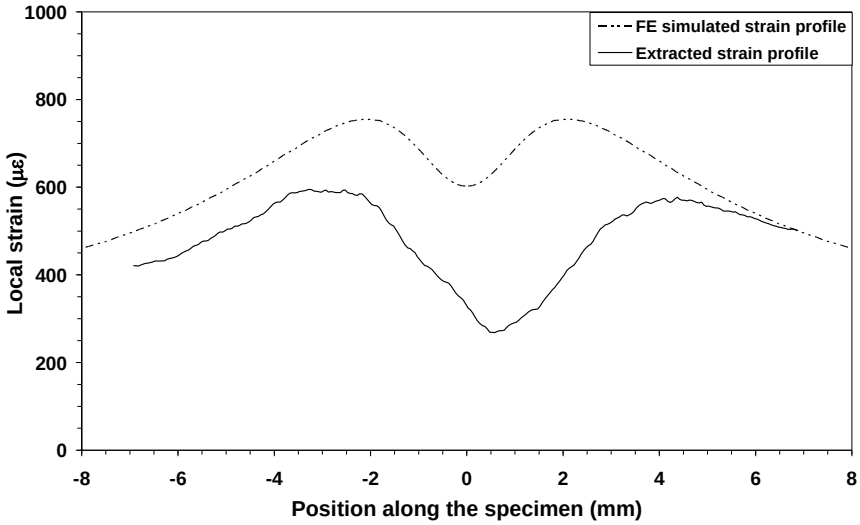

Figure 6.15 The extracted and the FEM modelled strain profiles around the notch centre for the CFBG sensor Q at an applied force of 1.0 kN.

Figure 6.16 shows the extracted and the FEM simulated strain profiles around the notch at an applied force of 5.5 kN for sensor *Q*. Though the occurrence of a pair of strain peaks, compare favourably with the FEM calculations, deviations are even larger when compared with the lower applied force of 1.0 kN. Deviations of approximately 1000 με along the sensor were observed with it being higher at the notch centre. This suggests that with an application of large stain gradient (sharp narrow strain field), the surface strain is poorly transferred to the fibre core.

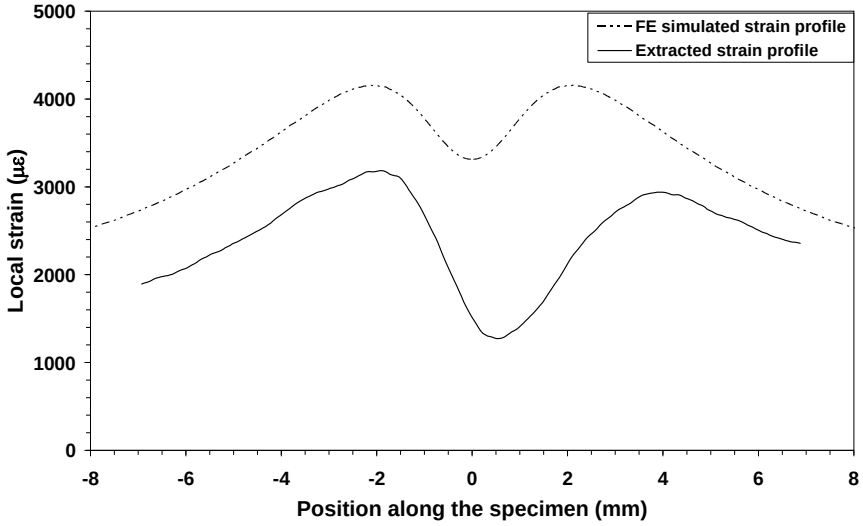

Figure 6.16 The extracted and the FEM modelled strain profiles around the notch centre for the CFBG sensor Q at an applied force of 5.5 kN.

6.7. Discussion and Performance of Sensors

This section investigates the performance of embedded CFBGs as intragrating strain sensors for the measurement of nonuniform localised strain distribution along a representative structural specimen. The performance of the sensors is investigated in relation to precision and repeatability of the recovered strain profiles. The extracted strain distributions are compared with that predicted by finite element modelling FEM. The discrepancies between the experimental and modelled strain distribution are explained in terms of strain transfer mechanisms.

The results of the two CFBG sensors (*P*, *Q*) employed for the measurement of localised non-uniform strain distribution compare reasonably with FEM simulation. The best performance was obtained for sensor *Q*. The reflection intensity spectra of all the sensors were modified around the notch indicating change in the local chirp rate (nonlinear) due to strain gradients. The shape of the recovered strain profiles, in particular the central dip surrounded by a pair of strain peaks, compare favourably with the FEM modelled strain distributions; however discrepancies were noted in the magnitude and the position of the peak strains.

6.7.1 Error in extracted strain profiles ε(z)

This section reports on the error budget for the recovered strain profiles. The strain error budget comprises of Bragg wavelength detection error at the OSA resolution used, the alignment (R_{ref} & R_{data}) error for the integration of difference algorithm and the strain error induced due to an applied force error of approximately 50 N.

Strain error budget

OSA resolution used	= 0.1 nm
$\Delta\lambda$ (span, FWHM bandwidth)	~30 nm
Sampling points	= 1000
Sampling resolution	= 30 nm/1000 = 30 pm
Maximum Bragg wavelength detection error($\partial\lambda_B$) for strain measurement with CFBGs (section 4.4.4)	= 0.02 nm
Bragg wavelength alignment error ($\partial\lambda_B$) from integration of difference program (section 6.5.1)	= 0.04 nm
Total ($\partial\lambda_B$)	= 0.06 nm = 60 pm
Strain sensitivity ($\partial\lambda_B/\partial\varepsilon$) of CFBG sensors (Table 6.1)	= 1.18 pm/με
Therefore strain error ($\partial\varepsilon$),	$\partial\varepsilon = (\partial\lambda_B/(\partial\lambda_B/\partial\varepsilon)$ = 60 pm/(1.18 pm/με) = 51 με
The strain error ($\partial\varepsilon$) due to an applied force error of ~50 N, calculated from the calibration equation of figure 6.4	= 120 με
Total strain error, $\partial\varepsilon$	**~170 με**

Thus if the systematic error in the strain profile due to the error in applied force is subtracted, a local strain error of approximately 50 με at all positions along the sensor is achieved.

6.7.2 Repeatability of extracted strain profiles

The repeatability error in strain profile was calculated as the rms variation of the extracted strain profile $[\varepsilon(z)_{extrcated} - \bar{\varepsilon}(z)_{extracted}]$ within the ten repeated measurements at each applied force. The repeatability rms errors as a function of position along the grating at each applied force were collated and the average rms repeatability of the whole data set (all $F_{applied}$) was calculated. Figure 6.17 shows the repeatability rms error in strain as a function of position along the grating (sensor *P*) at all values of applied

force. The repeatability rms error seems to be proportional to the strain gradient. That is, regions of high strain gradient along the sensor show poor repeatability.

Figure 6.18 shows the average repeatability rms error along the grating averaged over 100 measurements (i.e. 10 $F_{applied}$ × 10 repeat measurements at each F) for the three sensors. The best case performance was obtained for sensor *P* with an average repeatability rms error in the extracted strain profile of less than 4 με for the entire grating length. This is also consistent with the trend of improving repeatability with increasing grating strength (section 5.7.3). This could be explained as greater signal to noise ratio for sensor *P* which was the strongest grating with a reflectance of around 40%. The values reported here, are before the correction applied to the experimental force values. An experimental error of approximately 50 N in applied force was encountered during measurements. The tensile testing machine used was designed for the application of dynamic force to the specimen. Thus on application of static force, it was observed to be fluctuating around the required value with an error of approximately 50 N.

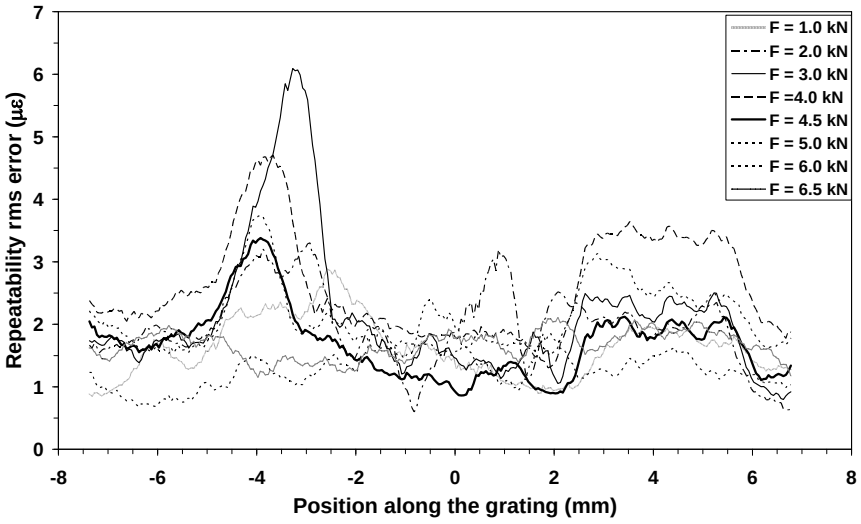

Figure 6.17 The repeatability rms error in strain profile as a function of position along the sensor P for various applied forces.

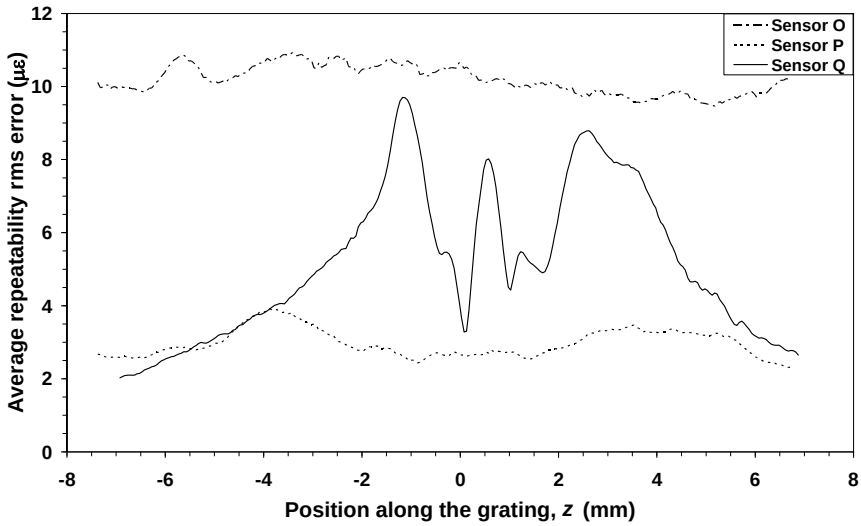

Figure 6.18 The average repeatability rms error in strain profile as a function of position along the grating for the three sensors investigated.

6.7.3 Strain Transfer Mechanisms

Generally in applications involving embedded CFBG sensors as strain sensors, it is assumed that the strain measured in the fibre core is the same as that experienced in the host material. This, however, is not a valid assumption as the strain transferred from the host material to an embedded CFBG sensor is influenced by a number of factors. The precision of the strain measured by the sensor depends on the strain transfer mechanism between the host and the fibre core. It is dependent on the bond formation between the CFBG sensor, the protective coating, the epoxy (adhesive layer) and the host material. Other factors which affect strain transfer are epoxy induced stress due to nonuniformity of the epoxy and the component of stress acting along other planes in a real application. Thus practically the surface strain experienced by the host specimen in not totally transferred through the layers of (host/epoxy/fibre) to the fibre core

To ensure that the axial strain from the host material is effectively transferred to the core of the sensing fibre the strain transfer mechanism of an embedded FBG needs further investigation. To correlate the strain measured by a FBG sensor with the host structural strain, strain transfer mechanisms of optical fibre embedded structures have been investigated (Duck *et al.,* 1999, 2000, Ling *et al.,* 2005, Betz *et al.,* 2006, Li *et al.,* 2006). Duck *et al.* (1999, 2000) developed mechanical models (two-cylinder) to predict the quality of strain transfer to the fibre core. The model showed that the strain transfer

is dependent on material parameters, geometric parameters and the steepness of the strain gradient (i.e. the variation of strain field in the host material).The model verified that quickly varying and sharp narrow strain fields were poorly transferred to the sensor.

The 4-cylinder model of (Ling *et al.,* 2005) was based on the bonding characterisation at the interfaces between the host material and the adhesive layer, the adhesive layer and the protective coating and the protective coating and the fibre core. This model also substantiated that the strain transfer efficiency was strongly dependent on the shape of the applied strain distribution.

All the models developed to-date are based on a low elasticity modulus for the host material. In the current research, a host material of large elasticity of 70 GPa with stiffness ratio of $(\frac{E_f}{E_h} \cong 1)$, in addition a sharp strain field of large strain gradient together with a bare fibre sensor with protective coating removed was employed for the measurements. For such a system, the strain transfer mechanism can be approximated by a 3-cylinder model similar to (Ling *et al.,* 2005). Development of such a model to investigate the bonding between the layers at the interfaces would significantly improve the accuracy of the results. However, such an investigation is beyond the scope of the current thesis.

Furthermore, since in this work the strain profiles were recovered directly from the integration of difference technique, which did not require the simulation of the experimental spectral response, $R(\lambda)$, using the in-fibre strain distribution, therefore the calculations are based on the assumption of 100% strain transfer to the fibre core. This seems to have significantly altered the recovered strain distribution due to strain attenuation for transferring strain through 3-material layers of (host/adhesive/fibre). Thus one option to improve the results would be to develop a strain transfer model to calculate the strain transfer efficiency (STE) of the system. The use of STE to correlate the experimental strain with the strain in the host specimen would improve the system performance.

Since the efficiency of the strain transferred to the core of the embedded sensing fibre is dependent on the geometry, material properties (stiffness), the strength of the bonding, strain gradient and the middle layers (adhesive and protective coating) between the host and the fibre, a specific strain transfer model needs to be implemented for the complete specimen and sensor system to predict accurately the actual structural strain in the host material.

Other factors that may be responsible for the discrepancy in the strain measured by the CFBG sensors in comparison with FEM model are the nonuniformity of the adhesive distribution along the fibre and cracking of the epoxy. Nonuniformity in adhesive distribution generates shear strains at the point of contact with the sensor which significantly affects the measured $R(\lambda)$ and the calculated $\varepsilon(z)$. Cracking of epoxy generates new strain fields which complicate the measured $R(\lambda)$ and the calculation of $\varepsilon(z)$ using the current algorithm. Thus further investigation on strain transfer mechanism, embedding techniques, selection of epoxy and the possibility of using gratings with low chirp rate to interpret correctly the structural strain in the host material from that measured by the CFBG sensor.

6.8. Conclusion

The measurement of nonuniform localised strain distribution within a notched aluminium specimen using embedded CFBG sensors has been demonstrated. The technique involved processing of power reflection spectra only and the sensing algorithm did not require a prior knowledge of the shape of the strain field. Such sensing systems have application in monitoring structural damage where the form of the strain field is expected to change continuously.

Table 6.2 shows the performance of the CFBG sensors investigated for the measurement of nonuniform localised stain distribution. A strain error of approximately 170 με and a repeatability rms error of less than 4 με in the strain profile, $\varepsilon(z)$, were obtained even before the implementation of a strain transfer mechanism for the system.

Parameters	Sensors		
	O	**P**	**Q**
Strain error in $\varepsilon(z)$, (με)	~170	~170	~170
RMS repeatability $\varepsilon(z)$, (με)	< 11	< 4	< 10
RMS error in $\varepsilon(z)$ in comparison with FE simulation at F = 1.0 kN, (με)	N.A	< 200	~190

Table 6.2 Performance of CFBG sensors as intragrating strain sensors.

CHAPTER 7

CONCLUSIONS

7.1 Summary of Key Outcomes

The use of the intensity (power) reflection spectrum based intragrating sensing scheme utilising chirped fibre Bragg gratings for the measurement of the position of a heat source and strain distribution have been demonstrated. The performance of the sensing schemes in relation to the measurement of the centre position of a localised heat source within a CFBG and nonuniform localised strain distribution near a stress concentration within a notched aluminium specimen have been investigated.

Initially, detailed literature reviews of distributed sensing (applications employing optical fibre as intrinsic sensing element) and intragrating sensing (applications employing fibre Bragg gratings as sensing elements) were presented. The capabilities of the four intragrating sensing (intensity, phase, combined intensity-phase and low coherence reflectometry) schemes were analysed in relation to their limitations, complexity of the measurement system, achievable resolution and practicality of application in order to design intragrating sensing schemes capable of detecting localised position and nonuniform strain distribution along the sensor length.

A significant aspect of the project was the fabrication and modelling of the CFBG spectra, controlling the grating spectral reflection response, bandwidth, length, chirp and strength suitable for intragrating sensing. It was theoretically (modelled) and experimentally verified that certain constraints exist for designing a suitable sensor using the prism technique. The invariably small lengths of grating possible with the system limited the spatial resolution desired for intragrating sensing. Thus most of the gratings used for the measurements were fabricated with the scanning phase mask system which allowed the spectral reflection responses of the CFBGs such as apodisation profile, length, bandwidth and reflectance be user defined and controlled.

The spectral responses of the CFBGs were simulated using a FFT grating reconstruction technique. In this work a comparison of the reflectance predicted by the FFT model against the conventional *TMM* for the case of an apodised CFBG subjected to a local temperature disturbance was made. It was justified that in the limit of the weak grating reflections investigated in this work, the FFT technique is in good agreement with the *TMM* technique. Thus due to its superior computation speed, (~1000 > *TTM*), as required for on-line processing of intragrating measurements, the FFT model was implemented for simulating the CFBG spectra and solving the inverse problem of obtaining the temperature distribution and the position of a localised heat source from the measured intensity reflection spectrum.

Nine gratings fabricated in hydrogen-loaded standard telecommunications Corning SMF-28 fibre were investigated for strain/temperature calibration. Three standard FBGs fabricated with the prism technique and six gratings (3 standard, 3 CFBGs) fabricated with the scanning phase mask technique were employed. Second order polynomial regressions were considered to fit experimental data for thermal response and linear regressions were used for strain response. The analysis of results for strain/temperature characterisation showed that CFBGs have a temperature coefficient approximately 20% higher than standard FBGs in the 1550 nm region with similar strain coefficients when wider temperature range is considered. Thus this research proposes a simple novel technique for strain-independent temperature measurement using a sensor head with a combination of a standard and a CFBG written in the same fibre. Strain-independent temperature measurements have been demonstrated over the temperature and strain range of 22-300 °C and 0-2500 με respectively. A temperature dependent sensitivity of 0.98 pm/°C and 2.37 pm/°C for strain–independent temperature measurements with rms errors of 2.2 °C and 1.5 °C at 22 °C and 300 °C respectively has been obtained.

Five linear CFBGs, of chirp rate 20 nm/cm, approximate length of 15 mm with varying levels of reflectance (6-53%), fabricated with the scanning phase mask technique were employed for the determination of the centre position of a localised heat source within a CFBG. An iterative approach in conjunction with a FFT was used for solving the inverse problem of obtaining the temperature distribution from the measured intensity reflection spectrum based intragrating sensing. In this technique, the measured spectrum

of a CFBG due to a localised temperature disturbance (heat source) was simulated using the FFT grating design model. The model operated on the reference spectrum and hypothesis temperature distributions, $T(z)$, to generate a spectrum of a CFBG subjected to a hypothesis temperature disturbance. The FFT simulated spectrum was iteratively fitted to the measured spectrum using a three-parameter automatic fitting of the centre position, width and amplitude of the temperature change to extract temperature distribution, $T(z)$, along the sensor length, z. The precision of the inferred centre position of the localised heat source as a function of grating strength (reflectance) was investigated.

The best performances were obtained for grating strengths (reflectance) in the range 20-30%. The position rms error improved from 0.053 mm for a $R(\lambda) = 5\%$ grating to 0.026 mm for a $R(\lambda) = 20\%$ grating with the moderate temperature amplitude, and from 0.043 mm for a $R(\lambda) = 5\%$ grating to 0.029 mm for a $R(\lambda) = 20\%$ grating with the large temperature amplitude. The trend of improving rms error with grating strength up to 20% reflectance, followed by a worsening of rms error for stronger gratings is consistent with theory when grating strengths are corrected for excess loss. Gratings stronger than 20% showed considerable excess loss, which varied somewhat along the grating. A higher excess loss imposed a lower limit to the level to which the disturbed spectrum could peak. This disrupted the estimate of temperature distribution and thus the precision of the inferred centre position.

The repeatability rms error in position measurement showed a clear trend of improving repeatability with increasing grating strength for both the high and the moderate temperature amplitudes. Increasing reflectance from 6 to 53% resulted in an improvement of rms repeatability from 0.011 mm to 0.004 mm with the moderate temperature amplitude, and from 0.009 mm to 0.005 mm with the large temperature amplitude. This can be understood as a straightforward effect of the improving signal/noise ratio with stronger gratings which return a stronger signal. It is noted that improvement is marginally slower than $\sqrt{R}$ for small signal cases and considerably slower than $\sqrt{R}$ for large signal measurements. This indicates that causes other than instrument noise were more significant in the large signal measurement cases.

Thus in this research, an iterative FFT technique for solving the inverse problem of obtaining the temperature distribution from the measured intensity reflection spectrum based intragrating sensing has been demonstrated. The position rms error of below 0.03 mm and repeatability rms error of below 0.005 mm obtained for the centre position measurements are an improvement on those reported previously for intragrating measurements employing chirped gratings (Won *et al.,* 2004). This is before the implementation of proper correction of interactions between temperature, width and position, which are expected to further enhance the performance of the measurement system. The use of CFBGs with a fast chirp rate of 20 nm/cm and with low reflectances resulted in spectra which were broader and more simple to interpret in comparison to previous work employing a much lower chirp rate (Won *et al.,* 2004). This reduced the resolution requirements of equipment to interrogate the sensor.

Three embedded linear CFBGs of chirp rate 20 nm/cm with approximate length of 15 mm, fabricated with the scanning phase mask technique, were employed for the measurement of nonuniform localised strain distribution near a stress concentration within a notched aluminium specimen subjected to an axial tensile force. The inverse problem of deducing the shape of the nonuniform strain distribution along the CFBG sensor was obtained as the cumulative sum of the normalized changes in the power reflectance spectra between the perturbed (measured data, R_m) and unperturbed (reference, R_{ref}) grating. Unlike other intragrating techniques, this sensing scheme did not require a hypothesis strain distribution to be postulated as a priori. An intragrating sensor of this type is expected to find many applications in the field of structural health monitoring.

The best case performance was obtained with the sensor having a reflectance of around 23%. The shape of the recovered strain distribution, in particular the occurrence of a pair of strain peaks, compare favourably with that predicted by the FEM simulation; however, the magnitude of the strain distribution evaluated by the CFBG sensor was approximately two-third of that calculated by FEM modeling. The discrepancy is most likely due to incomplete transfer of surface strain within the specimen through 3 material layers (host/adhesive/fibre) to the fibre core where the sensor is located. A repeatability rms error of less than 4 με in the extracted strain profiles was obtained.

In conclusion, intensity reflection spectrum based intragrating sensing scheme utilising CFBGs for the measurement of localised position of a heat source and nonuniform strain distribution have been demonstrated. In these measurements, linear CFBGs with a fast chirp rate of 20 nm/cm and low reflectances have been used. Such sensing schemes exhibit a number of advantages over other intragrating sensing systems:

- The broadband spectrum from a CFBG sensor provides high sensitivity and superior spatial resolution as the number of sampling points along the sensor can be enormously increased to provide a complete mapping of the disturbance field,

- The spectra from a fast chirp rate grating are simple to interpret and are an order of magnitude broader than low chirp rate gratings. This reduces the resolution requirement of the interrogation system. A position rms error of below 0.03 mm and repeatability rms error of below 0.005 mm obtained for the centre position measurements are better than those reported previously for intragrating measurements employing chirped gratings,

- The complex and expensive phase spectrum measurements are not required as the sensor operation is based on the measurement and analysis of the intensity reflection spectrum alone. This results in a simple and inexpensive measurement system,

- The use of an iterative FFT for solving the inverse problem of obtaining the temperature distribution significantly reduced the on-line processing time for intragrating measurements. The processing time for the FFT model is approximately 1000 times faster than the *TMM* model,

- The use of integration of changes in the power reflectance spectra between the perturbed and unperturbed grating to deduce the nonuniform strain distribution does not require an initial hypothesis strain distribution to be postulated.

7.2 Future Work

It is recommended that work be undertaken to improve the performance of CFBG based intragrating sensing systems to bridge the gap between laboratory and industrial applications. Such sensing systems have potential applications in measuring temperature profiles within electronic and power conversion devices and in structural health monitoring systems by providing real-time measurements on de-bonding around attachment points and propagation and location of cracks. Thus a number of issues recommended to be addressed are listed below.

- Improvements in grating fabrication and simulation techniques for designing flat top hat apodised linear CFBGs suitable for intragrating sensing applications. This would require better understanding of photosensitivity in optical fibres, photosensitisation techniques and refractive index modulation.

- Investigation of other parameters such as grating chirp rate in combination with grating strength (reflectance). These parameters together determine the effective length (L_{eff}) sensor length, bandwidth, the S/N ratio of the measured reflection spectrum and the sensor performance (precision and repeatability of position and strain measurements).The sensor performance is also dependent on the amplitude, width, shape and gradient of the applied disturbance and the interaction between these parameters. Thus implementation of proper correction of interactions between these parameters needs further investigation. This would lead to the design of an optimal CFBG intragrating sensor with the best set of parameters for the reflectance (grating strength) and chirp rate, which would significantly improve the sensor performance.

- An investigation of position resolution versus chirp rates. Without any experimental data, it can only be stated that the position resolution normally improves with chirp rate due to broader spectra for the same grating length, which reduces the resolution requirements of equipment to interrogate the sensor. High chirp rate also reduces the effective reflection length of the grating, which improves the resolution since the effective length (L_{eff}) is inversely proportional to square root the grating chirp (also strain or temperature

gradient). This can also be verified from spatial resolution equation proposed by Kersey *et al*., (1997). Low chirp gratings on the other hand, introduce an error at the grating end regions due to the effective length being almost equal to physical length of the grating. That is, a large part of the reflection wavelength is subjected to side distortion near grating ends. This leads to a significant error between the measured and simulated spectra reducing the resolution. However the grating chirp can not be infinitely high because this will reduce the grating reflectance as fewer grating pitches would contribute to a particular reflected wavelength. This low reflectance or low signal to noise ratio would result in poor position resolution. Thus an optimal chirp rate (upper limit) can only be determined from experimental measurements and it would depend on a number of factor such as index modulation (grating strength), power of the light source, resolution of the measurement and interrogation system, power loss and signal to noise level of the system.

- Further investigation of the four intragrating sensing (intensity, phase, combined intensity-phase and low coherence reflectometry) schemes together with review of grating reconstruction techniques for solving the inverse problem that can provide better fit and computationally inexpensive on-line processing system to enhance sensor performance.

- Design and automation of sensor interrogation systems that are inexpensive and meet the resolution requirement for Bragg wavelength detection together with spatial resolutions desired for specific applications. The success of FBG based intragrating sensing systems rely on the precision of interrogation techniques employed to detect the Bragg wavelength shift due to the external perturbations.

- Investigation of the techniques of bonding the sensor to the host material (e.g. surface mounting and embedding), type of epoxy, type and strength of bond formation at the interface layers would improve the system design and the expected performance.

- Development of a model for the strain transfer mechanism to calculate the strain transfer efficiency (STE) for the given set of parameters (geometry and mechanical properties of the host material, epoxy properties, strength of the bonding, expected strain gradient and the use of gratings with low chirp rate). The use of the STE to correlate the strain in the host material with that measured by the sensor would significantly enhance the system performance for intragrating strain sensing.

Bibliography

Achaerandio E., Jarabo S., Abad S. and Lopez-Amo M., New WDM amplified network for optical sensor multiplexing, *IEEE Photon. Technol. Lett.*, **11(12)**: 1644-1646, 1999.

Alahbabi M. N., Cho Y. T. and Newson T. P., 100 km distributed temperature sensor based on coherent detection of spontaneous Brillouin backscatter, *Meas. Sci. Technol*., **15**: 1544-1547, 2004b.

Alahbabi M. N., Cho Y. T. and Newson T. P., Long-range distributed temperature and strain optical fibre sensor based on the coherent detection of spontaneous Brillouin scattering with in-line Raman amplification, *Meas. Sci. Technol*., **17**: 1082-1090, 2006.

Alahbabi M. N., Lawrence N. P., Cho Y. T. and Newson T. P., High spatial resolution microwave detection system for Brillouin-based distributed temperature and strain sensors, *Meas. Sci. Technol*., **15**: 1539-1543, 2004a.

Anderson D. Z., Mizrahi V., Erdogan T. and White A. E., Production of in-fibre gratings using a diffractive optical element, *IEEE Photon. Technol. Lett*., **29(6)**: 566-568, 1993.

Aslund M. and Canning J., Annealing properties of gratings written into UV-presensitized hydrogen-outdiffused optical fiber, *Opt. Lett*., **25(10)**: 692-694, 2000.

Asseh A., Storoy H., Sahlgren B. E., Sandgren S. and Stubbe R. A. H., A writing technique for long fiber Bragg gratings with complex reflectivity profiles, *J. Lightwave Technol*., **15(8)**: 1419-1423, 1997.

Atkins R. M., Lemaire P. J., Erdogan T. and Mizrahi V., Mechanisms of enhanced UV photosensitivity via hydrogen loading in germanosilicate glasses, *Electron. Lett.,* **29(14)**: 1234-1235, 1993.

Azana J. and Muriel M. A., Reconstruction of fiber grating period profiles by use of Wigner-Ville distributions and spectrograms*, J. Opt. Soc. Am. A*, **17(12)**: 2496-2505, 2000.

Azana J., Muriel M. A., Chen L. R. and Smith P. W. E., Fiber Bragg grating period reconstruction using time-frequency signal analysis and application to distributed sensing, *J. Lightwave Technol*., **19(5)**: 646-654, 2001.

Baker S. R., Rourke H. N., Baker V. and Goodchild D., Thermal decay of fiber Bragg gratings written in boron and germanium codoped silica fiber, *J. Lightwave Technol*., **15(8)**: 1470-1477, 1997.

Bao X., DeMerchant M., Brown A. and Bremner T., Tensile and compressive strain measurement in the lab and field with the distributed Brillouin scattering sensor, *J. Lightwave Technol*., **19(11)**: 1698-1704, 2001.

Bao X., Webb D. J. and Jackson D. A., 22 km distributed temperature sensor using Brillouin gain in an optical fibre, *Opt. Lett*., **18**: 552-554, 1993.

Bao X., Dhliwayo J., Heron N., Webb D. J. and Jackson D. A., Experimental and theoretical studies on a distributed temperature sensor based on Brillouin scattering, *J. Lightwave Technol*., **13(7)**: 1340-1348, 1995.

Bernardin J. P. and Lawandy N. M., Dynamics of the formation of Bragg gratings in germanosilicate optical fibers, *Opt. Commun*., **79(3-4)**: 194-199, 1990.

Bernini R., Minardo A. and Zeni L., Accuracy enhancement in Brillouin distributed fiber-optic temperature sensors using signal processing techniques, *IEEE Photon. Technol. Lett.*, **16(4)**: 1143-1145, 2004.

Blows J. L., Hambley P. and Poladian L., Increasing fiber photosensitivity to near-UV radiation by rare earth doping, *IEEE Photon. Technol. Lett.,* **14(7)**: 938-940, 2002.

Boiarski A. A., Pilate G., Fink T., Nilsson N. and Edison O., Temperature measurements in power plant equipment using distributed fiber optic sensing, *IEEE Trans. On Power Delivery*, **10(4)**: 1771-1778, 1995.

Brambilla G. and Pruneri V., Enhanced photorefractivity in tin-doped silica optical fibers (review), *IEEE J. of Selected Topics in Quantum Electronics,* **7(3)**: 403-408, 2001.

Brambilla G., Pruneri V. and Reekie L., Photorefractive index gratings in SnO_2:SiO_2 optical fibers, *Appl. Phys. Lett*., **76(7)**: 807-809, 2000.

Brown A. W., DeMerchant M. D., Bao X. and Bremner T. W., Spatial resolution enhancement of a Brillouin-distributed sensor using a novel signal processing method, *J. Lightwave Technol*., **17(7)**: 1179-1183, 1999.

Byron I. C. and Rourke H. N., Fabrication of chirped fibre gratings by novel stretch and write technique, *Electron. Lett.,* **31(1)**: 60-61, 1995.

Byron K. C., Sugden K., Bricheno T. and Bennion I., Fabrication of chirped Bragg gratings in photosensitive fibre, *Electron. Lett*., **29(18)**: 1659 -1660, 1993.

Canning J., Photosensitization and photostabilization of laser-induced index changes in optical fibers, *Optical Fiber Technology: Materials, Devices & Systems*, **6(3)**: 275-289, 2000.

Casagrande F., Crespi P., Grassi A. M., Lulli A., Kenny R. P. and Whelan M. P., From the reflected spectrum to the properties of a fiber Bragg grating: A genetic algorithm approach with application to distributed strain sensing, *Appl. Opt.*, **41(25)**: 5238-5244, 2002.

Cheng H.-C. and Lo Y.-L., The synthesis of multiple parameters of arbitrary FBGs via a genetic algorithm and two thermally modulated intensity spectra, *J. Lightwave Technol*., **23(6)**: 2158-2168, 2005.

Chiang Y.-J., Wang L., Chen H.-S., Yang C.-C. and Liu W.-F., Multipoint temperature-independent fiber-Bragg-grating strain-sensing system employing an optical-power-detection scheme, *Appl. Opt.*, **41(9)**: 1661-1667, 2002.

Chisholm K. E., Everall L. A., Williams J. A. R., Zhang L. and Bennion I., Apodised fibre Bragg grating arrays for quasi-distributed strain sensing, *Lasers and Electro-Optics Society Annual Meeting, 1998, (LEOS '98. IEEE)*, **1**: 399-4000, 1998.

Cho S.-H., Park J., Kim B. and Kang M.-H., Fabrication and analysis of chirped fiber Bragg gratings by thermal diffusion, *ETRI Journal*, **26(4)**: 371-374, 2004.

Cho Y. T., Alahbabi M. N., Gunning M. J. and Newson T. P., Enhanced performance of long range Brillouin intensity based temperature sensors using remote Raman amplification, *Meas. Sci. Technol*., **15**: 1548-1552, 2004.

Chtcherbakov A. A. and Swart P. L., Chirped fiber-optic Bragg grating interrogator in a multiplexed Bragg grating sensor configuration, *J. Lightwave Technol*., **22(6)**: 1543-1547, 2004.

Cusano A., Capoluongo P., Cutolo A. and Giordano M., Chirped fiber-Bragg grating as self-temperature referenced strain sensor in nonisothermal thermoset processing, *IEEE Sensors J.*, **6(1)**: 111-117, 2006.

Davis M. A. and Kersey A. D., Simultaneous measurement of temperature and strain using fibre Bragg gratings and Brillouin scattering, *IEE Proc. Optoelectron*, **144(3)**: 151-155, 1997.

Davis M. A., Bellemore D. G., Putnam M. A. and Kersey A. D., Interrogation of 60 fibre Bragg grating sensors with microstrain resolution capability, *Electron. Lett*., **32(15)**: 1393-1394, 1996.

Dockney M. L., James S. W. and Tatam R. P., Fibre Bragg gratings fabricated using a wavelength tuneable laser source and a phase mask based interferometer, *Meas. Sci. Technol*., **7**: 445-448, 1996.

Dockney M. L., Read I. J., Foote P. D. and Tatam R. P., Embedded optical fibre Bragg gratings for aerospace monitoring, *Optical Techniques for Smart Structures and Structural monitoring (Digest No. 1997/033), IEE,* 8/1-8/6, 1997.

Dong L., Cruz J. L., Reekie L. and Archambault J. L., Tuning and chirping fiber Bragg gratings by deep etching, *IEEE Photon. Technol. Lett.,* **7(12)**: 1433-1435, 1995.

Dong L., Cruz J. L., Reekie L. and Tucknott J. A., Fabrication of chirped fibre gratings using etched tapers, *Electron. Lett.,* **31(11)**: 908-909, 1995.

Dong L., Cruz J. L., Reekie L., Xu M. G. and Payne D. N., Enhanced photosensitivity in tin-codoped germanosilicate optical fibers, *IEEE Photon. Technol. Lett.,* **7(9)**: 1048-1050, 1995.

Dong L., Cruz J. L., Tucknott J. A., Reekie L. and Payne D. N., Strong photosensitive gratings in tin- doped phosphosilicate optical fibers, *Opt. Lett*., **20(19)**: 1982-1984, 1995.

Dong X., Meng H., Liu Z., Kai G. and Dong X., Bend measurement with chirp of Bragg grating, *Smart Mater. Struct*., **10**: 1111-1113, 2001.

Dong X., Zhan C., Hu K., Shum P. and Chan C. C., Temperature-insensitive tilt sensor with strain-chirped fiber Bragg gratings, *IEEE Photon. Technol. Lett.*, **17(11)**: 2394-2396, 2005.

Douay M., Xie W. X., Taunay T., Bernage P., Niay P., Cordier P., Poumellec B., Dong L., Bayon J. F., Poignant H. and Delevaque E., Densification involved in the UV-based photosensitivity of silica glasses and optical fibers, *J. Lightwave Technol*., **15(8)**: 1329-1342, 1997.

Dragomir A., Nikogosyan D. N. and Brambilla G., Increased photosensitivity of Ge-doped and Ge-Sn-doped fibres under high-intensity 264 nm laser light, *Electron. Lett.,* **39(20)**: 1437-1439, 2003.

Dubaniewicz T. H., Kovalchik P. G., Scott L. W. and Fuller M. A., Distributed measurement of conductor temperatures in mine trailing cables using fibre-optic technology, *IEEE Trans. On Industry Applications,* **34(2)**: 395-398, 1998.

Duck G. and LeBlanc M., Arbitrary strain transfer from a host to an embedded fiber-optic sensor, *Smart Mater. Struct*., **9**: 492-497, 2000.

Erdogan T., Fiber grating spectra, *J. Lightwave Technol*., **15(8)**: 1277-1294, 1997.

Erdogan T., Mizrahi V., Lemaire P. J. and Monroe D., Decay of Ultraviolet-induced fiber Bragg gratings, *J. Appl. Phys.*, **76(1)**: 73-80, 1994.

Everard J. K. A. and Thomas R., Distributed optical fibre temperature sensor using spread-spectrum techniques, *Electron. Lett*., **25(2)**: 140-142, 1989.

Fallon R. W., Zhang L. and Bennion I., Multiplexed identical broad-band-chirped grating interrogation system for large-strain sensing applications, *IEEE Photon. Technol. Lett.,* **9(12)**: 1616-1618, 1997.

Fallon R. W., Zhang L., Gloag A. and Bennion I., Identical broadband chirped grating interrogation technique for temperature and strain sensing, *Electron. Lett*., **33(8)**: 705-707, 1997.

Farahani M. A. and Gogolla T., Spontaneous Raman scattering in optical fibers with modulated probe light for distributed temperature Raman sensing, *J. Lightwave Technol*., **17(8)**: 1379-1391, 1999.

Farries M. C., Sugden K., Reid D. C. J., Bennion I., Molony A. and Goodwin M. J., Very broad reflection bandwidth (44 nm) chirped fibre gratings and narrow bandpass filters produced by the use of an amplitude mask, *Electron. Lett.,* **30(11)**: 891-892, 1994.

Fells J. A. J., Goodwin M. J., Groves-Kirkby C. J., Reid D. C. J., Rule J. E. and Snell M. B. Fibre optic sensing for military bridge health and load monitoring, *Optical Techniques for Smart Structures and Structural Monitoring (Digest No. 1997/033)*, *IEE*, 10/1-10/11, 1997.

Floreani F., Gillooly A., Zhang L., Bennion I., Shu X. and Sugden K., A simple method for the fabrication of intrinsically apodized chirped fibre Bragg gratings, *J. Opt. A: Pure Appl. Opt*., **5**: S59-S62, 2003.

Frazao O., Melo M., Marques P. V. S. and Santos J. L., Chirped Bragg grating fabricated in fused fibre taper for strain-temperature discrimination, *Meas. Sci. Technol*., **16**: 984-988, 2005.

Friebele E. J., Askins C. G., Putnam M. A., Fosha A. A., Florio J., Donti R. P. and Blosser R. G., Distributed strain sensing with fiber Bragg grating arrays embedded in crtm^{tm} composites, *Electron. Lett*., **30(21)**: 1783-1784, 1994.

Garchev D. D., Vasiliev M. and Booth D. J., Wavelength-tunable chirped in-fibre Bragg gratings produced with a prism interferometer, *Opt. Commun*., **148**: 254 -258, 1998.

Gill A., Peters K. and Studer M., Genetic algorithm for the reconstruction of Bragg grating sensor strain profiles, *Meas. Sci. Technol*., **15**: 1877-1884, 2004.

Gillooly A. M., Chisholm K. E., Zhang L. and Bennion I., Chirped fibre Bragg grating optical wear sensor, *Meas. Sci. Technol*., **15**: 885-888, 2004.

Gillooly A. M., Dobb H., Zhang L. and Bennion I., Distributed load sensor by use of a chirped Moire fiber Bragg grating, *Appl. Opt.*, **43(35)**: 6454-6457, 2004.

Gillooly A. M., Zhang L. and Bennion I., Implementation of a distributed temperature sensor utilising a chirped Moire fiber Bragg grating, *Opt. Commun*., **242**: 511-515, 2004.

Guan B.-O., Tam H.-Y., Tao X.-M. and Dong X.-Y., Highly stable fiber Bragg gratings written in hydrogen-loaded fiber, *IEEE Photon. Technol. Lett.,* **12(10)**: 1349-1351, 2000.

Hara T., Terashima K., Takashima H., Suzuki H., Nakura Y., Makino Y., Yamamoto S. and Nakamura Y., Development of long range optical fiber sensors for composite submarine power cable maintenance, *IEEE Trans. on Power Delivery*, **14(1)**: 23-30, 1999.

Hartog A. H., A distributed temperature sensor based on liquid-core optical fibers, *J. Lightwave Technol*., **1(3)**: 498-509, 1983.

Hartog A., Distributed fibre-optic temperature sensors: Technology and applications in the power industry, *Power Eng. J*., 114-120, 1995.

Hill K. O. and Meltz G., Fiber Bragg grating technology fundamentals and overview, *J. Lightwave Technol*., **15(8)**: 1262 -1276, 1997.

Hill K. O., Jujii Y., Johnson D. C. and Kawasaki B. S., Photosensitivity in optical fiber waveguides: application to a reflection filter fabrication, *Appl. Phys. Lett*., **32(10)**: 647-649, 1978.

Hill K. O., Malo B., Bilodeau F. and Johnson D. C., Bragg gratings fabricated in monomode photosensitive optical fibres by uv exposure through a phase mask, *Appl. Phys. Lett*., **62**: 1035-1037, 1993.

Horiguchi T., Shimizu K., Kurashima T., Tateda M. and Koyamada Y., Development of a distributed sensing technique using Brillouin scattering, *J. Lightwave Technol*., **13(7)**: 1296-1302, 1995.

Hotate K. and Ong S. S. L., Distributed dynamic strain measurement using a correlation-based Brillouin sensing system, *IEEE Photon. Technol. Lett*., **15(2)**: 272-274, 2003.

Huang J.-F., Lo Y.-L., Cheng H.-C. and Huang S.-H., Reconstruction of chirped fiber Bragg grating parameters and phase spectrum using two thermally modulated intensity spectra and genetic algorithm, *IEEE Photon. Technol. Lett*., **18(2)**: 346-348, 2006.

Huang S., LeBlanc M., Ohn M. M. and Meaures R. M., Bragg intragrating structural sensing, *Appl. Opt.*, **34(22)**: 5003-5009, 1995.

Huang S., Ohn M. M. and Measure R. M., Phase-based Bragg intragrating distributed strain sensor, *Appl. Opt*., **35(7)**: 1135-1142, 1996.

Huang S., Ohn M. M. and Measures R. M., A novel Bragg grating distributed-strain sensor based on phase measurements, *Proc. SPIE* , **2444**: 158-169, 1995.

Huang S., Ohn M. M., LeBlanc M. and Measures R. M., Continuous arbitrary strain profile measurements with fiber Bragg gratings, *Smart Mater. Struct*., **7**: 248-256, 1998.

Iocco A., Limberger H. G., Salathe R. P., Everall L. A., Chisholm K. E., Williams J. A. R. and Bennion I., Bragg grating fast tunable filter for wavelength division multiplexing, *J. Lightwave Technol*., **17(7)**: 1217-1221, 1999.

Kannan S., Guo J. Z. Y. and Lemaire P. J., Thermal stability analysis of uv-induced fiber Bragg gratings, *J. Lightwave Technol*., **15(8)**: 1478-1483, 1997.

Kashyap R., Assessment of tuning the wavelength of chirped and unchirped fibre Bragg grating with single phase-masks, *Electron. Lett.,* **34(21)**: 2025-2027, 1998.

Kashyap R., *Fiber Bragg gratings*, 1st ed. P.L. Kelly. 1999, San Diego, USA, Academic Press, 458.

Kashyap R., McKee P. F., Campbell R. J. and WIlliams D. L., Novel method of producing all fibre photoinduced chirped gratings, *Electron. Lett.,* **30(12)**: 996-998, 1994.

Kashyap R., Swanton A. and Armes D. J., Simple techniques for apodising chirped and unchirped Bragg gratings, *Electron. Lett.,* **32(13)**: 1226-1228, 1996.

Kee H. H., Lees G. P. and Newson T. P., 1.65 um Raman-based distributed temperature sensor, *Electron. Lett*., **35(21)**: 1869-1871, 1999.

Kersey A. D., Davis M. A., Patrick H. J., LeBlanc M., Koo K. P., Askins C. G., Putnam M. A. and Friebele E. J., Fiber grating sensors, *J. Lightwave Technol*., **15(8)**: 1442 -1463, 1997.

Kim S., Kim S., Kwon J. and Lee B., Fiber Bragg grating strain sensor demodulator using a chirped fiber grating, *IEEE Photon. Technol. Lett*., **13(8)**: 839-841, 2001.

Kim S., Kwon J., Kim S. and Lee B., Temperature-independent strain sensor using a chirped grating partially embedded in a glass tube, *IEEE Photon. Technol. Lett.*, **12(6)**: 678-680, 2000.

Kimura A., Takada E., Fujita K., Nakazawa M., Takahashi H. and Ichige S., Application of a Raman distributed temperature sensor to the experimental fast reactor JOYO with correction techniques, *Meas. Sci. Technol*., **12**: 966-973, 2001.

Kitcher D. J., Nand A., Baxter G. W. and Collins S. F., Distributed temperature sensors in non-uniform and non-linearly chirped fibre Bragg gratings, *Proc. ACOFT, Canberra, Australia, CD-ROM "ACOFT/AOS '04"*,: Tue Morn, 2004.

Kitcher D. J., Nand A., Wade S. A., Baxter G. W., Jones R. and Collins S. F., Implementation of integration of differences method for extraction of temperature profiles along chirped fibre Bragg gratings, *ACOFT/AOS '06' 10-13 July, RMIT University, Melbourne, 2006.*: CD-ROM "ACOFT/AOS 2006": 57-59, 2006a.

Kitcher D. J., Nand A., Wade S. A., Baxter G. W., Jones R. and Collins S. F., Cross-correlation method to obtain temperature profiles from reflection spectra of a chirped fiber Bragg grating, *Proc. SPIE* **5855**, *OFS – 17, Bruges, Belgium* 816-819, 2005a.

Kitcher D. J., Nand A., Wade S. A., Baxter G. W. and Collins S. F., Phase errors and ripple in linearly chirped FBGs for temperature profile measurement by cross-correlation, *Proc. ACOFT Conference 4-8 July 2005, Sydney, Australia: CD-ROM BGPP/ACOFT 2005*, 552-555, 2005b

Kitcher D. J., Nand A., Wade S. A., Baxter G. W., Jones R. and Collins S. F., Influence of internal losses on reflectance spectra of non-uniform linearly chirped fibre Bragg gratings, *7th Australasian Conference on Optics, Lasers and Spectroscopy, Rotorua, New Zealand*, CD ROM: ThP29, 2005c.

Kitcher D. J., Nand A., Wade S. A., Jones R., Baxter G. W. and Collins S. F., Directional dependence of spectra of fiber Bragg gratings due to excess loss, *J. Opt. Soc. Am. A (Optics, Image Science and Vision)*, **23(11)**: 2906-2911, 2006.

Ko P. K. Y., Demokan M. S. and Tam H., Distributed temperature sensing with erbium-doped fiber amplifiers, *J. Lightwave Technol*., **14(10)**: 2236-2245, 1996.

Koo K. P., LeBlanc M., Tsai T. E. and Vohra S. T., Fiber-chirped grating fabry-perot sensor with multiple-wavelength-addressable free-spectral ranges, *IEEE Photon. Technol. Lett*., **10(7)**: 1006-1008, 1998.

Larkin A. G. and Sheridan J. T., Linear spatial temperature distribution fibre Bragg grating sensor, *J. Opt. A: Pure Appl. Opt.,* **6**: 439-446, 2004.

LeBlanc M., Huang S. Y., Ohn M., Measures R. M., Guemes A. and Othonos A., Distributed strain measurement based on a fiber Bragg grating and its reflection spectrum analysis, *Opt. Lett*., **21(17)**: 1405-1407, 1996.

Lecoeuche V., Hathaway M. W., Webb D. J., Pannell C. N. and Jackson D. A., 20-km distributed temperature sensor based on spontaneous Brillouin scattering, *IEEE Photon. Technol. Lett*., **12(10)**: 1367-1369, 2000.

Lee C. C., Chiang P. W. and Chi S., Utilization of a dispersion-shifted fiber for simultaneous measurement of distributed strain and temperature through Brillouin frequency shift, *IEEE Photon. Technol. Lett*., **13(10)**: 1094 -1096, 2001.

Lemaire P. J., Atkins R. M., Mizrahi V. and Reed W. A., High pressure H_2 loading as a technique for achieving ultrahigh UV photosensitivity and thermal sensitivity in GeO_2 doped optical fibres, *Electron. Lett.,* **29(13)**: 1191-1193, 1993.

Li M., Zeng N., Shi C. Z., Zhang M. and Liao Y. B., Fiber Bragg grating distributed strain sensing: An adaptive simulated annealing algorithm approach, *Opt. Laser Technol*., **37**: 454-457, 2005.

Lien V., Wu Y., Zhang D., Berdichevsky Y., Choi J. and Lo Y.-H., A novel technology for fabricating gratings of any chirp characteristics by design, *IEEE Photon. Technol. Lett.,* **15(5)**: 712-714, 2003.

Ling H.-Y., Lau K.-T., Cheng L. and Chow K.-W., Embedded fibre Bragg grating sensors for nonuniform strain sensing in composite structures, *Meas. Sci. Technol*., **16**: 2415-2424, 2005.

Liu H., Tjin S. C., Ngo N. Q., Tan K. B., Chan K. M., Ng J. H. and Lu C., A novel method for creating linearly and nonlinearly chirped fiber Bragg gratings, *Opt. Commun*., **217(1-6)**: 179-183, 2003.

Malo B., Hill K. O., Bilodeau F., Johnson D. C. and Albert J., Point-by-point fabrication of micro-Bragg gratings in photosensitive fibre using single excimer pulse refractive index modification techniques, *Electron. Lett.,* **29(18)**: 1668-1669, 1993.

Meltz G., Morey W. W. and Glenn W. H., Formation of Bragg gratings in optical fibers by a transverse holographic method, *Opt. Lett*., **14(15)**: 823-825, 1989.
Miller G. A., Askins C. G. and Friebele E. J., Modified F-matrix calculation of Bragg grating spectra and its use with a novel nonlinear index growth law, *J. Lightwave Technol*., **24(6)**: 2416-2427, 2006.

Miller G. A., Askins C. G., Skeath P., Wang C. C. and Friebele E. J., Fabricating fiber Bragg gratings with tailored spectral properties for strain sensor arrays using a post-exposure rescan technique, *Optical Fiber Sensors Conference Technical Digest, 2002. OFS 2002, 15th*, *IEEE*, 2002.

Mohanty L., Tjin S. C. and Ngo N. Q., Simultaneous measurement of load and position with an embedded chirped sampled fibre grating, *J. Opt. A: Pure Appl. Opt*., **7**: 29-34, 2005.

Murukeshan V. M., Chan P. Y., Ong L. S. and Asundi A., Intracore fiber Bragg gratings for strain measurement in embedded composite structures, *Appl. Opt*., **40(1)**: 145-149, 2001.

Nand A., Kitcher D. J., Wade S. A., Baxter G. W. and Collins S. F., Chirped fibre Bragg grating distributed temperature sensor, *16th Biennial congress of the Australian Institute of Physics incorporating the conference of the Australian Optical Society, Canberra, Abstracts p. 105*: 105, 2005a.

Nand A., Kitcher D. J., Wade S. A., Baxter G. W. and Collins S. F., Temperature profile measurements within a chirped fiber Bragg grating using a Fourier transform technique, *Proc. SPIE **5855**, OFS – 17, Bruges, Belgium.*: 820-823, 2005b.

Nand A., Kitcher D. J., Wade S. A., Baxter G. W. and Collins S. F., Determination of the position of a localised heat source within a chirped fibre Bragg grating, *Proc. BGGP Conference 4-8 July 2005, Sydney, Australia: CD-ROM "BGPP/ACOFT 2005",* 448-450, 2005c.

Nand A., Kitcher D. J., Wade S. A., Jones R., Baxter G. W. and Collins S. F., Strain independent temperature measurements using a standard and a chirped fibre Bragg grating, *Australian conference on optical fibre Technology, ACOFT/AOS '06' 10-13 July, RMIT University, Melbourne, 2006.*: *CD-ROM: "ACOFT/AOS 2006*", pp. 51-53, 2006a.

Nand A., Kitcher D. J., Wade S. A., Nguyen T. B., Baxter G. W., Jones R. and Collins S. F., Determination of the position of a localised heat source within a chirped fibre Bragg grating using a Fourier transform technique, *Meas. Sci. Technol*., **17**: 1436-1445, 2006.

Nand A., Kitcher D. J., Wade S. A., Jones R., Baxter G. W. and Collins S. F., Localized strain measurements using an integration method to process intensity reflection spectra from a chirped FBG, *accepted by 3rd European Workshop on Optical Fibre Sensors, 4-6 July, Napoli, Italy*, (accepted March 15, submitted 9 February 2007).

Oh K., Westbrook P. S., Atkins R. M., Reyes P., Windeler R. S., Reed W. A., Stockert T. E., Brownlow D. and DiGiovanni D., Ultraviolet photosensitive response in an antimony-doped optical fiber, *Opt. Lett*., **27(7)**: 488-490, 2002.

Ohn M. M., Huang S. Y., Measures R. M. and Chwang J., Arbitrary strain profile measurement within fibre gratings using interferometric Fourier transform technique, *Electron. Lett*., **33(14)**:1242-1243, 1997.

Okabe Y., Tsuji R. and Takeda N., Application of chirped fiber Bragg grating sensors for identification of crack locations in composites, *Compos. Part A: Appl. Sci. Manufact*., **35**: 59-65, 2004.

Okude S., Sakai T., Wada A. and Yamauchi R., Novel chirped fiber grating utilizing a thermally diffused taper-core fiber, *Optical Fiber Communications, 1996. OFC '96*. 1996.

Othonos A. and Kalli K., *Fibre Bragg Gratings: Fundamentals and Applications in Telecommunications and Sensing*. 1st ed. 1999, Boston, London, Artech House Publishers, 422.

Painchaud Y., Chandonnet A. and Lauzon J., Chirped fibre gratings produced by tilting the fibre, *Electron. Lett*., **31(3)**: 171-172, 1995.

Pal S., Sun T., Grattan K. T. V., Wade S. A., Collins S. F., Baxter G. W., Dussardier B. and Monnom G., Strain-independent temperature measurement using a type-I and type IIA optical fiber Bragg grating combination, *Rev. Sci. Instrum.,***75(5)**: 1327-1331, 2004.

Palaniappan J., Wang H., Ogin S. L., Thorne A., Reed G. T. and Tjin S. C., Use of conventional and chirped optical fibre Bragg gratings to detect matrix cracking damage in composite materials, *J. Phys. Conference Series: Sens and Appl. XIII*, **15:** 55-60, 2005.

Palaniappan J., Wang H., Ogin S. L., Thorne A., Reed G. T., Tjin S. C. and McCartney L. N., Prediction of the reflected spectra from chirped fibre Bragg gratings embedded within cracked crossply laminates, *Meas. Sci. Technol*., **17**: 1609-1614, 2006.

Parker T. R., Farhadiroushan M., Feced R., Handerek V. A. and Rogers A. J., Simultaneous distributed measurement of strain and temperature from noise-initiated Brillouin scattering in optical fibers, *IEEE J. Quantum Electron*., **34(4)**: 645-659, 1998.

Parker T. R., Farhadiroushan M., Handerek V. A. and Rogers A. J., A fully distributed simultaneous strain and temperature sensor using spontaneous Brillouin backscatter, *IEEE Photon. Technol. Lett*., **9(7)**: 979-981, 1997.

Patterson B. A., Sampson D. D., Krug P. A. and Jones S. K., In vivo quasi-distributed temperature sensing with fiber Bragg gratings, *Technical Digest Lasers and Electo-Optics Conference (IEEE, USA)*: 402-403, 2001.

Peters K., Pattis P., Botsis J. and Giaccari P., Experimental verification of response of embedded optical fibre Bragg grating sensors in non-homogeneous strain fields, *Opt. Lasers Eng*., **33**: 107-119, 2000.

Peters K., Studer M., Botsis J., Locco A., Limberger H. and Salathe R., Embedded optical fiber Bragg grating sensor in a nonuniform strain field: Measurements and simulations, *Experimental Mechanics*, **41(1)**: 19-28, 2001.

Posey R., Johnson G. A. and Vohra S. T., Strain sensing based on coherent Rayleigh scattering in an optical fibre, *Electron. Lett*., **36(20)**: 1688-1689, 2000.

Poumellec B., Niay P., Douay M. and Bayons J. F., The uv-induced refractive index grating in Ge:SiO_2 preforms: Additional CW experiments and the macroscopic origin of the change in index, *J. Phys. D: Appl. Phys*., **29**: 1842-1856, 1996.

Prabhugoud M. and Peters K., Modified transfer matrix formulation for Bragg grating strain sensors, *J. Lightwave Technol*., **22(10)**: 2302-2309, 2004.

Prohaska J. D., Snitzer E., Rishton S. and Boegli V., Magnification of mask fabricated fibre Bragg gratings, *Electron. Lett.,* **29(18)**: 16141-615, 1993.

Putnam M. A., Williams G. M. and Friebele E. J., Fabrication of tapered, strain-gradient chirped fibre Bragg gratings, *Electron. Lett.,* **31(4)**: 309-310, 1995.

Rao Y. J., In-fibre Bragg grating sensors, *Meas. Sci. Technol*., **8**: 355-375, 1997.

Rao Y. J., Recent progress in applications of in-fibre Bragg grating sensors, *Opt. Lasers Eng.,* **31**: 297-324, 1999.

Rao Y. J., Zeng X. K., Zhu Y., Wang Y. P., Zhu T., Ran Z. L., Zhang L. and Bennion I., Temperature-strain discrmination sensor using a WDM chirped in fibre-Bragg-grating and an extrinsic fabry-perot, *Chin. Phys. Lett.*, **18(5)**: 643-645, 2001.

Rogers A., Distributed optical-fibre sensing, *Meas. Sci. Technol*., **10**: R75-R99, 1999.

Shi C. Z., Zeng N., Chan C. C., Liao Y. B., Jin W. and Zhang L., Improving the performance of FBG sensors in a WDM network using a simulated annealing technique, *IEEE Photon. Technol. Lett*., **16(1)**: 227-229, 2004.

Shi C. Z., Zeng N., Zhang M., Liao Y. B. and Lai S. R., Adaptive simulated annealing algorithm for the fiber Bragg grating distribuited strain sensing, *Opt. Commun*., **226**: 167-173, 2003.

Shlyagin M. G., Miridonov S. V., Borbon I. M., Spirin V. V., Swart P. L. and Chtcherbakov A. A., Multiplexed twin Bragg grating interferometric sensor, *Optical Fiber Sensors Conference Technical Digest, IEEE*, 2002.

Shu X., Liu Y., Zhao D., Gwandu B., Floreani F., Zhang L. and Bennion I., Dependence of temperature and strain coefficients on fibre grating type and its application to simultaneous temperature and strain measurement, *Opt. Lett*., **27(8)**: 701-703, 2002.

Shu X., Zhao D., Zhang L. and Bennion I., Use of dual-grating sensors formed by different types of fiber Bragg gratings for the simultaneous temperature and strain measurements, *Appl. Opt*., **43(10)**: 2006-2012, 2004.

Smith E. D. J., Patterson B. A., Webster R. J., Krug P. A., Jones S. K. and Sampson D. D., Engineering a portable quasi-distributed fibre Bragg grating temperature sensing system for clinical hyperthermia, *Optical Fiber Sensors Conference Technical Digest, 2002*, *IEEE,* **1**: 269-272, 2002.

Souza K. D., Significance of coherent Rayleigh noise in fibre-optic distributed temperature sensing based on spontaneous Brillouin scattering, *Meas. Sci. Technol*., **17**: 1065-1069, 2006.

Sugden K., Bennion I., Molony A. and Copner N. J., Chirped gratings produced in photosensitive optical fibres by fibre deformation during exposure, *Electron. Lett.,* **30(5)**: 440-442, 1994.

Swart P. L., Lacquet B. M. and Chtcherbakov A. A., Chirped fibre Bragg grating sensor for pressure and position sensing, *Opt. Eng*., **44(5)**: 054402-(1-4), 2005.

Tian X. G. and Tao X. M., Torsion measurement using fiber Bragg grating sensors, *Experimental Mechanics*, **41(3)**: 248-253, 2001.

Tjin S. C., Wang Y., Sun X., Moyo P. and Brownjohn J. M. W., Application of quasi-distributed fibre Bragg grating sensors in reinforced concrete structures, *Meas. Sci. Technol*., **13**: 583-589, 2002.

Trpkovski S., Wade S. A., Collins S. F. and Baxter G. W., Er^{3+}:Yb^{3+} doped fiber with embedded FBG for simultaneous measurement of temperature and longitudinal strain, *Meas. Sci. Technol*., **16**: 488-496, 2005.

Volanthen M., Geiger H. and Dakin J. P., Distributed grating sensors using low-coherence reflectometry, *J. Lightwave Technol*., **15(11)**: 2076-2082, 1997.

Volanthen M., Geiger H., Cole M. J. and Dakin J. P., Measurement of arbitrary strain profiles within fibre gratings, *Electron. Lett*., **32(11)**: 1028 -1029, 1996.

Wait P. C. and Hartog A. H., Spontaneous Brillouin-based distributed temperature sensor utilizing a fiber Bragg grating notch filter for the separation of the Brillouin signal, *IEEE Photon. Technol. Lett*., **13(5)**: 508-510, 2001.

Wang Y., Grant J., Sharma A. and Myers G., Modified Talbot interferometer for the fabrication of fibre-optic grating filter over a wide range of Bragg wavelength and bandwidth using a single phase mask., *J. Lightwave Technol*., **19(10)**: 1569-1573, 2001.

Williams G. M., Tsung-Ein T., Merzbacher C. I. and Friebele E. J., Photosensitivity of rare-earth-doped ZBLAN fluoride glasses, *J. Lightwave Technol*., **15(8)**: 1357-1362, 1997.

Won P. C., Leng J., Lai Y. and Williams J. A. R., Distributed temperature sensing using a chirped fibre Bragg grating, *Meas. Sci. Technol*., **15**: 1501-1505, 2004.

Wu M.-C., Rogowski R. S. and Tedjojuwono K. K., Fabrication of extremely short length fiber Bragg gratings for sensor applications*, Sensors 2002, Proc. IEEE*, **1**: 49-55, 2002.

Xu M. G., Dong L., Reekie L., Tucknott J. A. and Cruz J. L., Temperature-independent strain sensor using chirped Bragg grating in a tapered optical fibre, *Electron. Lett*., **31(10)**: 823-825, 1995.

Yamada M. and Sakuda K., Analysis of almost-periodic distributed feedback slab waveguides via a fundamental matrix approach, *Appl. Opt*., **26**: 3474-3478, 1987.

Zhao D., Shu X., Lai Y., Zhang L. and Bennion I., Fiber Bragg grating sensor interrogation using chirped fiber grating-based Sagnac loop, *IEEE Sensors J*., **3(6)**: 734-738, 2003.

Zhao D., Shu X., Zhang L. and Bennion I., Sensor interrogation technique using chirped fibre grating based Sagnac loop, *Electron. Lett*., **38(7)**: 312-313, 2002.

Zheng R. T., Ngok N. Q., Binh L. N., Tjin S. C. and Yang J. L., Chirped fiber Bragg gratings with arbitrary group delay responses using stepped-stretching fiber method, *Appl. Phys. B (Lasers & Optics)*, **B82(1)**: 59-63, 2006.

Zhu Y., Lacquet B. M., Swart P. L. and Spammer S. J., Realization of chirped fibre Bragg gratings by using differently tapered transducers and loading procedures, *Meas. Sci. Technol*., **12**: 922-926, 2001.

Appendix

LIST OF PUBLICATIONS

A.1 Journal Articles

1. **Nand** A., Kitcher D. J., Wade S. A., Nguyen T. B., Baxter G. W., Jones R. and Collins S. F., Determination of the position of a localised heat source within a chirped fibre Bragg grating using a Fourier transform technique, *Meas. Sci. Technol*., **17**: 1436-1445, 2006.

2. Kitcher D. J., **Nand** A., Wade S. A., Jones R., Baxter G. W. and Collins S. F., Directional dependence of spectra of fiber Bragg gratings due to excess loss, *J Opt. Soc. Am. A (Optics, Image Science and Vision)*, **23(11)**: 2906-2911, 2006.

A.2 International Conference Proceedings

1. **Nand** A., Kitcher D. J., Wade S. A., Baxter G. W. and Collins S. F., Temperature profile measurements within a chirped fiber Bragg grating using a Fourier transform technique, *Proc. SPIE **5855**, OFS – 17, Bruges, Belgium.*: 820-823, 2005.

2. **Nand** A., Kitcher D. J., Wade S. A., Baxter G. W. and Collins S. F., Determination of the position of a localised heat source within a chirped fibre Bragg grating, *Proc. BGGP/ACOFT Conference 4-8 July 2005, Sydney, Australia: CD-ROM BGPP/ACOFT 2005,* 448-450, 2005.

3. **Nand** A., Kitcher D. J., Wade S. A., Jones R., Baxter G. W. and Collins S. F., Localized strain measurements using an integration method to process intensity reflection spectra from a chirped FBG, *accepted by 3rd European Workshop on Optical Fibre Sensors, 4-6 July, Napoli, Italy*, (accepted March 15, submitted 9 February 2007).

4. Kitcher D. J., **Nand** A., Wade S. A., Baxter G. W., Jones R. and Collins S. F., Cross-correlation method to obtain temperature profiles from reflection spectra of a chirped fiber Bragg grating, *Proc. SPIE* **5855**, *OFS – 17, Bruges, Belgium:* 816-819, 2005.

A.3 National Conference Proceedings

1. **Nand** A., Kitcher D. J., Wade S. A., Jones R., Baxter G. W. and Collins S. F., Strain independent temperature measurements using a standard and a chirped fibre Bragg grating, *Australian Conference on Optical Fibre Technology, ACOFT/AOS '06' 10-13 July, RMIT University, Melbourne, 2006.*: CD-ROM: ACOFT/AOS 2006, pp. 51-53, 2006

2. **Nand** A., Kitcher D. J., Wade S. A., Baxter G. W. and Collins S. F., Chirped fibre Bragg grating distributed temperature sensor, *16th Biennial congress of the Australian Institute of Physics incorporating the conference of the Australian Optical Society, Canberra,* Abstracts p. 105, 2005.

3. **Nand** A., Kitcher D. J., Wade S. A., Baxter G. W. and Collins S. F., Chirped fibre Bragg gratings for sensing applications, *Australasian Conference on Optics, Lasers and Spectroscopy 2003, Melbourne,* Abstracts p. 269, 2003.

4. Kitcher D. J., **Nand** A., Wade S. A., Baxter G. W., Jones R. and Collins S. F., Implementation of integration of differences method for extraction of temperature profiles along chirped fibre Bragg gratings, *ACOFT/AOS '06' 10-13 July, RMIT University, Melbourne, 2006.*: CD-ROM ACOFT/AOS 2006: 57-59, 2006.

5. Kitcher D. J., **Nand** A., Baxter G. W. and Collins S. F., Distributed temperature sensors in non-uniform and non-linearly chirped fibre Bragg gratings, *Proc. ACOFT, Canberra, Australia, CD-ROM "ACOFT/AOS '04"*,: Tue Morn, 2004.

6. Kitcher D. J., **Nand** A., Wade S. A., Baxter G. W. and Collins S. F., Phase errors and ripple in linearly chirped FBGs for temperature profile measurement by cross-correlation, *Proc. ACOFT Conference 4-8 July 2005, Sydney, Australia: CD-ROM BGPP/ACOFT 2005*, 552-555, 2005.

7. Kitcher D. J., **Nand** A., Wade S. A., Baxter G. W., Jones R. and Collins S. F., Influence of internal losses on reflectance spectra of non-uniform linearly chirped fibre Bragg gratings, *7th Australasian conference on optics, Lasers and Spectroscopy, Rotorua, New Zealand*, CD ROM: ThP29, 2005.